Abstract

Title of Dissertation: Experimental Investigation of a
Shrouded Rotor Micro Air Vehicle
in Hover and in Edgewise Gusts

Vikram Hrishikeshavan, Doctor of Philosophy, 2011

Dissertation directed by: Dr. Inderjit Chopra
Department of Aerospace Engineering

Due to the hover capability of rotary wing Micro Air Vehicles (MAVs), it is of interest to improve their aerodynamic performance, and hence hover endurance (or payload capability). In this research, a shrouded rotor configuration is studied and implemented, that has the potential to offer two key operational benefits: enhanced system thrust for a given input power, and improved structural rigidity and crashworthiness of an MAV platform. The main challenges involved in realising such a system for a lightweight craft are: design of a lightweight and stiff shroud, and increased sensitivity to external flow disturbances that can affect flight stability. These key aspects are addressed and studied in order to assess the capability of the shrouded rotor as a platform of choice for MAV applications.

A fully functional shrouded rotor vehicle (disk loading 60 N/m^2) was designed and constructed with key shroud design variables derived from previous studies on micro shrouded rotors. The vehicle weighed about 280 g (244 mm rotor diameter). The shrouded rotor had a 30% increase in power loading in hover compared to an unshrouded rotor. Due to the stiff, lightweight shroud construction, a net payload benefit of 20-30 g was achieved. The different components such as the rotor, stabilizer bar, yaw control vanes and the shroud were systematically studied for system efficiency and overall aerodynamic improvements. Analysis of the data showed that the chosen shroud dimensions was close to optimum for a design payload of 250 g. Risk reduction prototypes were built to sequentially arrive at the final configuration. In order to prevent periodic oscillations in flight, a hingeless rotor was incorporated in the shroud.

The vehicle was successfully flight tested in hover with a proportional-integral-derivative feedback controller. A flybarless rotor was incorporated for efficiency and control moment improvements. Time domain system identification of the attitude dynamics of the flybar and flybarless rotor vehicle was conducted about hover. Controllability metrics were extracted based on controllability gramian treatment for the flybar and flybarless rotor.

In edgewise gusts, the shrouded rotor generated up to 3 times greater pitching moment and 80% greater drag than an equivalent unshrouded rotor. In order to improve gust tolerance and control moments, rotor design optimizations were made by varying solidity, collective, operating RPM and planform. A rectangular planform rotor at a collective of 18 deg was seen to offer the highest control authority. The shrouded rotor produced 100% higher control moments due to pressure asymmetry arising from cyclic control of the rotor. It was seen that the control margin of the shrouded rotor increased as the disk loading increased, which is however deleterious in terms of hover performance. This is an important trade-off that needs to be considered. The flight performance of the vehicle in terms of edgewise gust disturbance rejection was tested in a series of bench top and free flight tests. A standard table fan and an open jet wind tunnel setup was used for bench top setup. The shrouded rotor had an edgewise gust tolerance of about 3 m/s while the unshrouded rotor could tolerate edgewise gusts greater than 5 m/s. Free flight tests on the vehicle, using VICON for position feedback control, indicated the capability of the vehicle to recover from gust impulse inputs from a pedestal fan at low gust values (up to 3 m/s).

Experimental Investigation of a Shrouded Rotor Micro Air Vehicle in Hover and in Edgewise Gusts

by

Vikram Hrishikeshavan

Dissertation submitted to the Faculty of the Graduate School of the
University of Maryland at College Park in partial fulfillment
of the requirements for the degree of
Doctor of Philosophy
2011

Advisory Committee:

Dr. Inderjit Chopra, Chairman/Advisor
Dr. James Baeder
Dr. Gordon Leishman
Dr. Sean Humbert
Dr. Balakumar Balachandran, Dean's Representative

Acknowledgements

My advisor, Dr. Chopra, has been incredibly patient in guiding me in my development as a researcher. This along with key inputs and criticisms have been an important factor in the completion of this research in a timely manner. He has given me freedom to explore and engage myself in other interesting projects also. For all these, I am immensely grateful to him. I would also like to thank all of my other committee members: Dr. Baeder, Dr. Leishman, Dr. Humbert and Dr. Balachandran for evaluating my research and providing me with useful advice and support. I would like to thank Dr. Humbert and Mr. Chris Kroninger for providing me with resources at the Autonomous Vehicle Lab (AVL) and Motile Robotics Inc. respectively at different points of this research.

I worked with Dr. Tishchenko in one of my first projects, whose work ethic and tricks of the trade have inspired and taught me greatly. Jayant Sirohi's sharp criticisms, knowledge and wit were other highlights early in my graduate studies that helped hone and sharpen my thinking. I am very thankful to Nitin Gupta and Peter Copp for introducing me to the daunting world of electronics and providing me with support as and when required. I would like to thank Ben Hance and Shane Boyer for assisting me in integrating the different vehicles and piloting them. I am also thankful to Joe Conroy, Greg Gremillion and Badri Ranganathan for providing technical assistance and support with VICON related tasks and other issues.

At different stages of my research, I have received many important suggestions for which I would like to thank Paul Samuel, VT, Shreyas Ananthan, Jason Pereira, Moble Benedict and Peter Copp. Discussions about the flow physics of a shrouded rotor with Vinod Lakshminarayan have been greatly useful and eye opening.

I cherish the JMP group luncheons with Arun, Abhishek, Asitav, Smita, Anand and Ria. All the people heretofore mentioned and others like Carlos, Jaye, Dean, Pranay, Monica, James and many others have made life in the lab interesting and fun. A big thanks to all my other friends who have made life outside the lab fun and exciting.

Finally, and most importantly, I would like to thank my parents and my companion-to-be, Prakruthi, for their constant love, support, guidance, patience and many many other things that one takes for granted. This would not have been possible without them.

Table of Contents

List of Tables

List of Figures

Nomenclature

A	rotor disk area, m^2
$c_{l\alpha}$	airfoil lift curve slope, $1/deg$
C_T	rotor thrust coefficient, $T/\rho A(\Omega R)^2$
C_T/σ	blade loading
c	airfoil chord, mm
c_d	airfoil drag coefficient
c_l	airfoil lift coefficient
D_t	shroud throat diameter, m
I_β	rotor flap moment of inertia, $kg-m^2$
$L_{p,q}$	lateral stability derivatives due to roll and pitch rate respectively, $1/s$
$L_{\delta_{lat},\delta_{lon}}$	lateral control derivatives due to roll and pitch cyclic input respectively, rad/s^2
L	lift/blade N
$M_{p,q}$	longitudinal stability derivatives due to roll and pitch rate respectively, $1/s$
$M_{\delta_{lat},\delta_{lon}}$	longitudinal control derivatives due to roll and pitch cyclic input respectively, rad/s^2
M	control moment, $N\ m$
p	body roll rate, rad/s
$\dot{p}$	body roll acceleration, rad/s^2
q	body pitch rate, rad/s
$\dot{q}$	body pitch acceleration, rad/s^2
r	body yaw rate, rad/s
R	rotor radius, m
t	airfoil thickness, mm
δ_{lat}	non-dimensional roll cyclic input
δ_{lon}	non-dimensional pitch cyclic input
Δ_{theta}	cyclic pitch variation, rad
η	motor efficiency
γ_R	rotor Lock Number
κ	induced power factor
ν_β	non-dimensional rotating natural flap frequency, $1/rev$
Ω	rotor angular speed, rad/s
ϕ	Euler roll angle, rad
ψ	Euler yaw angle, rad
ρ	air density, kg/m^3
σ	rotor solidity
σ_e	thrust weighted rotor solidity
σ_d	shroud diffuser expansion ratio

θ	Euler pitch angle, rad
θ_V	angle of incidence of vane chord with respect to rotor axis, deg
θ_{Swirl}	changei n angle of attack of rotor downwash due to swirl effects, deg
Θ	blade root collective, deg

BEMT	Blade-Element-Momentum Theory
CFD	Computational Fluid dynamics
DL	Disk Loading, N/m^2
FM	Figure of Merit
IGE	In Ground Effect
LE	Leading Edge of airfoil
LQR	Linear Quadratic Regulator
MAV	Micro Air Vehicle
MSLISA	Mean Sea Level International Standard Atmosphere
OGE	Out of Ground Effect
PID	Proportional-Integral-Derivative
PL	Power Loading, N/W or $gram/W$
RPM	Revolutions Per Minute
Re	Reynolds number
TE	Trailing Edge of airfoil
UAV	Unmanned Air Vehicle
VTOL	Vertical/Take-Off and Landing

Chapter 1

Introduction

1.1 Motivation and Background

1.1.1 Micro Air Vehicles

With the rapid progress in microelectronics and manufacturing capability of minitaturized components and microchips, a new class of small scale air vehicles have received significant interest in the last decade. These vehicles were termed Micro Air Vehicles (MAVs). According to the DARPA Small Business Innovation Research program in 1996 [1], the MAV was defined as an aircraft that would have no dimension larger than 15 cm, weigh about 100 g (with a payload of 20 g) and have an endurace of one hour. They were envisioned to complement existing unmanned air vehicles (UAV) in assisting military tasks as man-portable, 'eye-in-the-sky' flying robots to improve situational awareness and minimize exposure of the soldier to risk. In addition, other potential applications for MAVs include biochemical sensing, targeting, communications, search and rescue, traffic monitoring, fire rescue and power-line inspection. A recent collaborative research effort [2] undertaken by U.S. Army Research Laboratory

(ARL) recognized that small scale aerial platforms have the potential to surveil large areas of urban terrain and extend reach of small ground units into unknown environments. For these tactical operations, they require the fidelity and capability to operate in confined spaces like alleyways, interior rooms, or caves (Fig. 1.1). Their low detectability and low noise signatures, maneuverability within confined spaces, and potential for out of sight flight operations make them ideal for military and civilian missions. For some of these missions, there is a need to develop autonomous MAVs with good hover and loiter endurance capability, high maneuverability to enable operation in closed spaces, and ability to tolerate and overcome external aerodynamic disturbances such as wind gusts and flow recirculation due to ground effects while flying in the vicinity of walls.

Figure 1.1: Examples of MAV operations in aerial surveillance missions and confined spaces

MAVs have been developed in the past to accomplish some of these needs. The existing MAV configurations can be classified based on the mechanism used to generate aerodynamic forces for flight. These are fixed-wing, rotary-wing and

flapping-wing MAVs.

Fixed-wing MAVs: These were the first generation of MAVs developed, a good example of which is the 80 gram Black Widow [3]. Other models are explained in Refs. [4–7]. The wings are fixed to the airframe and lift is generated through forward velocity provided by onboard propulsion. From a flight endurance perspective, these are the best performers for a given size and weight constraint. For instance, the Black Widow has the best endurance/weight ratio of the existing MAVs (Fig. 1.2). Ongoing research in this area includes optimizing the aerodynamic, aeroelastic and propulsive performance of these MAVs. Flexible wing designs are studied in an attempt to improve tolerance to gusts and to achieve controls without the use of conventional control surfaces.

Rotary-wing MAVs: These offer a significant advantage over fixed-wing MAVs in that they have the ability to hover and thereby vastly enhance mission capabilities. Many rotary wing MAVs have been developed such as the mesicopter [8], quadcopter [9], micro coaxial rotor [10] and single rotor [11]. The hover endurance of these vehicles is low [12], due to dominant viscous effects of low Reynolds number flow regimes at which these rotors operate in. Additionally, from a flight mechanics perspective, there is significant cross coupling in lateral and longitudinal motions and these vehicles are inherently unstable. Therefore stability augmentation of a rotary-wing system can be challenging.

Flapping-wing MAVs: These configurations are inspired from avian based and insect based flight. In the avian based mode (ornithopters), the wings are flapped in a vertical plane which result in a propulsive force and the lift is subsequently generated by a combination of wing flapping and forward speed. Ornithopters have been built and flown successfully [13,14] especially by the hobby community [15]. These vehicles do not have hover capability, which is possible with insect

based flight. In insect flight mode, the wings are typically flapped in a horizontal plane, accompanied by large changes in wing pitch angle to produce lift even in the absence of forward flight. Insects wing kinematics is high frequency and is associated with unsteady aerodynamics including dynamic stall and stable leading edge vortices [16–19]. Engineering challenges in replicating insect flight include mechanical complexity and wear and tear of components due to high frequency back and forth motions. Mentor was the first flapping MAV developed using the clap and fling mechanism [21, 22]. Wood et. al. [23] developed a 3 gram flapper and conducted successful bench top hover tests albeit without onboard power. A recent pathbreaking flapping wing design that was successfully tested in free flight is Aerovironment's Nano Hummingbird [24] (Fig. 1.2) which weighs 19 g with a hover endurance of about 11 mins. It is modeled after the hummingbird, displayed agile maneuvering capabilities and has a low noise signature.

Among the hovering air platforms discussed above, rotor-based platforms are the most advanced. This category includes single main rotor and multiple rotors. A conventional single main rotor, tail rotor (SMTR) leads to a less compact configuration. A coaxial configuration while being compact can be less efficient in hover due to aerodynamic interference between rotors. Multiple rotors such as tandem or quad-rotors do not lead to efficient compact configurations. Therefore, it is important to investigate non-conventional configurations and anti-torque systems for MAVs to improve compactness and efficiency.

Therefore, in this dissertation, a rotary wing MAV configuration is studied that employs a shroud enclosing the rotor for performance and safety improvements. Controllable vanes are placed in the rotor downwash to counter the rotor torque. Key aspects such as aeromechanics, vehicle maneuverability and gust
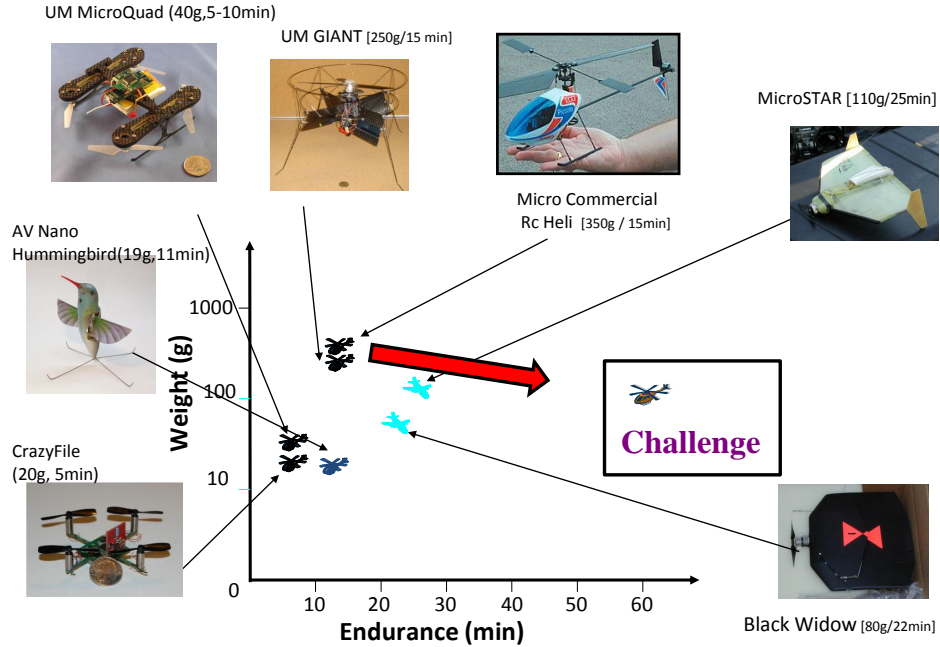
Figure 1.2: Endurance of existing micro air vehicles

tolerance of the shrouded rotor are also studied.

1.1.2   Technical challenges

There are unique challenges associated with the development of each of the three MAV configurations. The fluid flow is dominated by highly viscous and separation prone aerodynamic phenomena. The structural and propulsion design tools do not scale satisfactorily at MAV level. Areas of advancement that can lead to the development of high performance MAVs [12, 25, 26] include : 1) low Reynolds number aerodynamics, experimental, analytical and computational models, 2) micropropulsion/power sources, 3) lightweight, adaptive, and biologically inspired multifunctional materials and structures, 4) electronics minituarization, 5) efficient collision avoidance algorithms, robust navigation and control systems,

6) bio-inspired sensing techniques, and 7) system engineering tools . A discussion of all of these is beyond the scope of this dissertation. Some key technical challenges in the flight performance of small scale rotary wing vehicles are discussed in this section. For the purpose of this research, they are divided into two broad categories: 1) performance, and 2) flight stability and control.

1.1.2.1 Performance of micro rotors

MAVs operate in low Reynolds number (Re) flow regimes (between $10^4 - 10^5$) as can be seen from Fig. 1.3. At these Reynolds numbers, viscous forces dominate over inertial effects. The flow is mostly laminar, and the tendency for flow separation in the face of adverse pressure gradients is higher, which limits the maximum airfoil lift coefficients that can be achieved. McMasters and Henderson [28] found that the maximum lift-to-drag performance of various airfoils dramatically decreased for $Re < 10^5$. Figure 1.4 shows the drastically reduced lift-to-drag ratio of a N60 airfoil as the Re is reduced below a critical value. Baxter and East [25] found that as the Reynolds number decreases, the profile drag increases and that the minimum drag/minimum power configuration of fixed wing MAVs requires vehicles with lift coefficients in excess of three. These indicate that the operating C_L at which minimum drag and minimum power are obtained are significantly higher than those required at more conventional flight $(Re > 10^5)$.

The same flow physics affects rotary-wing aerodynamics. As can be seen from Fig. 1.2, the hover endurance of rotary wing MAVs is poor. The hover performance of various rotary wing MAVs can be compared using two metrics:

Figure of Merit (FM): It is the ratio of the ideal power to the actual power required to hover. The ideal power or the induced power consists of the power
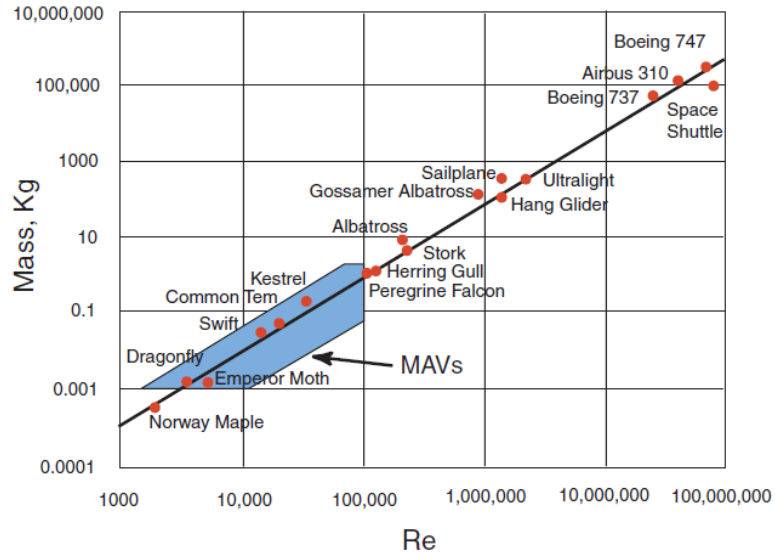
Figure 1.3: Mass vs. Re for various man-made and natural flyers (taken from [33])
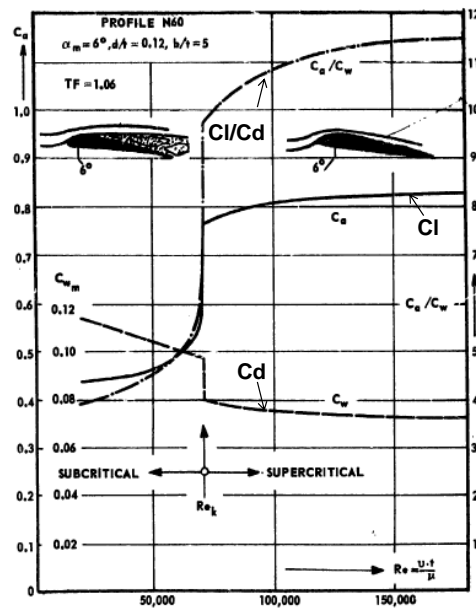
Figure 1.4: Effect of Re on maximum lift, minimum drag and maximum lift to drag coefficient [32]

7

required to change the momentum of the fluid through the rotor. The actual power is a combination of the non-ideal induced power (with losses included) and profile power.

$$FM = \cfrac{1}{\kappa_{ind} + \frac{2.6}{\sigma}\left(\frac{\overline{c_l}^{3/2}}{\overline{c_d}}\right)^{-1}} \tag{1.1}$$

where $\overline{c_l}$ is the mean blade lift coefficient, $\overline{c_d}$ is the mean drag coefficient, σ is rotor solidity and κ_{ind} the non-ideal induced power factor. The FM of full-scale rotors are in the range of 0.75-0.9 whereas MAV rotors have a maximum FM of about 0.6-0.65. In a full-scale rotor, induced power accounts for about 70% of the total power. At the MAV scale at high thrust coefficients, the profile power can be up to 45% [12].

Power Loading: It is defined as the ratio of the thrust to power required to hover. It can be expressed as a function of air density, disk loading (DL is ratio of thrust to rotor disc area) and FM,

$$\frac{T}{P} = FM\sqrt{\frac{2\rho}{DL}} \tag{1.2}$$

or as a function of non-dimensionalised thrust and power coefficients,

$$\frac{T}{P} = \frac{C_T}{C_P}\frac{1}{\Omega R} \tag{1.3}$$

Full-scale rotors have C_T/C_P ratios of about 12-14 [27] whereas micro rotors have maximum C_T/C_P values between 5-6.

In order to improve rotor efficiency, the design of the rotor system requires significant optimization of the airfoil shape, blade chord and twist distribution at low Re. From Eq.(1.1), it can be seen that both the induced power efficiency and

airfoil efficiency are important. Several studies [29–32] on low Re airfoils were conducted in a attempt to maximize $c_l^{3/2}/c_d$. It was found that at Re numbers between 10^4-10^5, thin curved plate airfoils do not suffer a large drop in maximum lift or an increase in minimum drag coefficients that airfoils such as N60 exhibit (Fig. 1.4). The superior aerodynamic performance of sharpened-leading-edge thin circular arc plates was shown by Laitone [29]. It was seen that the small nose radii of the sharp nosed airfoils prevented flow separation over a range of angles of attack. Hein and Chopra [34] and Bohorquez and Pines [35] carried out systematic hover tests on two bladed rotors using the optimized thin circular arc airfoils to examine the performance due to variations in airfoil camber, planform and twist at tip Re between 40,000 and 50,000. It was found that 6%-9% camber airfoils with a linear taper produced the best performance (Fig. 1.5). The effect of twist was generally found to be small. Flow visualization studies [34, 36, 37] of the rotor showed evidence of highly non-ideal inflow, spanwise distribution of lift and slower formation of tip vortices(Fig. 1.6).

Computational fluid dynamics (CFD) studies were also conducted to model and predict the flow structure of an MAV scale rotor. Schroeder and Baeder [38] implemented a low Mach preconditioner in a compressible Reynolds-averaged-Navier-Stokes overset structural mesh solver (OVERTURNS) to validate low Reynolds number airfoil aerodynamics for MAV applications. Lakshminarayan and Baeder [39] implemented the solver to investigate the flow characteristics of a MAV rotor (Fig. 1.7). They found that the performance of the sharp leading edge (LE) geometries increased FM by about 16% and power loading by 4%. The total thrust produced by the blunt and sharp LE geometries was similar but the blunt LE required larger power. It was also found that sharpening the trailing edge did not result in performance improvements over a sharpened LE
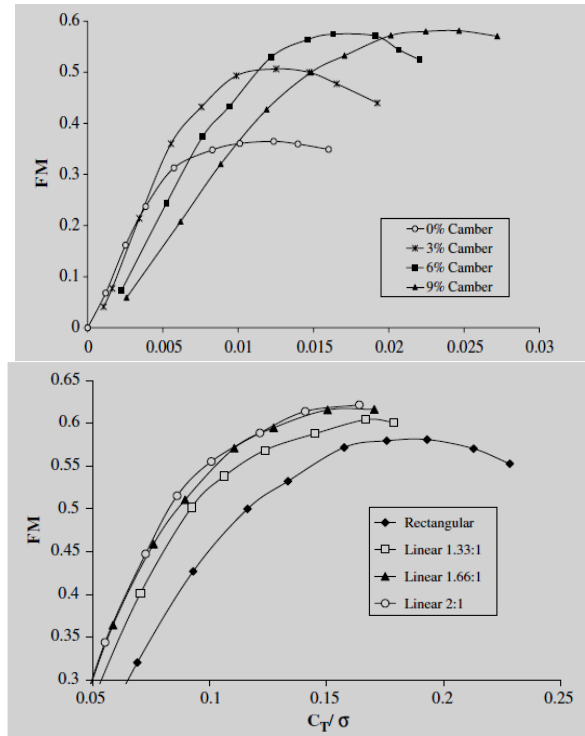
Figure 1.5: Effect of camber and taper on the FM of a 2 bladed rotor (tip Re 43,700) [35]
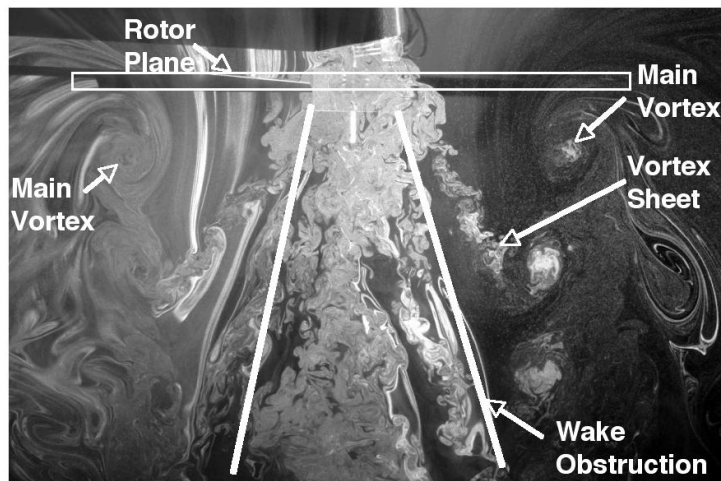
Figure 1.6: Flow visualization of a 2 bladed rotor using laser sheet at 30^0 wake age [34]
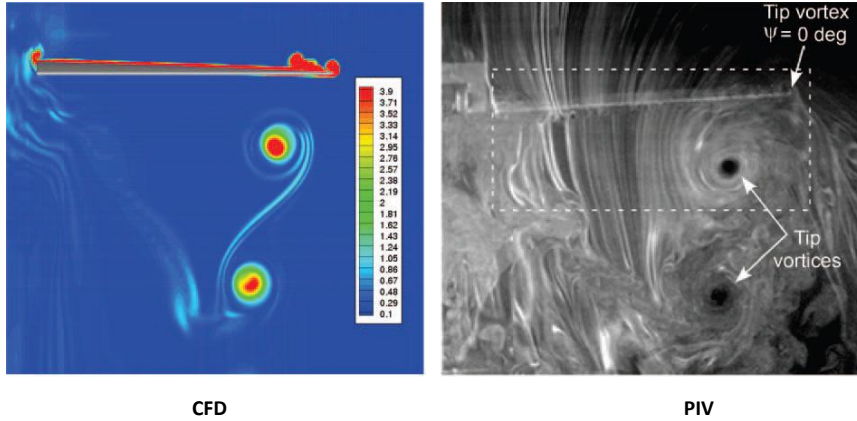
blade.

Figure 1.7: Tip vortex trajectory for a two bladed MAV rotor (tip Re= 32,400): CFD [39] and PIV [36]

As can be seen from above, there is scope for further improving rotor performance by expanding the parameter space and studying novel rotor configurations. In this research, one such configuration chosen is the shrouded rotor in which the thrust of the rotor system is sought to be increased for the same input power. The advantage of this configuration is that the previous improvements in MAV scale rotor designs can be incorporated along with performance augmentations from the shroud.

1.1.2.2 Flight stability and control

Helicopters are inherently unstable systems requiring constant attention from the pilot. It is a multivariable system that requires four control inputs for 6 degree of freedom (DOF) control. The coupling between longitudinal and lateral motions make flight controls of a rotary wing system very challenging.

Existing micro scale rotor based MAVs have similar configuration as their

full-scale counterparts. However, since scale operates on physical dimensions in different ways, the relative magnitude of the main forces change and thereby modify dynamic characteristics. These scaling effects depend on how the physical parameters and dimensions change with scale. For example, consider a full scale helicopter scaled down by a factor of N (all helicopter dimensions are scaled down by N) and that the material density remains unchanged. This implies that the weight will scale by a factor of $1/N^3$ and the moments of inertia by $1/N^5$. Clearly, the relative magnitude of the inertial and gravitational forces change resulting in a completely different dynamical system. In order to preserve dynamic similarity, Froude and Mach scaling rules will have to be applied. Mettler [40] applied these scaling laws on two full scale helicopters Bell UH-1H and Robinson R-22 and two model scale helicopters Yamaha R-50 and MIT's X-Cell. The scaling effects confirmed that as the size of the rotorcraft is reduced, the system bandwidth and sensitivity to control inputs increased.

This translates into an increased agility and also increases pilot workload. This also implies that scaled down helicopters are difficult to control, and stabilizer bars are typically used to compensate for these scaling effects. As we move down to the micro scale, it therefore becomes necessary to also implement high bandwidth electronic feedback systems for stability augmentation and control purposes. This can potentially enable the vehicle to have different dynamic characteristics at different flight conditions. For example, high maneuverability is desired while operating in cluttered environments (by increasing rate sensitivity and bandwidth) and increased stability is desired during unmeasurable input disturbances such as gusts. This opens up challenges in the control system design for optimal performance for different design points which may require nonlinear control schemes and other approaches such as gain scheduling/switching

schemes.

Fully autonomous flight for unmanned rotorcraft requires high-authority control systems. Autonomous control and high maneuverability appear to define today's unmanned rotorcraft research field [40]. Weilenmann [41] used a model helicopter as a test bed to evaluate the performance of various multivariable control design techniques $(LQ, H_\infty, \mu-\text{synthesis})$ using a classical single-input single-output (SISO) proportional-integral-derivative (PID) controller as a benchmark. The results show that the multivariable model-based control-design methods outperformed the classical SISO control systems using performance and stability metrics such as bandwidth, cross-axis effects, disturbance rejection and stability margin. Gavrilets et. al. [42] developed a simplified non-linear model of the X-Cell and a control logic for automated execution of aerobatic maneuvers [43] using a linear quadratic (LQ) control. Other studies involving dynamics modeling and control system design for autonomous unmanned helicopters include Refs. [44–46, 48, 49].

To summarize, rotary wing MAVs typically have much higher thrust/inertia ratios compared to full-scale rotorcraft, which translate into increased control sensitivity. Also, due to their small relative speeds, their sensitivity to input disturbances from aerodynamic perturbations such as external gusts increases. Therefore, the development of new configurations of rotary wing MAVs require that in addition to performance studies, they be systematically studied for their controllability, control system implementation and gust disturbance rejection, which will be a key focus in this research.

In this section, key technical challenges in the development of micro scale rotary wing vehicles are presented. In the next section, a basic introduction to the performance improvement aspects of the shrouded rotor will be described.

The literature survey section discusses research and developmental work done on ducted fan manned and unmanned vehicles in the area of experimental aerodynamics, analysis, flow control, flight dynamics and control, and the effect of gusts on MAV flight performance.

1.1.3 Performance improvement in hover: Shrouded rotor configuration

It was discussed earlier that the aerodynamic performance of micro rotors is poor compared to full-scale rotors. Previous studies showed that with a careful design of the airfoil and rotor, micro-rotor performance can be improved. In conjunction with these design improvements, alternate rotor configurations can be incorporated which may have potential for better performance than conventional micro-rotors. One such configuration considered in this research is the shrouded rotor.

Here the rotor is surrounded by a cylindrical shroud or duct. As mentioned in Ref. [50], an arbitrary convention is that the enclosing structure is a duct if the length of the cylinder is greater than the rotor diameter, otherwise it is called a shroud or a short-chord duct. In this dissertation, the terms 'shroud' and 'duct' will be used interchangeably since previous literature has not been consistent with the notation. Typically, the shroud has a rounded leading edge and straight or tapered trailing edge, which form the inlet and diffuser sections of the shroud respectively (Fig. 1.8). This configuration has been studied for over half a century for applications in marine propellers, helicopter tail rotors, manned and unmanned air vehicles. Past studies have shown significant improvement in aerodynamic performance when compared to an unshrouded or 'open' rotor.
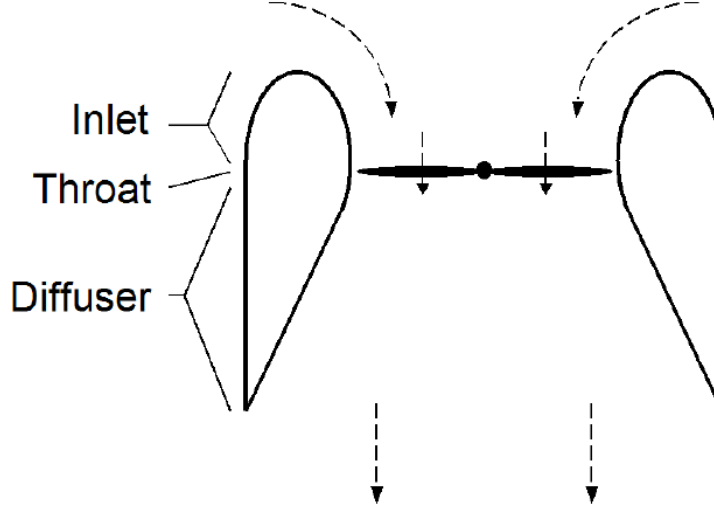
Figure 1.8: Cross section of a shroud enclosing the rotor [50]

Let T_{SR}, T_{OR}, P_{iSR} and P_{iOR} be the thrust generated by the shrouded rotor, open (or unshrouded) rotor, induced power consumed by the shrouded rotor and open rotor respectively. Also let σ_d be the contraction ratio of the shroud, i.e., the ratio of exit area of the rotor wake (area of cross section at diffuser exit) to the area of the rotor disk. If the rotor area of the shrouded and unshrouded rotors are the same, it can be shown from momentum theory that, *At constant induced power*: Here, $P_{iSR} = P_{iOR}$

$$\frac{T_{SR}}{T_{OR}} = (2\sigma_d)^{1/3} \tag{1.4}$$

At constant total thrust: Here, $T_{SR} = T_{OR}$

$$\frac{P_{iSR}}{P_{iOR}} = \frac{1}{\sqrt{2\sigma_d}} \tag{1.5}$$

15

For a straight diffuser section, $(\sigma_d = 1)$, it can be seen that momentum theory predicts a 26% improvement in thrust for a shrouded rotor over an unshrouded rotor at the same induced power. For the same total thrust, a 30% reduction in induced power is predicted. Section 2.6 discusses these aspects in further detail.

In addition to these aerodynamic benefits, shrouded rotor offers two other advantages over an unshrouded rotor: (1) the shroud protects the rotating blades from damage by other objects and greatly enhances structural integrity of the vehicle, and (2) it can potentially attenuate the noise signature of the rotor. Therefore, there is a great incentive in incorporating a shroud in an MAV rotor configuration.

1.1.3.1 Challenges in shrouded rotor implementation

However, it can be seen that to maximize thrust improvements, the weight of the shroud should be a key factor. The shrouded rotor configuration is a viable option as long as the increase in thrust over that of an open rotor is greater than the weight of the shroud. Therefore, the shroud construction that results in a sturdy lightweight structure is a significant challenge.

While ensuring efficient flight in hover, it is also important for the MAV to be tolerant to cross winds and be able to transition quickly to translational flight. However, the shrouded rotor has an undesirable characteristic of generating adverse pitching moments when faced with edgewise flow (Fig. 1.9). Therefore, this may limit the extent of operability of the MAV in gusty situations. An evaluation of these forces and the control moments required to overcome them is of importance in order to evaluate the effectiveness of the shrouded rotor MAV as a platform of choice. This research will carefully address each of these issues.
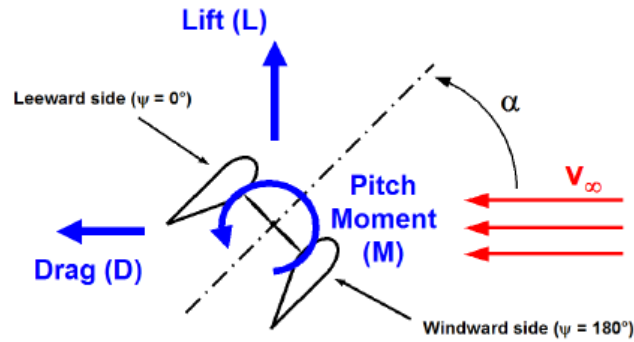
Figure 1.9: Shrouded rotor in non axial flow

1.2 Previous Work and Research

1.2.1 Shrouded rotor / Ducted fan based vehicles

As early as 1923, a patent was issued by George Hamel [51] illustrating a fixed wing aircraft with a fan-in-wing configuration in which the propellers were embedded in the wings with their axes perpendicular to the wing chord. This was in an attempt to combine the favourable characteristics of a helicopter in VTOL mode and an airplane in fixed wing mode. However, no knowledge of potential performance improvements of the fan shrouded in the wing was shown in the patent. About a decade later, there was awareness of improvements in propulsive efficiency of ship propellers [52] by surrounding them with nozzle-shaped appendages as indicated in a patent filed by Ludwig Kort [53]. Around 1933, Luigi Stipa from Italy integrated an air propeller with a hollow airplane fuselage [54] that was supposed to act as the diffuser section of the duct and he found performance improvements compared to the open propeller in terms of thrust

increase and power decrease [55].
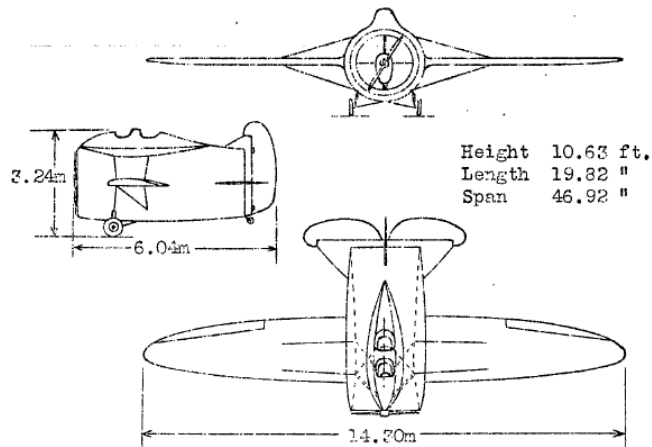
Figure 1.10: Venturi fuselage design by Stipa [54]

By the 1960s, there was considerable interest in the United States in developing vertical/short take-off and landing aircraft. This led to a lot of experimental work and design of flying crafts (Fig. 1.11) such as the single shrouded propeller Hiller VZ-1 [56], the tandem shrouded propeller Piasecki PA-59K Airgeep [57], twin and quad tilt-ducted aircrafts such as the Doak VZ-4 [58] and Bell X-22A [59] respectively and fan-in-wing aircraft such as the GE/Ryan XV-5 [60] and Vanguard Omniplane [61]. Interestingly, data collected during the flight tests of X-22 from 1960-1970 was used in the development of the V-22 Osprey. A notable effort from Europe to develop ducted VTOL aircraft is the Nord 500 'Cadet' with its tilt duct configuration (Fig. 1.12) [62]. In addition to V/STOL applications, the shrouded propellers were also used as a means of thrust compounding as found in aircrafts such as (Fig. 1.13) Mississippi State University's XV-11A Marvel [64] and Piasecki Pathfinder 16H,16H-1 [65]. Another application was the shrouded tail-rotor or 'fan-in-fin' helicopters which received research
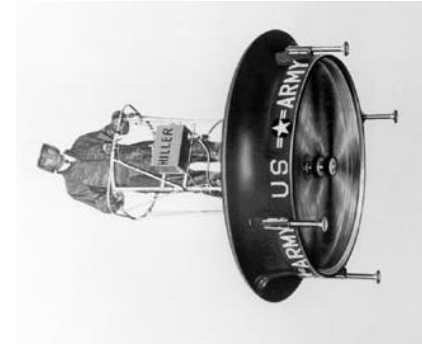
18

Doak VZ-4

Piasecki Airgeep

Hiller VZ-1
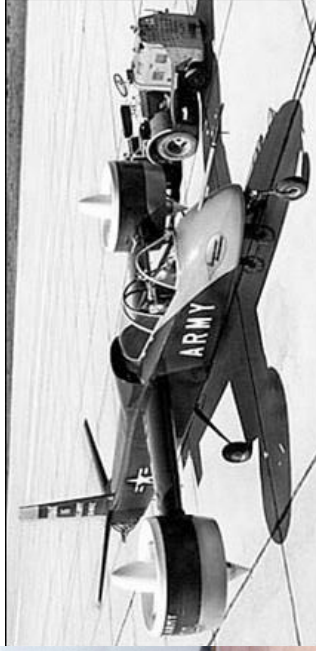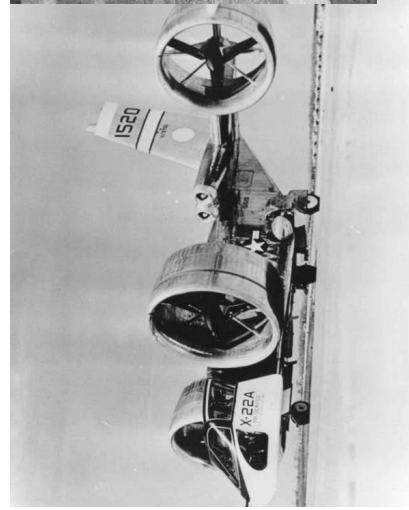
Vanguard Omniplane

Ryan XV-5

Bell X-22A
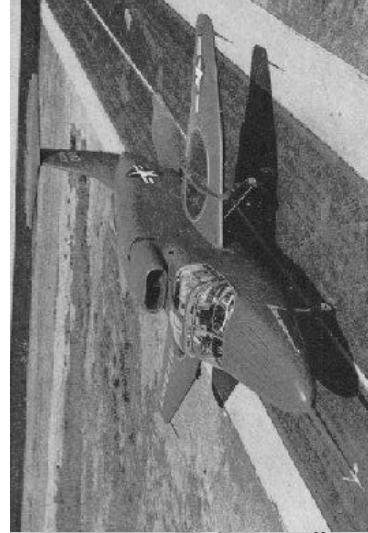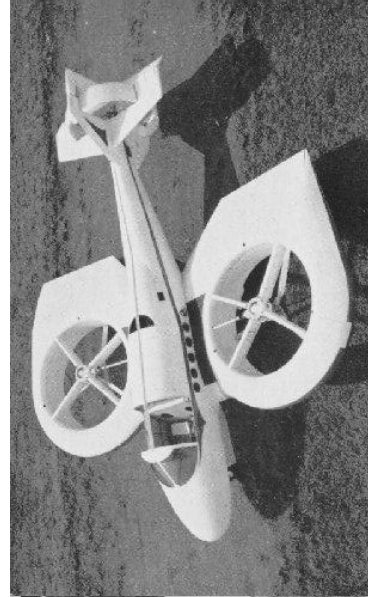
Figure 1.11: Shrouded rotors for manned V/STOL aircraft applications

Figure 1.12: Nord 500 Cadet tilt-duct aircraft

Marvel XV-11A

Piasecki Pathfinder 16H-1

RAH-66 Comanche

Dauphin

Figure 1.13: Shrouded rotors for thrust compounding and fan-in-fin applications

interest in the 1970s. It was originally termed the 'fenestron' as developed by Aérospatiale for their SA-341 Gazelle helicopter in 1970 [66]. In terms of power efficiency and operational safety, the fenestron tail rotor was found to be superior to a conventional tail rotor [67,118]. The Comanche and Dauphin helicopers employing the fenestron tail rotor are shown in Fig. 1.13. The XOH-1 observation helicopter from Japan [69] and the Ka-60 helicopter from the Kamov Company, Russia were examples of some other aircrafts with the fan-in-fin system.

Beyond the 1980s, interest grew in the development of unmanned VTOL aircrafts that could assist humans in cluttered environments. Since these crafts would operate in close proximity to humans, the shrouded rotor configuration was a preferred choice due to the protection offered by the shroud [9]. For attitude control, these vehicles either commonly used guide vanes placed in the propwash to generate moments or conventinoal rotor cyclic control. For countering the rotor torque, either stator vanes were used in the downwash or a coaxial rotor system was incorporated. Some prominent UAVs employing the shrouded/ducted rotor configuration are shown in Fig. 1.14. These include the Airborne Remote Operated Device (AROD), developed by Sandia national laboratories [70], the 'Cypher', developed by the Sikorsky Aircraft Corporation in the 1990s for the US military's Air-Mobile Ground Security and Surveillance System program [71,72], Honeywell's T-Hawk [73], Microcraft's iSTAR [74] and Georgia Tech's GTSpy [75].

The disk loading of these vehicles were very large (greater than 300 N/m^2). A high disk loading configuration is inefficient in an unshrouded rotor setup. The relative merits of reconfiguring an unshrouded rotor with a shroud are not clear from an observation of these vehicle designs.

Therefore, in this research, a low disk loading shrouded rotor vehicle, TiShrov

[76], is developed, which is one of the smallest in the category of ducted fan vehicles in both weight and size. Table 1.1 gives a comparison of the various characteristics of some of the existing shrouded rotor/ducted fan UAVs.

Sandia AROD (1989)

Sikorsky Cypher (1992)

Micro-craft iSTAR (2001)

Honeywell T-Hawk (2006)

Figure 1.14: Shrouded rotors for unmanned V/STOL applications

1.2.2 Experimental work: Shrouded rotor aerodynamic performance

The experimental work on ducted propellers carried out in the past can be divided into three categories corresponding to the three flight regimes of typical

Vehicle	GTOW (kg)	Rotor System, Lateral and Yaw control	Rotor diameter(m)	Thrust-power (installed) (N/W)	Disk Loading (N/m^2)
Cypher	200	Coaxial, variable pitch prop, swashplate (pitch,roll), vanes (yaw)	2.2	0.053	2062
iSTAR	1.4	Single, fixed pitch prop, fully deflectable vanes (pitch,roll,yaw)	0.23	0.015	340
T-Hawk MAV	7.7	Single, fixed pitch prop, fully deflectable vanes (pitch,roll, yaw)	0.33	0.025	882
TiShrov	0.28	single, fixed pitch rotor, swashplate (pitch,roll), partially deflectable vanes (yaw)	0.25	0.042	52

Table 1.1: Comparison between existing shrouded rotor UAVs

ducted fan VTOL aircraft: 1) Static operation (Hovering flight), (2) Axial flow (High-speed flight) and (3) Non-axial flow (transitional flight). The next two sections briefly survey previous work done in these categories in terms of aerodynamic performance. A more detailed review can be found in [50, 77].

1.2.2.1 Hover and axial flight

Here the flow field around the shroud is mostly axisymmetric and no lateral and longitudinal moments are expected. The literature credits Ludwig Kort [53] and Luigi Stipa [54] for performing some of the first scientific experimental studies on optimizing the performance of propellers (marine and air respectively) enclosed in a duct for improved thrust characteristics. The design of the ducted propeller involved a variation of multiple parameters such as, 1) duct variables: chord/diameter ratio, camber, leading edge radius, and chord line orientation relative to axis, (2) propeller variables: solidity, overal pitch setting, distribution, blade profile, and chord distribution, and (3) overall variable: propeller location within shroud, tip clearance, etc.

These initial efforts along with Krüger in Germany [78] and Soloviev and Churmack [79] in the USSR, van Manen [80], Küchemann and Weber [81] and Regenscheit in Germany [82] were limited to axial flow. These were not directly aimed at VTOL applications. Much of the early efforts were to improve the efficiency of regular airplane propellers designed for optimal performance in high-speed cruising flight. The experiments of Stipa were restricted to large values of chord/diameter ratio. The experiments of Soloviev and van Manen were performed in water, and the propellers of Soloviev were designed for ships. The effect of position of the propeller inside the shroud was not investigated.

Krüger [78] conducted tests on fifteen different annular-airfoil shrouds and

varied parameters such as the shroud chord, thickness, camber, inlet lip radius and angle of incidence between the profile chordline and propeller axis. The models were tested at rest and in axial flow. It was seen that in static conditions, flow separation was more prominent for shrouds with a sharper lip. In forward flight, the thinner shroud had lesser drag, but the propeller thrust decreased faster. External split rings were installed to alleviate this problem. Krüger noted that the diffuser angle was not a significant parameter. Platt [83] conducted static tests of contra-rotating, 48-inch diameter propellers with three shrouds of varying diffuser length and angle. In all cases, the difference in power consumption was within 10%, which were found to be marginal. However all the shrouded propellers performed twice as good as the open propeller. Along with tests from Hubbard in 1950 [84] and Mort in 1966 [85, 86], it was commonly found that increasing tip clearance led to a drop in shroud thrust (by up to 20% as reported by Mort). In Hubbard's and Platt's experiments, the flow was found to separate at the shroud leading edge at low propeller rotational speeds, but then was found to re-attach as the speed was increased. Parlett [87] and Taylor [88] varied the lip radius of the shroud and found that higher lip radii shrouds offered better Figures of Merit.

By around 1966, Black, Wainauski and Rohrbach [89] conducted a comprehensive investigation of the effects of various shroud parameters using twelve different shrouded propeller models, with a propeller diameter of 30 inches. The parameters investigated included the exit area ratio, lip shape, shroud chord, propeller location within shroud, number of blades, tip clearance and shroud external shape. They found that the most powerful shrouded propeller variable was the shroud exit area ratio. This was in contradiction with a few other studies, which noted that the diffuser angle was not very critical. They also obtained

greater than predicted improvements in thrust, up to 67% higher, for the same ideal power. In agreement with other studies, they found that increasing the input power by increasing rotational speed or collective, the suction forces on the shroud inlet increased. In axial flow, the drag from the shroud resulted in deteriorated performance, and also, a higher shroud exit area ratio was detrimental. In terms of propeller position within the duct, they found that having the propeller forward gives the wake more length to achieve desired diffusion, whereas having it rearward evens out any asymmetries in the inflow. They found that the forward location performed better in axial flight whereas the rearward location performed better in static conditions. A set of experiments conducted on a coaxial ducted rotor by Lee and Leishman in 2008-2009 [90] showed that the forward location of the propeller resulted in better performance in static conditions.

With emphasis on UAV development in the 1980s, tests were also conducted on smaller scale shrouded rotors. During the development of Sikorsky's Cypher, experiments were performed on the shroud design [91] and it was found that the performance deteriorated as the inlet lip radius was decreased. A most interesting result was that reducing the shroud length from $100\%D_t$ to $5\%D_t$ caused a deterioration in thrust by only 10%. This was important from a weight savings perspective. During the development of the 10-inch 'Perching Unmanned Aerial Vehicle' (PUAV) [92], Dyer [93] investigated effects of various shroud parameters and found that increasing the lip radius improved performance whereas increasing the diffuser angle decreased performance, contrary to predictions. In 2004, Martin and Tung [94] tested two 10-inch diameter shrouded rotor models. They obtained a 37% improvement in thrust over the open rotor at the highest inlet lip radius and lowest tip clearance. The trends they obtained were consistent with

expectations. From a potential flow analysis, they surmised that at increased tip gap and decreased lip radius, there was a decrease in inlet suction. In order to eliminate tip clearance, Martin and Boxwell [95] designed two shrouds, one with a notch that was cut into the inner shroud surface at the propeller tip path plane, and the other with a rearward-facing step that was cut into the inward facing profile just above the tip path plane to accommodate the propeller. However, they found that the notched-shroud did not differ from the baseline model, while the stepped shroud showed degraded performance. During the same time period, Graf et.al. [96] tested effects of five different lip geometries on hover and forward flight performance of a model based on the PUAV. It was found that the circular arc lip produced slightly more thrust than the elliptical lip.

In an attempt to reconcile the shroud design parameter space at the MAV scale, Pereira and Chopra [50] conducted systematic investigations of performance of a 6.3 inch shrouded rotor. Significant performance gains in hover of up to 50% reduction in power were obtained by optimizing parameters such as inlet lip radius, tip clearance and diffuser length (Fig. 2.46). However, these tests were conducted with a flat plate untwisted rotor and the reported performance gains would have been lesser had the rotor in the open configuration been optimized.

It can be seen from above that most of the rotors tested were in the sizes ranging from one to several feet in rotor diameter. The few studies in the smaller scale did not effectively true performance benefits between an optimized shrouded and an optimized unshrouded rotor. Therefore, one of the purposes of this research is to incorporate previous results in shroud design optimizations and systematically develop a shrouded rotor that has a better hover performance at a system level than an optimized unshrouded rotor. This is the topic of discussion in
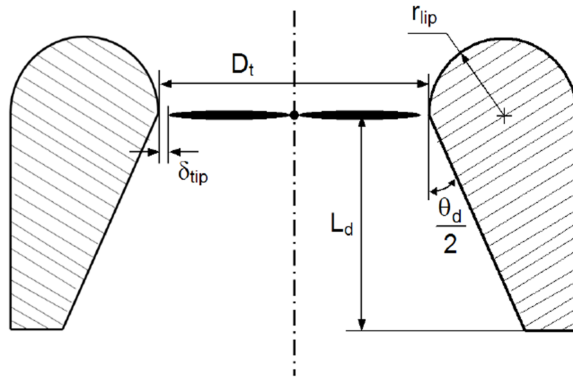
Figure 1.15: Shroud design parameters

Chapter 2.

1.2.2.2   Non-axial flow

This flow stage of the ducted fan usually occurs when the VTOL vehicle under-goes transition from hover to forward flight Fig. 1.16. Other situations include fan-in-fin applications and when the ducted fan acts as a source of propulsion and is flown at an angle of attack. Due to the very complex flow phenomena that can result in destabilizing and undesirable forces and moments, many experimental studies were conducted in the past.

One of the earlier wind tunnel tests for a shrouded rotor in non-axial flow was conducted by Parlett in 1955 [87] to investigate the effects of air speed and angle of attack on the lift, drag, and pitching moment of a shrouded propeller model over an angle of attack range from 0^0 to 90^0. Yaggy and Mort in 1961 [97, 98] conducted wing tunnel studies of a 4 foot diameter ducted fan in order to evaluate the forces and moments generated on a wing mounted duct. They found large pitch-up moments when the ducted fan was operated at an angle of attack to

28

Figure 1.16: Piasecki Airgeep in forward flight

the air stream. This was the first study where it was suggested to use guide vanes in the rotor downwash as a means to alleviate or reduce the magnitude of these moments. To study the transition performance of a tilt-duct VTOL type aircraft, Grunwald and Goodson [99, 100] investigated the aerodynamic loads on an isolated shrouded propeller at angles of attack from -10^0 to 100^0. They found that the pitching moment developed by the propeller was only a relatively small part of the overall pitching moment. Other studies investigating loads on a ducted fan in non axial flow for manned VTOL applications are Fletcher [101], Moser [102], Spreeman [103], Giulianetti [104].

During the design of the AROD UAV [70], Weir [105] conducted tests on six different shrouded propeller configurations with the aim of obtaining translational flight data. Fleming et. al. [106] conducted tests on the PUAV type ducted fan to evaluate effectiveness of flow control schemes to improve cross wind effectiveness of this aircraft. They found that the aerodynamic drag on the vehicle due to the deflection of the free stream through the diffuser was much greater

than the profile drag of the shroud itself. The pitch-up moment increased up to a certain airspeed and then decreased to nose-down pitch moments. The authors surmised that this was possibly due to separation of the flow from the windward side of the sharp leading edge. In Martin and Tung's experiments [94], the nose-down pitch moment at higher speeds was also observed. However the pitch moments of their sharper-inlet shroud model was lesser, which was attributed to separation of the flow from the inlet. Studies conducted by Graf et. al. [96] on PUAV type ducted fan model showed the pitching moments to initially increase with airspeed and then level off at higher airspeeds. For the different shroud models tested, the ram drag (or momentum drag) averaged to about 80% of the total drag. Lee and Leishman [122] conducted wind tunnel tests of a coaxial ducted rotor system in order to measure the thrust characteristics as a function of airpseed and angle of attack. However, pitching moment was not measured. Pereira and Chopra [107] provided surface pressure and load cell measurements of MAV scale shrouded rotor with varying airspeed and angle of attack. In axial flow, the net thrust of the shrouded rotor deteriorated at high speeds due to the drag of the shroud. In edgewise flow, the thrust of the shrouded and unshrouded rotors increased with increasing airspeed. The power consumption of the unshrouded rotor increased whereas for the shrouded it remained about constant. The drag of the shrouded rotor increased much more rapidly with airspeed. The center of pressure for the shrouded rotor lay approximately $0.75\ R$ further above the location for the unshrouded rotor. They did note the asymmetry in pressure distribution between the windward and leeward sides of the shroud in non-axial flow that was responsible for the pitching moment.

It was seen from these studies that the effect of edgewise flow on a shrouded rotor is that undesirable adverse pitching moment and drag are generated. This

problem can become severe for low disk-loading shrouded rotor configurations, such as the research vehicle discussed in this dissertation. Therefore, it is important to measure the forces acting on the vehicle under these aerodynamic conditions and isolate configurations and mechanisms that can improve the ability of the vehicle to tolerate and overcome these forces. This is the topic of discussion in Chapter 5.

1.2.3 Analytical and CFD modeling of shrouded rotor aerodynamics

To improve predictive capability that can aid shrouded rotor design as well as flow field analysis numerical tools have been developed in the past. Analytical methods for shrouded rotor performance prediction include blade element momentum theory, blade element vortex theory and more complicated potenital flow models with boundary layer coupling. Sacks and Burnell [77] provided an exhaustive account of different analytical methods existing till 1960. Recently computational fluid dynamics (CFD) methods have been developed to predict performance. The pioneers of potential-flow methods for shrouded rotors were Küchemann and Weber [108] who applied these solutions for annular airfoils in a uniform flow by modeling the bodies as distributions of vortex rings over their surfaces. Kriebel [109], and Mendenhall and Spangler [110, 111] developed and consolidated predictions for force and pitching moment coefficients of a shrouded propeller in steady flight at an angle of attack. Mendenhall's algorithm was later used by Weir in designing the AROD UAV. Fairchild [112] used a formulation where the shroud was modeled as chordwise distribution of vortex rings and was able to show that in axial flow, increasing the shroud chord causes greater re-

ductions in ideal power when compared to an open rotor. Goodman [113] was the first to model the effect of finite tip clearance and formulated a correction factor for efficiency measurements. Clark [114] and Wright et. al. [115] developed potential flow solutions for fan-in-fin applications. In 2003, Guerrero et. al. [116] developed AVID-OAV for the analysis of ducted fan UAVs.

Blade element and momentum methods could not represent geometric characteristics of the shroud unless empirical correction factors were used. Potential flow methods could not predict friction drag and stall characteristics [117]. Therefore, CFD methods have played an important, versatile role in design and analysis of these complicated flow phenomena. Most of the CFD research effort into shrouded rotors were for the fan-in-fin applications. Started by Aerospatiale, some important references are [118–120], which involve a coupled CFD-momentum theory analysis. More computationally-intensive, discrete blade CFD model was used by Ruzicka et. al. [121]. This analysis showed how the leakage flow around the blade tips is reduced as the tip clearance is reduced, which results in increased system thrust and figure of merit. Lee et. al. [122] demonstrated the importance of realistic 3-D tip modeling in a CFD analysis of the Kamov fan-in-fin. Ahn and Lee [123] used a CFD model to parametrically investigate the effects of varying inlet lip radius, diffuser angle and rotor radial strength distribution.

A recent CFD study based on the configuration of the shrouded rotor investigated in this research was conducted by Lakshminarayan and Baeder in 2010 [124]. They used an overset structured mesh solver OVERTURNS that solves the compressible RANS equations and employing low Mach preconditioning to take into account the low Reynolds number regimes of the shrouded rotor operation. They obtained good comparison between experiments [76] and CFD

prediction. Figure 1.17 shows the wake trajectory of the two bladed shrouded rotor. For a straight diffuser section and a chord-diameter ratio of 15%, the
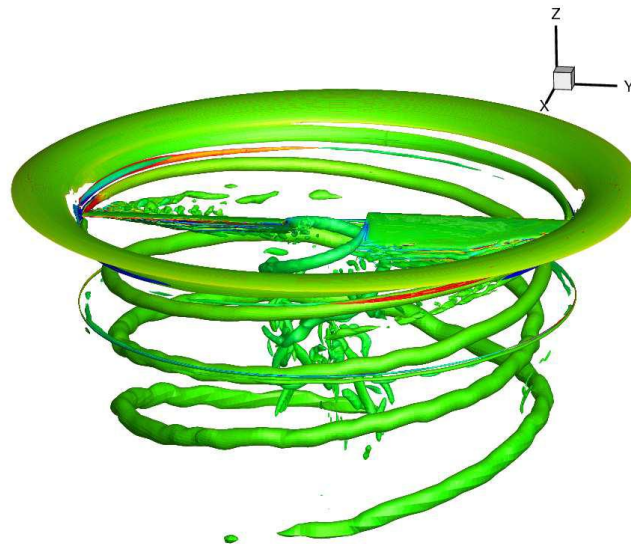
Figure 1.17: Wake trajectory of a two bladed shrouded rotor (Iso-surfaces of q-criterion) [124]

contraction ratio was observed to be about 0.85 and not 1 (as predicted from momentum theory). They extended the analysis to study the effect of tip clearance, diffuser angle, diffuser length and inlet shape (circular, elliptic). Of these, the lowest tip clearance and an elliptic inlet shape gave the best performance prediction. In an unpublished report by Lakshminarayan, the effect of edgewise flow on the loads and pressure distribution of the shrouded rotor was studied. Figure 1.18 shows the load distribution on the circular inlet shrouded rotor in 2 m/s of edgewise flow at the instant the two bladed rotor is aligned with the flow direction. The asymmetry in pressure distribution between the windward and leeward side can be clearly seen which was similar to the surface pressure distribution measurements by Pereira and Chopra [107]. Key results from this CFD study will be used to explain certain observations in Chapter 5.
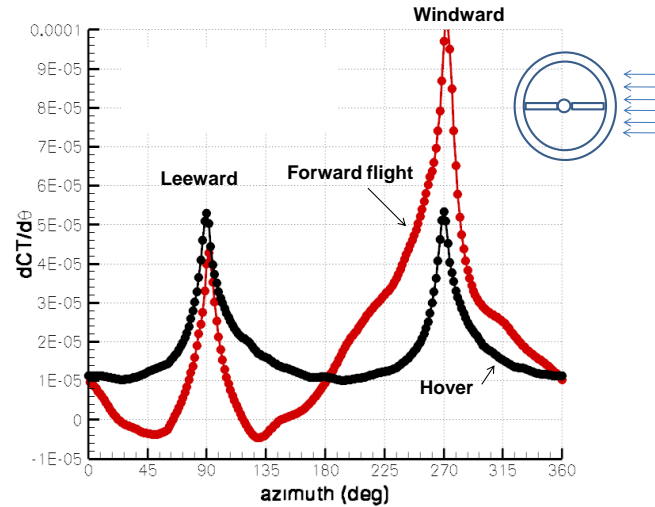
Figure 1.18: CFD load distribution prediction on a hovering circular inlet shrouded rotor facing edgewise flow [124]

1.2.4 Shrouded rotor flow control

When the shrouded rotor/ducted fan is in a non-axial flow regime at high angles of attack (flow is almost perpendicular to rotor axis), phenomena such as inlet lip separation at the leading edge of the shroud/duct occur. This can lead to undesirable areas of recirculation, pressure loss, pitching moment and drag. Therefore, studies have been conducted in the past to modify flow in the duct inlet or exit for the various ducted fan configurations. Yaggy and Mort [98] were probably the first to suggest and scientifically study the use of guide vanes in the inlet and duct exit to reduce the nose-up pitching moment encountered by the twin ducted Doak VZ-4 (Fig.1.11). They found significant reduction in the pitching moment by modifying the duct exit flow through the vanes.

Patents on ducted fan vehicle design illustrated concepts for modifying the flow in the duct inlet or exit. Piasecki's patent [126] of the Airgeep had a curious feature which was the use of a movable spoiler in the inner part of the

leading side of the duct. This had a serrated edge, which would control local flow characteristics over the lip radius in an effort to reduce the drag generated over this region primarily in edgewise flight. In the patent by Boyd et. al. [127], a VTOL ducted fan vehicle design was proposed, which used adjustable stator blades above the rotor for attitude control only.
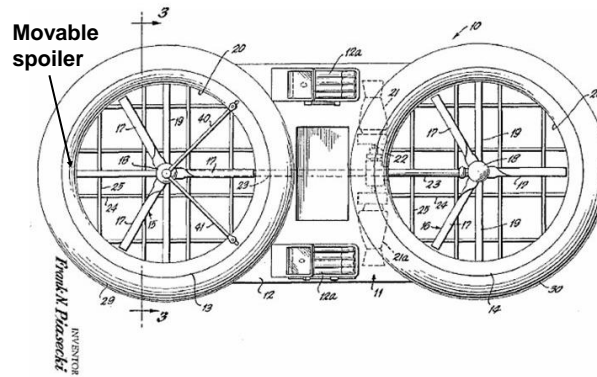
Figure 1.19: Piasecki's patent of the Airgeep with movable spoilers for inlet flow control [126]

Moller [128] in 1989 had a patent for a flying ducted fan platform with two mutually perpendicular vane systems with variable camber flaps and exit flow control features called multiple adjustable air deflector assemblies (Fig. 1.20). Cycon in 2001 [130] modified the original design of the Sikorsky Cypher by mounting high camber fixed wings to the ducted fan aft of the center of lift. This would serve to counteract the nose-up moments generated in forward flgiht.

Yoeli's [129] ducted fan based VTOL vehicle included a fuselage with two counter rotating ducted fans along the longitudinal axis. A system of inlet louvers and exit control surfaces were placed to produce side force, roll, pitch and yaw moments on the vehicle Fig. 1.21.
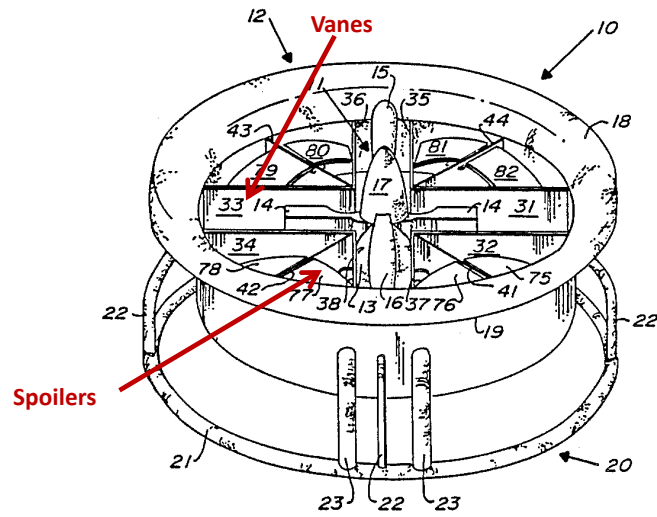
Figure 1.20: Ducted fan platform design with control vanes and spoilers [128]
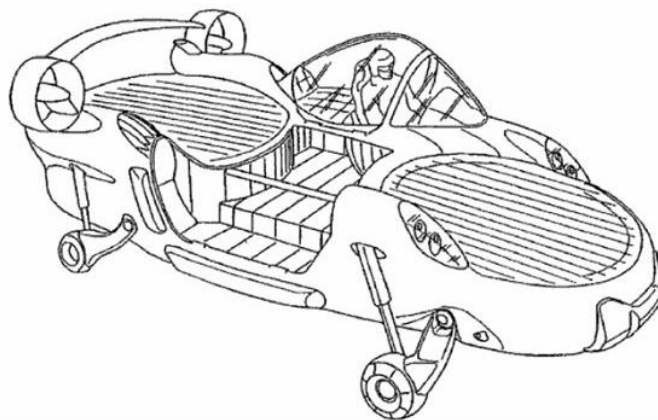
Figure 1.21: Tandem ducted fan design of Yoeli with inlet louvres and exit vane flaps [129]

Albrego and Bulaga [125] investigated the effect of exit vanes to generate side force that can be used to produce control moments. Their tests were conducted using a 5-bladed 38-inch diameter ducted fan. Fleming et. al. [106] conducted studies on the performance of ducted fan inlet lips and exit vanes in crosswind. They tested effectiveness of control vanes, duct deflectors, leading edge slats and other variations of these auxillary control devices in crosswind (Fig. 1.22). They found that at low cross wind speeds, the control vanes performed better than other methods, but they stalled at higher speeds. Researchers have also investigated the effect of steady blowing to create ducted fan control forces and moments in hover as well as forward flight conditions [131–133] (Fig.1.23). Recently, Camci and Akturk [134] introduced a novel double duct design, which uses a secondary duct system (Fig. 1.24) to control inlet lip separation which would "significantly improve the performance and controllability of VTOL UAVs and other ducted fan based systems". However, no reference to an added weight penalty with the double duct was given.

A significant issue with applying some of these flow control design modifications to an MAV system is the weight penalty. Nevertheless, certain viable flow control strategies such as inlet flaps and vents were studied in this research (Chapter 5).

1.2.5 Shrouded rotor flight control design and testing

Two typical ducted rotor UAV designs that have been studied for control design and modelling are shown in Fig. 1.25. The first is called "a generic ducted fan UAV" after which the iSTAR, Honeywell Kestrel and t-HAWK are designed. This consists of a single fixed pitch propeller with control surface vanes and fixed
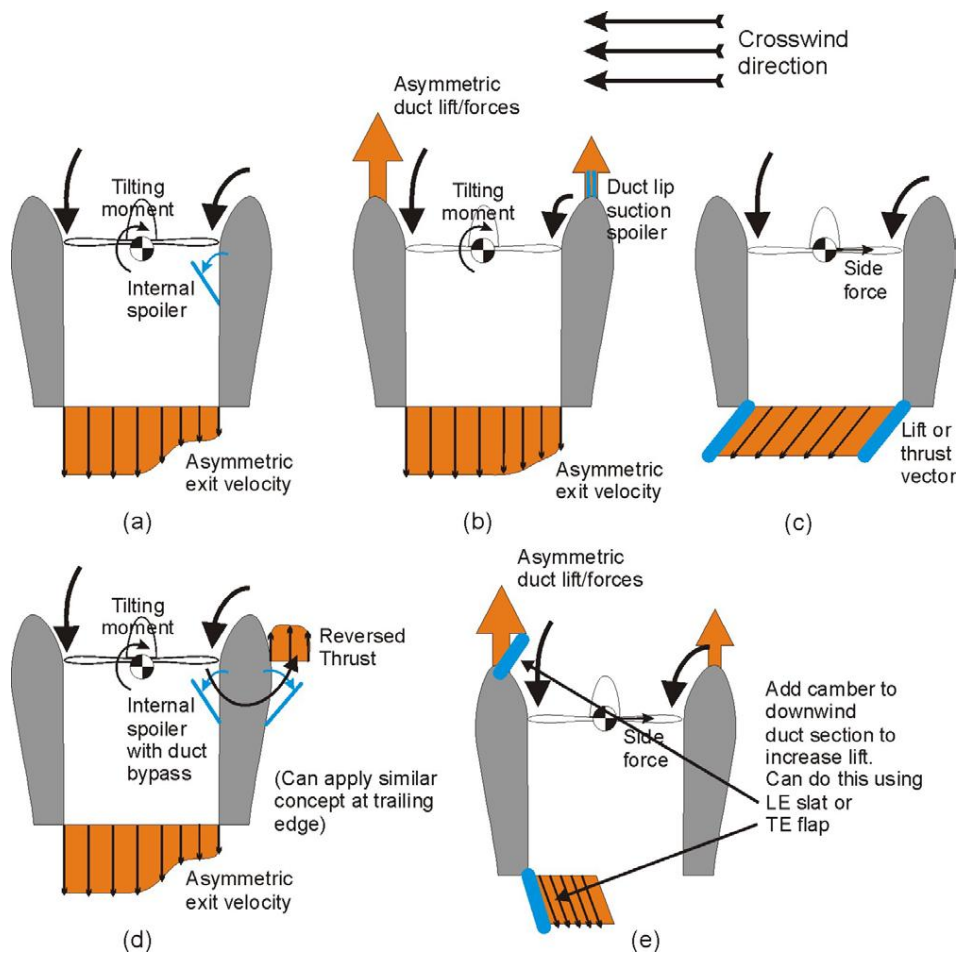
Figure 1.22: Auxillary control devices for flow control [106]
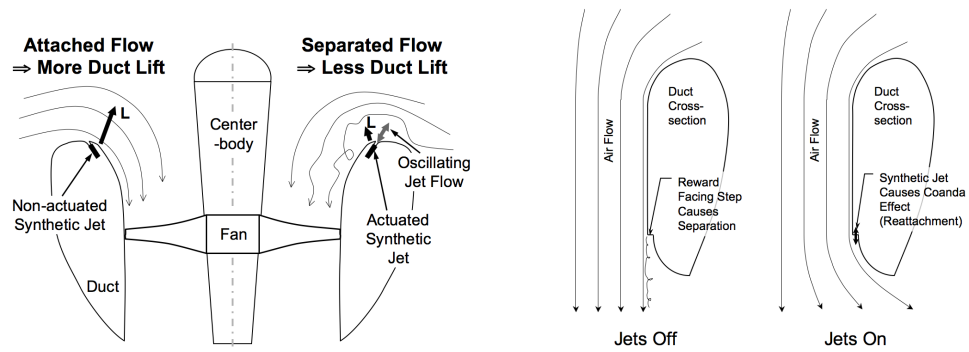
Figure 1.23: Synthetic jet flow control concept [133]
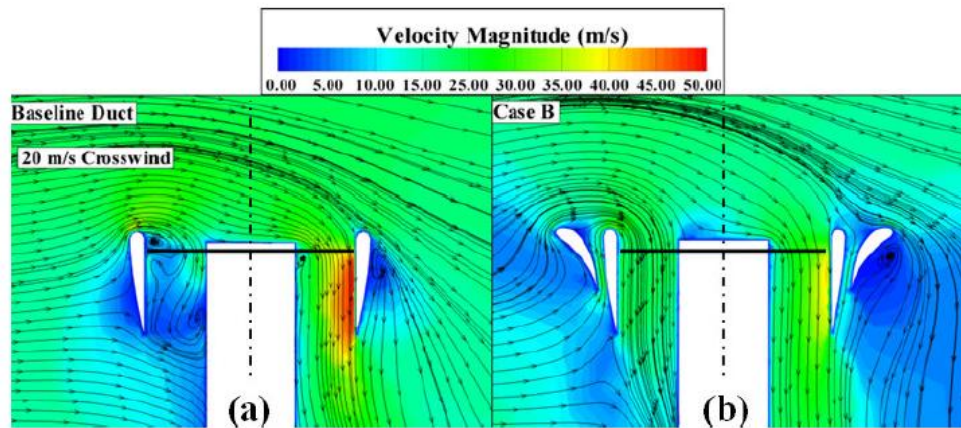
Figure 1.24: Elimination of inlet flow separation a through a double duct design [134]

stators placed in the propwash for achieving complete attitude control. The second is called the "tail sitter" after which the Hovereye [135] is built. It consists of two counter-rotating rigid props with control vanes (but no stators) in the propwash for attitude control. These UAVs are designed to hover with the propeller axis in the vertical direction and perform forward flight with the propeller axis along the horizontal direction. It can be seen that this involves various flight regimes involving the complex transition phase between hover and forward flight. The vehicle dynamics may not render itself to a linear assumption under these different modes. Therefore, many linear and non-linear control schemes have been studied and developed that include linear PID control, switched robust linear control, sliding mode control, linear and non-linear dynamic inversion, backstepping with adaptive control, H_∞ and receding horizon control.

(a) Generic ducted fan UAV   (b) Tail-sitter
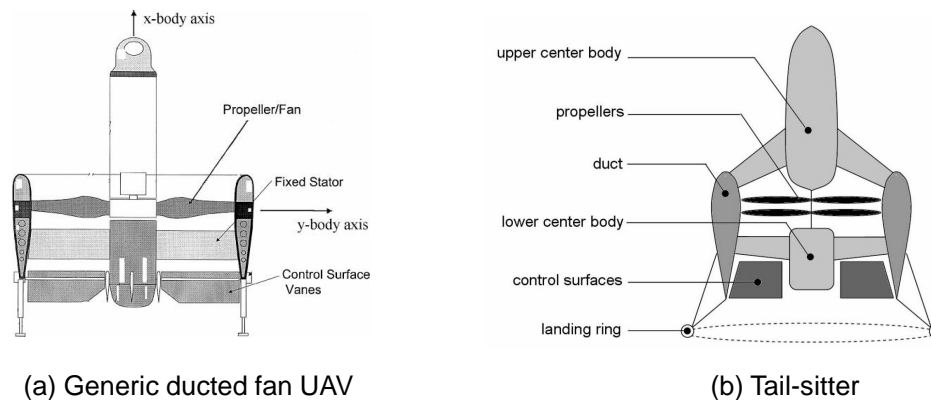
Figure 1.25: Past control system design methodologies usually applied to (a) Single prop, stator, control vane design (b) Coaxial prop, control vane design

Dunbar et. al. (2002) [136] presented a control system framework for the

Caltech ducted fan (a vehicle with the generic ducted UAV design with two wings attached on the sides). They designed a model predictive controller, which was successfully able to stabilize a step offset in x position (simulation). They found that the region of attraction of the MPC controller was larger than the static hover LQR controller and equivalent to a gain-scheduled LQR controller. Franz et. al. (2002) [137] extended the control design of the Caltech ducted fan to implement a receding horizon control. Here they found the performance to be better than a gain scheduled LQR controller in terms of step response and disturbance rejection.

Pflimlin et. al. (2004) [138] proposed a model for the tail sitter VTOL dynamics where the aerodynamic effects were seen as unknown perturbing terms. An adaptive controller by means of backstepping techniques allowed the stabilization of the vehicle's position.

Hess and Ussery (2004) [139] showed a design for MIMO sliding mode controllers for a generic ducted fan UAV. In order to reduce sensitivity to unmodeled dynamics, they used an asymptotic observer. In 2006, Hess and Bakhtiari-Nejad [140] applied a pseudo-sliding mode control. They found that the controller was robust to large steady wind gusts which was a problem for nonlinear dynamic inversion control design.

Spaulding et. al. (2005) [141] showed that the nonlinear dynamic inversion approach proved to be a good choice because it reduced the complex vehicle dynamics to that of a simple integrator and covered the full flight envelope of the ducted fan UAV without gain scheduling. The drawback, inherent with dynamic inversion, of lack of robustness to model uncertainty was addressed. They focused on the design of outer-loop regulators based on linear and non linear metrics to make the overall system robust to model uncertainties and was

proved successful in simulation.

Johnson and Turbe (2005) [142] augmented a simplified model of the ducted fan vehicle GTSpy (similar to the iSTAR design) with a neural network design for adapting to errors in the model. They used a combination of adaptation and dynamic inversion due to lack of an accurate model. Simulation results for vehicle trajectory in presence of turbulent winds were presented. They also performed flight testing, where the vehicle was air-dropped from an unmanned helicopter.

Li (2006) [143] presented an approach that combined linear control for hover and steady flight and nonlinear dynamic inversion for transition regimes. The vehicle that was analysed, comprised of two ducts with pitch and yaw control vanes.

Avanzini et. al. (2006) [144] designed two robust linear controllers, one for low-speed flight and another for high-speed flight. The two controllers were switched after a threshold velocity was achieved. Simulations showed good gust rejection performance and was robust to variations in C.G. position. The control system was applied to a 10 Kg counter-rotating shrouded rotor vehicle with collective and cyclic pitch controls (Fig. 1.26).

Figure 1.26: Shrouded rotor UAV prototype by Avanzini et. al. [144]

Peddle and Jones (2009) [145] present a control system development for near

hover flight control of the tail-sitter. Successive loop closure control strategy with feedback signal from linear decoupled estimators was used which provided a robust solution. The functionality was verified by simulation and flight test data.

Pflimlin et. al. (2010) [146] developed an aerodynamic model of the tail-sitter from wind tunnel tests, derived equations of motion and linearized about hover condition. Unstable poles in vehicle modes were identified and PID control was implemented to stabilize the vehicle. Good agreement between simulation and flight test results was shown.

These studies applied to conventional ducted fan designs that generate high downwash velocities over control vanes. However, it is also necessary to study and develop stability augmentation control systems for cyclic controlled, low disk loading, shrouded rotor configurations, which is discussed in Chapter 3.

1.2.6   MAV flight performance in gusts

It is expected that MAVs encounter degraded, time varying flows. A study of flight performance in these conditions is extremely important. Large commercial aircraft can generally tolerate extreme wind conditions, but as the size and mass of the aircraft decreases, the ability to maintain control reduces for a given wind condition [148–150]. This is mainly due to the relatively low flight speeds and moments of inertia of MAVs. A summary of flying speeds from Ref. [147] is shown in Fig. 1.27 indicating the tolerable wind conditions for animals and aircraft.

Since typical MAV missions involve low altitude flight, they operate in the 'roughness zone' of the atmospheric boundary layer where the flow is time-

Wind Speed, m/s	Beaufort Wind Scale		
	Force	Description	
0.6	1	Light air	Butterflies
1			
2	2	Light breeze	Gnats, midges, damselflies
3			
4	3	Gentle breeze	Human-powered aircraft, flies, dragonflies
5			
6	4	Moderate breeze	Bees, wasps, beetles, hummingbirds, swallows
8			
10	5	Fresh breeze	Sparrows, thrushes, finches, owls, buzzards
	6	Strong breeze	Blackbirds, crows
	7	Near gale	Gulls, falcons
20	8	Gale	Ducks, geese
	9	Strong gale	Swans, coots
	10	Storm	Sailplanes
30	11	Violent storm	Light aircraft
	12	Hurricane	

Figure 1.27: Typical operating flight conditions of animals and aircraft [147]

varying and the perturbations in local flow are comparable to the characteristic speeds of MAVs. In the presence of winds, flight performance is tremendously affected.

Hoover (1999) [151] stated that flexible wings could alleviate some of the flow perturbations, but that small gusts have extremely deleterious effects on small crafts. Jenkins et. al. in 2001 [152] analyzed the controllability of flexible and rigid fixed wing MAVs (of 6 inch dimension) as the pilot performed flights in steady and gusty wind situations. They performed spectral analysis of control input movement rates forming autospectra of differentiated stick position data which was seen to provide a convenient yardstick for comparing the flying qualities of their MAVs. They found that manueverability is strongly related to how often the pilot must make rapid (1-10Hz) stick movements to maintain stability during the flight. They also found the flexible wing MAVs outperform rigid wing MAVs in terms of reduced control workload. However, no specific information of the nature of the atmospheric condition or how it correlated it with the MAV flight performance was given. In the outdoor flight demonstrations of several flying wing MAVs by Walkins (2002) [153], it was noted that the largest challenge to MAV flight was overcoming time varying flow perturbations, particularly small vortices and eddies that produce random roll and pitch inputs. Watkins noted that this would restrict the number of possible days/year that the MAV could be used for outdoor activities.

Relatively little work has been done on quantifying the wind environment of relatively slow flying craft close to the ground. In 2005, Milbank et. al. [154] and later by Watkins et. al. [155] attempted to quantify and replicate typical flight environments for MAVs operating close to ground for the purposes of replicating the spatial and temporal turbulence characteristics in a wind tunnel.

Patel and Kroo (2006) [157] presented the design of simple control laws to extract energy from flow disturbances. They showed that significant energy savings are possible using active control laws. Due to the nature of the study, no mention of flight performance of the MAVs in gusts was made.

Bieniawski et. al. [158] utilized an indoor motion capture flight facility to evaluate the performance of a commercial quadrotor and fixed MAV, and control algorithms in a controlled, repeatable environment.

In order to study dynamics of a quadrotor in wind, Waslander and Chang (2009) [159] presented models for wind disturbances, developed an estimation algorithm for current wind velocity experienced by the vehicle. The wind estimate was used to improve positioning accuracy by eliminating effect of wind on feedback position control law and adding a wind compensator to mitigate effect of expected wind disturbance. Patrick and Humbert (2010) [160] applied optic flow and wide field integration (WFI) to perform station keeping and wind rejection of a quadrotor. They used a controller based on H_∞ formulation of LQR to perform these tasks. Zarovy et. al. (2010) [161] conducted flight tests of micro scale commercial coaxial rotorcraft in a motion capture flight testing facility and observed the deteriorated performance at wind conditions as low as 2 m/s.

It is of interest to build upon these efforts and systematically study the performance of a shrouded rotor MAV in degraded flow conditions, especially since shrouded rotors are known to be more sensitive to adverse flow conditions than unshrouded rotors. Details of these flight test experiments are discussed in Chapter 6.

1.3 Current Research: Objectives and Approach

Limitations with previous work: The previous sections showed the significant amount of experimental and analytical work performed in the area of ducted fan manned and unmanned vehicles in the field of aerodynamics, dynamics and control. However, most of these investigations were limited to rotors with diameters from one to seven feet with tip Reynolds numbers of the order of 100,000 to 1 million. The few existing studies on micro scale shrouded rotors did not carry out true assessment of shrouded rotor performance over that of efficient unshrouded rotors. The design of the shroud itself which is a significant challenge in the development of a lightweight MAV has not been discussed. Most of the existing ducted fan vehicles have disk loadings between 300-2000 N/m^2, and dimensions greater than one feet rotor diameter. Therefore, due to their high downwash velocities, control vanes were used to generate pitch and roll moments. This is however not practical for a compact MAV configuration with high control authority demands and therefore requires control mechanisms different from conventional ducted fan UAVs. It was seen that rotary wing MAVs have high bandwidth feedback requirements to successfully accomplish tasks that demand high degree of external disturbance rejection as well as maneuverability. This problem is exacerbated in the case of a shrouded rotor due to their increased sensitivity to flow disturbances. Studies that have examined the capabilities of a shrouded rotor MAV operating in external wind disturbances are generally lacking in the literature. All the above factors need to be systematically studied in order to determine the true capability of the shrouded rotor as a platform of choice in MAV applications.

Objectives of present work: In order to reconcile the above needs, the fol-

lowing are the objectives of the present work:

1. To design and develop a low disk loading (< 100 N/m^2) shrouded rotor micro air vehicle with systematic hover performance measurements and emphasis on lightweight shroud design and compare the hover performance of a shrouded rotor with an unshrouded rotor system.

2. To design and implement classical and model based feedback control in the MAV for semi-autonomous attitude stability augmentation in hover. Conduct time domain system identification to assess feedback and sensing requirements, and control sensitivity for the shrouded rotor in configurations with and without a stabilizer bar.

3. Finally, to systematically study the aeromechanics of the shrouded rotor in edgewise flow, compare gust disturbance rejection characteristics with those of an unshrouded rotor and to study free flight performance in the presence of external winds.

Organization of thesis: Chapter 2 describes the design of the shrouded rotor MAV considered in this research. The performance and design issues of each of the sub-components - low Re rotor design, Hiller stabilizer bar, anti-torque vanes, shroud - are detailed. A comparison in system performance between the shrouded and unshrouded rotor is made. The final section of the chapter discusses some initial vehicle prototypes constructed during this effort. In chapter 3, the open loop experiments detailing the attitude stability of the shrouded rotor in comparison with an unshrouded rotor are presented. The need for incorporating a rotor with minimal excursions in tip path plane inside the shroud is shown. A PID control system through a Ziegler-Nichols based gain tuning

is developed and flight tested on different vehicle prototypes in quiescent flow conditions. In chapter 4, the attitude dynamics of the shrouded rotor vehicle is studied about hover as the equilibrium condition. The salient advantages and drawbacks of incorporating a flybarless rotor are discussed. System identification of the vehicle constrained in translation is conducted in the time domain based on a reduced order model. The effect of flybar and flybarless rotor on the attitude dynamics is described.

Chapter 5 describes the performance of the shrouded when exposed to edgewise flow. The forces including thrust, drag and pitching moment produced by a shrouded and unshrouded rotor configuration are measured and compared. Control authority was compared and the ability to overcome destabilizing forces in edgewise flows is studied. An open jet wind tunnel is used as the source for edgewise flow. A few strategies to minimize adverse moments are discussed and methods to improve control authority of the rotor configurations through rotor planform design are detailed. In the final chapter, the ability of the vehicle provided with attiude feedback control to correct for nose-up disturbance is described in a series of bench top and free flight tests. For free flight, the ability of the vehicle to perform station keeping in the presence of cross flow is studied in a motion capture flight testing facility.

Chapter 2

Vehicle Design and Hover Performance Studies

2.1 Overview

The main aim of developing a shrouded rotor vehicle is to realize performance benefits over an unshrouded rotor vehicle of the same diameter while significantly improving the crashworthiness of the system. As discussed in Chapter 1 the vehicle developed in this research is the smallest in the class of shrouded rotor vehicles in weight and size. The design of the shrouded rotor micro air vehicle (MAV) is described in this chapter. Salient features in construction, configuration and control mechanisms are compared with previously developed shrouded rotor vehicles. The design, hover performance and integration of the sub-components of the vehicle system are then described.

2.2 Design

Most ducted fan UAVs such as the iSTAR, T-Hawk and AROD incorporate a fixed pitch propeller placed in the diffuser section of the duct. In order to counteract the propeller torque, a set of static stator vanes are placed in the propwash. Additionally, for pitch and roll attitude control, a secondary set of vanes are appropriately actuated to provide control moments. This is schematically shown in Fig. 2.1. It can be seen that for maximum attitude control

Swashplate

Vanes

Existing single prop ducted fan UAVs:
Vanes for pitch, roll and yaw control

TiShrov MAV:
Vanes for yaw control only
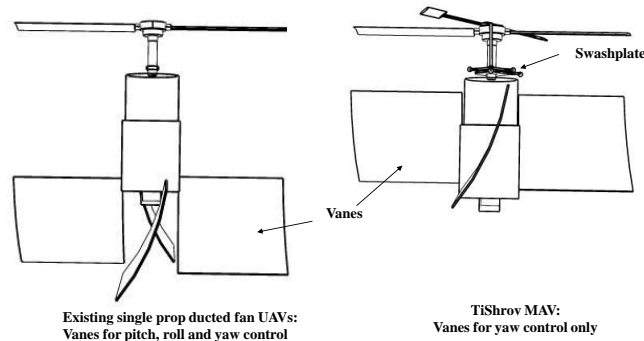
Figure 2.1: Differences in configuration for attitude control of a shrouded rotor vehicle

moments the distance between the vane center of pressure and vehicle C.G. has to be increased. This may not be appropriate from a consideration of vehicle compactness. It will also be shown later that the performance of vanes deteriorates in ground effect. Sikorsky's Cypher, however, has a pair of coaxial counter rotating rotors and does not require vanes for yaw control. It achieves attitude control through cyclic pitch actuation. A recent experimental study showed that performance benefits may not be realized by incorporating a coaxial rotor in a duct [90]. Therefore, a single shrouded rotor is considered in this research.

Presently, most existing single rotor MAVs have a two bladed rotor due to simplicity in the construction and control mechanism. From a consideration of the above discussion, the present vehicle design (Fig. 2.68) incorporates a single two bladed rotor enclosed in a shroud.
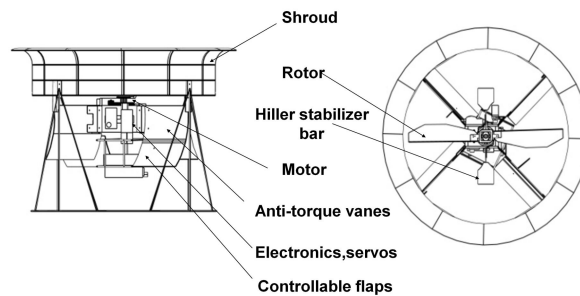
Figure 2.2: TiShrov: Shrouded rotor MAV design

Vanes with deflectable flaps are placed in the rotor downwash for anti-torque and yaw control purposes only (Sec. 2.5). Attitude control is achieved from a swashplate configuration. A Hiller stabilizer bar is incorporated with the main rotor to transfer cyclic inputs to the rotor and improve stability characteristics of the vehicle by offering passive gyroscopic feedback to the rotor. The Hiller bar links are attached to a COTS swashplate actuated by two servos. The swashplate actuation is transferred to pitching of the aerodynamic paddles of the Hiller bar. Subsequent flapping of the Hiller bar results in a 1/rev cyclic input to the rotor. (Fig. 2.3). A more detailed description of the Hiller bar is given in Sec. 2.4. A third servo is mechanically linked to the controllable vane flaps to deflect the flaps in a symmetric manner. The shroud is integrated into the fuselage through the vanes. A brushless DC motor was chosen as the power plant to minimize

the noise signature and for ease of operation. A receiver, speed controller and yaw gyro constitute the remainder of the on-board electronics.
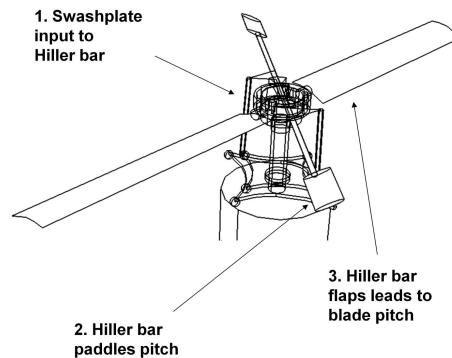
Figure 2.3: Cyclic pitch actuation set-up

2.3 Rotor

To analyze the effectiveness of the shroud, it was first necessary to determine an efficient unshrouded rotor design. This section describes the selection of an unshrouded rotor that is later used for performance comparison when enclosed in a shroud. A two bladed rotor was considered in this study.

2.3.1 Experiment set-up

The two bladed rotor was mounted on a rigid hub and driven by a 12 mm Feigao brushless inrunner DC motor with an 8:1 reduction gearbox. A shaft
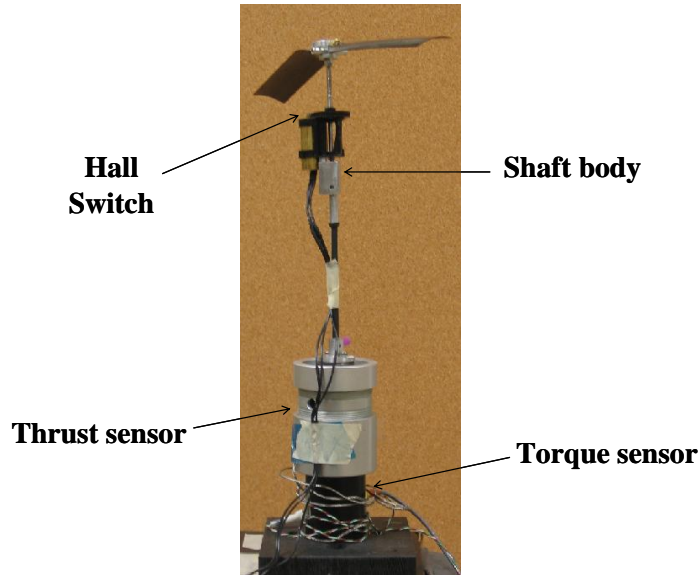
Figure 2.4: Micro rotor hover test stand

coupled the rotor with a thrust[1] and torque load sensor[2] assembly as shown in Fig. 2.4. A pair of magnets installed on the gearwheel were used to trigger a Hall sensor[3] thereby determining the rotor speed. An optical tachometer[4] was used to verify the speed of the rotor. The performance metrics of the rotor were derived from a measurement of the thrust, torque and rotor RPM. The sensor data were acquired by a National Instruments DAQCard 6062-E data acquisition system and processed in LabVIEW. The data was sampled at 1000 Hz which was about 15 times the maximum rotor RPM of interest. This enabled sufficient filter bandwidth for signal conditioning purposes. The

---

[1] 1000 g load sensor with a resolution of 0.1 g. measurementsensors.honeywell.com. This was later replaced by a 5000 g thrust balance ohaus.balances.com

[2] 25 in-oz capacity torque sensor from Transducer Techniques www.transducertechniques.com/rts-torque-sensor.cfm

[3] www.allegromicro.com

[4] www.monarchinstruments.com

thrust and torque measurements were an average of about 5000 data samples. The average measurement errors in thrust,torque and RPM were determined to be about 0.5 g, 0.2mN-m and 50 about statistical average respectively. The mechanical power was determined by the product of torque(N-m) and rotor speed(radians/second).

2.3.1.1   Variation in air density

The variation of air density with respect to sea level at 75^0 F is shown in Fig. 2.5 over the course of experimental tests in this research (the temperature in the laboratory was maintained roughly at $75^0 F$). This fluctuation is due to external pressure variation on an hourly,daily and seasonal basis[5]. A comparison in density fluctuation between summer and winter months is shown in Fig. 2.6. Therefore the measured thrust and power data are normalised with respect to the sea level conditions (MSLISA[6] as follows,

$$T' = T\left(\frac{\rho_{SL}}{\rho}\right) \tag{2.1}$$

$$P' = P\left(\frac{\rho_{SL}}{\rho}\right) \tag{2.2}$$

Dimensional data presented in this research is normalized to the MSLISA conditions at $75^0 F$. For accurate treatment, the pressure and temperature data should be logged each time the experiment is performed. Similarly, the non dimensional thrust coefficient $(C_T = T'/\rho \mathrm{A}(\Omega \mathrm{R})^2)$, power coefficient $(C_P = P'/\rho \mathrm{A}(\Omega \mathrm{R})^3)$and Figure of Merit $(FM = (C_T)^{3/2}/\sqrt{2}C_P)$ were extracted. It must be noted that

---

[5]Pressure information at the nearest weather station can be obtained from http://cdo.ncdc.noaa.gov/qclcd/QCLCD

[6]MSLISA - Mean sea level international standard atmosphere

the error bars must incorporate fluctuations due to density. In the present case a maximum variation in density of about 2% is considered.
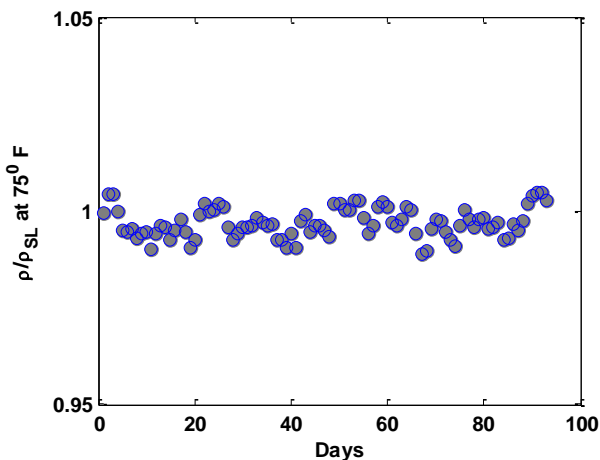
Figure 2.5: Variation of air density during experimental runs
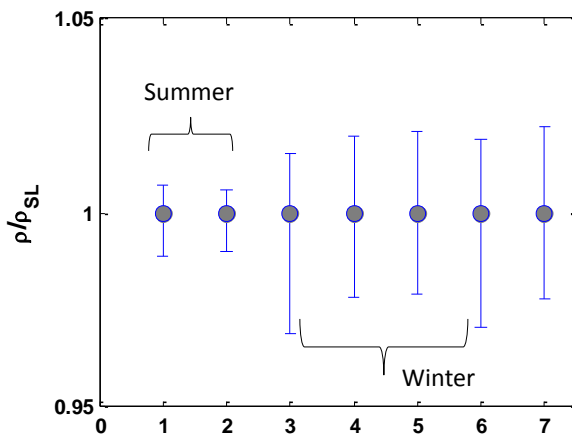
Figure 2.6: Maximum air density variation in summer and winter

For each test, a set(3) of RPM sweeps were done for each rotor collective setting. This produces a variation in thrust and mechanical power that was quadratic and cubic with RPM respectively. The trend was observed to be fairly repeatable over multiple runs. Figure 2.7 shows the variation of MSLISA thrust and power for a two bladed rectangular rotor

It can be seen that the thrust, power coefficients and FM (Fig. 2.8) were fairly independent of operating RPM, indicating that Reynolds number effects are not present at sufficiently high RPMs (greater than 2000). An average Figure of Merit (FM) measured between 2500-3000 RPM was extracted.

2.3.2 Airfoil

The design of an MAV rotor has two main considerations - airfoil and blade planform. At Reynolds numbers between 30,000 - 100,000, studies have shown
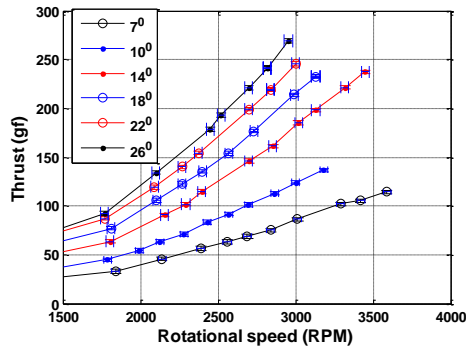
(a) Thrust vs.RPM
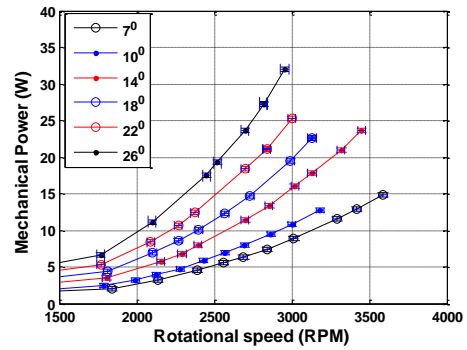
(b) Power vs.RPM

Figure 2.7: Variation of thrust and power with RPM for a two bladed rectangular rotor at different blade root collective
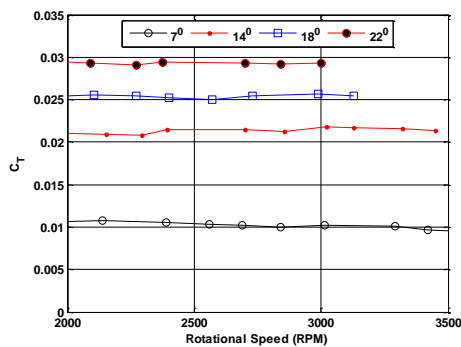
(a) Thrust coefficient vs.RPM
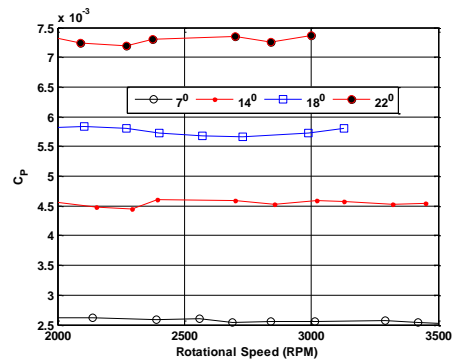
(b) Power coefficient vs.RPM
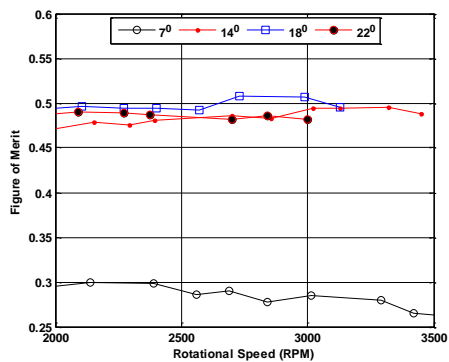
(c) Figure of Merit vs.RPM

Figure 2.8: Variation of thrust,power coefficient and FM with RPM for a two bladed rectangular rotor at different blade root collective

that thin cambered airfoils have the best lift-to-drag ratios [29–31]. Additionally, experiment and CFD studies [33, 34, 38, 39] have shown that sharpened leading edge (LE) airfoils at these Re numbers have a lower drag coefficient and result in rotors with lower profile losses. Therefore, a circular camber airfoil with a sharpened LE and a thickness ratio (t/c) of about 2% was implemented in the blade design (Fig. 2.9). Camber of the blade was set at 10% and is calculated as

$$Camber = d/c = \left(\frac{1}{2} tan(\frac{\theta}{2}) \right) \tag{2.3}$$

It must be noted that when taper is included, the effective camber of the airfoil section decreases since the radius of curvature remains the same.
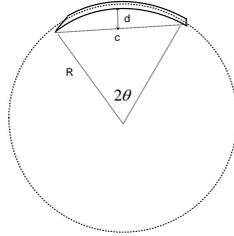
Figure 2.9: Circular camber airfoil

The micro and full-scale airfoil characteristics are shown in Figs. 2.10 and 2.11. The data for the MAV airfoils is from CFD prediction (Ref. [124]), since there was no available experimental data. It can be clearly seen the MAV airfoils have much lower lift to drag ratios than the full scale airfoils. Also at the low reynolds numbers, as the camber of the airfoil is increased, C_{lmax} and $(C_l^{1.5}/C_d)_{max}$ increases.
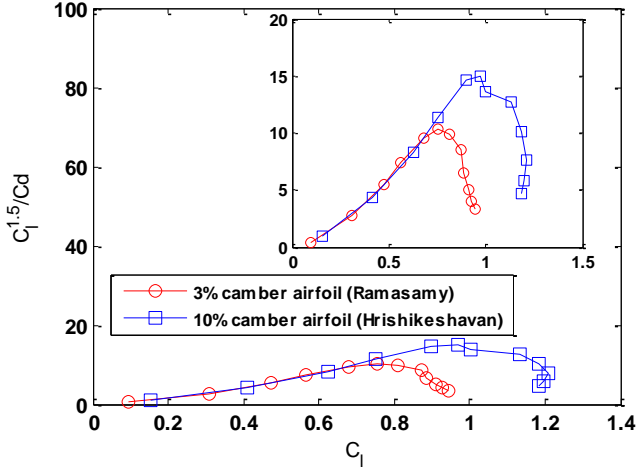
Figure 2.10: Airfoil performance (CFD prediction), Re = 50,000
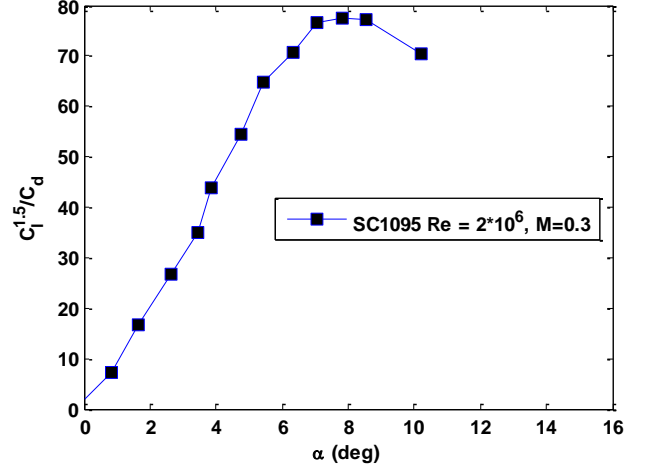
Figure 2.11: Airfoil performance (Noonan, 1989), Re ¿ 1 million

2.3.3 Blade planform

As was observed by previous studies (Ref. [33,34]), the blade chord distribution plays an important role in the performance of an MAV rotor. It was generally found that tapering the blade towards the blade tip resulted in an improved efficiency of the rotor. Therefore a baseline blade profile was chosen as shown in Fig. 2.12. In order to study the effect of solidity and to determine an efficient blade planform, different rotors were tested: (1) the baseline tapered blade ($\sigma_e = 0.11$), (2) rectangular blade I with the same root chord as the baseline blade ($\sigma_e = 0.13$), (3) tapered blade with 140% of the baseline chord ($\sigma_e = 0.15$), (4) rectangular blade II with same root chord as blade profile 3 ($\sigma_e = 0.18$). These are shown in Fig. 2.13.

The thrust weighted solidity was calculated as,

$$\sigma_e = 3 \int_0^1 \sigma(r) r^2 \mathrm{d}r \tag{2.4}$$
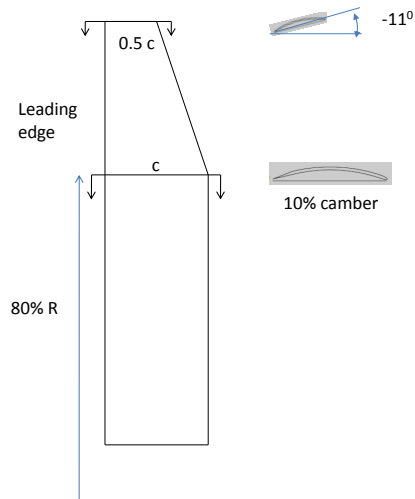
Figure 2.12: Taper and twise distribution of baseline blade
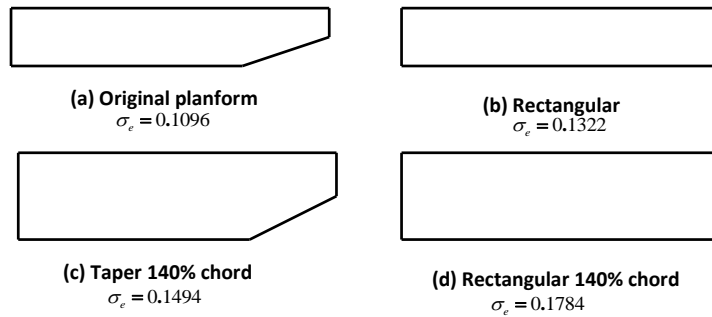
Figure 2.13: Blade planforms tested for performance comparison

It was used to account for the rotor planform, weighting the influence of the tips more heavily than the inner rotor regions. The blades were constructed from 3-layered 0/45/0 temperature cured carbon-epoxy prepreg fibers. This construction produced stiff and lightweight blades . The blade chord was set at 25 mm and the radius was 122 mm. Each two bladed rotor was tested on the micro rotor test stand using the procedure described in Sec. 2.3.1. The blade collective was varied up to 30 deg. Figure 2.14 shows the non-dimensional power polar for the different blade planforms. As the solidity of the blade is increased, expectedly C_P also increased for a given C_T. In order to remove the effect of solidity, as suggested in Ref. [27], C_P/σ^3 is plotted versus C_T/σ^2 in Fig. 2.15. It can be seen that for a given planform shape, the power polar collapses for different solidities. In general, the tapered blades perform better than the rectangular blades. The effect of solidity can also be seen in the Figure of Merit variation as a function of C_T/σ (Fig. 2.16) and C_T/σ^2 (Fig. 2.17). For the tapered or the rectangular planform, solidity did not significantly affect rotor performance. A maximum FM of about 0.64 for the tapered blade was obtained at a blade loading of between 0.15-0.2. The dimensional power polars for the different blades are shown in Fig. 2.18.

The power polars with the largest slopes for each blade profile are compared in the form of power loading in Fig. 2.19. It can be clearly seen that the tapered blades had the best performance. It must be mentioned that since the comparison is made at the same disk loading, the efficient blade configuration can be derived from the non-dimensional FM variation as well as the dimensional power loading comparison. In conclusion, the baseline tapered blade was chosen to be the optimum unshrouded rotor configuration for comparison purposes. Maximum power loading was achieved at a wide range of collective ($14^0 - 22^0$).
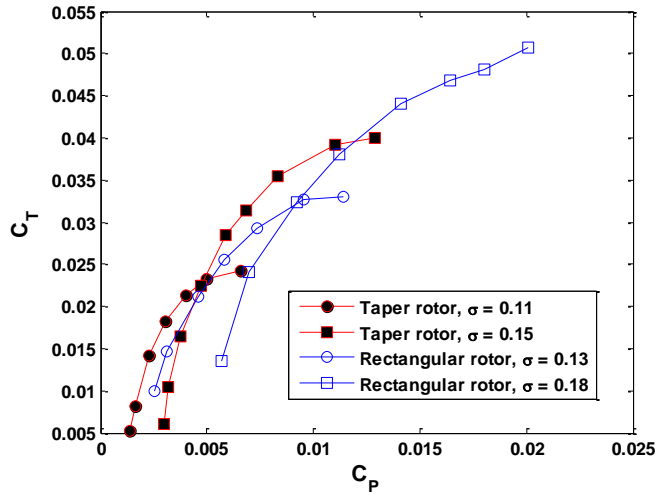
Figure 2.14: C_T vs. C_P
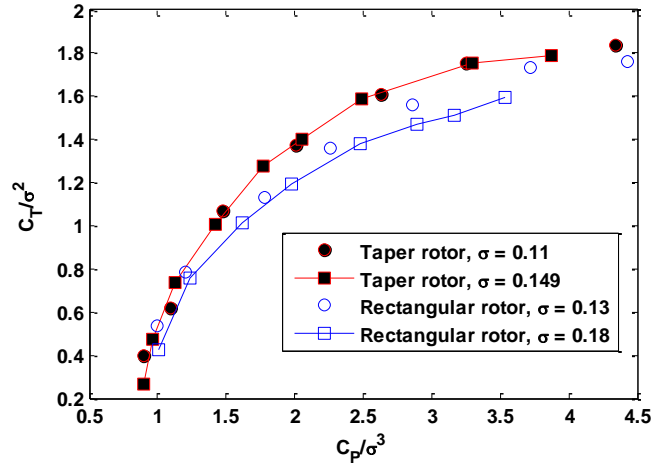
Figure 2.15: C_T/σ^2 vs. C_P/σ^3 to remove effect of solidity
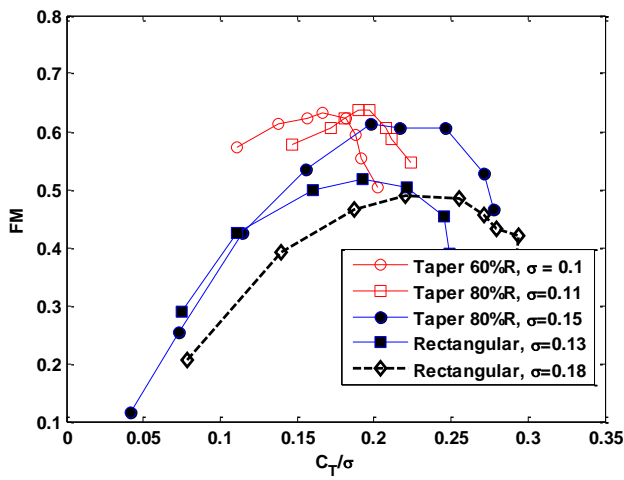
Figure 2.16: FM vs. C_T/σ
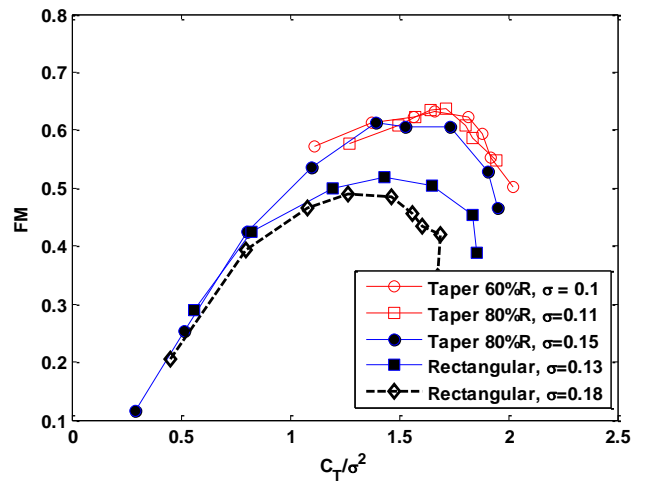
Figure 2.17: FM vs. C_T/σ^2 to remove effect of solidity
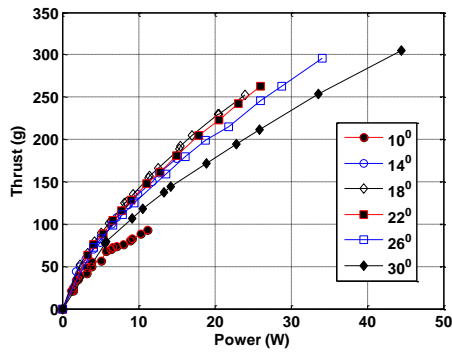
(a) Baseline taper blade
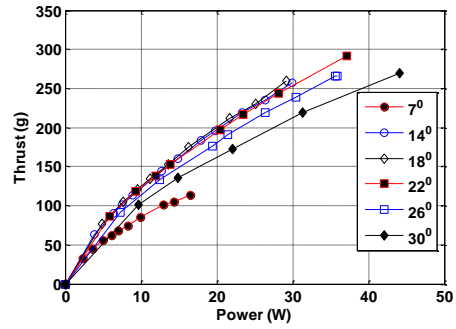
(b) Rectangular blade
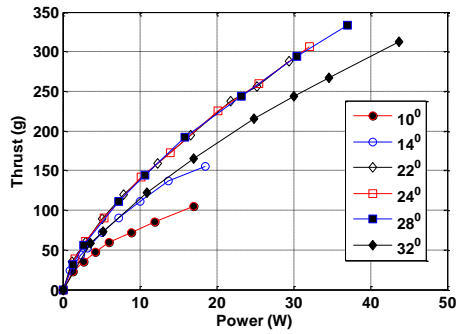
(c) Taper blade, 140% chord
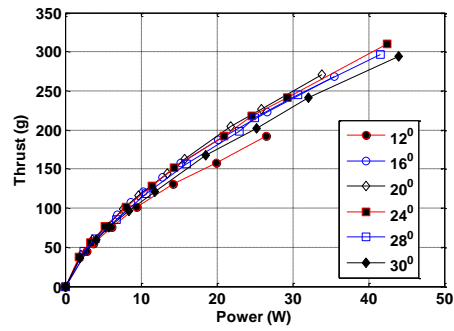
(d) Rectangular blade, 140% chord

Figure 2.18: Mecanical power vs. thrust for different blade planforms and collective settings
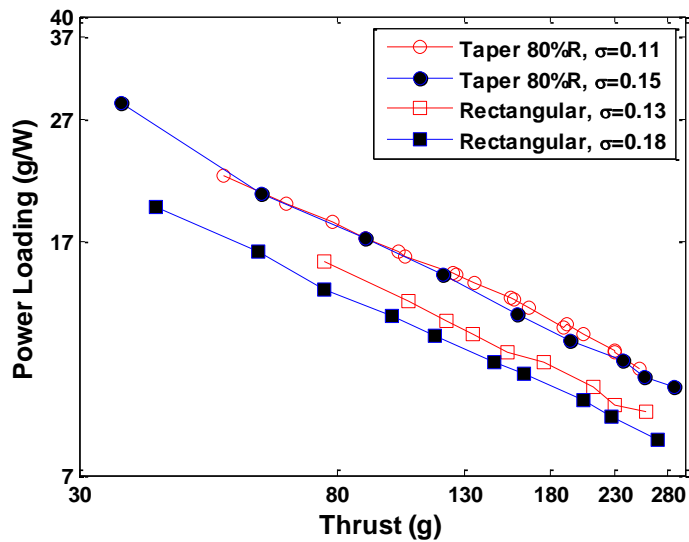
Figure 2.19: Comparison in power loading for different blade profiles

2.3.3.1 Note: micro rotor performance

From Fig. 2.16 it is curious to see that the operating blade loading values (C_T/σ) for efficient performance of MAV scale rotors is generally high. The maximum FM values of these rotors were plotted along with other micro rotor studies published in literature [33, 34, 37], and are shown in Fig. 2.20.
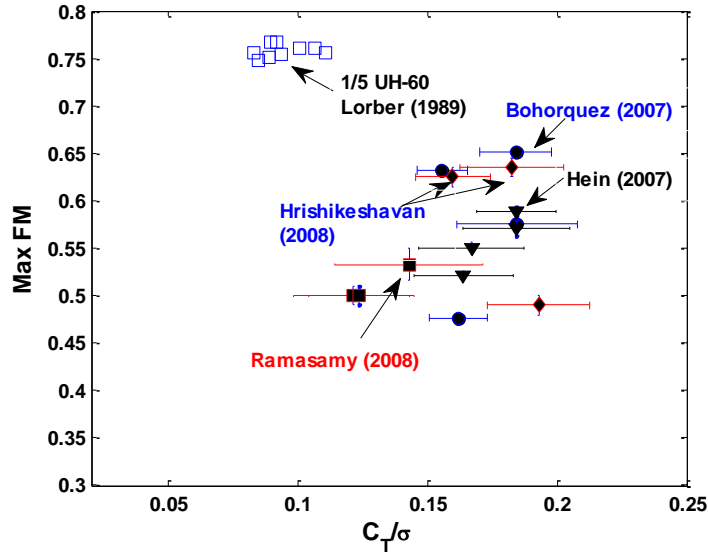
Figure 2.20: Operating blade loading for efficient rotor performance: comparison between micro and full scale rotor

Now, the mean lift coefficient of a rotor can be written as

$$\overline{C_L} = 6\left(\frac{C_T}{\sigma}\right) \tag{2.5}$$

So, a high blade loading implies a high average lift coefficient. The rotors tested by Ramasamy et al [37]. had circular airfoils with 3% camber while the other rotors had cambers greater than 7%. We know from Fig. 2.10 that the maximum lift coefficient is greater for airfoils with higher camber. Therefore from Eq. (2.5), the operating blade loading for the Ramasamy blades would be lower than

the higher camber blades which is what is observed in Fig. 2.20. Also, the lower camber blades tested by Ramasamy would have mean lift coefficients between 0.6-0.9 while those tested by others would have $\overline{C_L}$ between 0.9-1.2. From, Fig. 2.10 it can be seen that the operating lift coefficients for efficient airfoil performance are higher for the 10% camber airfoil when compared with the 3% camber airfoil. However, for the 10% camber airfoil, optimum airfoil performance is obtained for lift coefficients below 1.2. Nevertheless, the rotor performance can be qualitatively related at the airfoil and rotor level. However, in order to truly reconcile micro airfoil characteristics with micro rotor performance, detailed experiments need to be conducted to characterize airfoil performance at these low Reynolds numbers.

2.4 Hiller Stabilizer Bar

MAV scale rotors are characterized by low time constants, i.e., they are more agile compared to full scale rotors. This makes pilot control a difficult task. To overcome this, stabilizer bars are usually coupled with the main rotor. The Lock number (γ_R) of the rotor is defined as the ratio of the aerodynamic force to the inertial force

$$\gamma_R = \frac{\rho C_{l\alpha} c_R R^4}{I_{b_R}} \tag{2.6}$$

where, $C_{l\alpha}$ is the average lift curve slope of the rotor, c_R is the chord of an equivalent rectangular blade, R is the rotor radius and I_{b_R} is the flapping inertia of the rotor. By incorporating a Hiller bar with the main rotor, the inertial force contribution is increased, thus reducing the Lock number. Now, the rotor time

constant is defined as,

$$\tau = \frac{16}{\gamma_R \Omega} \qquad (2.7)$$

With the stabilizer bar, it becomes,

$$\tau = \frac{16}{\gamma_S \Omega} \qquad (2.8)$$

where, γ_S is the Lock number of the coupled rotor and stabilizer bar. Given that $\gamma_S < \gamma_R$, we can see that the rotor time constant is significantly increased. This implies a greater delay in response to external perturbations.

Additionally, the stabilizer bar can also be used as a control device by transferring cyclic pitch command to the main rotor blade, either directly (Hiller bar), or through a swashplate mixer (Bell/Hiller bar). An advantage of the Hiller bar is the reduction in servo power required to introduce cyclic commands.

The basic configuration of the rotor/Hiller-bar is shown in Fig. 2.3. It consists of a thin rigid rod with aerodynamic paddles attached to both ends. The bar is connected to the main shaft by means of a teetering hinge. A flapping of the Hiller bar directly results in feathering of the main rotor. Also, the blade flapping axis is aligned with the Hiller bar axis for a teetering rotor, but not necessarily so for a Hingeless rotor (Sec. 2.4.1). This section discusses two important aspects while incorporating a Hiller bar with the main rotor: phased Hiller bar concept and aerodynamic losses.

2.4.1 Phased Hiller bar concept

Experimental results show that as the clearance between the rotor blade tip and the shroud diffuser wall increases, the shrouded rotor performance decreases.

This is very likely to occur with a shrouded teetering rotor. Consider the tip plath plane (TPP) orientation shown in Fig. 2.21.
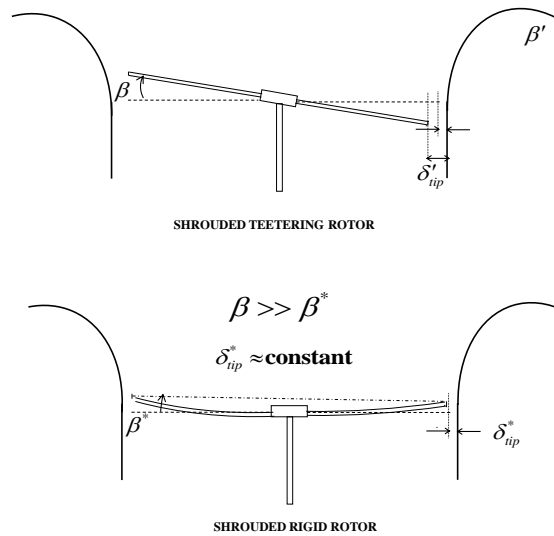
Figure 2.21: Tip path plane variation for teetering and hingeless rotor

It is clear that the tip clearance variation (δ_{tip}) is greater for the teetering rotor. In order to eliminate this, the flapping of the rotor must be restricted by incorporating a hingeless rotor. A later section describes another reason for incorporating a Hingless rotor. In addition to the restricted TPP motion, the hingeless rotor transfers control moments to the body of higher magnitude than a teetering or an articulated rotor. Therefore, the maneuverability of the vehicle is significantly increased.

Now, a teetering rotor has a non dimensional rotational flap frequency $\nu_\beta = 1$. This implies that when a blade pitch input is given, the rotor responds in flap with a 90^0 phase delay. The Hiller bar flap (placed 90^0 with respect to the blade) coincides with the blade pitch. Therefore, it can be seen that the Hiller bar and the blade flap are in phase. In other words, a longitudinal cyclic input produces a longitudinal control moment. However, for a hingeless rotor $\nu_\beta > 1$, the force

response has a phase delay of less than 90^0. From a similar argument, it can now be seen that a longitudinal cyclic input produces lateral and longitudinal control moments. In addition to this control cross coupling, there also exists a passive cross coupling in pitch and roll when a gust or a shaft disturbance is given. This is schematically shown in Figs. 2.22, 2.23

Teetering rotor:
Longitudinal cyclic input
results in pitch moment

Hingeless rotor:
Longitudinal cyclic input
(control hub moments) occurs
before 90 deg phase
delay : Pitch and roll moment
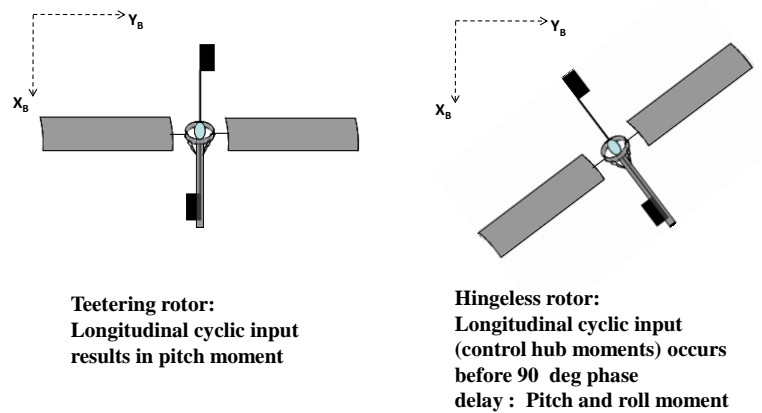
Figure 2.22: Control cross coupling with a hingeless rotor

A time marching ODE solver was implemented to highlight the cross-coupling in the hingeless rotor system to cyclic inputs as well as to gusts and shaft per-

Shaft perturbation (in pitch along $-Y_B$)
Desired response: Pitch down moment
Actual response: Pitch and roll moment

Gust disturbance (along $-X_B$)
Desired response: Pitch down moment
Actual response: Pitch and roll moment
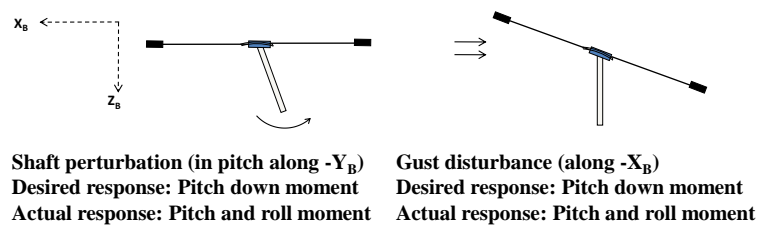
Figure 2.23: Passive cross coupling with a hingeless rotor

turbations. The Hiller bar and the hingeless rotor were modeled as a coupled teetering rotor and a spring-restrained(spring constant k_β) teetering rotor respectively. Servo pitch commands are given to the Hiller bar. The subsequent flap response of the bar translates to cyclic inputs to the main rotor which determines the pitch and roll response at the C.G. The external perturbations such as gusts, p, q, are introduced simultaneously to the Hiller bar and the main rotor. The inflow ratio is assumed to be uniform. The effect of the different forms of cross coupling is shown in Fig. 2.24. The cyclic input and the disturbances are normalized to unity. It can be seen that as the spring stiffness is increased, off-axis response increases.

In order to eliminate the control and passive cross coupling, the Hiller bar flapping must be phased appropriately with the main rotor feathering. Therefore, a hub was designed with circular slots to allow for adjustments in the Hiller bar phasing as can be seen from Fig. 2.25.

The phase angle may be either determined from a knowledge of the rotating flap frequency of the rotor blade or from a direct measurement of off-axis moments.

Theoretical Method: The force response delay for a given feathering input for a rotor is given by

$$\phi = tan^{-1}\left(\frac{\gamma_R}{\nu_\beta^2 - 1}\right) \tag{2.9}$$

where ν_β is the non-dimensional rotating natural flap frequency of the rotor and γ_R is the Lock number of the rotor. For a teetering rotor case, the phasing is exactly 90 degrees ($\nu_\beta = 1$). For a hingeless rotor, this is less than 90 degrees as $\nu_\beta > 1$. First, the non-dimensional non-rotating flap frequency $\nu_{\beta_{NR}}$ was determined. A blade impulse response setup (Fig: 2.26) was used to determine
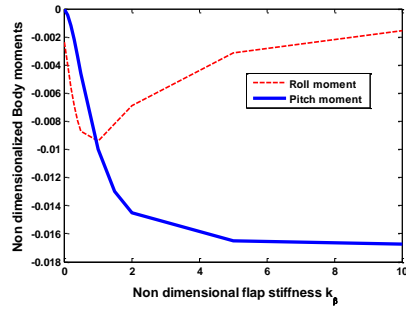
(a) Response to lateral cyclic input
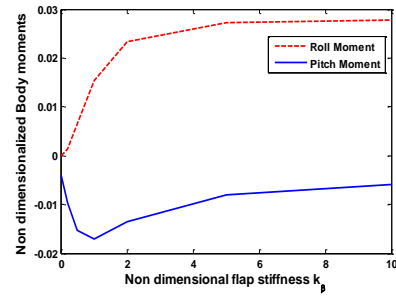
(b) Response to shaft perturbation in pitch
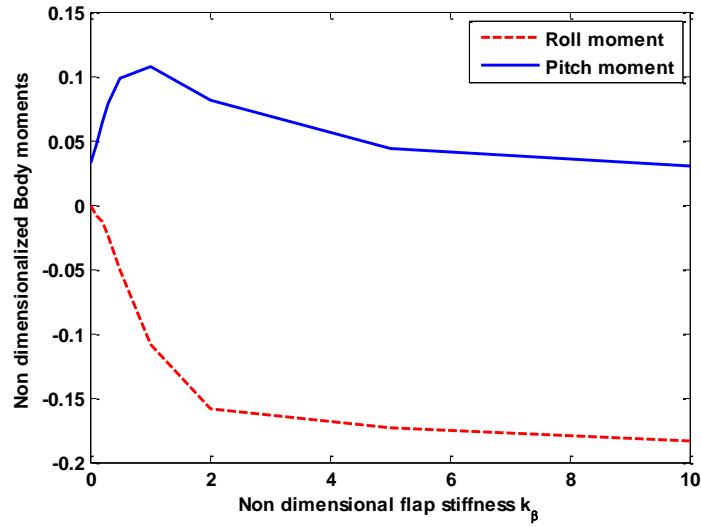
(c) Response to gust disturbance

Figure 2.24: Cross coupling in Hingeless rotor (Numerical)
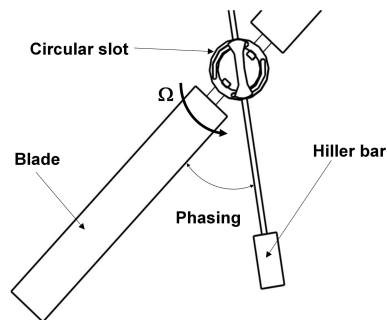
Figure 2.25: Hingeless hub: phased Hiller bar
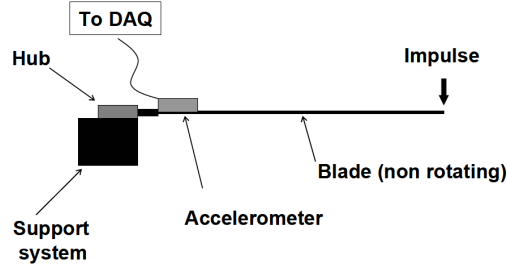
Figure 2.26: Measurement of non-rotating flap frequency of the rotor blade

$\nu_{\beta_{NR}}$. The blade was attached to the hub with a cantilever boundary condition. An accelerometer was placed at the root of the blade such that the bending dynamics was not affected. Analysis of the FFT of the accelerometer response to an impulse provided a measure of $\nu_{\beta_{NR}}$. From this, ν_β was extracted for a range of RPMs. The phasing was then determined using Eq. (2.9).

Experimental Method: The phase angle of the Hiller bar was then experimentally validated using the set-up shown in Fig. 2.27. The rotor system was attached to a shaft that was connected to a torque load cell at the other end. Cyclic input was given such that the torque cell measured the off-axis moment. The Hiller bar was manually adjusted over a range of angles for each rotor speed. At each RPM, the desired phasing angle was determined as the angle when zero off-axis moment was measured (Fig. 2.28).

Figure 2.29 shows the variation of the desired phasing angle Ψ_{C_0} as a function of operating RPM. It can be seen that Ψ_{C_0} increased with operating RPM. This is due to the fact that ν_β decreases with RPM. Overall, there was a satisfactory agreement between the predicted (Eq. (2.9)) and measured phase angles.

Finally, the control authority of the rotor was evaluated using the set-up
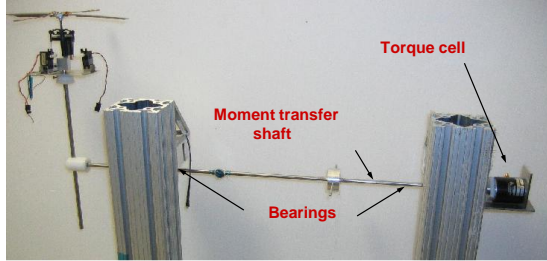
Figure 2.27: Set-up to measure Hiller bar phasing angle
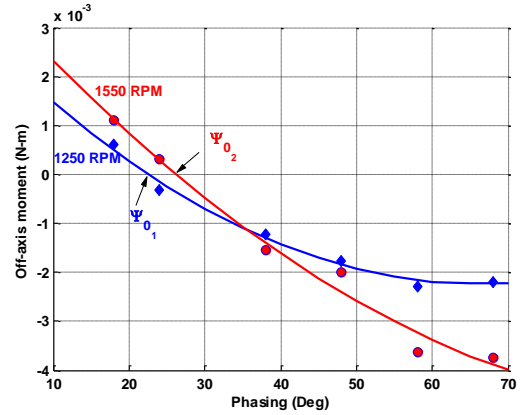
Figure 2.28: Variation of off-axis moment with phasing angle

shown in Fig. 2.27. The longitudinal control moment for maximum longitudinal control input was measured as a function of rotor RPM (Fig. 2.30). The cyclic pitch travel was $\pm 10^0$. Additionally, with the appropriate phasing, off-axis moments were eliminated.

2.4.2 Aerodynamic performance

The Hiller stabilizer bar consists of aerodynamic paddles attached at each end of a teetering bar. These paddles and the bar increase the profile drag of the rotor. It is important to measure the profile losses and identify a Hiller bar design that minimizes these losses.

The main parameters chosen for the Hiller bar design were the radius, paddle area and paddle collective. Two representative designs were considered (Table 2.1).

HB-1 had a shorter paddle length as compared to HB-2 in order to maintain the Lock numbers of the two designs in the same range. It can be seen that both the designs significantly improved the rotor time constant (by up to a factor of
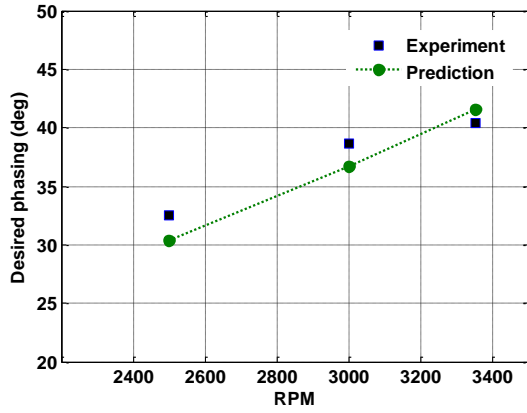
Figure 2.29: Variation of desired phasing with RPM
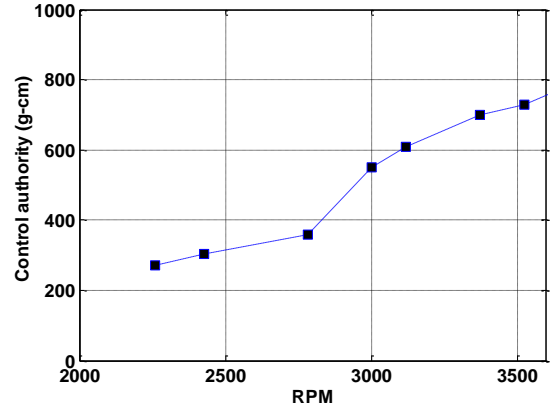
Figure 2.30: Longitudinal control moment versus RPM for $\pm 10^0$ longitudinal cyclic input

Component	Radius(mm)	Chord(mm)	Paddle length(mm)	Lock no.	τ(s)
Tapered blade (Sec. 2.3.3)	122	23	–	4.2	0.015
HB-1	60	27	30	0.56	0.11
HB-2	90	27	60	0.84	0.073

Table 2.1: Hiller bar design parameters

5-8). It was then sought to investigate the effects of these design parameters on the aerodynamic efficiency of the rotor.

The coupled rotor-Hiller bar system was tested on the micro rotor hover stand with the paddle collectives varied from 0 to 30 degrees. The Hiller bar was phased at 45^0 leading the blade motion (Fig. 2.27). Figure 2.31(a) shows the variation of Figure of merit as a function of the paddle collective for the two Hiller bar designs. From Fig. 2.31(a), the coupled hingeless rotor Hiller bar system had decreased performance when compared to the bare rotor. It can be seen that HB-1 performed better than HB-2 due to lower profile area and hence reduced profile power losses. It was observed that at low paddle collectives, there was a drop in the effective C_T (Fig. 2.31(b)) and consequently FM. This could probably be due to the paddles operating at a negative angle of attack due to rotor inflow, thus decreasing the total thrust. However, since the paddles have a negligible contribution to the rotor thrust, this drop in C_T is not significant. At high paddle collectives, the profile power significantly increased (Fig. 2.31(c)). In an intermediate range of collectives of about 10-15 degrees, a minimum drop in FM was observed (about 6% for HB-1). The setting that resulted in the least drop of FM was chosen for the final Hiller bar design. It was also interesting to see the effect of phasing on performance. The Hiller bar was mounted at 45^0, 90^0 and 135^0 forward of the blade feathering axis. The rotor C_T was 0.0225. Figure 2.32 shows that there is a slight drop in performance (4% reduction in FM) when the Hiller bar is closer to the blade trailing edge (135^0) than when it is closer to the leading edge (45^0).
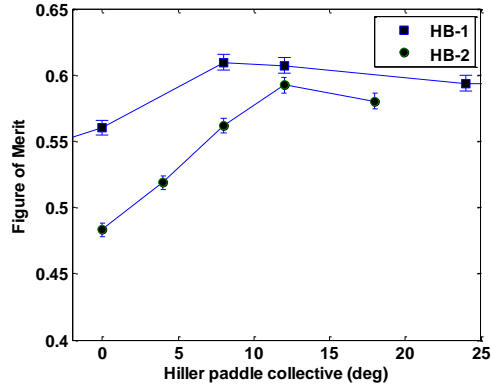
(a) Figure of merit
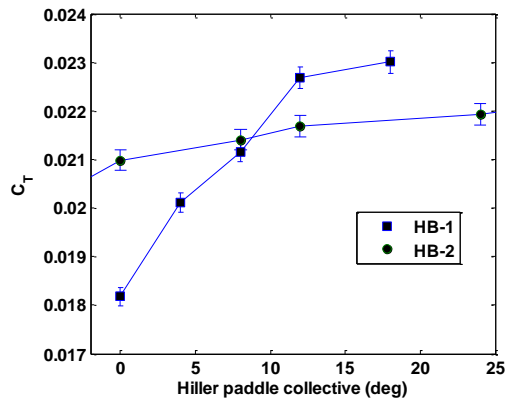
(b) Rotor thrust coefficient
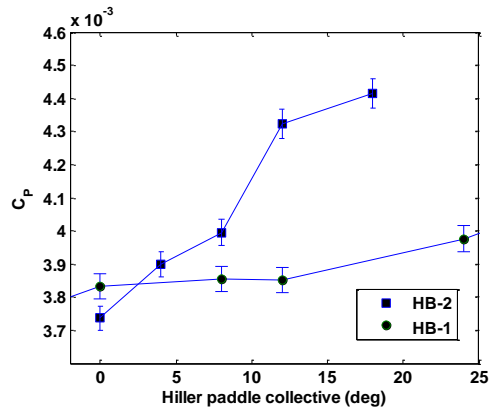
(c) Rotor power coefficient

Figure 2.31: Effect of Hiller bar paddle collective on rotor performance (Bare rotor FM   0.64)
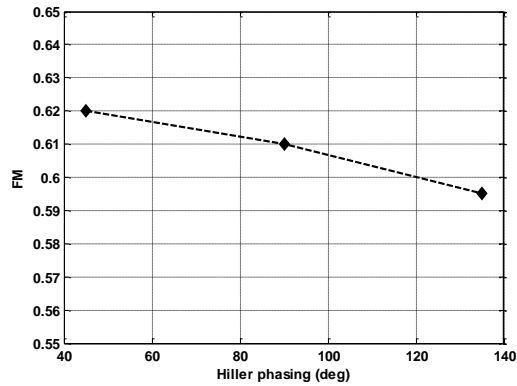
Figure 2.32: Effect of Hiller bar phasing on FM

2.5 Anti-torque Vanes

The anti-torque vane concept is one of the key design features for the prototype vehicle designs described in this chapter. To improve the compactness of the vehicle, the anti-torque system was designed with vanes installed in the downwash of the main rotor instead of a conventional tail rotor.

2.5.1 Proof of concept and analysis

A series of experimental tests were performed to study the effectiveness of the vane concept. For these studies, a 3 bladed fixed pitch rotor with a solidity of 0.15 and a diameter of 6″ was used. The blades were rectangular in panform, untwisted and with a circular arc airfoil section with a 6% camber. The blades were set at a collective pitch of 18^0. The anti-torque vanes were assembled to the central body holding the DC motor driving the main rotor. Four vanes were installed, each with a chord of 3". First, flat plates were used as vanes, which were installed parallel to the rotor axis to study the presence of swirl in the rotor downwash. The effect on the net torque on the body was measured. Then, vanes with an 8% circular arc cross-section were tested. The vanes could be set
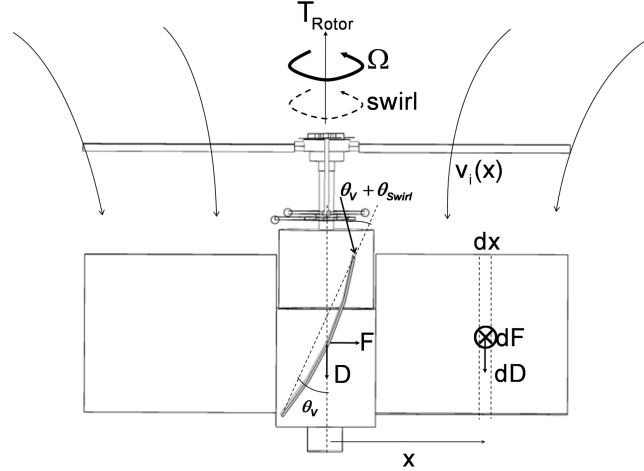
Figure 2.33: Schematic of the vane set-up

at a given pitch angle with respect to the central axis of the rotor. The amount
of anti-torque generated by the vanes was measured at different values of vane
incidence θ_V.

A blade element momentum theory (BEMT) analysis was performed to estimate
two important factors: anti-torque capability of the vanes and the drop in net
thrust due to vane drag for a given input power. The aerodynamic lift (F) and
drag (D) generated by a single vane are shown in the schematic (Fig. 2.33).
The downwash encountered by the vanes is v_v such that $v_i < v_v < v_{exit}$. While
BEMT requires v_v to be parallel to the rotor axis, in reality, it will include
a swirl component such that the net vane angle of attack is $\theta_v + \theta_{swirl}$. This
swirl angle is estimated from flat plate vane experiments. For the analysis, the
basic assumptions are : (1) $v_v = 1.5v_i$, (2) area of rotor downwash influencing
the vanes contracts up to about 80%. (3) the aerodynamic forces L and D are
perpendicular and parallel to the rotor axis respectively, (4) Prandtl tip loss
function is not included, and (5) swirl angle does not change based on vane

77

incidence and geometry. Based on these assumptions,

Rotor thrust,

$$T_{Rotor} = \rho A (\Omega R)^2 C_T \tag{2.10}$$

Inflow velocity,

$$v_i(x) = \Omega R \frac{\sigma C_{l\alpha}}{16} \left(\sqrt{1 + \frac{32\theta_0 x}{R\sigma C_{l\alpha}}} - 1 \right), \lambda_i(c) = \frac{v_i(x)}{\Omega R} \tag{2.11}$$

where, R is the rotor radius, Ω is the rotor speed, σ is the rotor solidity, $C_{l\alpha}$ is the lift curve slope around 0.05/deg for a 6% circula-arc camber airfoil, $Re = 5 \times 10^4$ [162] and θ_0 is the blade collevtive in degrees.

Rotor torque,

$$Q_{Rotor} = \rho A (\Omega R)^2 R \left(\kappa \frac{C_T^{3/2}}{\sqrt{2}} + \sigma \frac{C_{D_R}}{8} \right) \tag{2.12}$$

where, κ is the induced power correction factor chosen to be 1.75 [27] for MAV scale rotors, C_T is the rotor thrust coefficient and C_{D_R} is the average drag coefficent of the rotor blade around 0.1 for a 6% camber circular camber airfoil [162].

Vane torque,

$$Q_{Vanes} = \frac{N_{Vanes} \rho v_v^2}{2} \int_0^{0.9 L_V} C_{l\alpha}(\theta_V + \theta_{swirl}) c_V x \mathrm{d}x \tag{2.13}$$

where, N_{vanes} is the number of vanes equal to 4 for the present set-up, v_v is the downwash velocity encountered by the vanes, $c_{l\alpha}$ for circular-arc camber vanes is chosen to be around 0.05/deg, θ_V is the vane pitch setting equal to 12^0, L_V is the distance between the shaft axis and outer vane edge and c_V is the vane chord.

$$D_{Vanes} = \frac{N_{Vanes} \rho v_v^2}{2} \int_0^{0.9 L_V} C_{d_V} c_V x \mathrm{d}x \tag{2.14}$$

where, C_{d_V} for the 8% circular camber vanes, around 0.2 for an incidence angle of about 15^0 [162].

Net torque (from (2.12) and (2.13)),

$$Q_{Net} = Q_{Rotor} - Q_{vanes} \tag{2.15}$$

Net thrust (from (2.10) and (2.14)),

$$T = T_{Rotor} - D_{Vanes} \tag{2.16}$$

Input electrical power,

$$P_{Elec} = \frac{Q_{Rotor}\Omega}{\eta} \tag{2.17}$$

where η is the motor-gearbox efficiency chosen to be about 50% based on measured motor performance.

The experimentally measured torque on the body obtained by installing flat plates in the downwash, parallel to the axis of the rotor (0^0 inclination), is shown in Fig. 2.34. It can be seen that by just installing these flat vanes, the total torque on the body is reduced by approximately 40% (θ_V for this flat plate vane case is 0^0). Using this, the swirl angle was determined to be about 4^0. This result was used to update the net vane angle of incidence and predict the effect of vanes on the net body torque (2.15) and input power (2.17) at different thrust levels (Fig. 2.35). It can be seen that with 8% circular camber vanes set at 12^0 pitch setting, a 75% torque balance was achieved. From Fig. 2.36, a 10% reduction in thrust was observed for a given input power due to the vane drag.

The results of the analysis compares satisfactorily with the experimental results. The circular arc vanes at a pitch angle of 12^0 reduce the torque on the
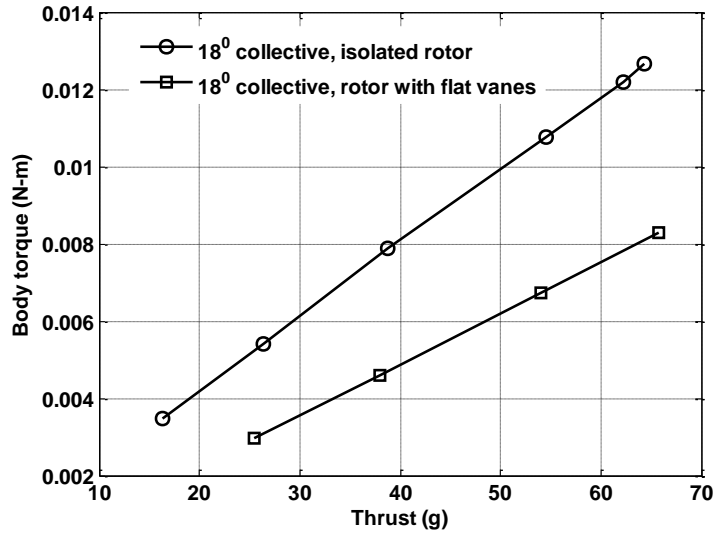
Figure 2.34: Body torque versus thrust for rotor with flat vanes at 0^0 inclination in rotor downwash
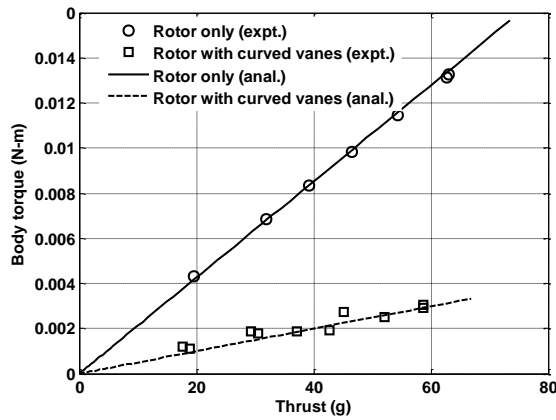
Figure 2.35: Net body torque versus thrust for curved vanes in downwash
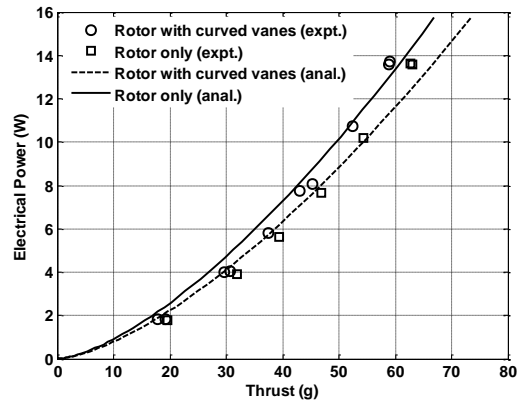
Figure 2.36: Effect of vanes on power consumed
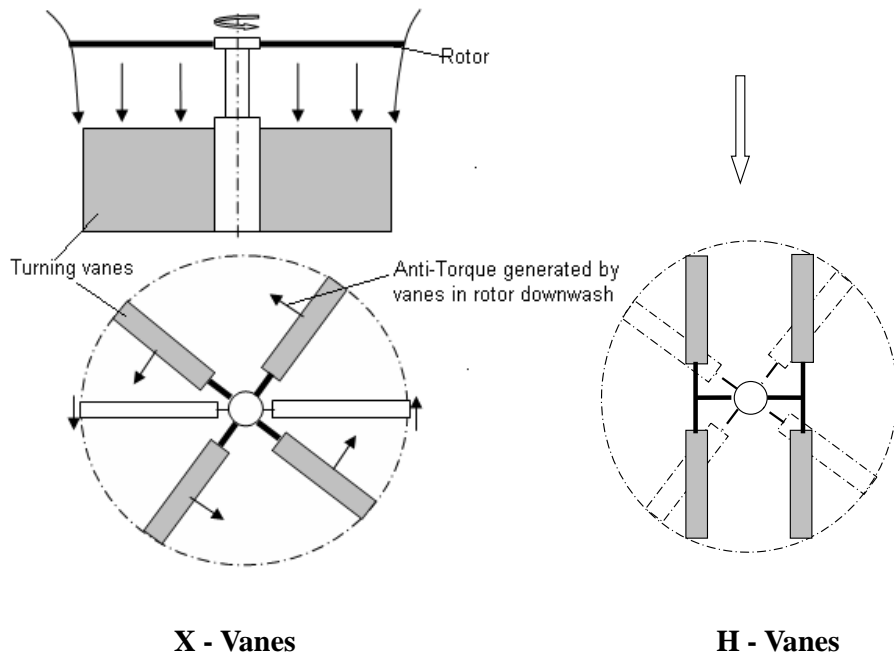
Figure 2.37: Vane arrangement

body by almost 80% (Fig. 2.35). The installation of the vanes results in an increase in power required for a given thrust by approximately 10%. This percentage increase in power is similar to that typically required by a conventional full-scale tail rotor. Based on the above results, it was seen that the concept of vanes placed in the rotor downwash for countering rotor torque was viable. For the final design, two fixed vanes and two vanes provided with controllable trailing edge flaps for yaw control were incorporated.

2.5.2 Integration and yaw control

These vanes can be incorporated in the vehicle either in an X or an H configuration. This is schematically shown in Fig. 2.37. With the X configuration,

the vehicle axisymmetry is maintained and the structure of the vehicle becomes sturdier. However in edgewise flight, the vanes could be a significant source of profile drag. This limitation can be alleviated with the H configuration. The effectiveness of the two configurations were measured using the set-up shown in Fig. 2.38). Four rectangular (3"×5"), 8% camber circular arc carbon fiber vanes
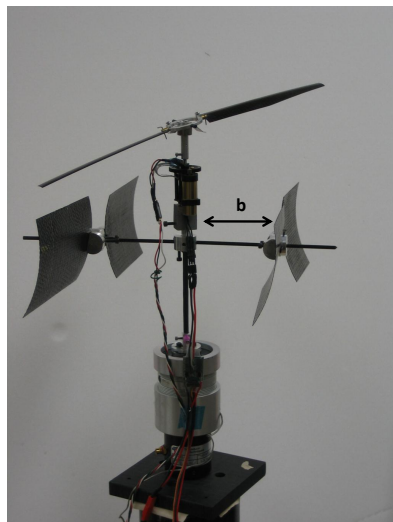
Figure 2.38: Set-up to measure anti-torque and power penalty of X and H vanes

were attached to the shaft under the downwash of the rotor. The rotor thrust coefficient was set at $C_T = 0.02$. The H configuration was tested with different spacing (b) between the vanes.

The results are shown in Fig. 2.39. For the rotor without vanes, the torque increased linearly with thrust as expected. With the X configuration, torque is reduced to almost zero irrespective of thrust for a vane collective of 12^0. Similar torque reduction was observed with the H configuration for $b = 25mm$. However, with higher values of b, the anti-torque reduced. This can be explained by the fact that for $b > 25mm$, a portion of the vanes was 'outside' the rotor downwash resulting in a decrease in the effective aerodynamic surface capable of countering
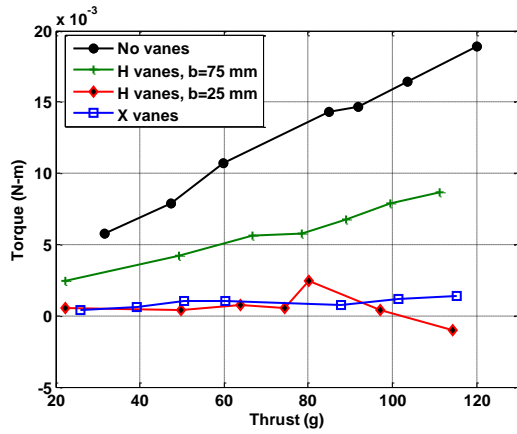
Figure 2.39: Anti-torque capability of X and H vanes
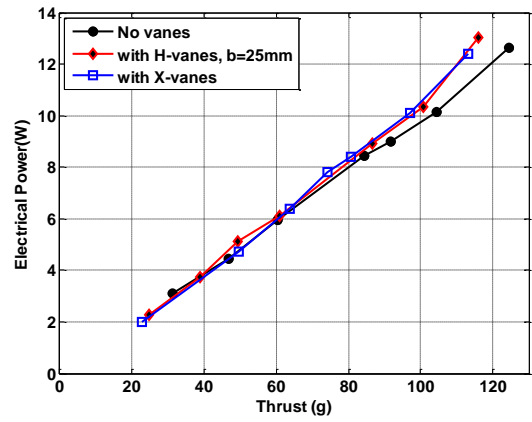
Figure 2.40: Power penalty with X and H vane configuration

the torque. Figure 2.40 shows electrical power versus thrust for the three configurations. Both X and H vanes incurred a similar power penalty of about 10% when compared to the isolated rotor case. Presently, for the purposes of axisymmetry and a sturdy structure, the X vanes are incorporated. The vanes with the controllable flaps are integrated into the vehicle as shown in Fig. 2.41 The
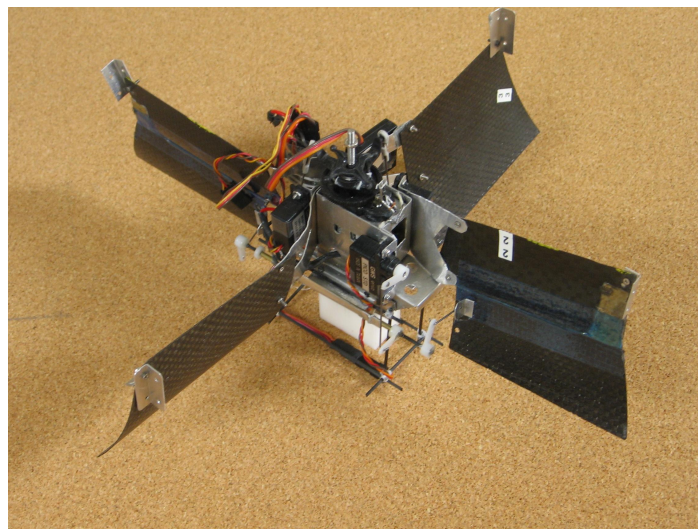
Figure 2.41: X vanes integrated into body

controllable flaps changed the vane incidence of two of the vanes by about 16^0 with maximum control input. As desired, the vane deflection for a given control input was linear (Fig. 2.42). The yaw control authority at operating thrust of about 250 g was measured as a function of control vane angle. The fixed vanes had a collective of about 23^0. It can be seen that yaw control authority was perfectly bi-directional and linear about trim (Fig. 2.43).
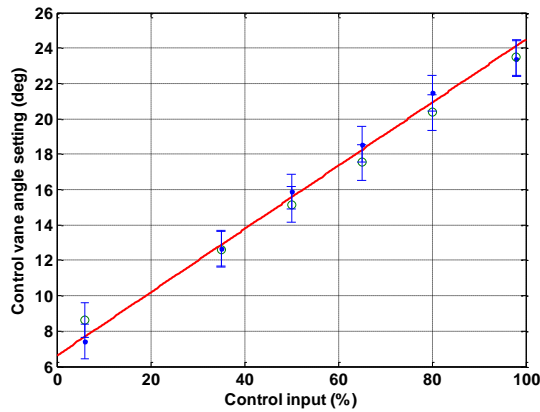
Figure 2.42: Control vane deflection for a given control input
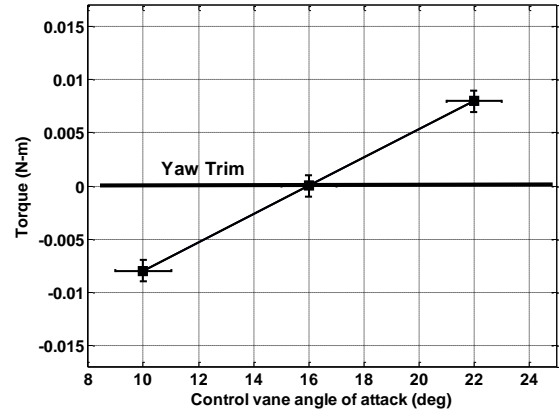
Figure 2.43: Effect of control vane deflection on vane torque

2.6 Shroud

In this section, improvements in hover power loading of an efficient unshrouded rotor (discussed in 2.3.3) by enclosing the rotor in a shroud are discussed.

2.6.1 Principle

In a shrouded rotor configuration, the thrust of a shrouded rotor includes two parts, the thrust of the rotor and the additional thrust from the shroud. Figure (2.44) shows a schematic of the principle of the shrouded rotor. The shroud

Figure 2.44: Shrouded rotor operating principle

consists of two sections: the inlet and the diffuser. The diffuser recovers kinetic energy of the slipstream and increases mass flow rate through the rotor (for the same total thrust produced by the shrouded and an unshrouded rotor). Operation of the rotor creates a low pressure above the rotor plane. This accelerates flow over the shroud inlet surface. Suction force is generated as a result of this airflow which results in an additional lift force. A summary of the momentum theory analysis for the shrouded rotor aerodynamics is shown here which can be used to explain improvements in hover performance. Detailed derivations of these results can be found in [27, 50].

Consider Fig. 2.45 that shows a schematic of the 2-D rotor wake for the unshrouded and shrouded rotor. Momentum theory assumes inviscid, incompressible, steady and quadi-one-dimensional flow. The rotor imparts only axial momentum with no wake swirl. The wake of the shrouded rotor is assumed to have expanded to ambient atmospheric pressure at the diffuser exit plane.

Figure 2.45: Effect of shroud on wake contraction [50]

Open rotor: Mass flow rate:

$$\dot{m}_{OR} = \rho A v_{iOR} \tag{2.18}$$

Thrust of open rotor system from conservation of momentum:

$$T_{OR} = \dot{m}_{OR} w_{OR} \tag{2.19}$$

Induced power:

$$P_{iOR} = \frac{1}{2} \dot{m}_{OR} w_{OR}^2 \tag{2.20}$$

Thrust of open rotor system from actuator-disk model of rotor:

$$T_{OR} = \Delta p A \tag{2.21}$$

Here, A is the rotor disk area, v_{iOR} is the induced velocity of flow across the rotor disk, w_{OR} is the velocity of the rotor wake at the location where wake pressure is ambient and Δp is the pressure differential across the rotor plane. From conservation of energy and actuator-disk model of the rotor,

$$\Delta p = \frac{1}{2} \rho w_{OR}^2 \tag{2.22}$$

It follows that,

$$w_{OR} = v_{iOR} \tag{2.23}$$

$$v_{iOR} = \sqrt{\frac{T_{OR}}{2\rho A}} \tag{2.24}$$

$$P_{iOR} = \frac{T_{OR}^{3/2}}{\sqrt{2\rho A}} \tag{2.25}$$

Shrouded rotor: Unlike the open rotor, the exit area of the shrouded rotor wake (A_e) is prescribed as the area of the diffuser exit plane.

Mass flow rate:

$$\dot{m}_{SR} = \rho A v_{iSR}$$
$$= \rho A_e w_{SR} \tag{2.26}$$

$$\Rightarrow w_{SR} = \frac{v_{iSR}}{\sigma_d} \tag{2.27}$$

Total thrust of shrouded rotor system from conservation of momentum:

$$T_{SR} = \dot{m}_{SR} w_{SR}$$
$$= \rho A \frac{v_{iSR}^2}{\sigma_d} \tag{2.28}$$

$$\Rightarrow v_{iSR} = \sqrt{\frac{\sigma_d T_{SR}}{\rho A}} \tag{2.29}$$

Induced Power:

$$P_{iSR} = \frac{T_{SR}^{3/2}}{\sqrt{4\sigma_d \rho A}} \tag{2.30}$$

where σ_d is the contraction ratio of the rotor wake (it is 0.5 for an open rotor based on momentum theory). From Fig. 1.8 it can be seen that contribution to total thrust of the shrouded rotor system comes from the rotor, inlet and diffuser. It can be shown that,

Rotor thrust:

$$T_{rotor} = \frac{T_{SR}}{2\sigma_d} \tag{2.31}$$

Diffuser thrust:

$$T_{diffuser} = -\frac{T_{SR}(\sigma_d - 1)^2}{2\sigma_d} \tag{2.32}$$

Inlet thrust:

$$T_{inlet} = \frac{T_{SR}\sigma_d}{2} \tag{2.33}$$

It can be seen that as the expansion ratio is increased, the diffuser increases the downforce on the system (negative thrust), the rotor thrust decreases and the inlet thrust increases. For a straight diffuser ($\sigma_d = 1$), the rotor and shroud inlet share about 50% of the total thrust (this was experimentally measured in Sec. 2.6).

Comparisons between open and shrouded rotor performance: If the rotor disk area for both the configurations are equal, the performance can be compared in two ways,

At constant induced power: Here, $P_{iSR} = P_{iOR}$

$$\frac{\dot{m}_{SR}}{\dot{m}_{OR}} = \frac{v_{iSR}}{v_{iOR}} = (2\sigma_d)^{2/3} \tag{2.34}$$

$$\frac{w_{SR}}{w_{OR}} = \frac{1}{(2\sigma_d)^{1/3}} \tag{2.35}$$

$$\Rightarrow \frac{T_{SR}}{T_{OR}} = (2\sigma_d)^{1/3} \tag{2.36}$$

It can be seen that for a straight diffuser section, the momentum theory predicts a 26% improvement in thrust for a shrouded rotor over an unshrouded rotor at the same induced power.

At constant total thrust: Here, $T_{SR} = T_{OR}$

$$\frac{\dot{m}_{SR}}{\dot{m}_{OR}} = \frac{v_{iSR}}{v_{iOR}} = \sqrt{2\sigma_d} \tag{2.37}$$

$$\frac{w_{SR}}{w_{OR}} = \frac{1}{\sqrt{2\sigma_d}} \tag{2.38}$$

$$\Rightarrow \frac{P_{SR}}{P_{OR}} = \frac{1}{\sqrt{2\sigma_d}} \tag{2.39}$$

It can be seen that for a straight diffuser section, the momentum theory predicts a 30% reduction in induced power for a shrouded rotor over an unshrouded rotor for the same total thrust. In reality, this number is lower due to losses that may be attributed to tip losses, duct skin friction, slipstream rotation and flow separation over the inlet and/or diffuser. Whether the comparison is made at constant thrust or constant power, the mass flow rate through the shrouded rotor increases, while the exit wake velocity reduces. One important consideration not made here is the net improvement in system thrust after taking the weight of the shroud into concern. This is explained in the next section.
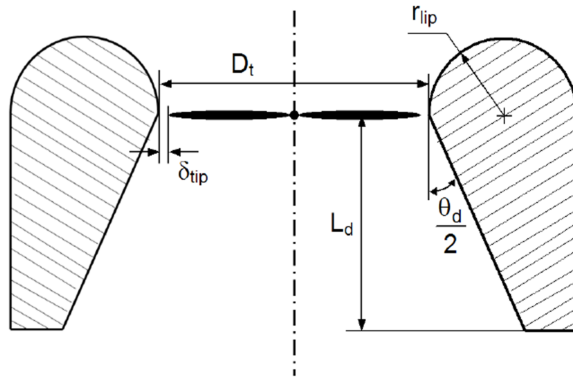
Figure 2.46: Shroud design parameters

2.6.2 Design

In the recent study by Pereira and Chopra [50], an optimum combination of design parameters for an MAV scale shrouded rotor (Fig. 2.46) was identified to minimize these losses. Key conclusions from this study relevant to the present design were: (1) a blade tip clearance $\delta_{tip} < 0.012R$ should be maintained for good performance, (2) the diffuser angle (θ_d) plays a more important role than the diffuser length (L), and (3) the outer portion of the shroud lip does not play a major role in thrust production. Hence for weight savings, the lip chord can be shortened.

It can be seen that for this concept to be viable, the thrust improvement offered by a shrouded rotor for a given operating power should be at least greater than the weight of the shroud itself. A design analysis based on simple momentum theory to estimate the upper limit for the shroud mass is described below.

Let W_{US} be the weight of the unshrouded MAV, W_{Shroud} be the weight of the

shroud and W_S be the weight of the shrouded MAV. Consequently,

$$W_S = W_{Shroud} + W_{US} \tag{2.40}$$

The mechanical power consumed by any rotor can be written as,

$$P = P_P + P_I \tag{2.41}$$

The profile power (P_P) is mainly a function of rotor solidity and airfoil drag coefficient. The induced power (P_I) however depends on the structure of the wake. Since the rotor configuration is fixed, it can be logically assumed that the main differences in mechanical power consumption between an unshrouded and shrouded rotor is from the induced power. Therefore, for a beneficial shroud design,

$$P_{I_S} < P_{U_S} \tag{2.42}$$

In non dimensional terms,

$$C_{P_{I_S}} < C_{P_{I_U}S} \tag{2.43}$$

From simple momentum theory, for a given contraction ratio σ_D, the non-dimensional induced power is given by,

$$C_{P_I} = \kappa \frac{W^{3/2}}{\sqrt{4\sigma_D \rho A}} \tag{2.44}$$

Where, κ is the induced power factor that accounts for tip loss effects, non-uniform inflow and swirl effects. W is the weight of the vehicle, A is the area of

the rotor disk which is maintained constant and ρ is the air density. Hence, for

$$C_{P_{I_S}} < C_{P_{I_{US}}} \tag{2.45}$$

It is required that,

$$\kappa_S \frac{W_S^{3/2}}{\sqrt{4\sigma_D \rho A}} < \kappa_{US} \frac{W_{US}^{3/2}}{2\rho A} \tag{2.46}$$

This leads to,

$$\frac{W_S}{W_{US}} < \left(\frac{\kappa_{US}}{\kappa_S}\right)^{2/3} (2\sigma_D)^{1/3} \tag{2.47}$$

Since the shroud diffuses the rotor tip vortex [113], the induced losses from a shrouded rotor are expected to be lower than an unshrouded rotor. Consequently, $\kappa_{US} > \kappa_S$. A conservative estimate for the weight restriction for the shroud can be made by assuming $\kappa_{US} \sim \kappa_S$. Hence, from (2.47) and (2.40),

$$W_{Shroud} < \left((2\sigma_D)^{1/3} - 1\right) W_{US} \tag{2.48}$$

For example, if the weight of the unshrouded vehicle is 250 grams, and if $\sigma_D = 1$, the power loading of the vehicle can be improved by enclosing the rotor in a shroud weighing less than 65 grams.

However, due to the shroud lip, the dimension of a shrouded rotor MAV in the rotor plane is equal to an unshrouded rotor MAV with a larger rotor diameter. To accommodate the effect of this increased size, the revised restriction for the shroud weight becomes

$$W_{Shroud} < \left(\left(2\frac{A}{A'}\sigma_D\right)^{1/3}\right) W_{US} \tag{2.49}$$

where A is the area of the rotor disk and A' is the area of the shroud including the shroud lip. Consider the previous example of a 250 grams unshrouded rotor MAV with an 11" diameter rotor. For the same dimension, the shroud would have a diameter of 11". If the diameter of the rotor is 9" (1" shroud lip), for power loading improvements, the weight of the shroud should not exceed 25 grams. In further discussion, this restriction is not made and a shrouded rotor is compared with an unshrouded rotor with the same rotor diameter.

It can be seen that these weight restrictions pose challenges for the shroud construction that include (1) lightweight material construction without compromising on shroud stiffness, and (2) smooth surface construction to ensure uniformity in pressure distribution over the shroud inlet. Shroud construction iterations were carried out based on two designs to determine a stiff, lightweight structure.

Shroud design 1: A shroud structural frame was constructed out of 1-2 mm thick strips made from cured carbon/epoxy that were suitably arranged to stiffen the structure in torsion and in the radial direction. The frame was covered with clear cellophane tape. The design is shown in Fig. 2.47. The shroud weight was 41 grams. For this design, $r_{lip} = 9\%D_t$, $L = 15\%D_t$, $\sigma_D = 1$. The diffuser length was restricted to save weight and minimize surface friction losses.

Shroud design 2: This design consisted of a single ply of carbon fiber/epoxy weave on a framework of unidirectional graphite epoxy stiffeners. The shroud was constructed by laying up the plies on a female metal mold, vacuum bagging and curing in an oven (Fig. 2.48). A chord-diameter ratio of 0.5 was chosen to save weight. The shroud weighed about 45 grams.

Shroud design 1 was stiffer in the radial and out of plane torsion mode as compared to shroud design 2, while the second design had a uniform shroud inlet surface. However, a stiffer shroud was preferred to avoid undesirable rotor

Shroud Design 1   **Shroud Design 2**
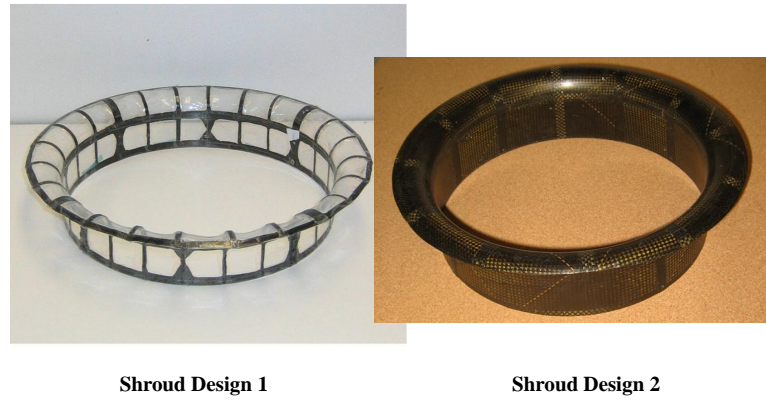
Figure 2.47: Shroud designs

shroud interference. Hence, results of the performance tests discussed here are with shroud design 1.
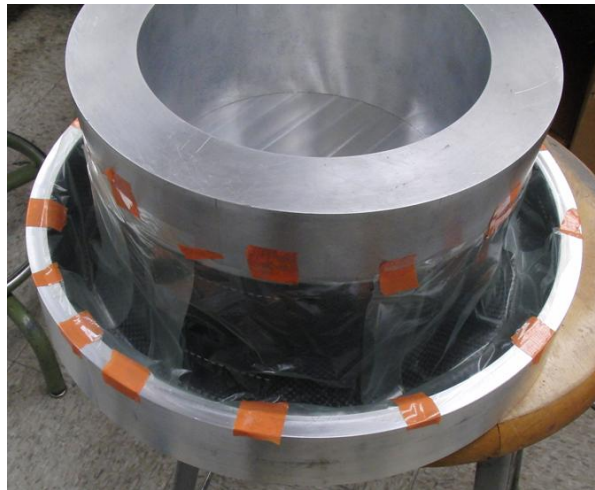
Figure 2.48: Shroud construction using vacuum bagging and oven treament

2.6.3 Aerodynamic performance

To estimate the aerodynamic performance of the shrouded rotor, shroud design 1 was tested on the micro rotor hover stand (Fig. 2.49). The shroud was integrated

to the rotor shaft stand through metal struts having a diameter of about 3 mm[6].
The shroud was held to the struts through aluminum supports. This ensured a
sturdy shroud structure enclosing the rotor. The thrust and torque measurement
was the total force generated by the shrouded rotor system.

2.6.3.1 Comparison with unshrouded rotor

The most efficient unshrouded rotor from Fig. 2.19 was then tested in the
shrouded configuration (Fig. 2.49). A blade tip clearance of $0.015R$ was main-
tained. Care was taken to keep the clearance as uniform as possible. A lower
tip clearance resulted in rotor-shroud interference. This was one of the main
challenges in the operation of the shrouded rotor - trade off between higher tip
clearance and mechanical interaction between the rotor and shroud.
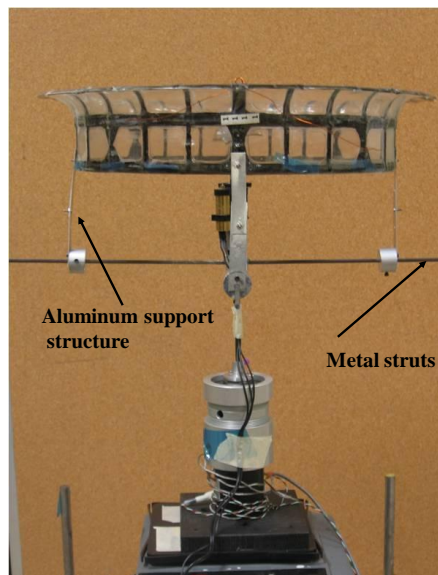
Figure 2.49: Set-up to measure shrouded rotor performance

Figure 2.50 shows the variation of thrust and mechanical power coefficient of

---

[6]It was seen that the struts led to a thrust penalty that was within measurement error.
Therefore this penalty was not factored into the results.

the shrouded rotor as a function of RPM. Like the unshrouded rotor case, it can be seen that the shrouded rotor did not exhibit significant Reynolds number effects in the range of RPMs considered although the power coefficient did increase (by about 5%) at lower RPMs. From Figure 2.50, it can also be de-

(a) Thrust coefficient v.RPM

(b) Power coefficient v.RPM
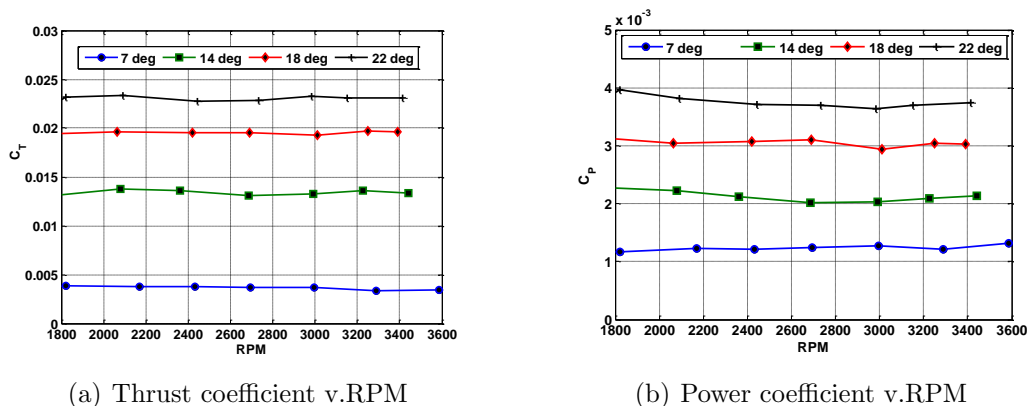
Figure 2.50: Variation of thrust and power coefficient with RPM for a two bladed tapered shrouded rotor at different blade root collective

duced that the thrust of the shrouded rotor system increased quadratically with RPM and the power increased cubically with RPM. Figure 2.51(a)) compares the most efficient performance obtained for the shrouded rotor with respect to the unshrouded rotor. It can be clearly seen that the shrouded rotor has a better aerodynamic performance than the unshrouded rotor. For example, for an input mechanical power of 15 watts, the improvement in shrouded rotor thrust was about 70 grams. This exceeded the weight of the shroud thus resulting in a payload benefit of about 20-30 grams. Alternatively, by looking at the power loading of the shrouded rotor system (Fig. 2.51(b)), it can be seen that at an operating thrust of about 300 grams, the improvement in power loading is about 30%[7].

---

[7]A previous study of an MAV scale shrouded rotor system showed a 60% improvement in power loading with the shrouded rotor. It was noted in that study that comparisons were made
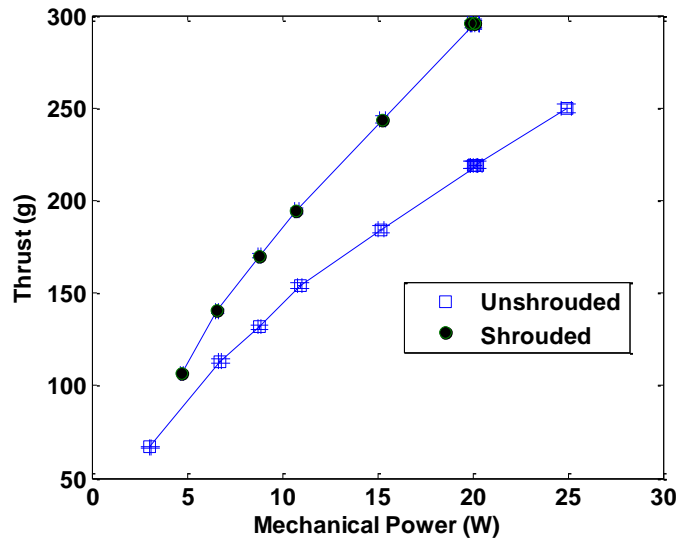
(a) Mechanical power versus thrust
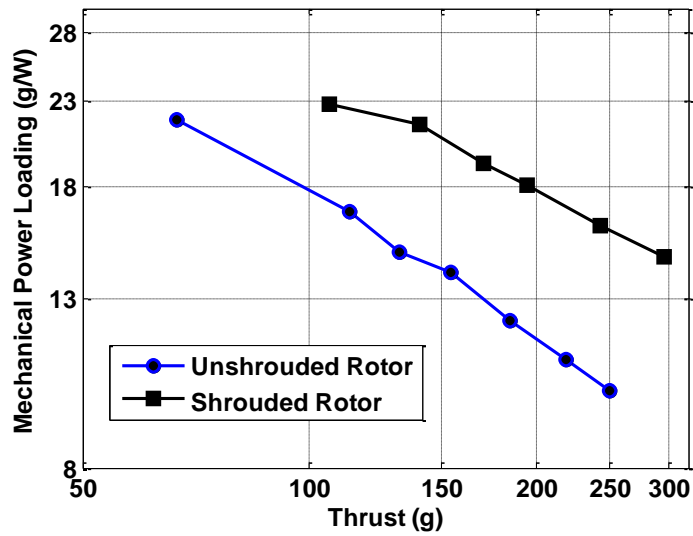
(b) Mechanical power loading versus thrust

Figure 2.51: Comparison in aerodynamic performance between shrouded and unshrouded rotor

2.6.3.2   Division of thrust between rotor and shroud

In order to measure the thrust individually generated by the rotor and shroud, it was necessary to detach the shroud from the rotor stand and mount it separately. This was done using the set-up shown in Fig. 2.52. Here, the rotor stand was mounted on the first load balance. A metal structure was placed beneath this balance and held a shroud through 4 aluminum struts. The shroud was positioned in the rotor plane accordingly. This entire system including the rotor stand and shroud was then mounted on a second balance. This balance measured the total thrust generated by the shroud and the rotor, while the top balance measured the rotor thrust alone. A subtraction of the two provides the thrust generated by the shroud alone. For this experiment, it was necessary to increase the tip clearance of the rotor to $0.03R$ since the rotor shaft was not directly attached to the shroud. Hence any vibration in the shaft resulted in rotor-shroud interference.

Figure 2.53 shows the division of thrust between the shroud and the rotor for the rotor operated at 26^0 collective. It can be seen that a quadratic trend is maintained with RPM for the three components. The rotor shared a higher proportion of the total thrust compared to the shroud. The shroud also had a significant contribution to the total thrust which was between 0.3 and 0.4 (Fig. 2.54). This is below the ideal momentum theory estimate of 0.5 which is expected due to tip loss effects and diffuser wall skin friction drag. It is interesting to note that this ratio increased marginally at higher RPMs. This could probably be due to the effective establishment of suction pressure forces over the shroud inlet as

with an inefficient unshrouded rotor. The results shown in Fig. 2.51 show that performance improvements are indeed possible even with an efficient unshrouded rotor albeit not as high as 60%

the inflow velocity increases. It was also observed that the contribution to total thrust from the rotor was less than the rotor thrust generated in the unshrouded configuration. This can be explained by the fact that the inflow velocity in the shrouded configuration is higher than the unshrouded configuration. Thus the effective angle of attack is reduced and the rotor generates a lower thrust.
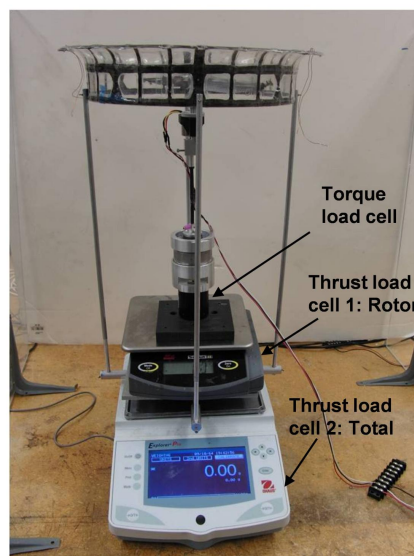
Figure 2.52: Set-up to measure individual contribution to total thrust from rotor and shroud

2.6.3.3 Effect of blade planform

It was seen in 2.3.3 that rectangular blades had a lower power loading than the tapered blades. An explanation of this is that the tapered blades promote more uniform inflow while keeping profile losses at a minimum. In order to study the effect of rotor planform on the performance of the shrouded rotor, parametric studies were conducted on a representative range of blade profiles (Fig. 2.55). These are listed as follows: (1) the baseline tapered blade ($\sigma_e = 0.11$), (2) rectangular blade I with the same root chord as the baseline blade ($\sigma_e = 0.13$),
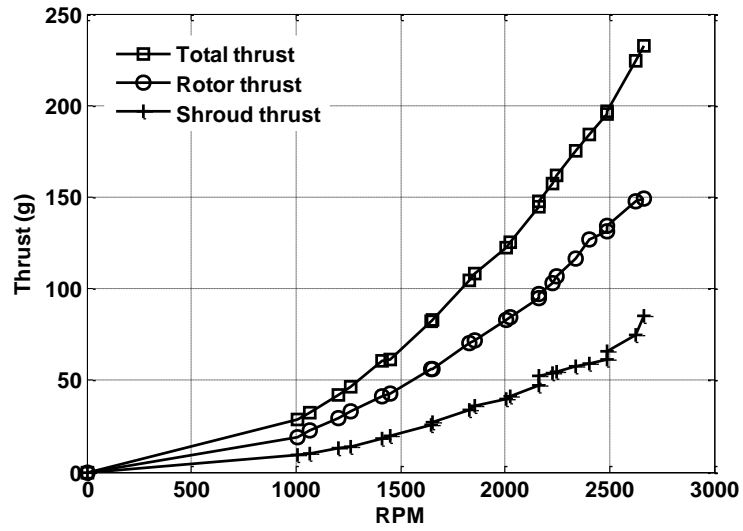
Figure 2.53: Contribution to total thrust from rotor and shroud
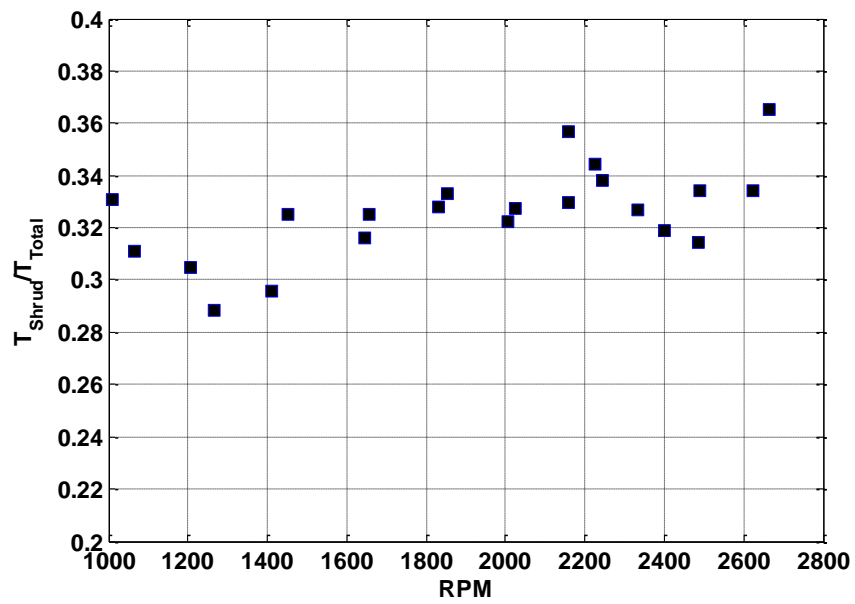
Figure 2.54: Ratio of thrust from shroud to total thrust

(a) Original planform
$\sigma_e = 0.1096$

(b) Rectangular
$\sigma_e = 0.1322$

(c) Taper 140% chord
$\sigma_e = 0.1494$

(d) Rectangular 140% chord
$\sigma_e = 0.1784$

(e) Inverse taper
$\sigma_e = 0.1325$

(f) Rectangular Hiller
$\sigma_e = 0.132$
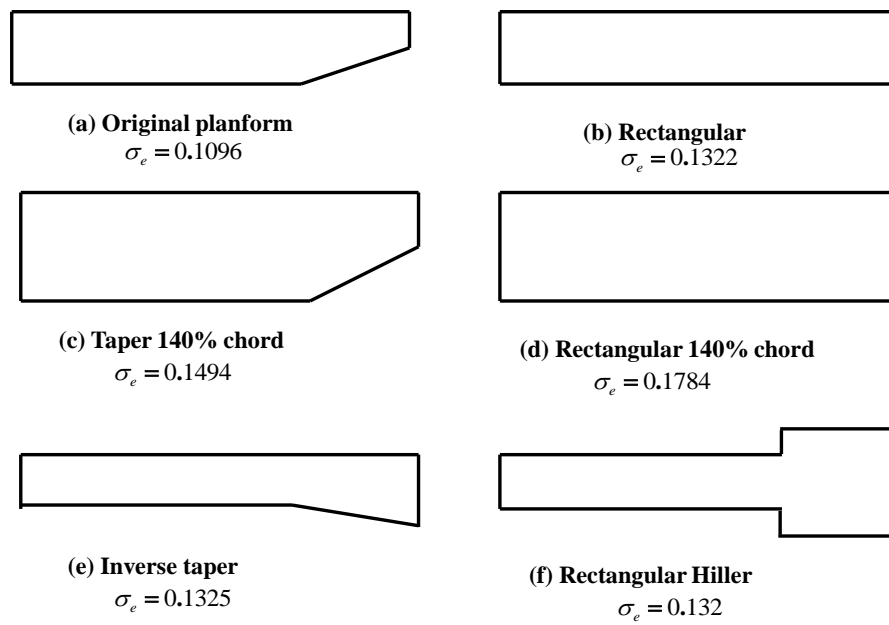
Figure 2.55: Blade profiles tested in shroud configuration

(3) tapered blade with 140% of the baseline chord ($\sigma_e = 0.15$), (4) rectangular blade II with same root chord as blade profile 3 ($\sigma_e = 0.18$), (5) inverse tapered blade ($\sigma_e = 0.13$), and (6) rectangular hiller ($\sigma_e = 0.13$). Blade profiles 5 and 6 were designed with the same thrust weighted solidity as rectangular blade I. The rotors were tested with shroud design 2 (Fig. 2.47) on the rotor hover stand ($\delta_{tip} = 0.03R$). A collective and RPM sweep was performed for each profile and the thrust and power coefficients were extracted.

The shrouded rotor thrust coefficient (C_T) is plotted as a function of rotor collective (θ) in Fig. 2.56. It can be seen that as the solidity of the rotor is increased, the $C_T - \theta$ slope increases. By normalizing the thrust coefficient with rotor solidity, the variation in the slope is reduced (Fig. 2.60). It can be seen that the thrust coefficient stays linear up to about 34 degrees. Beyond this, the rotor appeared to enter into stall. In comparison, Fig. 2.58 shows the $C_T - \theta$ variation for the profiles tested in the unshrouded configuration. The variation in $C_T - \theta$ slope for planforms with different solidities was eliminated by normalizing it with rotor solidity (Fig. 2.59). The interesting observation is that the unshrouded rotors entered stall at a much lower angle (25^0) than the shrouded rotors. This indicates that blade stall is delayed for shrouded rotors, which could be attributed to higher rotor inflow velocities. This implies that the blades can operate at a higher range of collectives, or a larger cyclic input can be provided in the shrouded rotor configuration to extract useful control moments.

Figure 2.61 shows the variation of power coefficient versus collective for blade profiles 1-4 in the shrouded and unshrouded configuration. Interestingly, the power coefficients of the blades 1 and 2 remain unchanged for the shrouded and unshrouded case. For the 140% chord tapered blade and the 140% chord rectangular blade, the change in power coefficient is not significant either. This is an
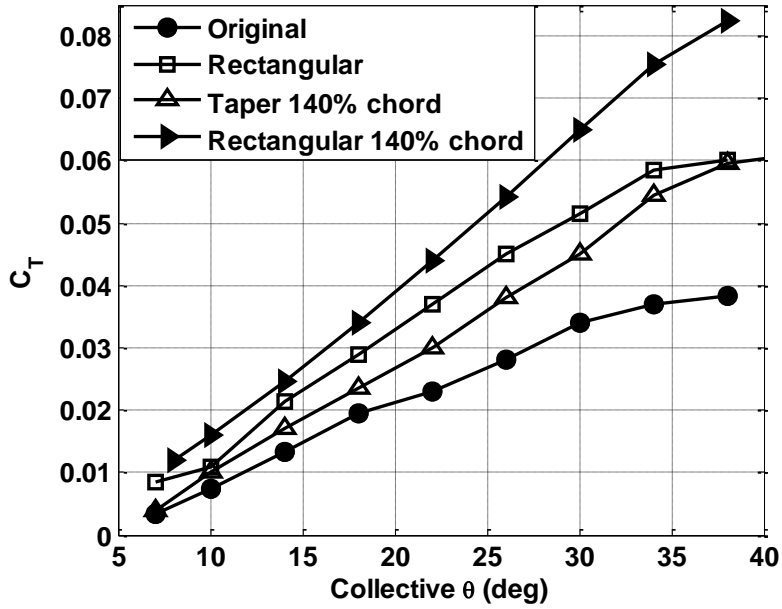
Figure 2.56: C_T versus θ for shrouded rotor
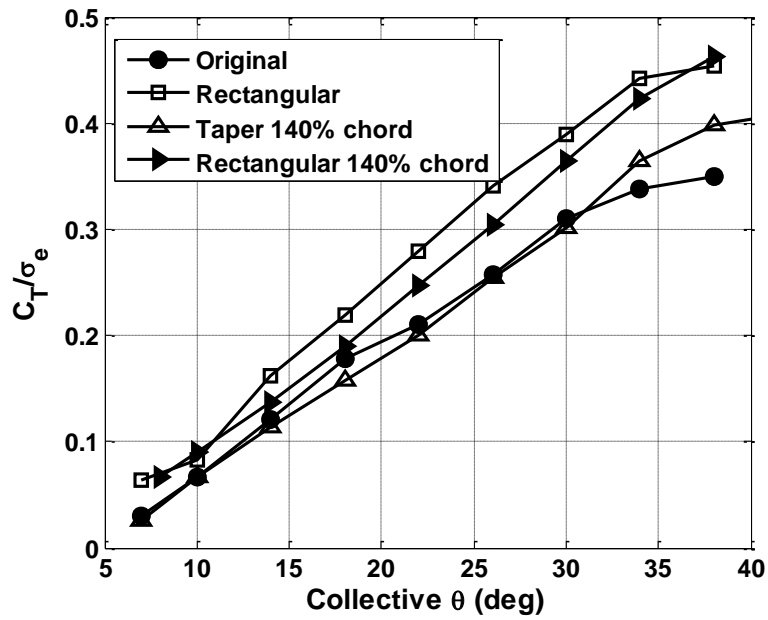
Figure 2.57: $C_{T_{\sigma_e}}$ versus θ for shrouded rotor
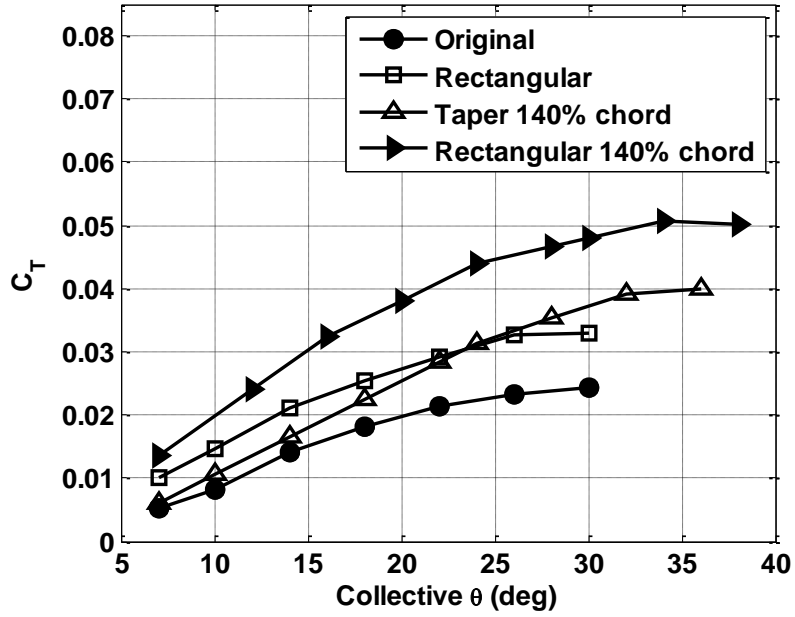
Figure 2.58: C_T versus θ for unshrouded rotor
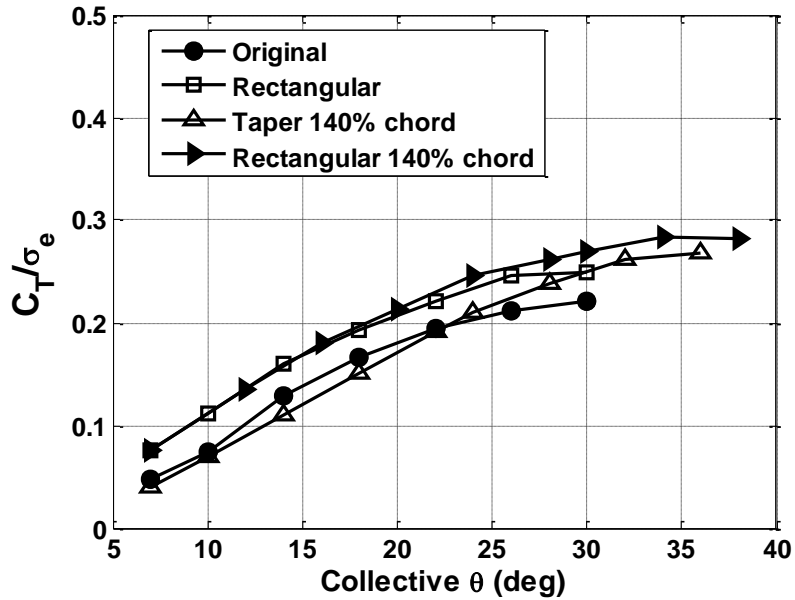
Figure 2.59: $C_{T_{\sigma_e}}$ versus θ for unshrouded rotor
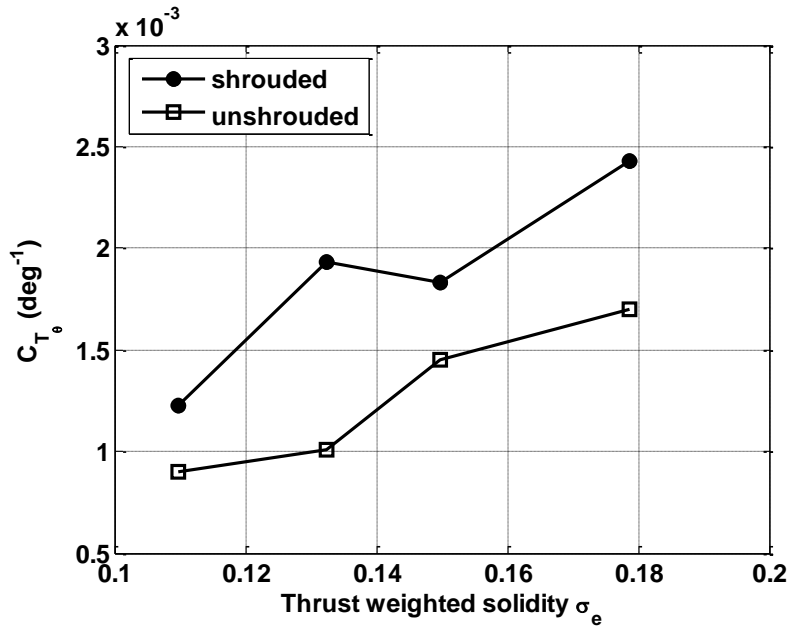
Figure 2.60: Effect of solidity on thrust coefficient

important conclusion, since it shows that at practicallly feasible tip clearances of about $0.03R$, the shroud does not significantly affect the power consumed by the rotor. The main performance improvement is from the thrust augmentation from the shroud.

Finally, a comparison of the power loading of the blade profiles at an operating thrust of about 300 g is shown in Fig. 2.62. It can be seen that most of the blade profiles have a similar maximum power loading between 14 and 15 g/W. The optimum collective increased as the solidity of the rotor increased. The best performance was achieved using the higher solidity rectangular blade. Interestingly, the rectangular planform blade was as efficient as the tapered blade in the shrouded configuration, while it was shown earlier that this was not the case in the unshrouded rotor configuration (Fig. 2.19). An interesting conclusion from this result is that a choice of planform is very important for the unshrouded

rotor, but is not a significant factor for the shroud. For the unshrouded rotor, the rise in C_P for the rectangular blade was not equally offset by a rise in C_T. Therefore, the unshrouded tapered blade had a better performance. In the shrouded case, the rise in C_P for the rectangular blade compared to the tapered blade was the same as for the unshrouded rotor. However, the rise in C_T was much higher in the shrouded rotor case. An explanation for this could be that the shroud diffuses the tip vortex, thus extracting extra thrust from the tip of the shrouded rectangular blade.

It will be discussed in a later chapter (Chap. 5) about the requirement of a specific planform for the shrouded rotor for improving control moments. The results discussed until that section will be for the shrouded tapered blade enclosed in shroud design 2.

2.6.3.4 Brushed blade tips

It was discussed earlier that by increasing the tip clearance, the performance of the shrouded rotor drops. A reason for this is that the suction pressure at the blade tip is lost due to the tip vortex. This reduces the flow acceleration over the shroud inlet and reduces the thrust generated by the shrouded rotor. Therefore the tip clearance has to be minimized. The danger of this is the undesirable rotor-shroud interactions. In order to minimize the tip-shroud interactions and to effectively reduce tip clearance, brushes were included in the blade tips. It was thought that the brushes would help sustain the suction pressure of the blade tips.

As described before, the blades were constructed from a carbon fiber epoxy pre-preg weave. After curing the blade, heat treatment from a soldering iron was given to the tips of the blade until the epoxy was dissolved. The cross fibers were

106
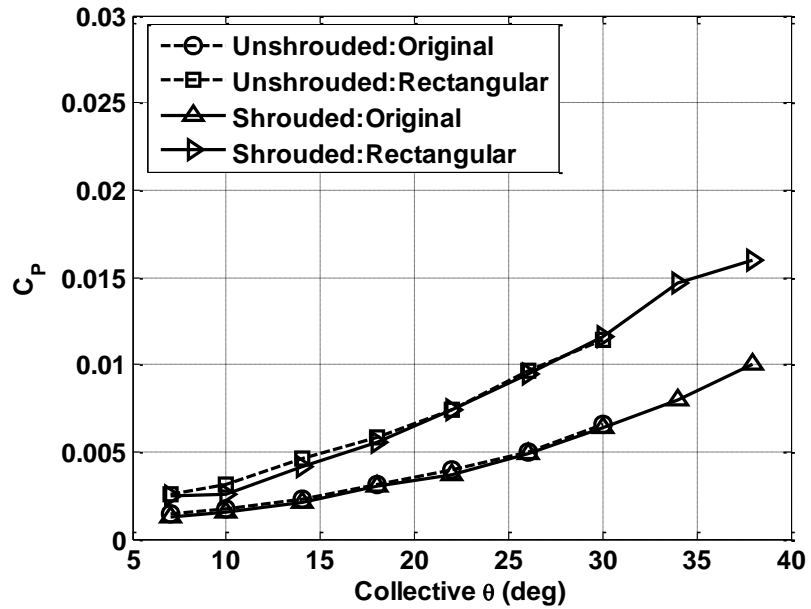
(a) Power coefficient versus collective for original chord blade profiles
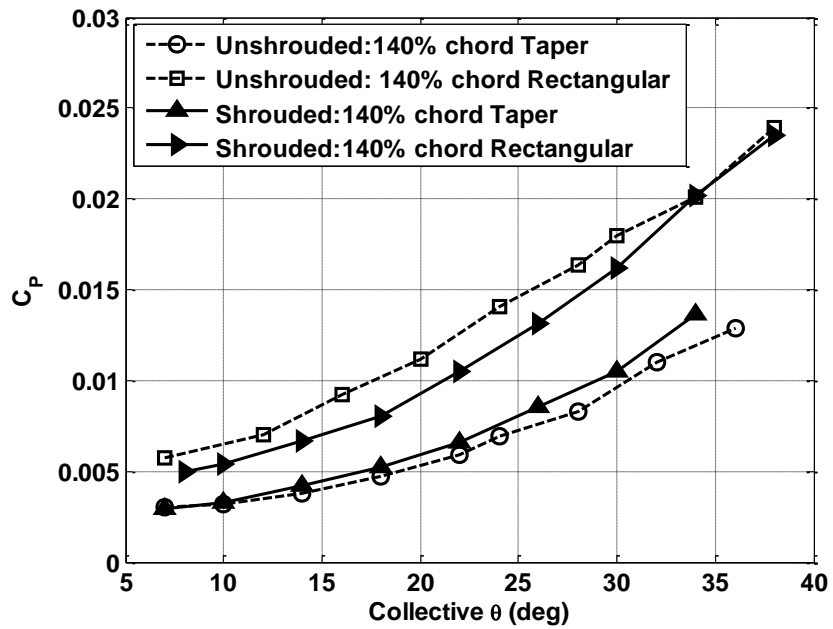
(b) Power coefficient versus collective for 140% chord blade profiles

Figure 2.61: Comparison in C_P versus θ for shrouded and unshrouded rotor
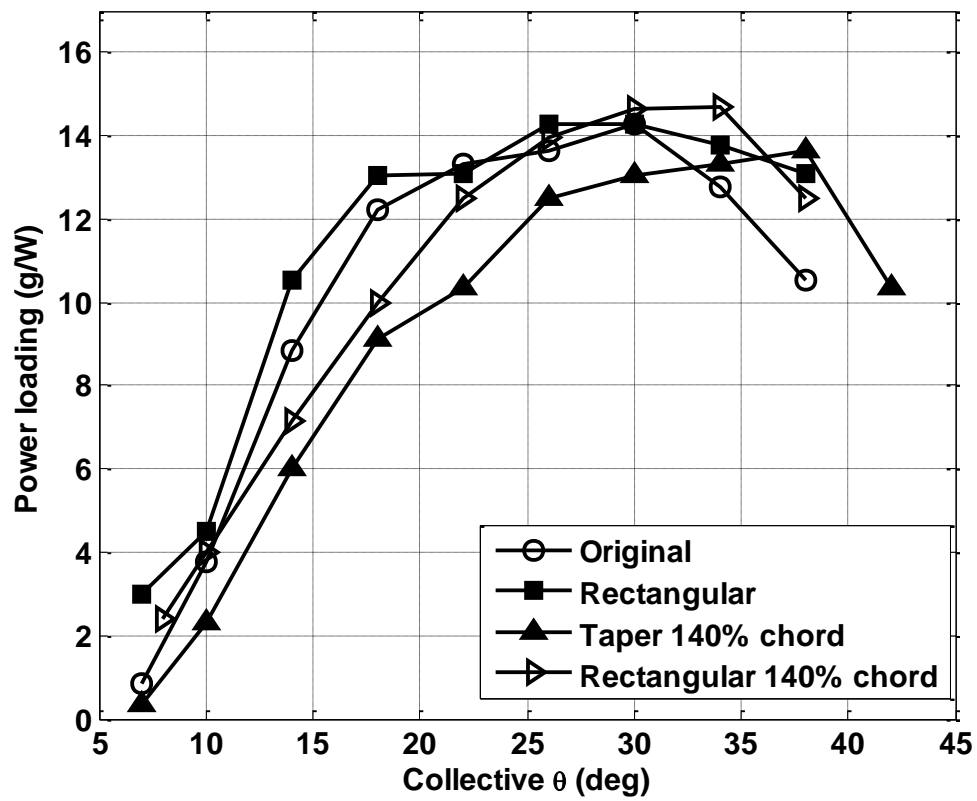
Figure 2.62: Comparison of power loading for the different blade profiles at 300 g operating thrust

removed and a smooth brush pattern consisting of carbon fibers remained. Care was taken to avoid stressing the fibers during the heat treatment, as it resulted in the fibers becoming brittle and withering. Figure 2.63 shows the brushed blade tips and incorporation into the vehicle.

Figure 2.63: Brushes incorporated in blade tips to improve performance

The performance of the brushes were tested on the rotor hover stand. The no-brush tip clearance was 3 mm. Two sets of brushes were tested, (1) short brushes of length 3 mm, and (2) long brushes of length 6 mm. Figure 2.64(a) shows a representative variation of thrust with RPM for the different blades at a blade collective of 24^0. It can be seen that there was a slight improvement in total thrust generated when the brushes were added. A comparison of the torque-RPM (Fig. 2.64(b)), showed that the torque for the brushes were higher
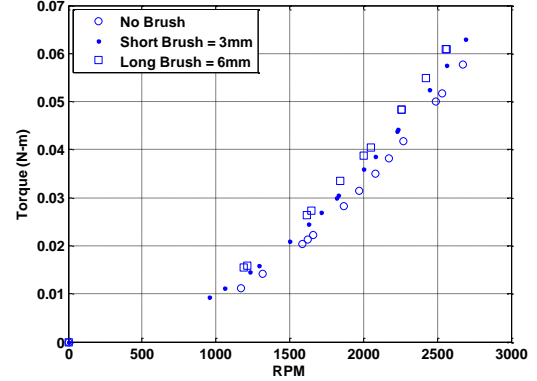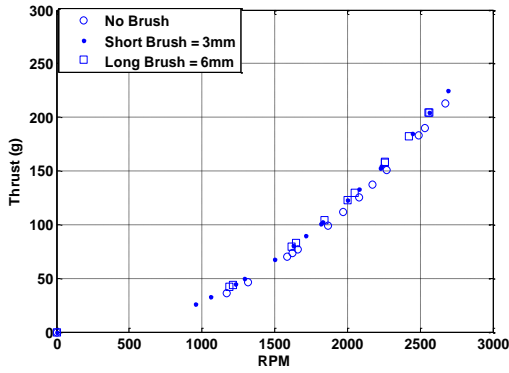
(a) Effect of brushed blade tips on thrust   (b) Effect of brushed blade tips on torque

Figure 2.64: Performance of brushed blade tips

than the no brush case. This was due to the brushes dragging along the shroud diffuser wall as can be explained by the torque variation for the 6 mm brush case. This can be eliminated by shortening the brushes further. However, there were no significant improvements in thrust to warrant an extra involved treatment of the blades to incorporate the brushes.

2.6.4   Design of optimum shroud

So far we have looked at the design of a lightweight shroud and have obtained significant aerodynamic benefits over an efficient unshrouded rotor system. Given this information, it is important to know if the shroud dimension chosen is optimum. In other words, what is the shroud size required to lift a given vehicle weight that results in the least power consumed?

In order to explain this, consider Fig. 2.51(b). The power required to lift a given vehicle weight in hover can be derived empirically from Fig. 2.51(b) as follows,

$$P_{unshrouded} = \beta_{US} \frac{T_{US}^{3/2}}{R}(watts) \tag{2.50}$$
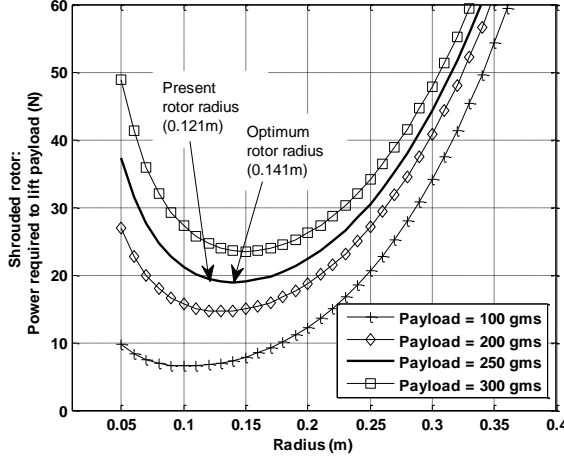
Figure 2.65: Power required vs. rotor radius at different desired payloads
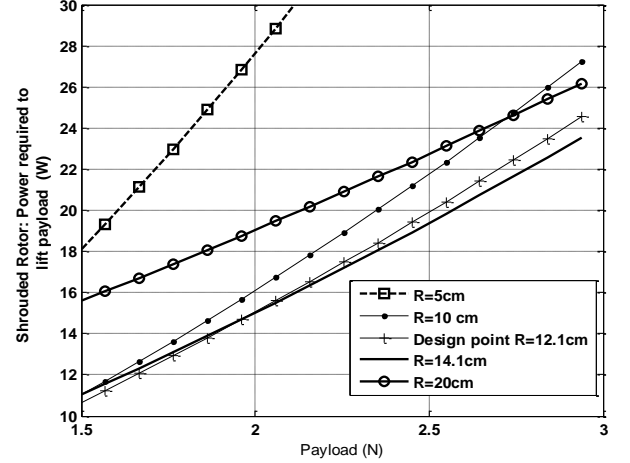
Figure 2.66: Power required to lift payload at different radii

$$P_{shrouded} = \beta_S \frac{T_{US}^{3/2} + kR^3}{R} (watts) \qquad (2.51)$$

where T_{US} is the weight of the unshrouded rotor vehicle (or payload), R is the rotor radius (or shroud size), and $\beta_{US} = 0.789$, $\beta_S = 0.478$, and $k = 250(N/m^3)$ are the empirical factors extracted from present data. It is assumed that the weight of the shroud (kR^3) increases as the cube of size. Using Eq. (2.51) the power is plotted as a function of shroud size at different desired payloads in Fig. 2.65. It can be seen that at the design payload of 250 g, a 14 cm radius shroud would require the least power for hover. However as can be seen from Fig. 2.66, this power reduction is less than 5% when compared with the present design. Therefore, the shroud size chosen in this research is close to optimum for a 250 g design payload.

2.7 Vehicle Prototypes

A series of risk reduction prototypes were constructed (2.2) and tested prior to the testing of the shrouded rotor vehicle[8].

Table 2.2: Vehicle prototypes tested

Prototype	Description
TiFlyer	Unshrouded, teetering rotor with vanes. Metal body construction, Mass: 350 grams
Giant	Unshrouded, teetering rotor with vanes. Carbon fiber structure. Mass: 240 grams
TiShrov	Shrouded, hingeless rotor with vanes. Carbon fiber structure. Mass: 260 grams

2.7.1 TiFlyer

The main goal of this prototype was to demonstrate the anti-torque vanes concept in flight. It was constructed as shown in Fig. 2.67. A two bladed aluminum sheet teetering rotor was incorporated with a Hiller stabilizer bar. The rotor had a diameter of 250 mm and a blade solidity of 0.13. Lateral and longitudinal control was achieved through cyclic control. A lightweight carbon fiber frame was installed to protect the rotor and to add stiffness to the body. the vanes were made of curved metal sheets and were held to the center body through metal connector plates. Two of the vanes were provided with controllable surfaces which were actuated by a single servo in a symmetric manner. The weight breakdown of the vehicle is given in Table 2.2. TiFlyer exhibited stable hover characteristics and satisfactory maneuverability during flight testing.

---

[8]TiFlyer-1 and GIANT were developed by Dr. Jayant Sirohi and Dr. Marat Tishchenko

2.7.2 Giant

The next prototype was built with the goal of minimizing the vehicle weight. The aluminum sheet blades were replaced with carbon/epoxy blades. This decreased the blade weight from 4.2 to 2.6 grams. As a result, it was possible to construct the hum from a lighter material (Delrin). Thin sheet carbon fiber vanes were held to the center body through connector plates and to the outer carbon fiber frame. A spider type swashplate was incorporated. Here, the swashplate motion occured in the plane of the rotor. The two servos move the non-rotating part in two orthogonal directions. The rotating part is attached to the non-rotating part by a radial bearing, and the result of the servo motion is an eccentricity of the center of rotation of the rotating part with respect to the main rotor shaft. This eccentricity is used to transfer a cyclic pitch angle to the servo-paddle by means of a control linkage sliding in a slot in the rotating part of the swashplate. This reduced the number of moving parts and the mechanical integrity of the actuation system was improved. The electronics, battery and motor remained unchanged from that of TiFlyer. The weight breakdown of Giant is given in Table. 2.3. It can be seen that a structural weight reduction was achieved by using composite materials.

2.7.3 TiShrov

A third prototype vehicle to demonstrate the shrouded rotor concept was constructed. It can be seen that apart from the shroud, the key difference between Giant and TiShrov was the choice of the hingless rotor. The phased Hiller bar-rotor was driven by a 55 watt DC brushless motor. A COTS swashplate was used to transfer inputs from two GWS micro servos to the phased Hiller bar

Table 2.3: Vehicles - weight breakdown

Prototype	TiFlyer	Giant	TiShrov
Component	Mass (g)	Mass (g)	Mass (g)
Rotor System	30.5	18.3	25
Swashplate	20	8.1	12
Battery	106.2	53.3	53.3
Motor	52.7	52.7	16.9
Electronics and servos	38	38	38
Structure	96.5	69.2	112
Total	**344**	**240**	**260**
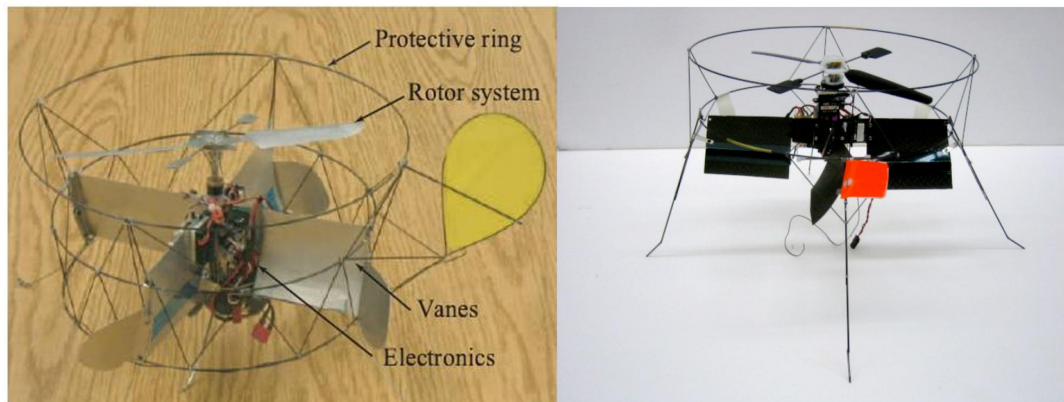
(a) TiFlyer   (b) Giant

Figure 2.67: Unshrouded rotor vehicle prototypes

for pitch and roll control. The yaw control surfaces were actuated in a manner similar to TiFlyer and Giant. The motor and gearbox were enclosed in an aluminum central body to which vanes, electronics and servos were attached. The weight breakdown of the vehicle is shown in Table. 2.3. The Hingeless rotor of TiShrov resulted in a much faster rotor response making it extremely difficult for a human pilot to control. The development and implementation of a controller for onboard stability augmentation will be discussed in the next chapter. With shroud design 1, vehicle instabilities in flight were excessive. It was thought that this could be due to the non uniform surface of the shroud that would result in unstable moments transferred to the fuselage. Therefore shroud design 2 was incorporated due to its smooth inlet surface. the modified shrouded rotor vehicle TiShrov is shown in Fig. 2.68. The final vehicle dimension was about 245 mm rotor diameter and weighed about 280 g.

(a) TiShrov -1   (b) TiShrov -2
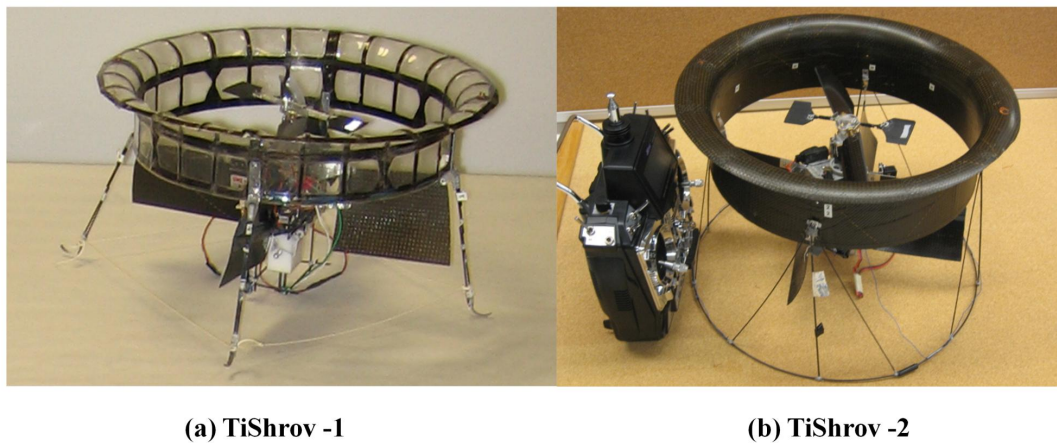
Figure 2.68: TiShrov - Shrouded rotor MAV

2.8 Summary

In this chapter, a low disk loading shrouded rotor vehicle was designed and constructed with key shroud design variables derived from previous studies on micro shrouded rotors. The different components such as the rotor, stabilizer bar, yaw control vanes and the shroud were systematically studied for system efficiency and overall aerodynamic improvements. Risk reduction prototypes were built to sequentially arrive at the final configuration. The final vehicle weighed about 280 g with a rotor diameter of about 244 mm.

For both the shrouded and unshrouded rotors, the use of a sharpened leading edge airfoil yielded the best hover performance. While the tapered blade planform had the best power loading in the unshrouded rotor configuration, the effect of planform was negligible in the shrouded rotor setup. The shrouded rotor yielded a 30% higher power loading than the unshrouded rotor, with the shroud generating up to 30-35% of the total thrust. The stall angle of the blades was about 40 deg for the shrouded rotor, more than 10 deg higher than that for the unshrouded rotor. The Hiller stabilizer bar increased profile losses of the rotor. By suitably adjusting the collective of the Hiller paddles, these losses were minimized by about 6%. The anti torque vanes effectively countered rotor torque, irrespective of rotor thrust. However, due to the vane drag (acting in the vertical direction), the increase in power to maintain a given thrust was abotu 10% of the main rotor power.

Chapter 3

Control System Development and Hover Flight Testing

3.1 Overview

The previous chapter discussed the development and testing of the subcomponents of the vehicle and vehicle integration. It was seen that the vehicle construction was modular thus enabling a simple conversion from a shrouded to an unshrouded rotor configuration. Taking advantage of this construction, the differences in passive stabliity in attitude rate dynamics (effect of translation not considered) between a shrouded and unshrouded rotor MAV while incorporating a teetering as well as a hingeless rotor are studied in this chapter. The development of a closed loop flight controller to augment stability in hover flight is then described. It must be mentioned that this chapter discusses hover flight results in quiescent flow (no external gusts).

3.2 Definition of Axes

Figure 3.1 shows a rotary wing MAV in hover. The lateral, longitudinal and vertical axes are chosen based on the standard helicopter convention. The rotor is spinning counterclockwise with a rotation speed Ω. The position of the blade (azimuth) is defined as follows: (a) negative lateral axis is 0^0, (b) positive longitudinal axis is 90^0, (c) positive lateral axis is 180^0, and (d) negative longitudinal axis is 270^0. The body attitude rates about the longitudinal, lateral and vertical axes are pitch rate(q), roll rate(p) and yaw rate(r) respectively. The Euler angles ϕ, θ and ψ represent the attitude position of the vehicle with respect to the inertial frame. The mathematical expressions for these are described in a later section.
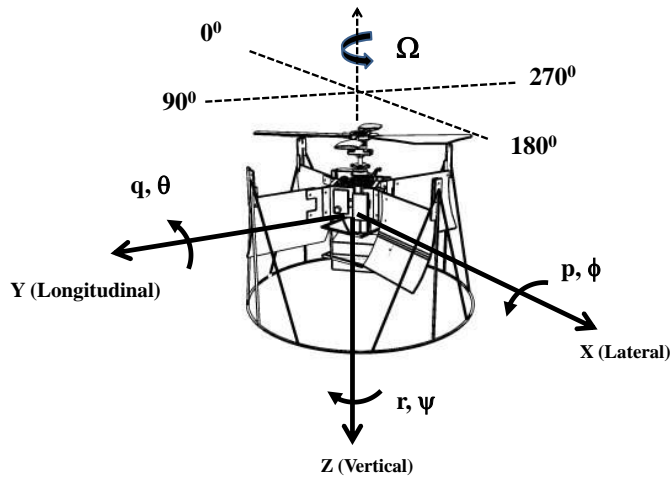
Figure 3.1: Body fixed reference frame

3.3   Open Loop Attitude Stability

3.3.1   Attitude damping in unshrouded rotor system

When an external disturbance in p or q is given to a hovering rotary wing MAV, it is important for the vehicle to reject this disturbance. This enhances controllability and is possible through passive damping mechanisms available in the rotor head. This is explained for the case of an unshrouded teetering and hingeless rotor.

Unshrouded teetering rotor: Consider a hovering teetering rotor spinning counterclockwise as shown in Fig. 3.2. The rotor is free to flap about a chordwise axis perpendicular to the rotor shaft. It is assumed that the rotor shaft passes through the C.G of the vehicle. A positive pitch rate disturbance is then given to the rotor shaft. At that instant, due to the rotational inertia of the rotor, the plane of rotation of the rotor remains unchanged. However, the tilting of the shaft introduces a change in angle of attack of the two blades. Due to a positive pitch rate, the angle of attack of the blade at 90^0 azimuth increases (maximum positive lift) while the angle of attack of the blade at 270^0 decreases (maximum negative lift). With the 90^0 force-response delay of the teetering rotor, the plane of rotation of the rotor tilts and realigns itself with the shaft albeit with a lag. Thus, if the shaft continues to tilt, the plane of rotation will continue to lag behind the shaft. This lag is expressed as,

$$\frac{\delta}{q} = \frac{16}{\gamma\Omega} \tag{3.1}$$

As a result of this lag, the thrust vector is inclined at an angle δ with respect to the shaft. Therefore, a restoring moment is generated that opposes and mitigates

the disturbance. The restoring moment is directly proportional to the pitch or roll rate and is the primary source of attitude damping in a teetering rotor system.
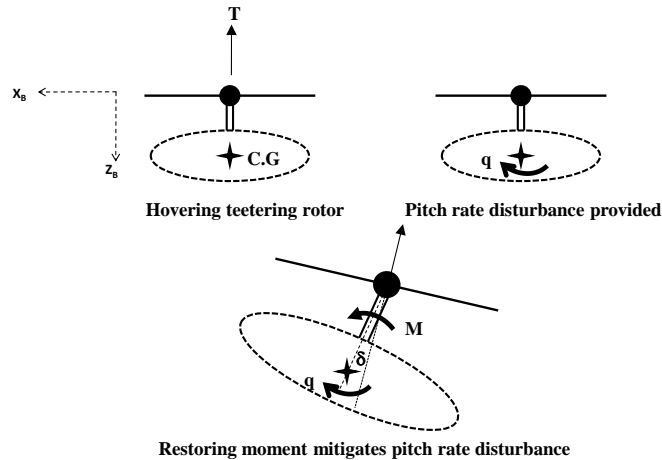
Figure 3.2: Attitude damping in a teetering rotor system

Unshrouded hingeless rotor: From the above discussion, it can be seen that if the tilting of the rotor plane of rotation with respect to the shaft is restricted, the restoring moment ceases to exist. Therefore, for a hingeless rotor, a Hiller bar (flybar) has to be incorporated to enable damping in attitude. This is illustrated in Fig. 3.3. When a pitch rate disturbance is given to a hovering flybar-hingeless rotor, the hingeless rotor plane of rotation tilts along with the rotor shaft with negligible lag. However, the flybar behaves similar to the teetering rotor. This difference in the plane of rotation between the hingeless rotor and the flybar results in a cyclic variation in angle of attack of the rotor. If the flybar is appropriately phased to the rotor (Sec. 2.4.1), a restoring moment is generated that is transferred to the rotor hub. This is the primary source of atttude damping in a flybar-hingeless rotor system.
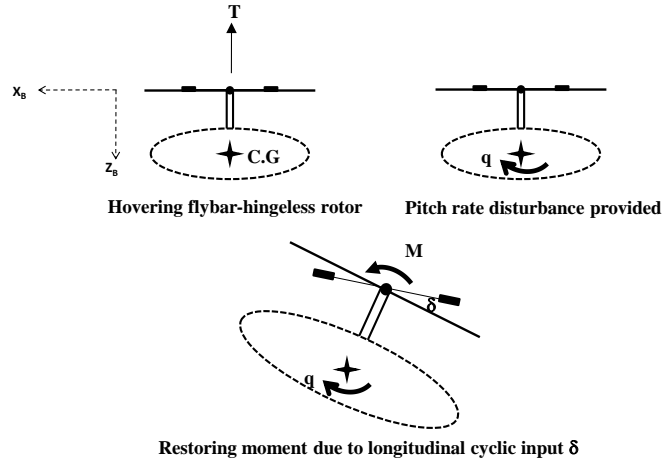
Figure 3.3: Attitude damping in a hingeless rotor system

3.3.2 Ceiling suspension tests

When the teetering rotor system was flight tested with the shroud in one of the initial prototypes, violent oscillations were observed. As seen from Sec. 2.6.3, a significant portion of the total thrust of a shrouded rotor is produced by the shroud. Any variations in shroud center of pressure are immediately transferred to the fuselage. Therefore, the mechanism of attitude damping in an unshrouded teetering rotor may not be present in the shrouded case. In order to study the passive attitude stability of the shrouded rotor and compare it to an unshrouded rotor, a series of ceiling suspension tests were performed with a teetering and hingeless rotor (Fig. 3.4). The vehicle was constructed in a modular fashion. A shroud skeleton with no shroud surface was incorporated with the body to give the unshrouded rotor configuration. A teetering and hingeless rotor set-up was tested on both the shrouded and unshrouded MAVs. A carbon rod attached to the shroud inlet served as the plane of suspension. The center of the carbon rod

was connected to the ceiling through a flexible nylon string with low torsional stiffness.

The main advantages of the ceiling suspension tests over free flight tests for preliminary understanding are: safety of vehicle from crashes and ability to study vehicle oscillations for a wide range of RPMs. It must be mentioned that this does not completely simulate a free flight condition since the fuselage motion occurs about the point of suspension and not about the C.G.[1]. Therefore, these tests were meant to be a qualitative indicator of passive stability. Figure 3.5 shows a schematic of the suspended vehicle. Here, A is the point of suspension, B is the center of rotor plane and C is the center of gravity. From Fig. 3.6 it can be seen that this is a double spherical pendulum setup. However, preliminary tests suggested that θ_1 was negligible. So, oscillations of the vehicle were effectively considered about A.

Each configuration was tested with a teetering and hingeless rotor (Fig. 3.7). The rotors were subjected to an RPM sweep (0-4200 RPM). An inertial measurement unit (IMU) placed below the C.G measured oscillations about the point of suspension A. It should be noted that oscillations arising were due to self induced moments about A. The natural frequency of the suspended vehicle configurations about A was determined to be greater than 4 Hz and not found to influence the vehicle oscillations.

The baseline case of the suspended unshrouded teetering rotor vehicle was found to be passively stable. Minor oscillations that may have developed were quickly damped out (Fig. 3.8). Similar behavior was observed with the unshrouded hingeless rotor (Fig. 3.9). This is an expected result (Sec. 3.3.1) because of the

---

[1]A direct access to the vehicle C.G. was incorporated in a later vehicle design iteration
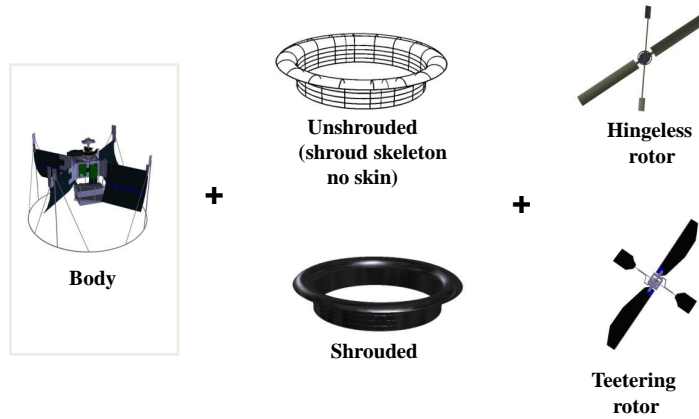
Figure 3.4: Rotor configurations tested
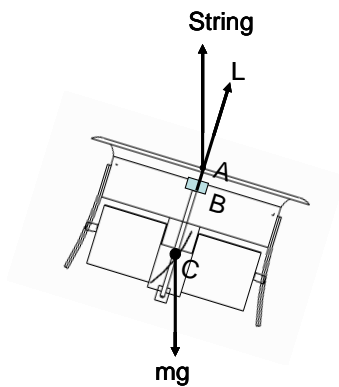
Figure 3.5: Schematic of the suspended vehicle
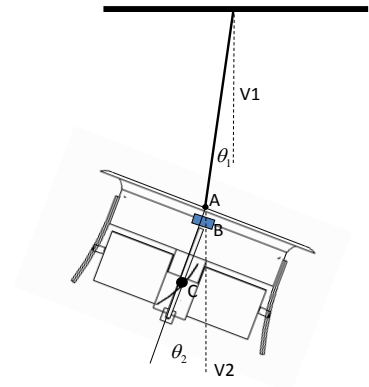
Figure 3.6: Vehicle oscillations considered about A

stabilizing response of the flybar-rotor.

However, when the teetering rotor was enclosed by the shroud, self-sustained periodic oscillations resulted starting at RPMs as low as 1700 (Fig. 3.10). Due to a minor perturbation, the teetering rotor tilts with respect to the shroud axis. This asymmetric tilting of the rotor tip path plane results in a non-uniform

Figure 3.7: Suspended unshrouded and shrouded rotor vehicles
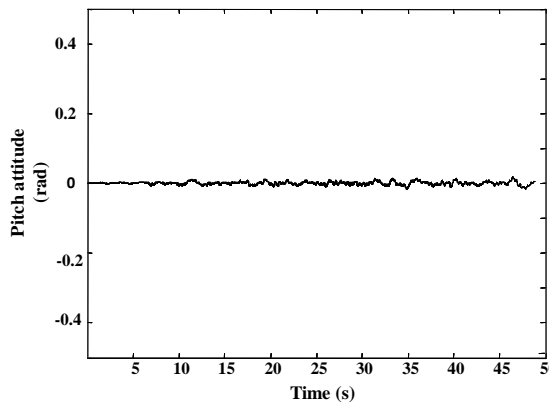
Figure 3.8: Unshrouded teetering rotor up to 4000 RPM. Stable in attitude
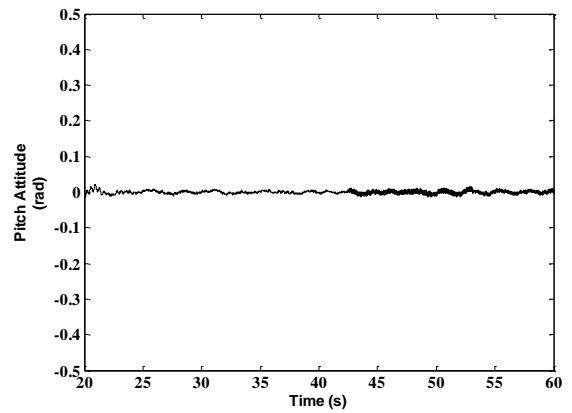
Figure 3.9: Unshrouded hingeless rotor up to 4000 RPM. Stable in attitude
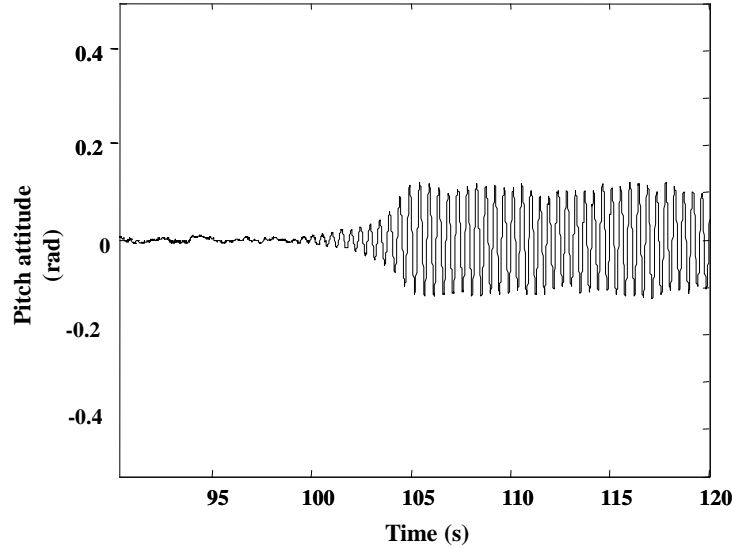
Figure 3.10: Shrouded teetering rotor (1700 RPM and upwards). Self sustained oscillations

pressure distribution over the shroud inlet. As a result, oscillations of the vehicle about the suspension point are induced. This is schematically shown in Fig. 3.11. Figure 3.12 shows the variation of oscillation frequency with rotor RPM. It can be clearly seen that there is an approximate inverse relationship between the oscillation frequency and the rotor RPM (angular momentum). This may suggest gyroscopic precessional effects although a detailed analysis of this phenomenon was not performed.

It can be logically seen that a way of eliminating these periodic oscillations is to incorporate a hingeless rotor. As expected, the shrouded flybar-hingeless rotor ($\delta_{tip} = 0.03R$) did not produce any oscillations at all RPMs (Fig. 3.13). Figure 3.14 shows that external disturbances in attitude get damped out effectively for the shrouded hingeless rotor case. Another observation was that when the tip clearance between the rotor tip and the shroud wall was not uniform azimuthally,
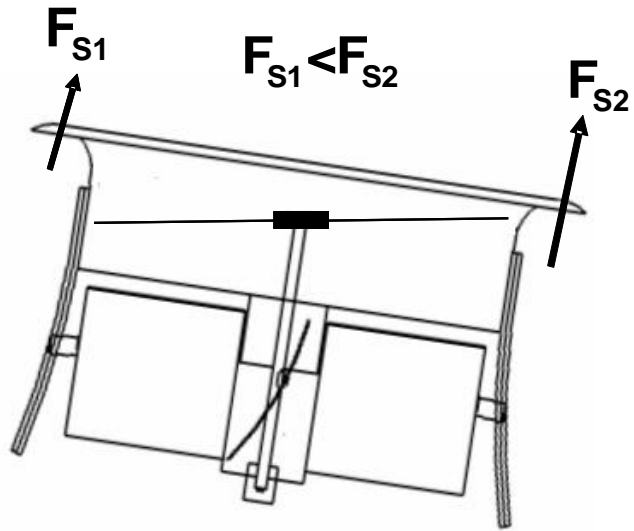
Figure 3.11: Non-uniform pressure distribution due to tilting of tip path plane (teetering rotor)
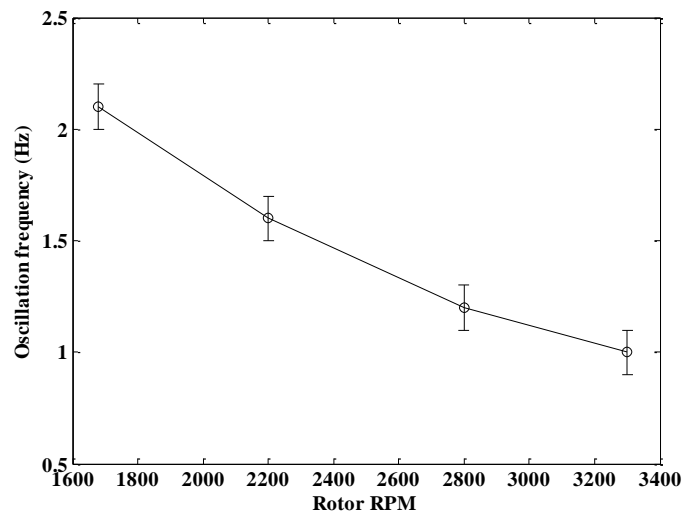
Figure 3.12: Variation of oscillation frequency with rotor RPM (shrouded teetering rotor)
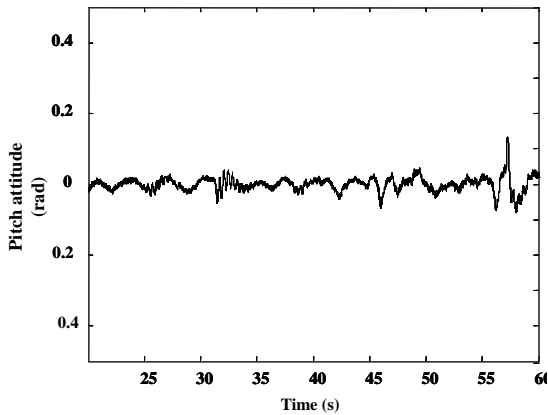
Figure 3.13: Shrouded hingeless rotor (3300 RPM)
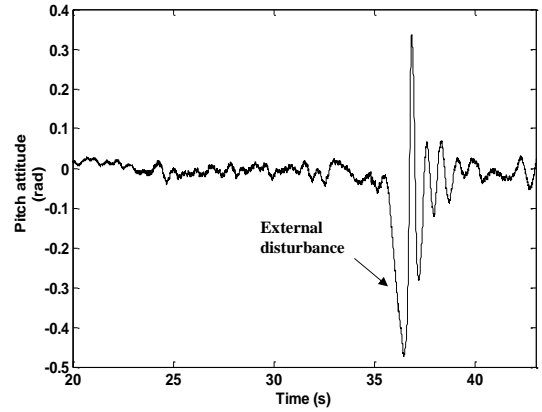
Figure 3.14: Mitigation of external attitude disturbance (shrouded hingeless rotor)

self-sustained oscillations ocurred at high RPMs (greater than 3300). A possible explanation for this is that at these high RPMs, any imbalance in the shroud pressure distribution arising due to azimuthal non-uniformity in rotor-shroud geometry could be pronounced enough to initiate and sustain the oscillations. Two key conclusions derived from the above ceiling suspension tests are: (1) it is necessary to incorporate a hingeless rotor in a shroud and minimize tip path plane motion inside the shroud, and (2) a practical lightweight shroud design may include non-uniformities in rotor-shroud geometry which could result in oscillations in flight. As a result it is necessary to incorporate a closed loop stability augmentation system to aid flight in hover.

3.4 Control System Development

This section looks at the development of a closed loop system to augment stability of the hingeless shrouded rotor vehicle in hover.
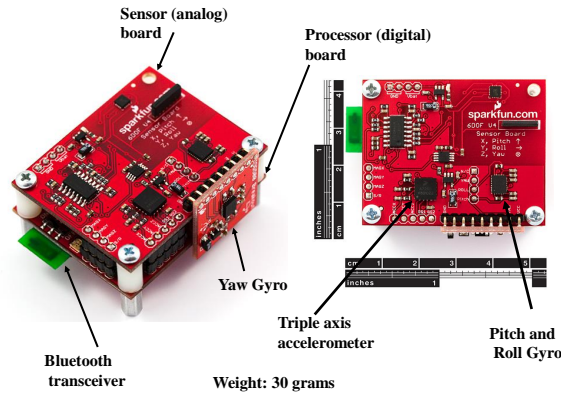
Figure 3.15: Inertial measurement unit for attitude estimation

3.4.1 Sensor

In order to provide closed loop feedback control, changes in the vehicle attitude
have to be measured. Inertial measurement unit (IMU) provides an established
method for estimating the changes in vehicle motion. It is a self contained sys-
tem and does not need information from an external source. The sensor used for
this study is a 6 degree of freedom MEMS based IMU [2]. Figure 3.15 shows the
components and dimensions of the IMU. It weighs about 30 grams and is placed
on the orthogonal axes of the vehicle.

The IMU is a double decker unit with the sensor board on the top and a con-
troller board on the bottom. One IC triple axis MMA7260Q acclerometer [3], two
invensense IDG500 gyroscopes [4] are the sensors of interest that constitute the
sensor board. The controller board consists of a LPC2138 ARM7 processor that
converts the analog signal from each sensor into a 10 bit digital output with a

---

[2]www.sparkfun.com/products/8454

[3]www.sparkfun.com/datasheets/Accelerometers/MMA7260Q-Rev1.pdf

[4]www.sparkfun.com/datasheets/Components/SMD/DatasheetIDG500.pdf

128

user defined sampling frequency. The processor then concatenates the outputs into a data packet with a head and tail bit for synchronization purposes. This data packet is then streamed to a ground station via the integrated bluetooth transmitter in the controller board. A sampling frequency of 200 Hz was chosen. The accelerometer provides translational accelerations of the vehicle in the X,Y and Z axes in the body frame including gravity. Therefore by suitable transformations, the total acceleration vector of the body in inertial space can be measured. If the body were stationary in space and merely tilting, the accelerometer would provide information of the component of the gravity in the X,Y and Z direction. It would hence act as an inclinometer. For hover control purposes, it is reasonable to assume that translational accelerations will be minimal. Hence the acclerometer is treated as an inclinometer. Calibration was done by individually aligning the gravity vector along each axis of the accelerometer. This was determined to be $0.004gs^2/m$ at a 6 'g' sensitivity setting.

The gyroscopes provide the angular rates (p, q, r) of the vehicle about the X,Y and Z axes in the body frame. Calibration of the gyroscope was done using a stepper-motor rotary table[5] (Fig. 3.16). The IMU was placed on the table such that the axis of rotation aligned with each gyro axis. The gyro response was constant for a given rotation speed (Fig 3.17(a)) and increased linearly with speed (Fig 3.17(b)). The calibration for each gyro axis was found to be 0.03 rad/s.

---

[5]provided by the Autonomous Vehicle Lab, UMD
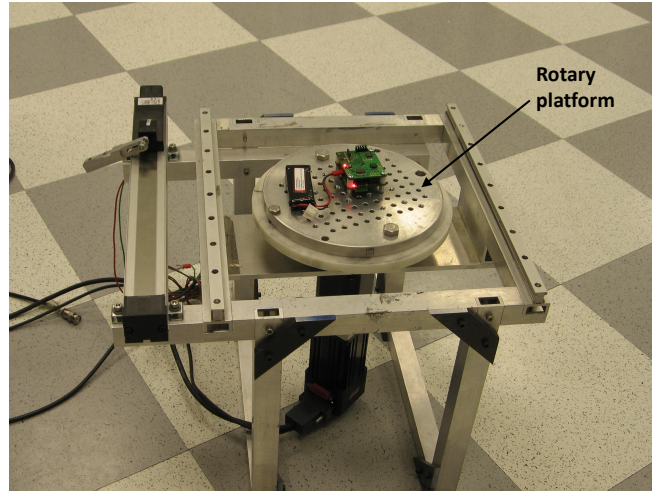
Figure 3.16: Rotary platform for gyro calibration
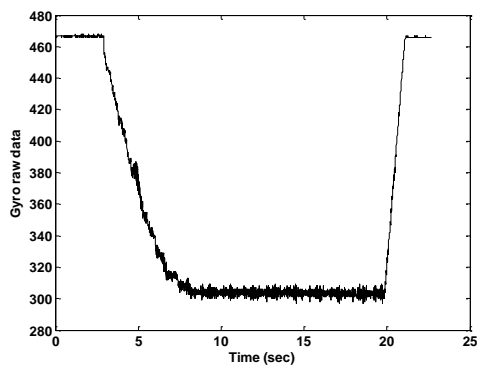
(a) Gyro response to a constant rotation rate
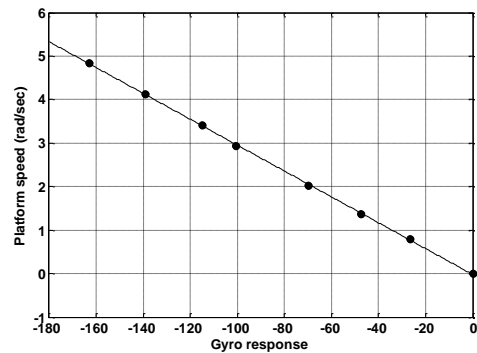
(b) Calibration of gyro

Figure 3.17: Gyroscope response to rotational input

3.4.2   Attitude estimation

The two frames of reference of concern are the inertial frame and the body frame. In order to estimate the absolute vehicle orientation, the data from the IMU in the body frame have to be converted to in the inertial frame. Assume the vehicle axes to be initially aligned with a fixed observer axis. After a certain maneuver, the vehicle takes a new position (as shown in Fig. 3.18). In order to estimate the vehicle orientation from IMU data, a transformation is required to convert the initial fixed axes to the final body axes. For this study, the aircraft 3-2-1 sequence using Euler angles is employed.
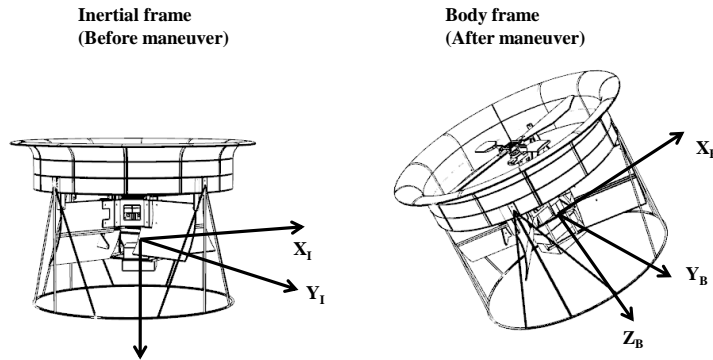
Figure 3.18: Vehicle orientation during maneuver

3.4.2.1   Rotation transformation

Let x_I, y_I, z_I be the initial frame of reference (observer) and x_B, y_B, z_B be the final body frame of reference. These two frames can be related to each other by three Euler angles: ψ (yaw angle), θ (pitch angle) and ϕ (roll angle). The orientation change between the frames is divided into a sequence of three rotations (Fig. 3.19).
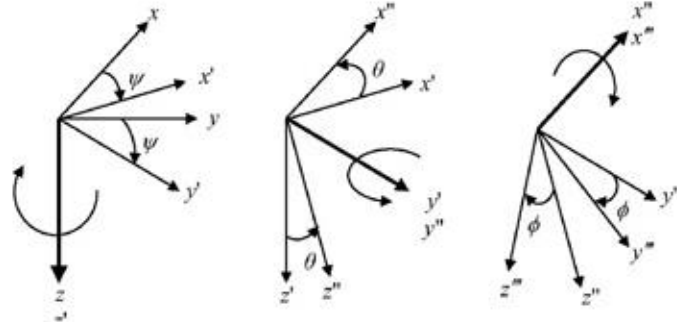
Figure 3.19: Rotation sequence using Euler angles

First, a rotation of ψ is made about the z axis to give the first intermediate body axes (x', y', z'). The transformation matrix $(R(\psi))$ for this is given as,

$$\begin{pmatrix} x' \\ y' \\ z' \end{pmatrix} = \begin{bmatrix} cos\psi & sin\psi & 0 \\ -sin\psi & cos\psi & 0 \\ 0 & 0 & 1 \end{bmatrix} \begin{pmatrix} x \\ y \\ z \end{pmatrix} \tag{3.2}$$

Next, a rotation of θ is made about the y' axis to give the second intermediate body axes (x'', y'', z''). The transformation matrix $(R(\theta))$ is given as,

$$\begin{pmatrix} x'' \\ y'' \\ z'' \end{pmatrix} = \begin{bmatrix} cos\theta & 0 & -sin\theta \\ 0 & 1 & 0 \\ sin\theta & 0 & cos\theta \end{bmatrix} \begin{pmatrix} x' \\ y' \\ z' \end{pmatrix} \tag{3.3}$$

Finally, a rotation of ϕ is made about x'' axis to give the final body axes $(x''',$

y''', z''') or (x_b, y_b, z_b). The transformation matrix ($R(\phi)$) is given as,

$$\begin{pmatrix} x''' \\ y''' \\ z''' \end{pmatrix} = \begin{bmatrix} 1 & 0 & 0 \\ 0 & cos\phi & -sin\phi \\ 0 & sin\phi & cos\phi \end{bmatrix} \begin{pmatrix} x'' \\ y'' \\ z'' \end{pmatrix} \tag{3.4}$$

The equivalent transformation from x, y, z to x_b, y_b, z_b is obtained by multiplying the individual transformation matrices $R(\phi)$, $R(\theta)$ and $R(\psi)$ in that order to give $R(\phi, \theta, \psi)$,

$$\begin{pmatrix} x_b \\ y_b \\ z_b \end{pmatrix} = \begin{bmatrix} c\theta c\psi & c\theta s\psi & -s\theta \\ -s\psi c\phi + s\theta s\phi c\psi & c\psi c\phi + s\psi s\theta s\phi & s\phi c\theta \\ s\psi s\phi + s\theta c\phi c\psi & -c\psi s\phi + s\psi s\theta c\phi & c\phi c\theta \end{bmatrix} \begin{pmatrix} x \\ y \\ z \end{pmatrix} \tag{3.5}$$

An important property of these transformation matrices is that they are orthonormal. This implies that the inverse transformation (from body to inertial frame) can be easily obtained by taking a transpose of the rotation matrix $R(\phi, \theta, \psi)$.

3.4.2.2 Attitude estimation from gyroscope

It can be seen that the above rotation matrix provides a transformation between two frames of reference at a given instant in time. For a continuous vehicle motion, the Euler angles are time dependent. The rate of change of the Euler angles are $\dot{\psi}$, $\dot{\theta}$ and $\dot{\phi}$ respectively. Therefore, a first order time marching scheme

can be used to update the Euler angles as shown below,

$$\psi(t + \delta t) = \psi(t) + \dot{\phi}(t)\delta t$$

$$\theta(t + \delta t) = \theta(t) + \dot{\theta}(t)\delta t$$

$$\phi(t + \delta t) = \phi(t) + \dot{\psi}(t)\delta t \tag{3.6}$$

In order to estimate the Euler rates, an appropriate transformation of the gyro angular rates has to be performed. The angular velocity ω provided by the gyro data is

$$\omega = p\hat{x}_b + q\hat{y}_b + r\hat{z}_b \tag{3.7}$$

Equivalently, ω can also be expressed in terms of the Euler rates,

$$\omega = \dot{\psi}\hat{x}_b + \dot{\theta}\hat{y}'' + \dot{\phi}\hat{z} \tag{3.8}$$

Using Eqs. (3.2), (3.3), (3.4), (3.7) and (3.8), the Euler rates can be expressed in terms of the body rates measured by the gyro as,

$$\begin{pmatrix} \dot{\phi} \\ \dot{\theta} \\ \dot{\psi} \end{pmatrix} = \begin{bmatrix} 1 & sin\phi tan\theta & cos\phi tan\theta \\ 0 & cos\phi & -sin\phi \\ 0 & \frac{sin\phi}{cos\theta} & \frac{cos\phi}{cos\theta} \end{bmatrix} \begin{pmatrix} p \\ q \\ r \end{pmatrix} \tag{3.9}$$

From the above equation, it can be seen that a drawback of the Euler angle method is the singularity that occurs at $\theta = 90^0$. In applications where high values of pitch angle are expected to occur, a different way of measuring the orientation will be required (Quarternions, Euler parameters etc). Since hover flight is of interest in this study, the pitch angle is expected to be small. The Euler angles can then be updated using Eqs. (3.9) and (3.6).

3.4.2.3 Attitude estimation using accelerometer

As discussed earlier, the accelerometers used for this study are used as inclinometers. This implies, the changes in the component of gravity along the body axes are registered by the accelerometer. Here, a_x, a_y and a_z are the components of the gravity vector along x_b, y_b and z_b axes respectively. Using the transformation matrix (Eq. (3.5)) we get,

$$a_x = -gsin\theta$$
$$a_y = gsin\phi cos\theta$$
$$a_z = gcos\phi cos\theta \tag{3.10}$$

The pitch and roll angles can therefore be extracted as,

$$\theta = sin^{-1}\frac{-a_x}{g}$$
$$\phi = tan^{-1}\frac{a_y}{a_z} \tag{3.11}$$

3.4.2.4 Complementary filter

The last two sections discussed the extraction of Euler angles from two sources: gyroscope and accelerometer. Each sensor has specific limitations when used alone. The gyroscope is prone to drift in gyro bias. Integration of gyro data will result in a rapid growth in error of the Euler angle estimate (as high as 1 deg /s for low cost MEMS gyros). Therefore it is not suitable for extracting low frequency information. On the other hand, accelerometers are highly sensitive to vibration (especially so in a rotor environment). Low pass filtering will cause significant phase delays. As a result, accelerometers are not suitable for measur-

ing high frequency motion.

These limitations were illustrated using a pendulum set-up shown in Fig. 3.20 The IMU is placed about 10 inches below the axis of rotation. A shaker is at-
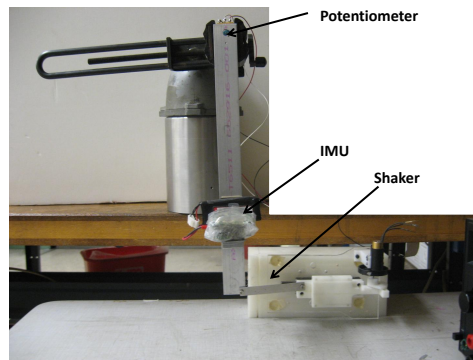
Figure 3.20: Pendulum set-up to compare gyro and accelerometer measurements

tached to the end of the pendulum to provide an adjustable oscillation input to the pendulum. The gyro and accelerometer data were sampled at 200 Hz. The attitude estimates from these sensors were compared to the output of a potentiometer placed on the pendulum axis. A comparison between pitch angle measurements by the gyro, accelerometer and potentiometer is shown for a steady pitch hold case (Fig. 3.21(a)) and for an oscillatory case (Fig. 3.21(b)). It can be clearly seen that the accelerometer provides accurate estimates when the IMU is held steady. These estimates deteriorate at high frequencies. The opposite is true for the gyroscope. When the IMU is oscillating, the gyro readings capture the high frequency motion satisfactorily wheras the gyro drift corrupts the angular measurements when the IMU is held steady (or in low frequency motion).

In order to combine the favourable high frequency characteristics of the gyro
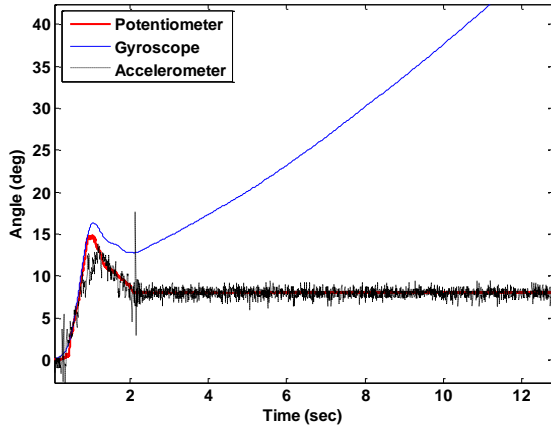
(a) Pitch-hold case
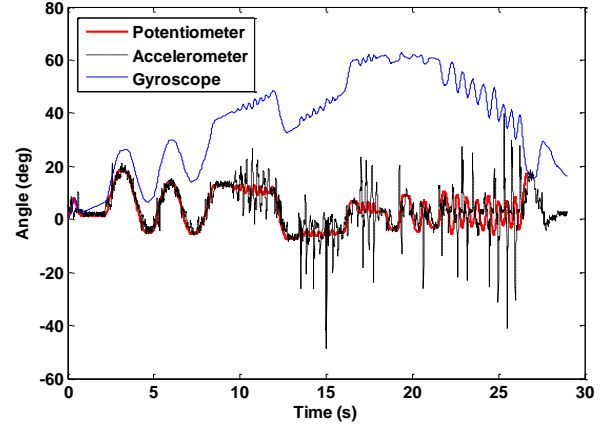
(b) Oscillating case

Figure 3.21: Attitude estimate comparison between gyro, accelerometer and potentiometer

and low frequency response of the accelerometer, a complementary filter is used as shown in Fig. 3.22 to provide the best estimation of the orientation. The accelerometer data is filtered using $G_a(s)$ to provide the low frequency estimate of attitude and the gyro output is fed to $G_g(s)$ to provide the high frequency attitude estimate. A combination of the two provided the complementary filter estimate of the attitude. For the study, a first order low and high pass filter was found to be sufficient. The cut-off frequencies were 7 and 5 Hz respectively.

$$G_g(s) = \frac{4s}{(2s+1)^2}$$
$$G_a(s) = \frac{4s+1}{(2s+1)^2} \qquad (3.12)$$

Figure 3.23 shows a comparison between the complementary filter estimate and the potentiometer measurement for the pendulum experiment. It can be
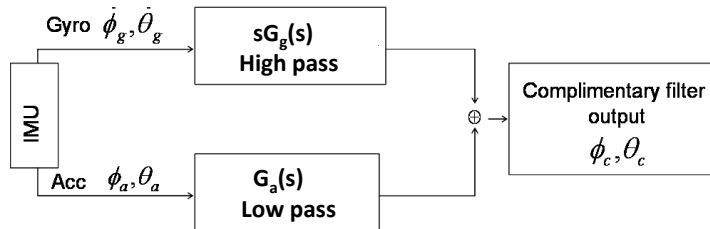
Figure 3.22: Complementary filter for attitude estimation

seen that the resulting complementary filter output matches satisfactorily with
the potentiometer reading.
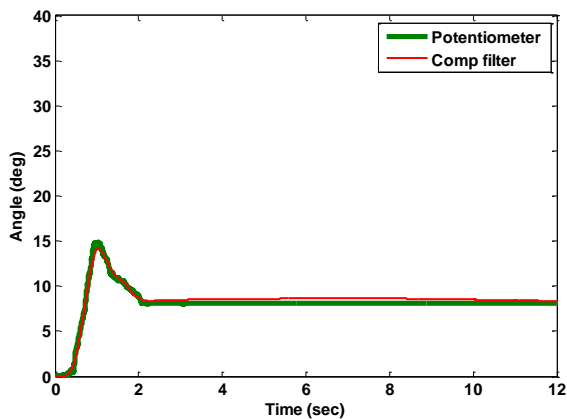
(a) Pitch-hold case
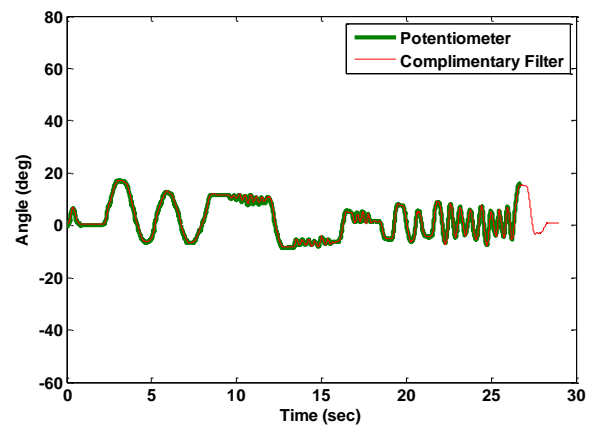
(b) Oscillating case

Figure 3.23: Attitude estimate comparison between complementary filter output
and potentiometer

Data from the two sensors were used to provide pitch and roll attitude esti-
mates. An available secondary sensor for yaw attitude was the magnetometer.
However, data fusion of the yaw gyro and the magnetometers was not found to
be suitable. This was due to the fact that the magnetometer bias and sensitivity

were affected by the electromagnetic interference from the motor (Fig. 3.24). Additionally, integration on the yaw gyro data was not performed. Later on, flight tests demonstrated that yaw rate information was sufficient for yaw stabilization.
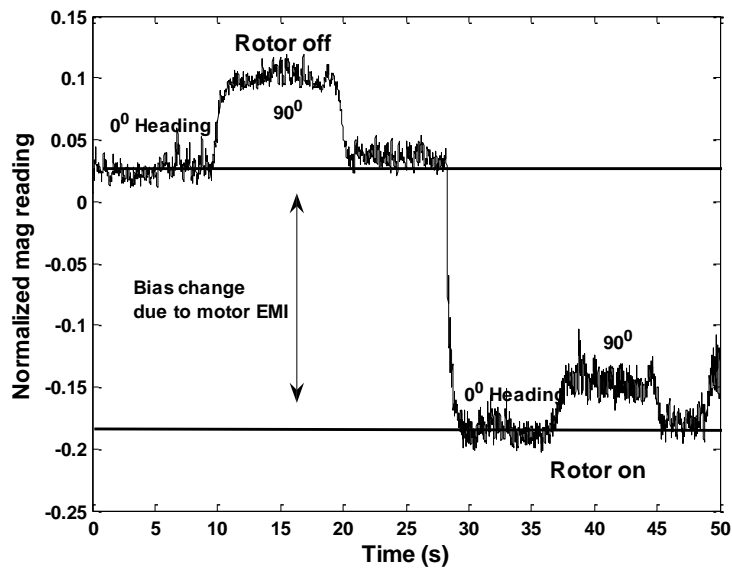
Figure 3.24: Magnetometers not suitable for heading feedback

In conclusion, the vehicle states used for feedback control were ϕ_C, θ_C and $\dot{\psi}_g$.

3.4.3 Telemetry

Figure 3.25 shows the data communication set-up for the off-board vehicle control system. A ground station processes the IMU data. A change in vehicle state triggers a control algorithm to initiate feedback action via signals generated by a microcontroller. The signals are uplinked to an onboard radio receiver via the trainer channel of an RC transmitter.

Off-board processing: The concatenated serial output from the gyros and
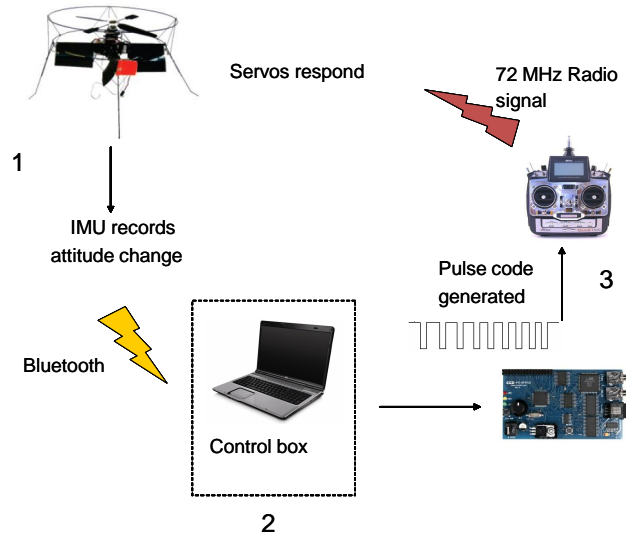
Figure 3.25: Telemetry of the control system set-up

accelerometers are downlinked wirelessly via Bluetooth from the IMU to a bases-tation for additional processing (Eqs. (3.6) - (3.12)). The reason for employing a ground based setup is to enable minimal onboard processing. The ground station can utilize faster processors and also enable monitoring of the data graphically. This can be very useful for debugging purposes. Integration of an onboard con-troller was also later achieved but is not described here to remain within scope. The basestation processes the errors in vehicle attitude, and computes corrective signals.

Signal pulse generation and transmission: It is then sought to emu-late these corrective signals into stick commands just like a human pilot would produce using the standard radio-control transmitter and receiver. The radio-control (RC) transmitter (Fig. 3.26) converts the control stick movements and bundles it serially into a multi channel signal. This coded radio signal car-

ries information from the control channels (pitch, roll, throttle and yaw) and additional programmable channels. A typical RC transmitter codes about 5-8 channels. The structure of the signal is shown in Fig. 3.27. Typically the normal state of the pin is high and each signal frame has a width between 20-22 ms and the number of inverted pulses is equal to the number of channels. The width of the first pulse corresponds to the position of the first servo and so on. Each channel frame consists of two parts - a fixed time T_f 0.5 ms and a variable time T_v $1 - 2$ ms. So when a control input is given, T_v is varied. The space between the pulse relating to the final channel and the start of the next frame is called the synchronization time. This coded signal is referred to as a pulse position modulated (PPM) signal. The PPM signal is transmitted wirelessly to a receiver module installed on the vehicle. The transmission is done using frequency modulation (intially at 72 MHz, later replaced with 2.4 GHz).
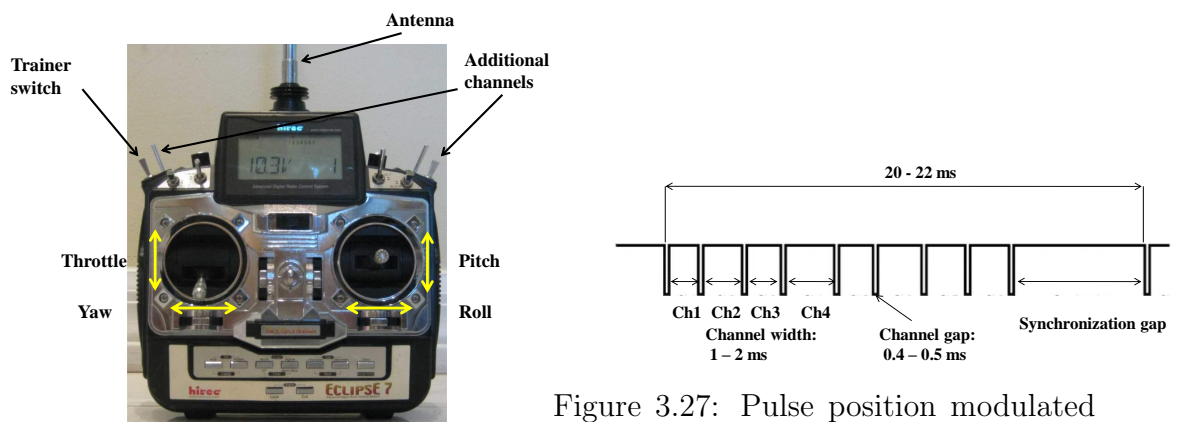
Figure 3.27: Pulse position modulated (PPM) signal from transmitter

Figure 3.26: Radio control transmitter interface

The generation and sampling of these high frequency PPM signals is time critical and cannot be done by a PC running on a non-real time operating system.

141

To achieve this, a microcontroller is interfaced with the PC. This is cheaper and faster to implement and simplifies application development using LabVIEW. A PIC 18F8722 microcontroller was used for this purpose. The PIC individually communicates with the PC (using a RS232 serial port) and with the transmitter data port (from pins A4 and A5 on the PIC) . The microcontroller receives the corrective signals from the basestation and converts it to a PPM signal that can be wirelessly transmitted by flipping a trainer switch (Fig: 3.26). This set-up was chosen since it provides system redundancy. Should the control system fail, the vehicle can be reverted back to manual control.

Receiver and actuator: The purpose of the receiver is to decode the radio PPM signal into pulse width modulated (PWM) signals. The individual PWM signals are then fed into the pitch, roll, yaw servo actuators and speed controller (for rotor RPM variation). The servo motor consists of a servo circuit, that drives a motor to whose output shaft is connected a lever arm that tilts the swashplate. The servo circuit interprets the width (T_v) as the amount of angular rotation of the motor shaft. A potentiometer is used as a feedback element for this purpose.

Latency: An important consideration for this set-up is the time delay (latency) between stages 1 and 4 (Fig. 3.25) since this can affect the control system bandwidth. The latency was experimentally determined using the set-up shown in Fig. 3.28. The IMU and a potentiometer were attached to a pendulum. A change in state of the IMU was instantly recorded by the potentiometer. A control law was invoked such that the servo responded to any disturbance in the IMU position. This servo response was instantly recorded by a laser displacement sensor. A comparison in time history between the potentiometer and the laser displacement sensor provided an estimate of the lumped time delay.

The average time delay between stages 1 and 4 was measured to be about 95 ms (Fig. 3.29). Table 3.1 presents estimates of the delays between each stage. These estimates were compiled from various sources such as Avanzini [144]. It can be seen that this compared well with the experimental latency measurement. The time delay reduces the phase margin of the closed loop system. Tischler [47] relates the control system bandwith to the lumped time delay as,

$$\omega_{BW} = \frac{0.37}{\tau_{delay}} \qquad (3.13)$$

This translated to a bandwidth of about 3.7 rad/s for the closed loop system. Experimental flight testing indicated that the vehicle open loop rigid body modes did not exceed 3 rad/s. The effectiveness of the present telemetry system for closed loop
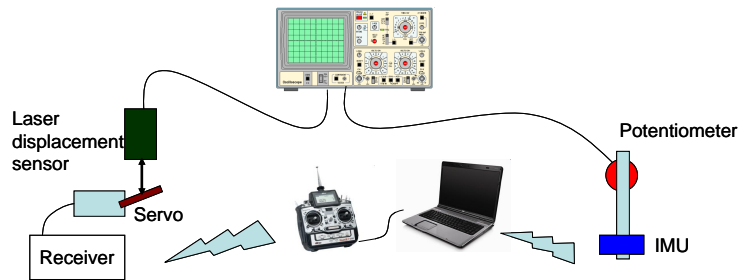
Figure 3.28: Lumped time delay measurement in telemetry system

Table 3.1: Time delay estimates (breakdown)

Stage	Delay estimate (ms)
IMU-Computer	25
Processing	5-10
Transmitter-receiver	25-30
Receiver-servo response	30
Total	**85-95**
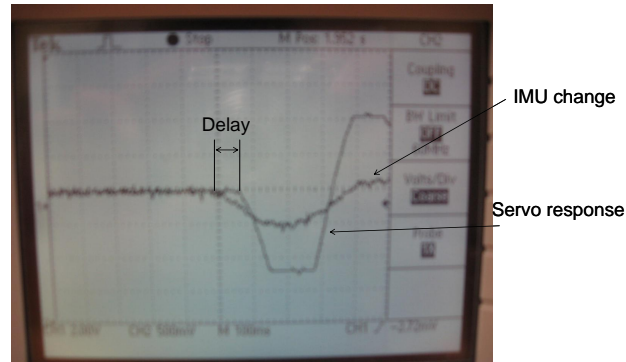
Figure 3.29: Delay between IMU state change and subsequent servo response

3.4.4 Control feedback configuration

For autonomous hover flight of TiShrov, a suitable control algorithm must be determined. For manual control, the pilot applies lateral, longitudinal cyclic and vane inputs for changing the vehicle attitude in roll, pitch and yaw respectively. For a full envelope flight, it is important to take into account the coupling between different axes and non-linear dynamical effects. However for the present study, since near hover flight is of concern, the roll, pitch and yaw inputs are treated as uncoupled and a linear single-input single-output (SISO) proportional-integral-derivative (PID) controller was chosen and expected to give satisfactory flight control results. The schematic of the PID control scheme is shown in Fig. 3.30.

It can be seen that the control loop is divided into two parts: inner (attitude) and outer (translation) loop. The inner loop, which has a high bandwidth forms the core of the controller and interacts directly to achieve the desired attitudes.
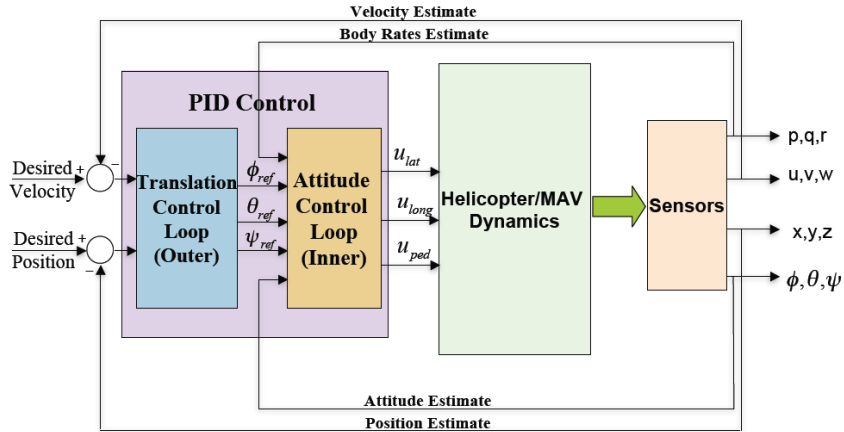
Figure 3.30: PID control scheme for hover control of TiShrov

The outer translational loop (lower bandwidth) is the secondarly controller which develops translation commands through a generation of primary attitude commands. From Sec. 3.4.1, the extraction of the attitude rates (p, q, r) and the Euler angles (ϕ, θ, ψ) was described. The fundamental limitation of obtaining translation velocity estimates for outer loop feedback is the integration of accelerometer data. It is a well observed phenomenon that due to the acelerometer noise levels, any integrated data will develop errors that would grow with time. Figure 3.31 shows the drift in velocity estimates obtained through an integration of the accelerometer data with and without a low pass filter. A simplified theoretical analysis [163] indicates that the error in estimated velocity for a stationary accelerometer is $\alpha\sqrt{T}$ where T is the integration time and α depends on the standard deviation of the accelerometer noise and sampling frequency of the data.
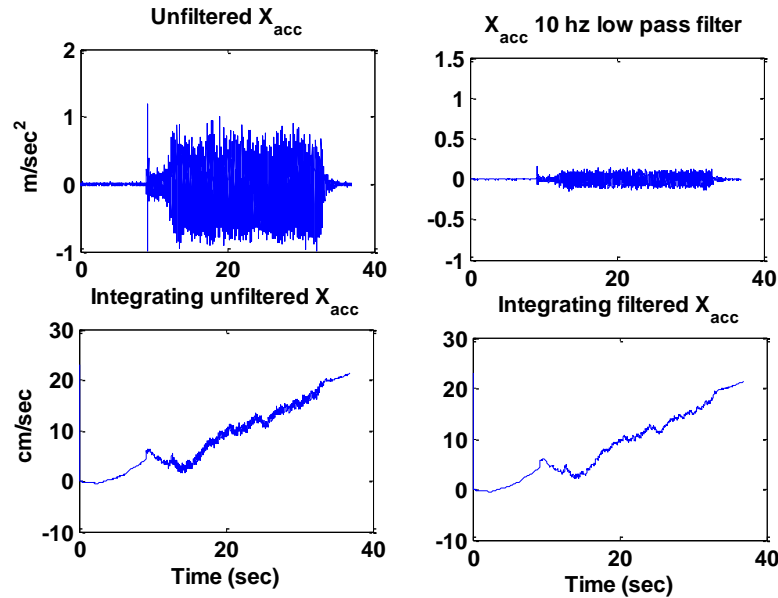
Figure 3.31: Error in velocity estimate from integrating accelerometer data

A common approach to overcome this is to periodically compare and reset the integrated data to an external reference. It was found that external velocity/pressure sensors did not have sufficient resolution for the present application in addition to the possibility of incorrect estimates due to effects of rotor downwash. Other potential techniques of position/velocity feedback suitable for indoor applications such as optic flow, visual feedback and Markov localization techniques were beyond the scope of the present study and are not considered. Therefore, only inner loop control was considered as shown in Fig. 3.32

Ziegler-Nichols PID gain tuning: The gains K_p, K_i, K_d are the proportional, integral and derivative gains in the feedback loop with respect to each of the Euler
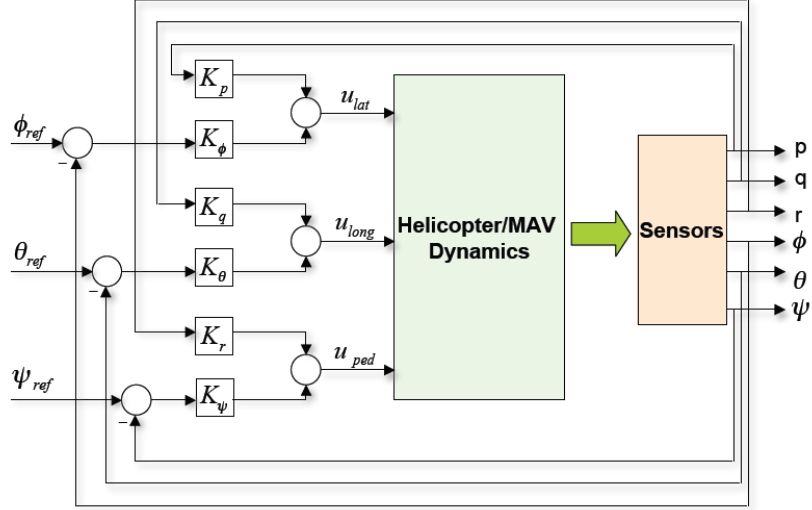
Figure 3.32: Inner loop feedback control

angles. Let $e(t)$ be the deviation in vehicle pitch attitude from hover. Then,

$$e(t) = desired - \theta_{measured}(t)$$

$$= -\theta_{measured}(t) \tag{3.14}$$

The PID controller in s-domain is,

$$G_c(s) = K_p \left(1 + \frac{1}{T_i s} + T_d s \right) \tag{3.15}$$

where, T_i is the integration time and T_d is the derivative time. Therefore, the resulting controller action in time domain due to the pitch attitude error is,

$$G_c(t) = K_p e(t) + K_i \int_0^t e(\tau) d\tau + K_d \frac{de}{dt} \tag{3.16}$$

147

Here the derivative gain K_d and the integral gain k_i are related to T_d and T_i as,

$$K_i = \frac{K_p}{T_i} K_d = K_p T_d \qquad (3.17)$$

In order to determine the gains for appropriate control action, the Ziegler-Nichols method of gain-tuning is followed. Here, based on experimental step response, the gains that result in marginal stability are chosen. The rules give a first-order estimage of the gain values and provide a starting point for finer tuning. First, the proportional gain is increased up to a critical value K_{cr} when the output exhibits sustained oscillations. The period of these oscillations is P_{cr}. Once the critical gain and corresponding period are experimentally determined, the values of the different gains are chosen based on the rules shown in Table. 3.2

Table 3.2: Ziegler-Nichols Tuning Method

Controller	K_p	T_i	T_d
P	$0.5K_{cr}$	∞	0
PI	$0.45K_{cr}$	$0.83\ P_{cr}$	0
PID	$0.6K_{cr}$	$0.5P_{cr}$	$0.125P_{cr}$

3.5   Bench-top test results

Prior to free flight hover tests, the controller was tested on different bench-top configurations: (1) servo set-up, (2) pitch, roll DOF, and (3) yaw DOF.

3.5.1 Servo tests

The actuators used for providing pitch and roll cyclic control were GWS sub-micro servos[6]. The servos were tested on a 1 DOF (Fig. 3.33(a)) and a 2 DOF set-up (Fig. 3.33(b)). The 2 DOF set-up served to simulate a swashplate configuration. In both cases, the IMU was incorporated as the servo load. Based on a desired IMU (pitch or roll) attitude, the PID controller would drive the servo to achieve that particular attitude. First, the servo was calibrated in open-loop using the 1 DOF set-up. The servo rotation was found to be linear with the duty cycle of the PWM input signal. Figure 3.34 shows the open loop step response of the servo to a commanded position.
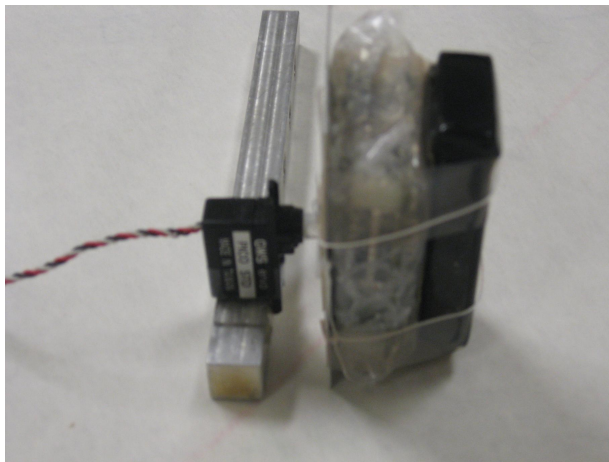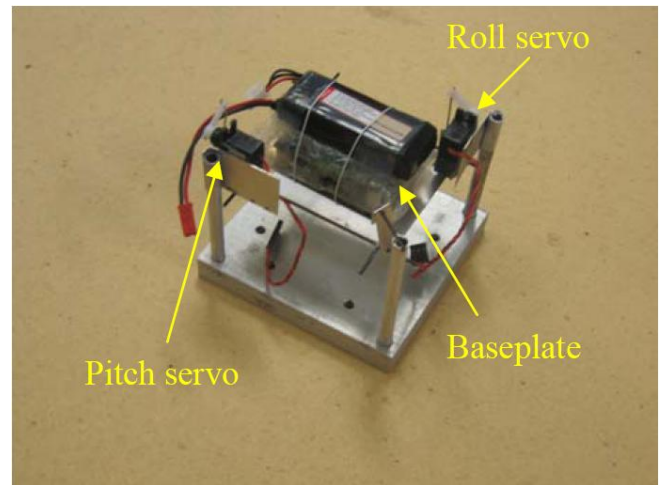
(a) 1 DOF   (b) 2 DOF swashplate configuration

Figure 3.33: Servo set-up for controller testing

Next, the 2 DOF was driven in closed loop to achieve a specific commanded position for the baseplate. Figure 3.35 shows the step response of the servo for different proportional gains. The unit of K_p is 1/rad. It can be clearly seen that

---

[6]GWS sub-micro servos: www.bphobbies.com/view.asp?id=A0780189pid=S510303img=l
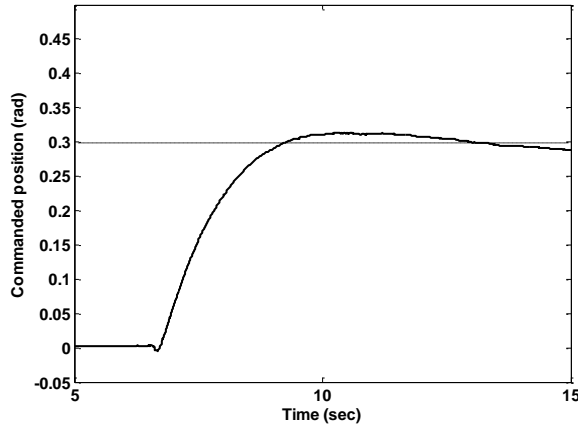
Figure 3.34: Open loop step response of servo

as the value of K_p increases, the system damping reduces as K_p increases, and the servo exhibits undampled oscillations at a K_{cr}. Based on Ziegler-Nichols tuning method, a value of $K_p/2$ was chosen. It can also be seen that there is a steady state error between the final swashplate position and the commanded position. Figure 3.36 shows the variation of the steady state error with proportional gain. it can be seen that this error reduces as the proportional gain increases. The steady state error at a chosen value of K_p was eliminated by including an appropriate integral gain K_i. This is shown in Fig. 3.37. The overshoot in servo response can be reduced by incorporating K_d. However due to undesirable spikes in servo response arising from data noise, the differential control was discarded.

3.5.2 Pitch and roll DOF gimbal tests

The controller was next tested in the vehicle configuration in pitch and roll degrees of freedom. In order to achieve this, the vehicle was mounted on a gimbal stand as shown in Fig. 3.38. The gimbal stand would permit attitude
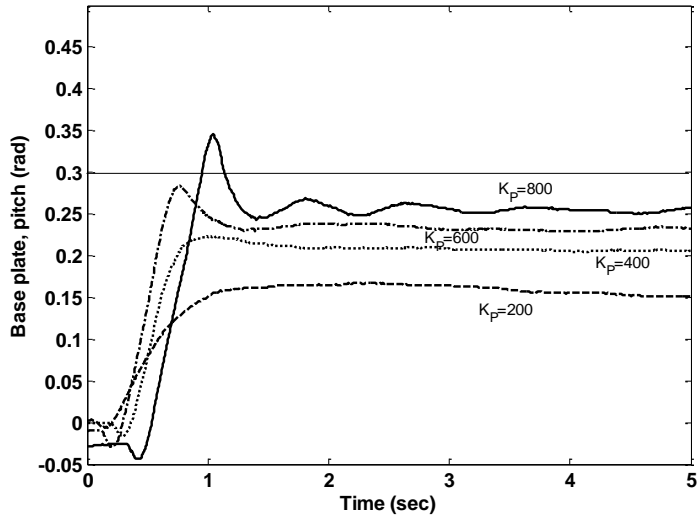
Figure 3.35: Response of the pitch servo to a commanded baseplate position with proportional feedback control
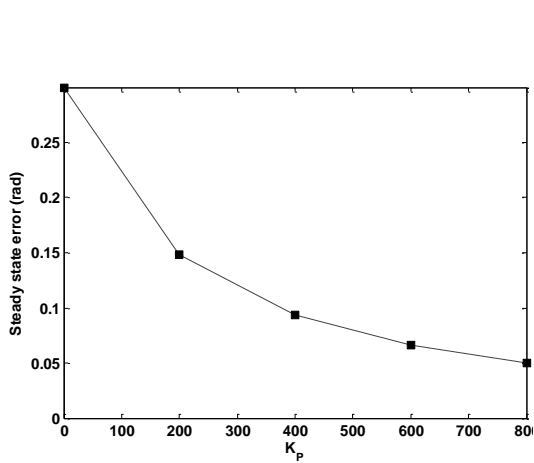
Figure 3.36: Variation of steady state error with proportional gain
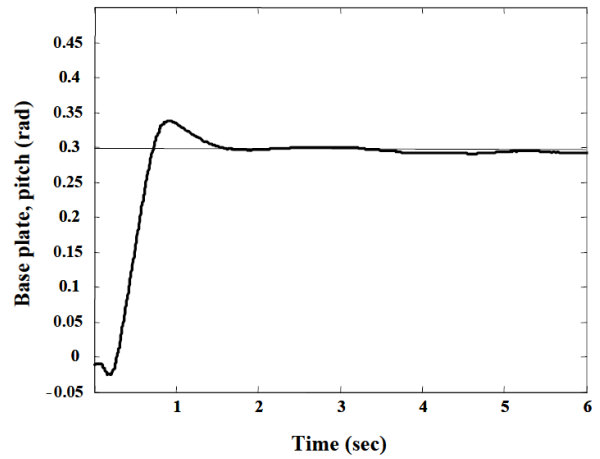
Figure 3.37: Response of the pitch servo to a commanded baseplate position with proportional and integral feedback control

control tests to be carried out safely without the danger of crashing or running out of indoor space. The gimbal ring was constructed from rigid, low density industrial foam. Two sets of delrin bearings were inserted into the gimbal to form the outer and inner axis of the gimbal (Fig. 3.39). Care was taken to ensure that the pitch and roll axes of the gimbal coincided with the C.G. of the vehicle. Even with the foam design, the pitch and roll inertias of the vehicle with the gimbal had increased by up to 100%. In addition, taking the damping effect of friction in the gimbal bearings into consideration, it is clear that the gimbal stand does not completely simulate free flight conditions. Nevertheless, this was viewed to be an important test for the controller prior to free flight tests. When the vehicle was commanded for hover attitude with proportional feedback, it was seen that the controller was able to achieve zero pitch and roll states of the vehicle. Additionally the response to external disturbance was satisfactory (Fig. 3.40). The disturbance was mitigated within about 4 seconds. Figure 3.41 shows the response of the vehicle to a pitch attitude command with external disturbances using a PI controller. It can be seen that the vehice was able to successfully achieve attitude hold as well as reject disturbances.

3.5.3   Yaw DOF tests

In order to test for control in yaw DOF, the vehicle was mounted on the stand shown in Fig. 3.42. The vehicle was connected to a shaft that was mounted on two radial bearings. It was ensured that the C.G of the vehicle lay on the shaft axis. A disturbance in yaw was sought to be mitigated. As discussed earlier, an appropriate feedback state for the yaw DOF was chosen to be the yaw rate. Figure 3.43 shows the performance of the proportional (in yaw rate) feedback

Figure 3.38: Vehicle mounted on gimbal to test pitch/roll control
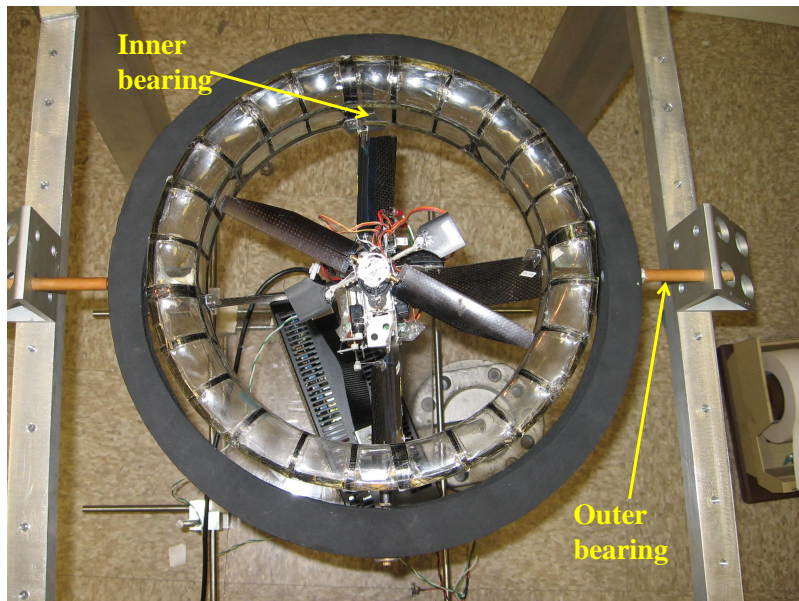
Figure 3.39: Inner and outer bearings on gimbal set-up, top view
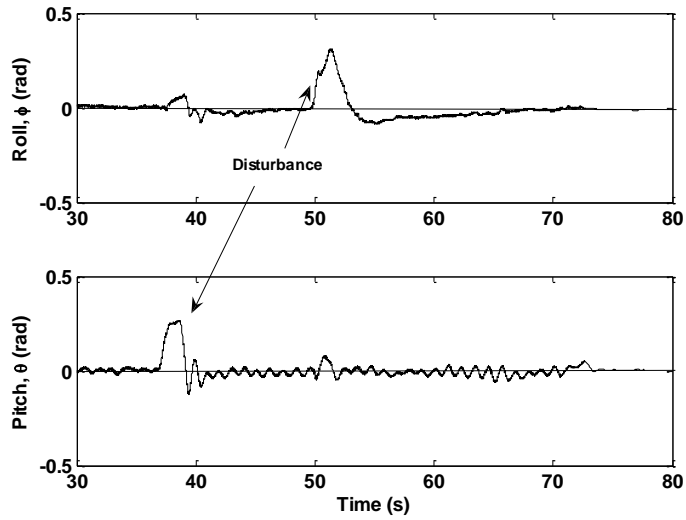
Figure 3.40: Vehicle stabilized for hover in gimbal stand with P controller
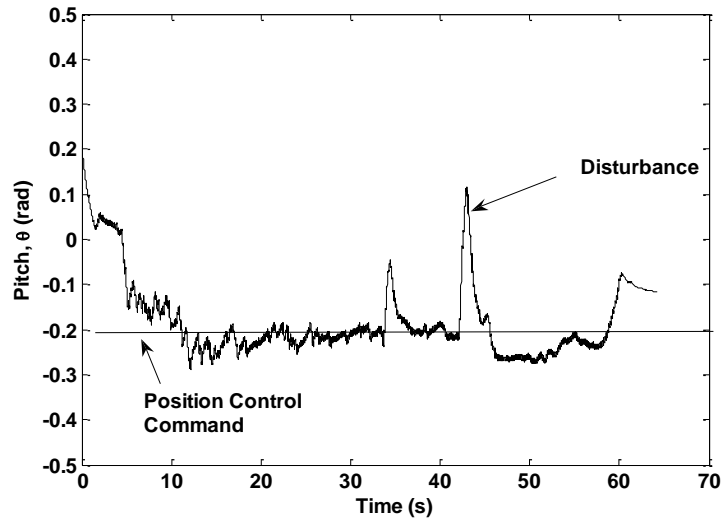
Figure 3.41: Vehicle commanded for pitch attitude in gimbal stand with PI controller

controller in mitigating yaw disturbances. It was seen that the vehicle control response in yaw was acceptable.
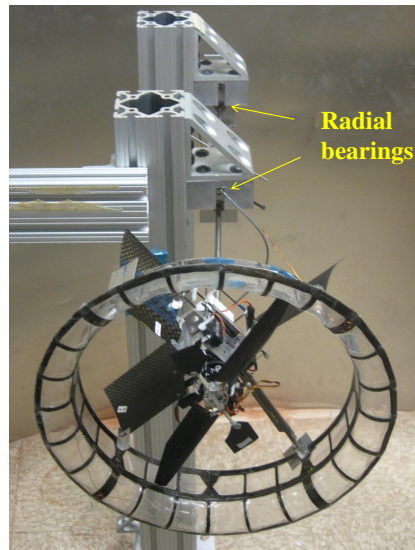
Figure 3.42: Test stand for yaw control
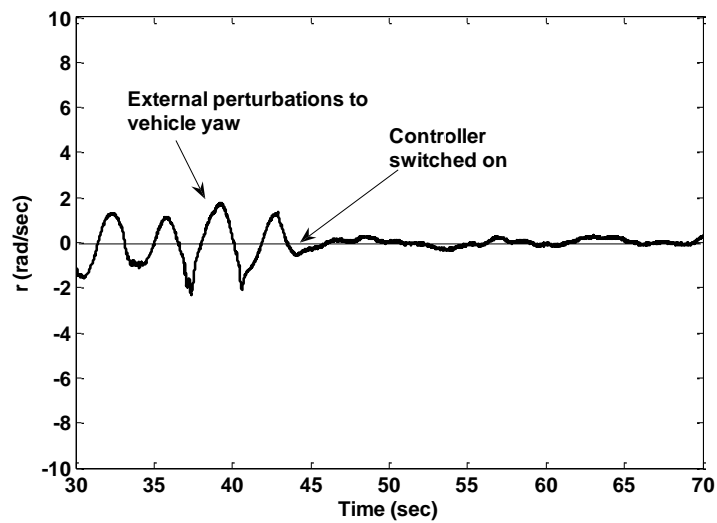
Figure 3.43: Yaw stabilization of the vehicle with proportional control

3.5.3.1 Effect of ground on anti-torque capability of vanes

Based on observation and pilot feedback during manual flight testing of the initial prototypes (Sec. 2.7), it was noticed that the anti-torque capability of the vanes when operated in ground effect (IGE) was reduced. A possible explanation for the deteriorated yaw control authority IGE is illustrated in Fig. 3.44. With ground proximity, the pressure in the center of the rotor downwash increases. This has two effects: (1) inflow velocity through the rotor decreases, and (2) the rotor downwash is pushed radialy outward. A combination of these factors is probably responsible for the degradation in vane effectiveness in ground effect. This effect was studied through unconstrained (string suspension) and constrained set-ups. TiShrov was used for these studies since the presence of the hingeless rotor and shroud was favorable for performing string suspension studies.

IGE **OGE**
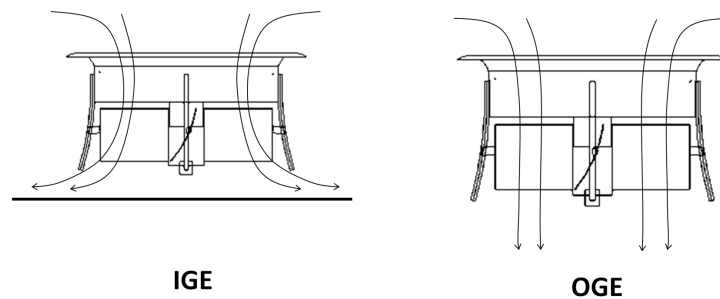
Figure 3.44: Loss of vane effectiveness in ground effect (IGE)

Unconstrained setup to study vehicle yaw authority: The vehicle was suspended by a string fixed to a carbon rod that was attached to the shroud

structure (Fig. 3.45). The height of the vehicle above the ground was varied from IGE to OGE (out of ground effect) condition. The IMU yaw rate data and rudder-throttle input from the transmitter was recorded. Yaw rate response of the vehicle as a function of height was recorded. Also measured were the pilot throttle and rudder stick inputs. Extra weight was added to the vehicle to prevent string slackening. The rudder input was symmetrically swept about the mean position in clockwise and anti-clockwise rotation. The rotor was spun in the anti-clockwise direction (looking from top). As expected, a significant difference in vehicle yaw response was observed between IGE (Fig. 3.46(a)) and OGE conditions (Fig. 3.46(c)). With maximum control deflection, the vanes were not able to counter the rotor torque in ground effect (height above ground $z/R = 1.3$. It was seen that yaw authority improved as the vehicle came out of ground effect. A maximum yaw rate of about 1.8-2 rad/s was attainable.
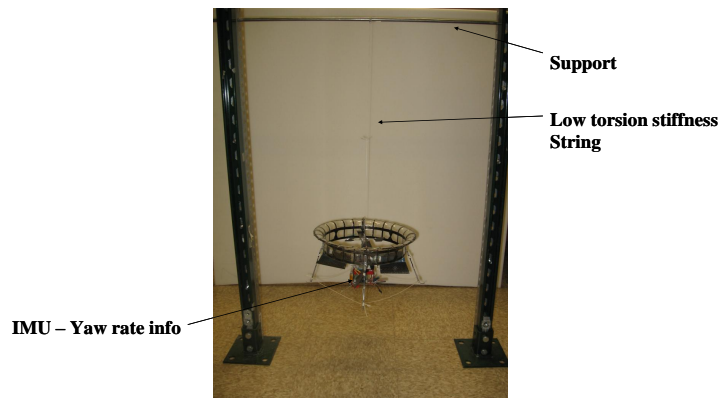
Figure 3.45: Yaw rate measurement as a function of height above ground

Constrained set-up to study yaw authority: By adjusting the vane angle settings, it might be possible to achieve bi-directional yaw control for both
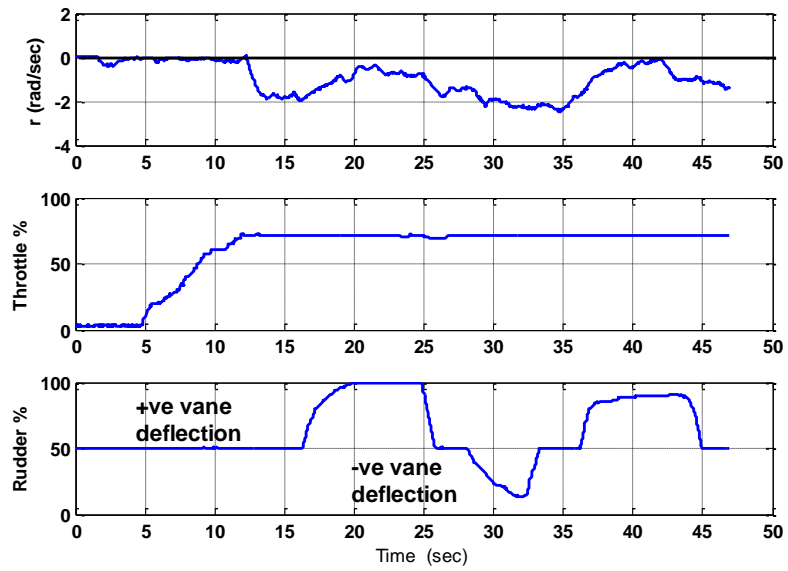
(a) z/R = 1.3
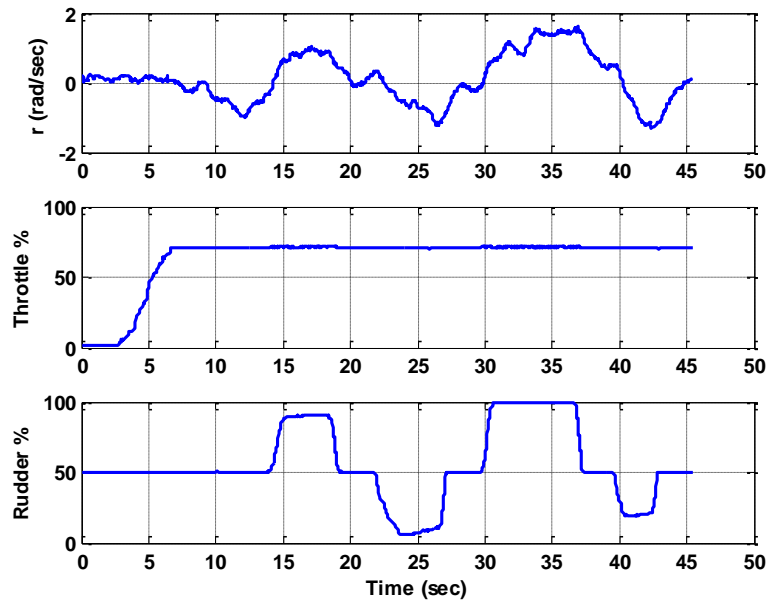
(b) z/R = 1.9
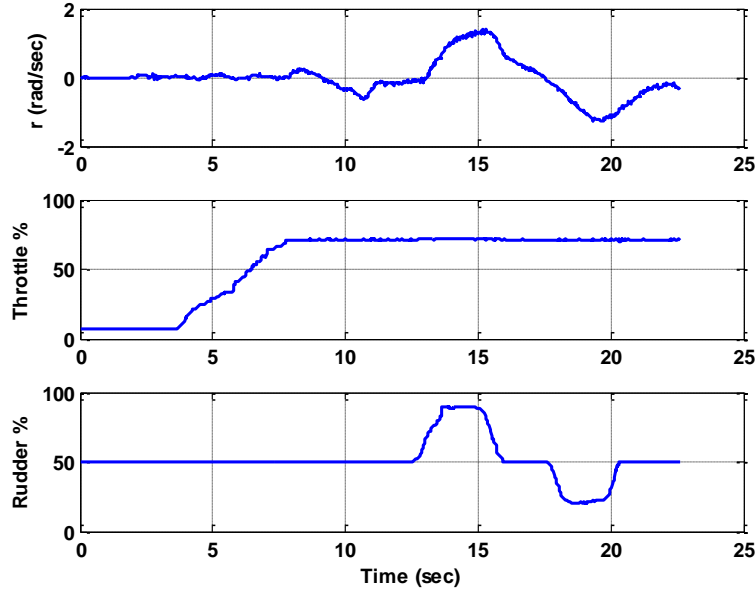
(c) z/R = 2.5

Figure 3.46: Effect of height above ground and rudder input on yaw rate (clockwise: -ve yaw rate)

IGE and OGE conditions. This was tested in an experimental set-up illustrated in Fig. 3.47. Maximum obtainable body torque from vane deflections was measured as a function of height above ground. From Fig. 3.48, it can be observed that in OGE condition, the vehicle trimmed in yaw. This implied equal control authority in clockwise and counterclockwise directions. Such was not the case when the vehicle operated closer to the ground. It can be seen that for a fixed vane and undeflected control vane setting of 23 and 16 deg respectively, equal bi-directional yaw authority was achieved in OGE condition (Fig. 3.49). However, for the IGE condition, the vane angles had to be increased. Thus for a given vane setting similar yaw authortiy cannot be achieved in IGE and OGE conditions. Based on the above study, the vane pitch setting was appropriately varied depending on the region of operation (IGE or OGE). Additionally, for an

OGE vane setting, fast take-off would be required for free flight testing to avoid undesirable loss of yaw control in ground effect.
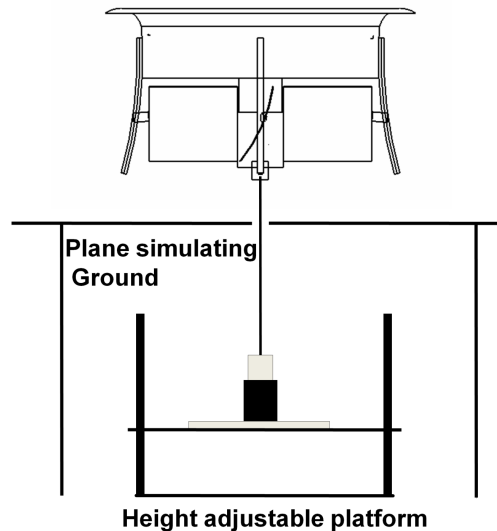
Figure 3.47: Set-up to measure effect of ground on vane effectiveness: constrained in yaw

3.6   Free Flight Test Results

In the constrained tests described in the previous section, the controller was tested to be effective in controlling the vehicle pitch, roll and yaw degrees of freedom. However, the system parameters and conditions still differed from the free flight case. It was therefore important to further test the controller in two steps: First, with a couple of unshrouded teetering rotor vehicles that were known to be open loop stable. Finally, to install the shroud and perform closed loop flight tests. The first configuration tested was GIANT (described in Sec. 2.7). It is an unshrouded teetering rotor vehicle with anti-torque vanes. The trim inputs for hover were initially determined from piloted flight tests. Proportional
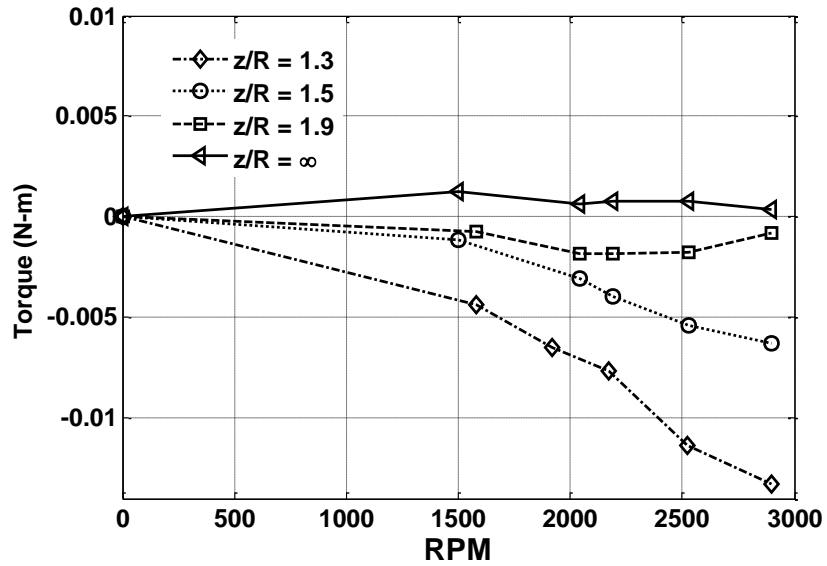
(a) Vanes undeflected
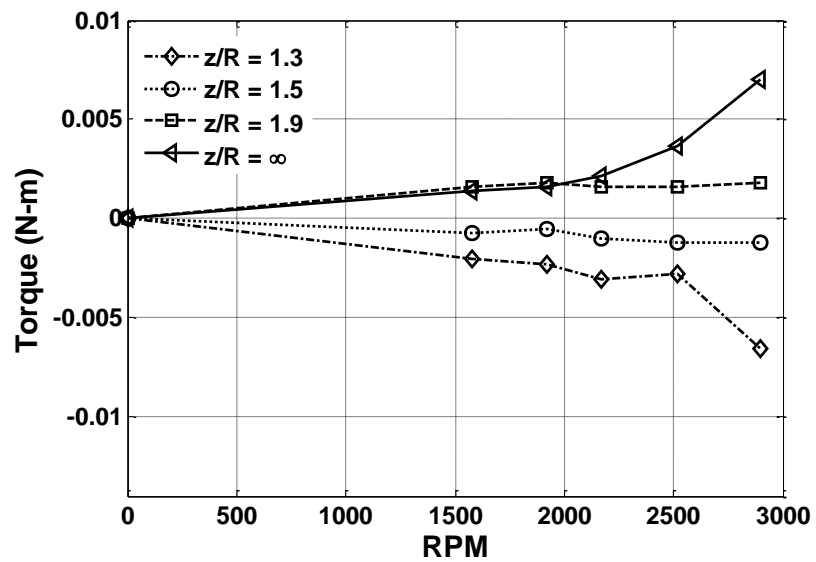
(b) vanes deflected

Figure 3.48: Loss of vane effectiveness as vehicle approaches ground
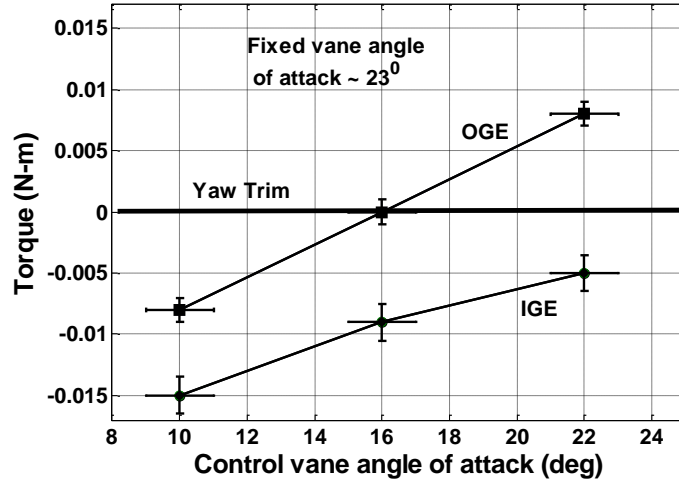
Figure 3.49: Bi-directinal yaw authority IGE and OGE

feedback based on the vehicle pitch and roll attitude was superimposed on the trim inputs. Closed loop control tests were then performed. Figure 3.50 shows a snapshot of GIANT in free flight hover. The performance of the controller was satisfactory when the trim inputs were exact (Fig. 3.51). However, in practice, trim values changed due to vehicle crashes that resulted changes in CG position.

As a result, the controller operated on an erroneous trim input, and hover attitude was not maintained (Fig. 3.52). This can be eliminiated by adding integral control (Figs. 3.53, 3.54). It should be mentioned that integral feedback reduces the stability margin of the closed loop system. It is therefore not a preferred technique, if the trim inputs are known.

With the controller successfully tested on GIANT, the next configuration that was tested for free flight was the unshrouded version of TiShrov (Fig. 3.55). The procedure for controller testing was followed similar to that mentioned for GIANT. Care was taken to maintain consistency in trim values to avoid the need for inclusion of integral control. It can be seen from Figs. 3.56 and 3.57 that the

Figure 3.50: Bi-directinal yaw authority IGE and OGE
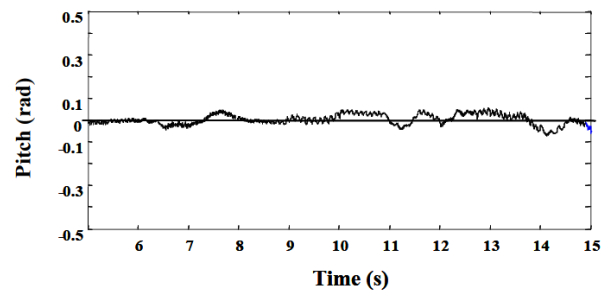
Figure 3.51: Hover control of GIANT with no trim disturbance. Proportional control.
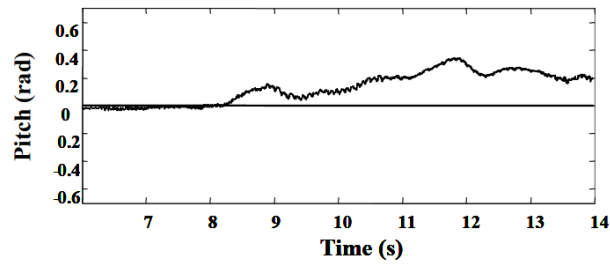
Figure 3.52: Hover control of GIANT with pitch forward trim disturbance. Proportional control.

163
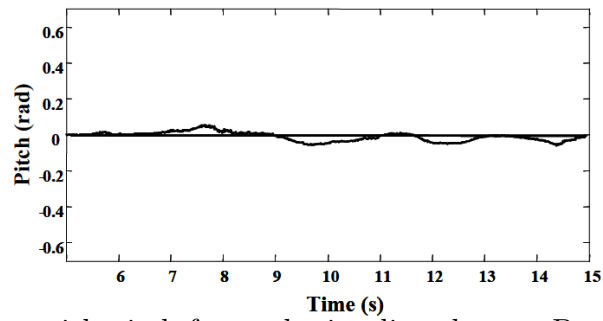
Figure 3.53: Hover with pitch forward trim disturbance. Proportional and integral control
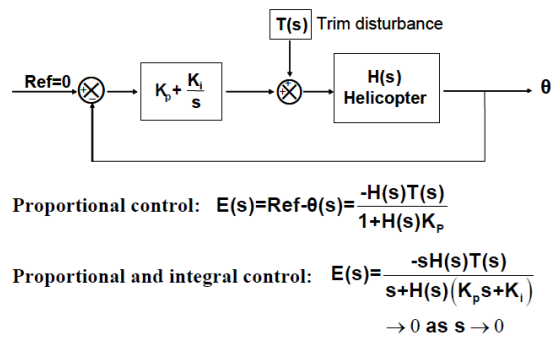
Figure 3.54: Elimination of error due to trim disturbance by adding integral feedback

164

vehicle achieved stable free flight hover.

Figure 3.55: Unshrouded TiShrov

Figure 3.56: Free flight closed loop hover control. Proportional feedback

Next, flight tests were conducted with the shrouded rotor vehicle TiShrov. The vehicle was tested with a hingeless rotor with a tip clearance of $3.2\%R$. A series of trial and error tests were conducted to determine trim inputs such that the vehicle lifted off vertically. With zero to low proportional gains, it can be clearly seen that the vehicle was not stable (Fig. 3.58). The free flight rigid body
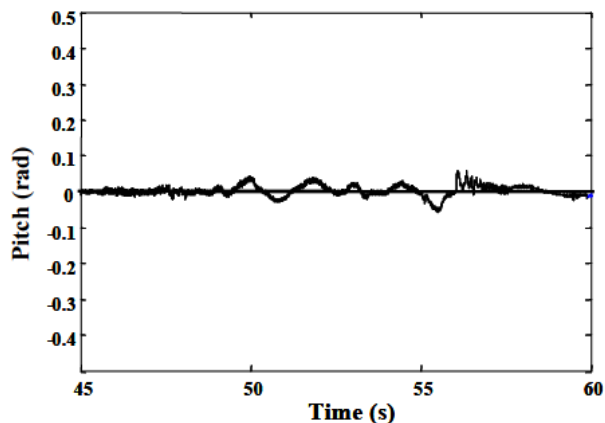
Figure 3.57: Hover control of unshrouded TiShrov

oscillation was about 0.5 Hz. As the gains were increased to between 50-80% of the stick input range per radian, good hover performance was achieved with very minimal oscillations about zero state (Figs. 3.59 and 3.60). However, once the gains were increased further (>100% of the stick input range per radian), the effect of reduced damping described earlier was observed (Fig. 3.61). It was seen that the rigid body oscillation frequency increased to about 0.9 Hz at high gains. The Ziegler-Nichols tuning criteria set the proportional gain to about 60% of the stick input range per radian.

TiShrov was also found to be sensitive to ground effect. It was observed that on a few occasions, upon slow rotor start up, the vehicle went into ground-effect-induced instability and failed to gain altitude. As a result, fast start ups were done, which solved the problem. Figure 3.62 shows the oscillations arising from ground effect and the correction for attitude from the controller as soon as the vehicle gained altitude.
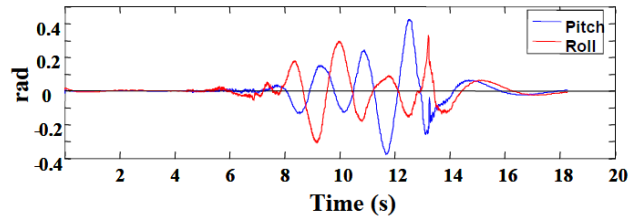
Figure 3.58: Low proportional gain: <20% stick input range/radian. Poor hover.
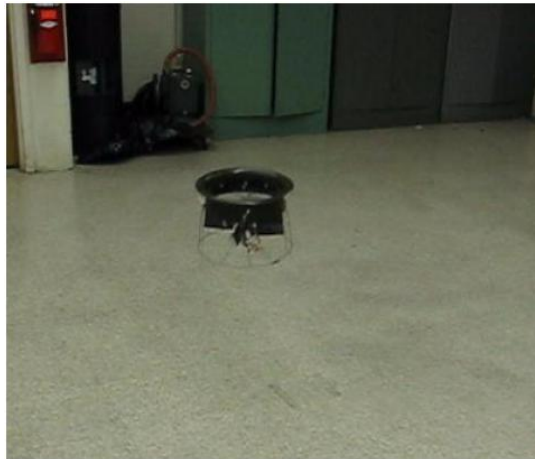
Figure 3.59: Stable hover control of TiShrov
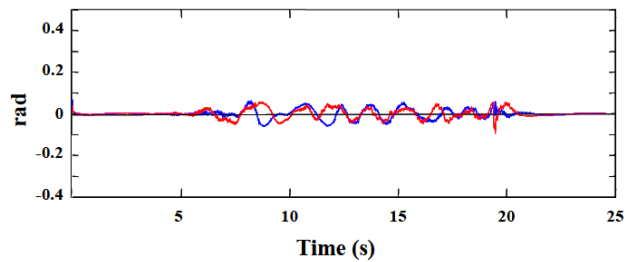
Figure 3.60: Medium proportional gain: 50-80% stick input range/radian. Satisfactory hover.
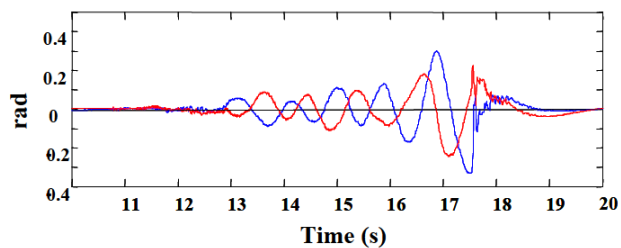
Figure 3.61: High proportional gain: >120% stick input range/radian. Unstable hover.
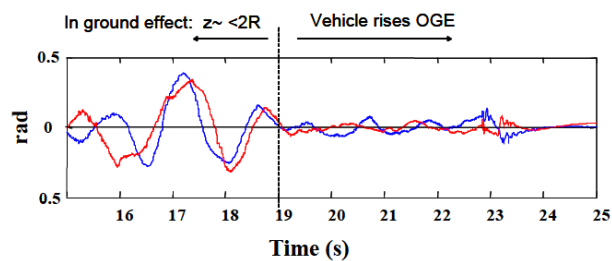
Figure 3.62: Controller works satisfactorily as soon as vehicle comes out of ground effect

3.7 Summary

From tests that studied passive stability of the shrouded rotor system, it was seen that with a teetering rotor system, the shrouded rotor exhibited limit cycle oscillations. Therefore it is necessary to incorporate a hingeless rotor in a shroud to minimize tip path plane motion inside the shroud. A practical lightweight shroud design may include non-uniformities in rotor-shroud geometry which could result in oscillations in flight. Therefore a closed loop stability augmentation system is required to aid flight in hover. A closed loop feedback system with wireless telemetry was implemented which had a latency of about 95 ms. This was seen to provide satisfactory closed loop performance in pitch, roll and yaw using a proportional-integral-derivative feedback controller. The various gains were determined using the Ziegler Nichols method. The shrouded rotor vehicle performed satisfactorily in free flight hover. To prevent ground effect induced instability, it was important to conduct fast lift-off of the vehicle. Constrained and unconstrained tests of the vehicle yaw control indicated that the control authority of the anti-torque vanes deteriorated in ground effect (IGE). This is possibly due to the fact that in IGE conditions, the downwash velocity is reduced and the region of flow over the vanes decreases.

Chapter 4

Attitude Dynamics Identification in Hover

4.1 Overview

In the previous chapter, the hover flight tests of the vehicle incorporating a phased Hiller bar (flybar) was discussed. A PID controller was used to satisfactorliy obtain stable hover in free flight. In this chapter, the attitude dynamics of the shrouded rotor vehicle is studied about hover as the equilibrium condition. The salient advantages and drawbacks of incorporating a flybarless rotor are discussed. The vehicle is constrained in translation to remove the effects of translation on vehicle attitude. System identification of the vehicle is conducted in the time domain, based on a reduced order attitude dynamics model. The effect of the flybar and the flybarless rotor on the attitude dynamics is described. Finally a model based controller framework is incorporated using the derived model from system identification. This would serve as a platform for incorporating an extended 6-DOF vehicle model in the future.

170

4.2   Rigid Body Equations of Motion

Consider the vehicle schematic shown in Fig. 4.1. Here, X,Y,Z are the forces acting along the lateral, longitudinal and vertical directions respectively. The moments applied to the vehicle about the X,Y and Z axes are L, M and N respectively. The non linear rigid body equations of motion can be summarized as:

1. Force equilibrium equations

$$m(\dot{u} + qw - rv) = X \tag{4.1}$$

$$m(\dot{v} + ru - pw) = Y \tag{4.2}$$

$$m(\dot{w} + pv - qu) = Z \tag{4.3}$$

2. Moment equilibrium equations

$$I_{xx}\dot{p} - (I_{yy} - I_{zz})qr + I_{yz}(r^2 - q^2) - Ixz(pq + \dot{r}) + I_{xy}(pr - \dot{q}) = L \tag{4.4}$$

$$I_{yy}\dot{q} - (I_{zz} - I_{xz})pr + I_{xz}(p^2 - r^2) - Ixy(qr + \dot{p}) + I_{yz}(pq - \dot{r}) = M \tag{4.5}$$

$$I_{zz}\dot{r} - (I_{xz} - I_{yy})qr + I_{xy}(q^2 - p^2) - Iyz(pr + \dot{q}) + I_{xz}(qr - \dot{p}) = N \tag{4.6}$$

3. Kinematic equations

$$p = \dot{\phi} - \dot{\psi}sin\theta \tag{4.7}$$

$$q = \dot{\theta}cos\phi + \dot{\psi}sin\phi cos\theta \tag{4.8}$$

$$r = \dot{\psi}cos\phi cos\theta - \dot{\theta}sin\phi \tag{4.9}$$
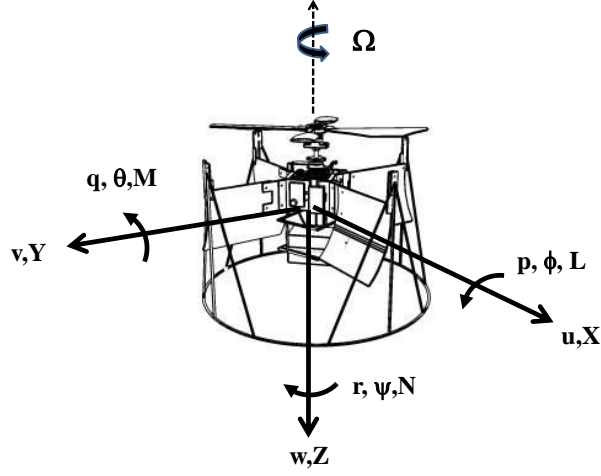
Figure 4.1: Force, moment and kinematic notations

The above equations can be expressed as

$$\dot{\mathbf{x}} = f(\mathbf{x}, \mathbf{u}) \tag{4.10}$$

where $\mathbf{x}$ is the vehicle state vector, and $\mathbf{u}$ is the control input vector. Here,

$$\mathbf{x} = [u, v, w, \phi, \theta, \psi, p, q, r]^T \tag{4.11}$$

$$\mathbf{u} = [u_{lat}, u_{lon}, u_{throttle}, u_{ped}]; \tag{4.12}$$

it is useful to linearize $f(\mathbf{x}, \mathbf{u})$ about a trim condition. Of interest in this study is the hover equilibrium condition where the linear and angular velocities are zero. The linearized small perturbation equations of motion can be written as:

$$\dot{u} = X/m, \dot{v} = Y/m, \dot{w} = Z/m \tag{4.13}$$

$$\dot{p} = L/I_{xx}, \dot{q} = M/I_{yy}, \dot{r} = N/I_{zz} \tag{4.14}$$

$$\dot{\phi} = p, \dot{\theta} = q, \dot{\psi} = r \tag{4.15}$$

where X, Y, Z, L, M, N are assumed to be continuous functions of the vehicle states and control variables. Using Taylor series expansion and retaining the first order terms,

$$X/m = X_u u + X_v v + X_w w + X_p p + X_q q + X_r r + X_{\delta_{lat}} \delta_{lat} + .. \tag{4.16}$$

where

$$X_\alpha = \frac{\partial X/m}{\partial \alpha} \tag{4.17}$$

The partial derivatives of the forces or moments with respect to the vehicle states are the stability derivatives. The derivatives of the forces or moments with respect to the vehicle control inputs are termed control derivatives. The expressions for the other force and moment terms can be written in a similar manner to Eq. (4.16). Therefore the non-linear differential equation of motion (Eq. (4.10)) can be written in the linearized state-space form as,

$$\dot{\mathbf{x}} = A\mathbf{x} + B\mathbf{u} \tag{4.18}$$

where A and B are the stability and control matrices. In the present study, the attitude dynamics about hover is of interest. As a result, the reduced order vehicle attitude dynamics model chosen for this purpose is,

$$\begin{bmatrix} \dot{p} \\ \dot{q} \end{bmatrix} = \begin{bmatrix} L_p & L_q \\ M_p & M_q \end{bmatrix} \begin{bmatrix} p \\ q \end{bmatrix} + \begin{bmatrix} L_{\delta_{lat}} & L_{\delta_{lon}} \\ M_{\delta_{lat}} & M_{\delta_{lon}} \end{bmatrix} \begin{bmatrix} \delta_{lat} \\ \delta_{lon} \end{bmatrix} \tag{4.19}$$

$$y = \begin{bmatrix} 1 & 0 \\ 0 & 1 \end{bmatrix} \begin{bmatrix} p \\ q \end{bmatrix} \qquad (4.20)$$

where L_p and L_q are the stability derivatives for roll dynamics and M_p and M_q are the stability derivatives for pitch dynamics. Similarly, $L_{\delta_{lat}}, L_{\delta_{lon}}, M_{\delta_{lat}}, M_{\delta_{lon}}$ are the control derivatives for roll and pitch dynamics respectively.

4.2.1 Model simplifications

The primary response of the shrouded rotor vehicle to an external flow disturbance is in pitch and roll attitude. Therefore, the pitch and roll dynamics of the vehicle in quiescent hover condition was sought to be identified to aid in the development of a simple model based controller for gust disturbance rejection purposes and to assess the feedback requirements with and without a flybar. During vehicle control tests in Chapter 3, it was seen that the yaw degree of freedom (DOF) did not couple into the pitch and roll dynamics. As a result, the yaw DOF was de-coupled in the present model and was not identified. Identification of the complete 6 DOF model including lateral and longitudinal moment derivatives such as M_u and L_v was beyond the scope of this study. Pitching moments from edgewise gusts were treated purely as disturbance inputs that the control system would have to mitigate to achieve hover attitude.

The non-dimensional rotating natural flap frequency of the rotor was determined to be about 1.3 at 3700 RPM. Therefore, the regressive flap frequency of the rotor was much higher than the fuselage mode in the frequency of interest and a coupled rotor-fuselage model structure was not considered. Additionally, the effect of the flybar was treated as an implicit source of damping. Since low input frequencies were considered, the flybar flapping states were not included

in the model. The use of a reduced order model for low frequency validation was seen to be comparable with a higher order hybrid rotor-fuselage model [45]. Therefore, a reduced order 2 DOF linear model was used.

4.3 Flybarless Rotor

For the identification experiments, two rotor set-ups are studied. They are the flybar (Sec. 2.4) and the flybarless rotor. These are shown in Figs. 4.2 and 4.3.
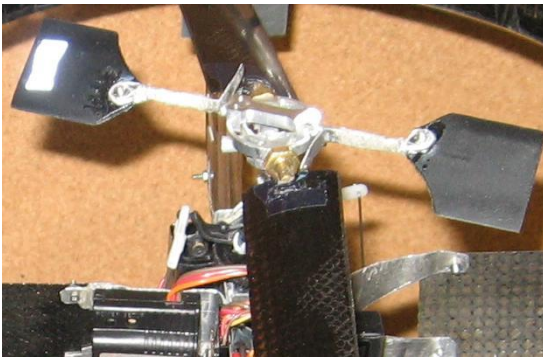
Figure 4.2: Flybar rotor head   Figure 4.3: Flybarless rotor head
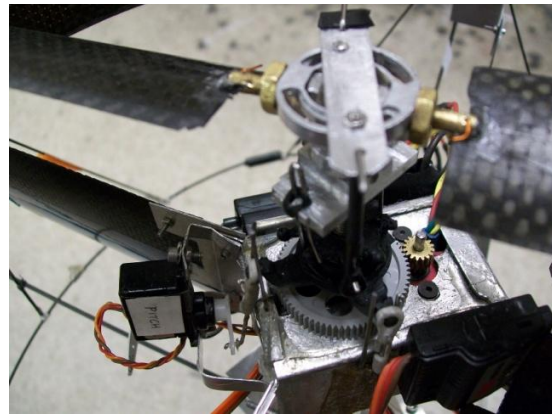
The flybar rotor head offers passive gyroscopic stability but requires additional power to rotate the Hiller bar. It was seen earlier (Fig. 2.31(a)) that there was a 6-7% drop in Figure of Merit with the flybar rotor. On the other hand, the flybarless rotor head has no inherent damping, but is mechanically simple, cyclic transfer is efficient and there is no power penalty due to the aerodynamic drag of the flybar. Therefore, it can be desirable to operate the rotor in the absence of the flybar. In order to measure the control moments of the rotor systems, the vehicle was mounted on the set-up shown in Fig. 4.4. The vehicle was constrained to a steel rod, attached to a torque sensor through a system

of bearings. The maximum travel of the swashplate was $\pm 10^0$ out of the rotor plane. The pitch servo was actuated from trim with maximum deflection in the pitch-up and pitch-down direction. The total control moment generated was used for comparison. It can be seen that the maximum control moment was up to 100% higher for the flybarless rotor. This may be attributed to aerodynamic losses in the Hiller paddles which reduce flybar flapping for a given swashplate input, and mechanical design limitations.
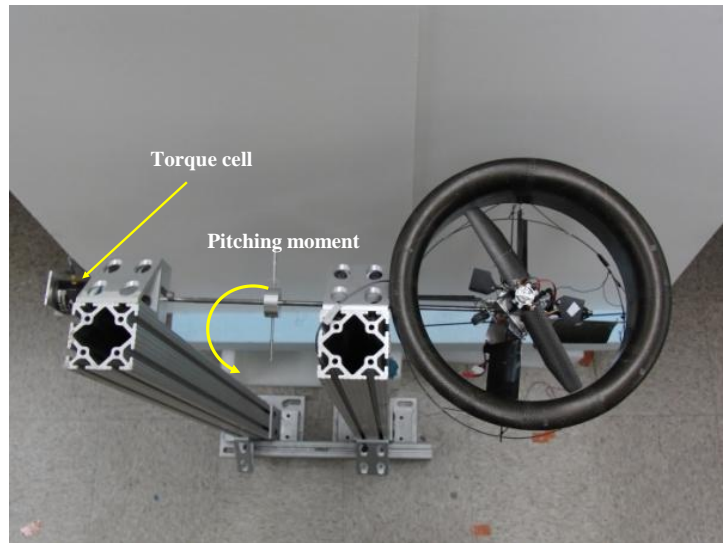
Figure 4.4: Set-up to measure control moment

4.4 System Identification

This section seeks to identify the model structure defined in Eq. (4.19) by observation of input and output of the flybar and flybarless shrouded rotor system.
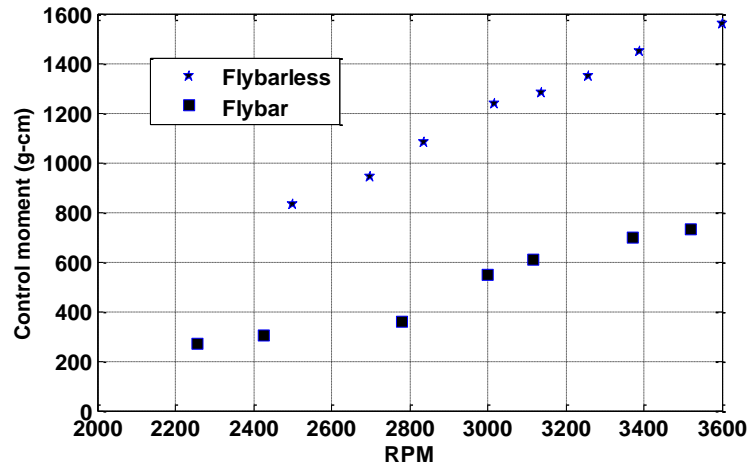
Figure 4.5: Control moments generated by flybar and flybarless rotor

Figure 4.6: System Identification

Frequency-response methods	Time-response methods
Provides a linear system model	Can be used to obtain linear or nonlinear models
Time-history data is converted to frequency responses	Consist of time-history data
Models are identified by matching predicted frequency responses against measured frequency responses	Predicted time histories are matched against measured time histories
Bias effects of noise eliminated	Bias effects may be introduced
Involves longer flight records	Involves shorter record lengths

Table 4.1: Comparison between frequency and time response methods

4.4.1 Methodology

Two system identification methodologies to identify and characterize the stability and control derivatives of the vehicle include frequency domain based approaches (CIFER) and time domain based methods (SIDPAC). A comparison of frequency and time response methods is given in Table. 4.1. This is discussed in further detail in Ref. [45]

We can see that for the frequency domain technique, relatively large amounts of flight data are required that span a wide frequency range. It also requires averaging techniques when performing Fourier transforms and estimating spectral densities which introduce errors. The time domain technique lends itself to a direct physical representation of the system. Based on these arguments, time-domain response method was used for the identification process where the frequencies of inputs were restricted to within 1-2 Hz. Specific routines involving stepwise regression, equation-error(EE) and output-error(OE) developed by Morelli [164] in the SIDPAC module on MATLAB is employed.

The procedure involved is schematically shown in Fig. 4.7

```
MODEL STRUCTURE                         EXPERIMENT
(Engineering simplifications,
Prior knowledge of dynamics)

                                        INPUT-OUTPUT DATA
                                        COLLECTION

                                        PARAMETER ESTIMATION
                                        (Stepwise regression, Equation-Error)

                                            PARAMETER ESTIMATION
                                            (Output-error)

DIFFERENT SETS OF                       MODEL VALIDATION
DATA
```
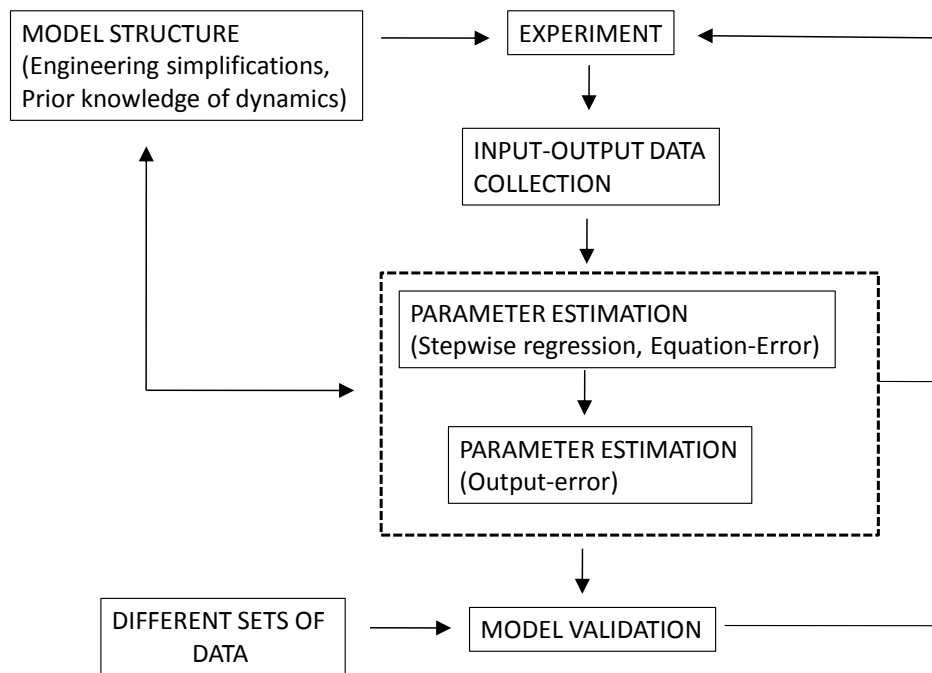
Figure 4.7: System identification procedure: Time-response method

4.4.1.1 Equation-error parameter estimation

If θ is the constant parameter vector to be estimated and x, u are the state and input vectors respectively, then the output equation of the linear system is,

$$y(t) = \dot{x} = X(x(t), u(t))\theta \tag{4.21}$$

and the measurement equation,

$$z(t) = y(t) + v(t) \tag{4.22}$$

where v is random noise. It is therefore desired to choose θ such that the error $z(t) - y(t)$ is minimized. Let n be the size of θ. Typically, the size (N) of the measurement vector is much larger than n. Therefore least squares parameter estimation is performed. Here, we seek θ that minimizes a cost function,

$$\hat{\theta} = \min_{\theta} \frac{1}{2}(z - X\theta)^T(z - X\theta) \tag{4.23}$$

This can be re-written as,

$$\hat{\theta} = (X^T X)^{-1} X^T z \tag{4.24}$$

So the estimated vector is given by,

$$\hat{y} = X\hat{\theta} = X(X^T X)^{-1} X^T z \tag{4.25}$$

The columns of X are the regressors in the model. Care must be taken to ensure that the regressors are not linearly dependent for the matrix inverse $(X^T X)^{-1}$ to exist. The equation-error formulation is a linear estimation problem and the

least-squres solution does not require iteration.

4.4.1.2 Stepwise regression

This is a computation technique to evaluate the relevance of a candidate regressor for inclusion in the linear model, by deleting or adding regressors one at a time. Stepwise regression starts by constructing a set of candidate regressors. The first regressor that produces the highest absolute value of correlation with z is chosen. This regressor is then removed from the subset of regressors and the procedure is repeated. Two statistical metrics are used to evaluate the candidate model terms that quantify the closeness of $\hat{y}$ and z.

Coefficient of determination, R^2: This is defined as

$$R^2 = \frac{SS_R}{SS_T} \tag{4.26}$$

where SS_T is the total sum of squares,

$$SS_T = z^T z - N\bar{z}^2 \tag{4.27}$$

and SS_R is the regression sum of squares,

$$SS_R = \sum_{i=1}^{\infty} [\hat{y(i)} - \bar{z}]^2 \tag{4.28}$$

Here, N is the size of the measurement vector and $\bar{z}$ is the mean of the measurement vector. R^2 is expressed as a percentage. The addition of a regressor always increases R^2, with the more influential term resulting in a greater change in R^2. An adequate model is achieved when R^2 is not substantially changed by the addition of a new model term.

F-ratio: The F ratio for testing significance of a regression is given as,

$$F = \frac{SS_R/n}{(SS_T - SS_R)/N}$$
$$= \frac{N}{n} \frac{\hat{\theta}^T X^T z - N\bar{z}^2}{z^T z - \hat{\theta}^T X^T z} \qquad (4.29)$$

Additionally, the partial F ratio can be computed for an individual parameter vector $(\hat{\theta}_j)$,

$$F_p = \frac{\hat{\theta}_j^{\,2}}{Var(\theta_j)} \qquad (4.30)$$

Any regressor with F_p less than a cut-off value is removed from the model. For 95% confidence, the cut off value is taken as 20.

4.4.1.3   Output-error method

Here, it is assumed that the process noise (in the state equation) is neglected. Therefore the states can be computed deterministically by a direct numerical integration. A maximum likelihood cost function is chosen that involves weighted squared differences between measured and computed outputs. This resulting estimator is known as the output error method. It is a non linear least-squares method for multiple outputs with output weighting that iteratively arrives at a converged parameter vector θ and covariance matrix R. The initial estimates for θ are taken from those estimated in the stepwise regression procedure. The iterative scheme adopted is a modified Newton-Raphson method. The details of this can be obtained from Ref. [164].

4.4.2 Input-output data collection

In order to remove the effect of translation on the attitude dynamics, the vehicle was suspended from its C.G. position on a low-friction spherical gimbal set-up[1]. This restricted the motion in yaw, but since the yaw DOF was decoupled from the model, it is acceptable. The dynamics of the vehicle with and without the
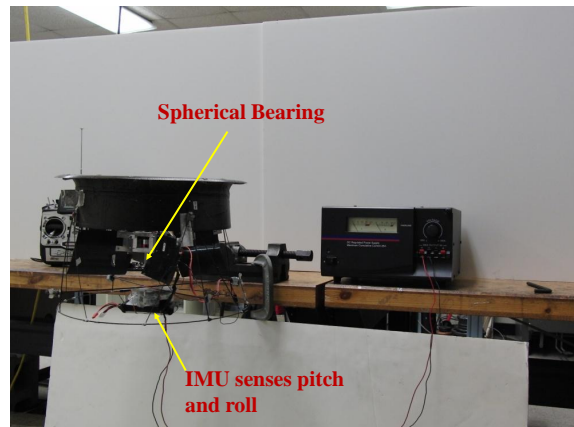
Figure 4.8: Gimbal set-up for vehicle pitch and roll motion

flybar was extracted in a separate sequence of tests. For each sequence, the vehicle was powered up to an operating RPM on the gimbal and trimmed out to a level attitude. Care was taken that trim in yaw was also performed. Next, a series of uncoupled lateral and longitudinal input sweeps were provided about trim. The onboard IMU captured the vehicle response in terms of pitch (q) and roll (p) rate. The frequency content of the inputs were restricted to less than about 6 rad/s which was within the observed free flight pitch-roll body modes (Fig. 3.59). Time history data for each input-output sequence was obtained by combining data from individual tests and were sampled at 200Hz. The latency in

---

[1]This set-up differed from the one shown in Fig. 3.38. A modification in the vehicle design allowed a direct access to the vehicle C.G., unlike the previous set-up which had to incorporate an external gimbal ring.

open loop telemetry including actuator lag was measured to be about 50 ms and was factored into the treatment of the output data. Figure 4.9 shows a sample data of the unfiltered pitch rate of the vehicle measured by the IMU. A short term fourier transform of the data (at t=15 s) shows that the noise content of the signal (Fig. 4.10) is predominantly due to the rotor rotational frequency which is at a sufficiently higher frequency than the body modes of interest. Therefore a zero phase lag low pass filter can be applied to filter out the noise due to rotor vibration (Fig. 4.11).
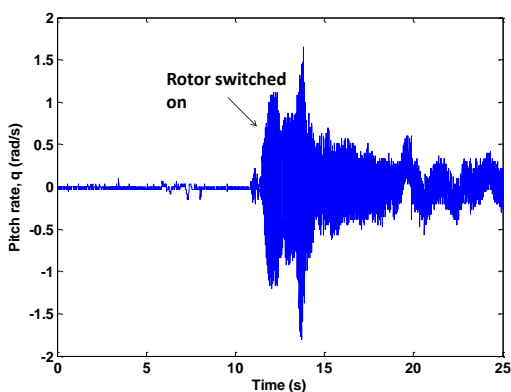
Figure 4.9: Unfiltered gyro data
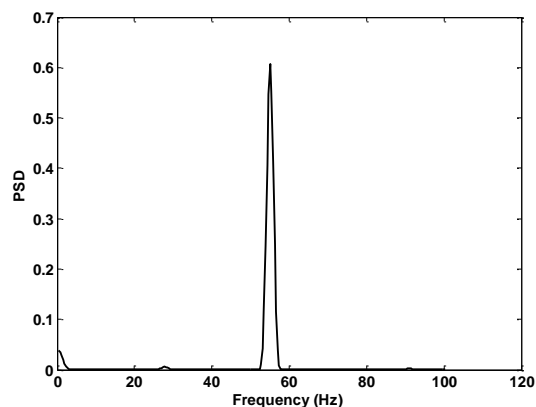
Figure 4.10: Short term fourier transform at t=15 s, predominantly rotor noise

The lateral and longitudinal cyclic inputs were non dimensionalized using the input control limits as the scaling factor such that, $(\delta_{lat}, \delta_{lon}) \in [-1, 1]$. Care was taken to provide lateral and longitudinal inputs one at a time without cross coupling of inputs. Figures 4.12 - 4.15 show sample input-output data in pitch and roll for the flybar and flybarless rotor. The bias errors in inputs were removed before performing system identification.
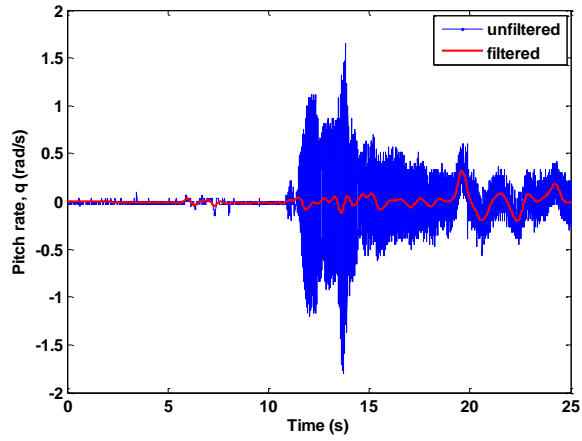
Figure 4.11: Gyro data filtered with zero phase lag low pass filter
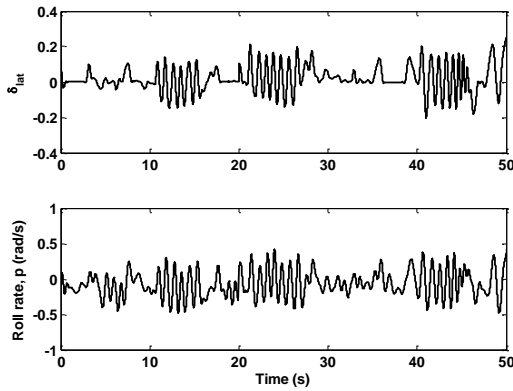
Figure 4.12: Input-output data for fly-bar rotor in lateral direction
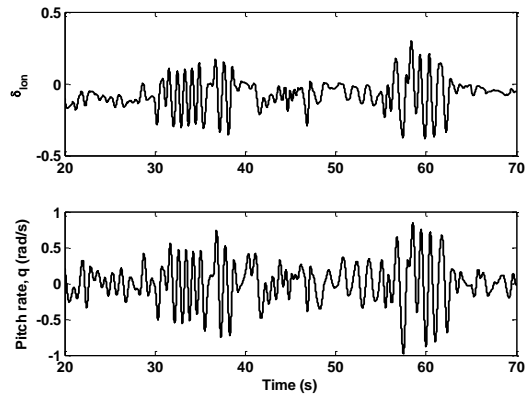
Figure 4.13: Input-output data for fly-bar rotor in longitudinal direction
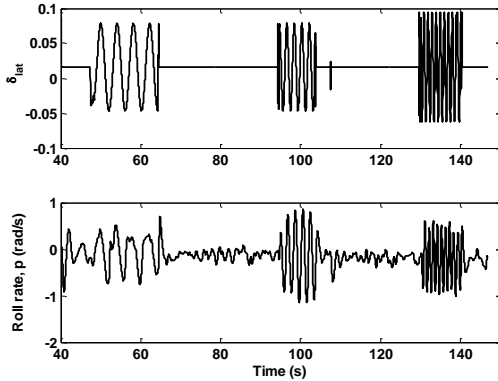
Figure 4.14: Input-output data for fly-barless rotor in lateral direction
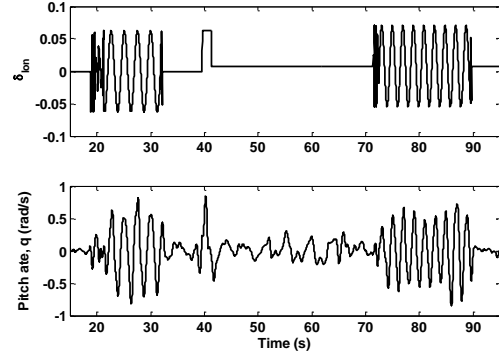
Figure 4.15: Input-output data for fly-barless rotor in longitudinal direction

4.4.3 Results

The identified parameter vector for the flybar and flybarless rotor using the model structure from Eq. (4.19) along with the statistical metrics is shown in Table 4.4.3. The R^2 and F_p values were seen to be satisfactory. It must be mentioned that this is a first order model in attitude rates. Model accuracy may be improved by including rotor and flybar dynamics as well. Time domain verification of the identified model with actual flight data (a different input-output data set than the one used for model extraction) for the flybar and flybarless rotor shows a satisfactory comparison between model and flight data. This is shown in Figs. $4.16 - 4.19$. From the identified eigenvalues, it can be seen that the flybar rotor has a stable pair of poles, whereas the flybarless rotor has a pair of poles that suggest that the system is marginally unstable (Fig. 4.20). Additionally, this shows that the primary source of damping is the flybar. The off-axis terms in the state matrix did not change significantly between the flybar and flybarless set-up. This indicates gyroscopic cross-coupling, which is purely a function of rotor angular momentum. The control derivatives in the

186

Parameter	Flybar rotor		Flybarless rotor	
	$\hat{\theta}$	F_p (min. 20)	$\hat{\theta}$	F_p
L_p(rad/s)	-6.79	475	0.76	385
L_q(rad/s)	1.7	400	1.65	370
$L_{\delta_{lat}}$(1/s)	23.85	2350	47	2020
$L_{\delta_{lon}}$(1/s)	1.6	2400	2	1950
R^2(Lateral,%)	86	–	82	–
M_q(rad/s)	-6.85	510	0	410
M_p(rad/s)	-2.1	500	-1.66	380
$M_{\delta_{lon}}$(1/s)	24	2200	54.1	1970
$M_{\delta_{lat}}$(1/s)	-1.56	2150	-2.96	1950
R^2(Long,%)	83	–	83	–
Eigenvalues	-6.82 $\pm$1.882i		0.38 $\pm$1.61i	

Table 4.2: Identified model parameters for the flybar and flybarless rotor

control matrix is significantly higher (up to 100%) for the flybarless rotor. This result agreed well with the control moment measurement (Fig. 4.5). Based on these results, it can be seen that the vehicle can be satisfactorily modeled as a system, which is of first order with respect to attitude rates. The control system has to provide external rate damping to stabilize the system for the flybarless set-up. This is a significant challenge considering the limited latency in off-board telemetry. This problem can be circumvented by including electronic damping on board the vehicle.

4.5   Controllability metrics

The above attitude dynamics models can be used to compare the two bare airframes (flybar and flybarless) in their effectiveness in arriving at a set of reachable states x_0 resulting from an arbitrary input $u(t) \in L_2^P(-\infty, 0]$ of unit norm. A controllability operator Ψ_c is considered which maps the time history of the input $u(t)$ from $t = -\infty$ to a final state x_0 at $t = 0$. The set of reachable states is
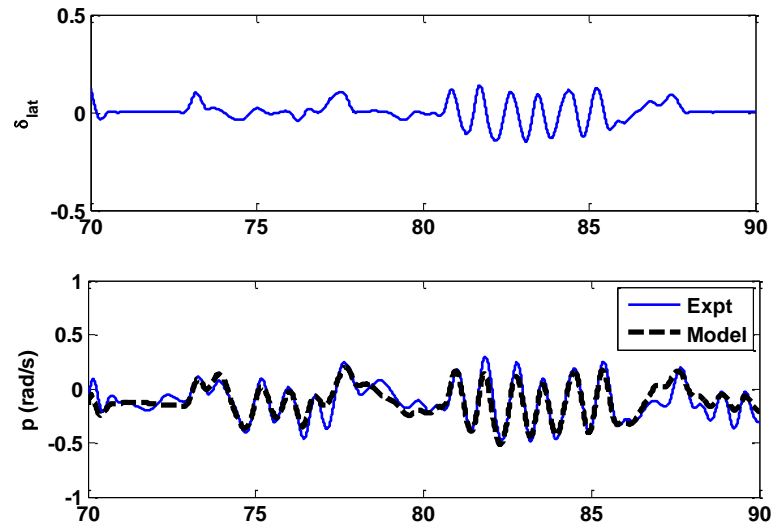
Figure 4.16: Time domain verification: Flybar rotor (Lateral)
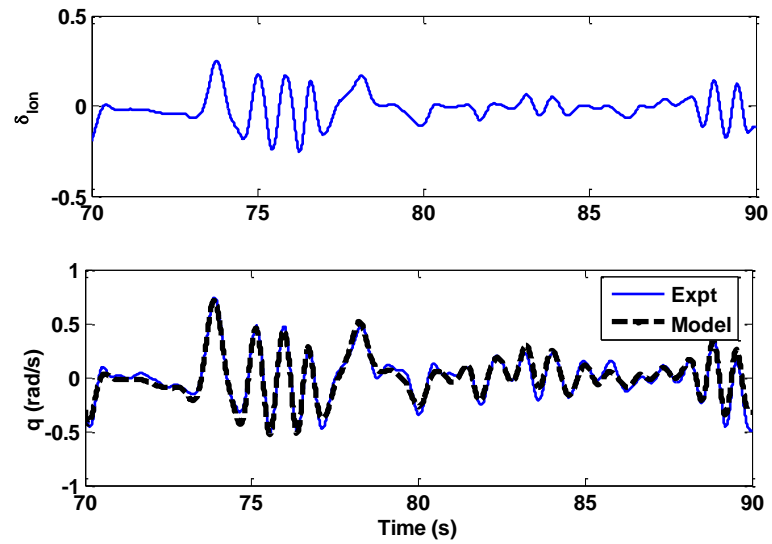
Figure 4.17: Time domain verification: Flybar rotor (Longitudinal)
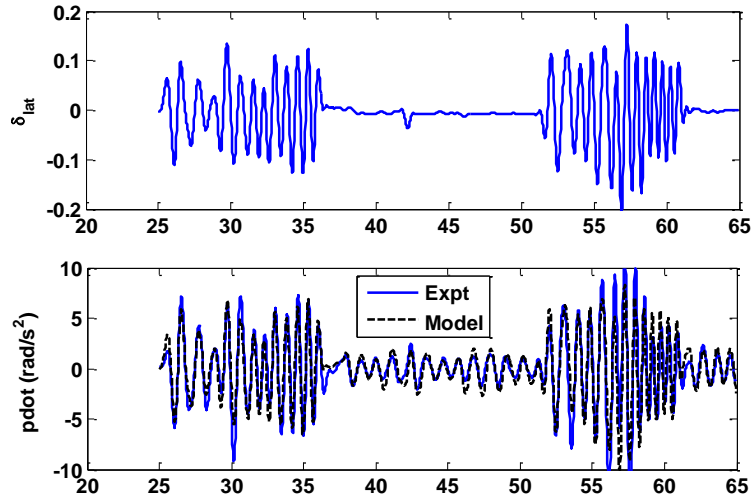
Figure 4.18: Time domain verification: Flybarless rotor (Lateral)
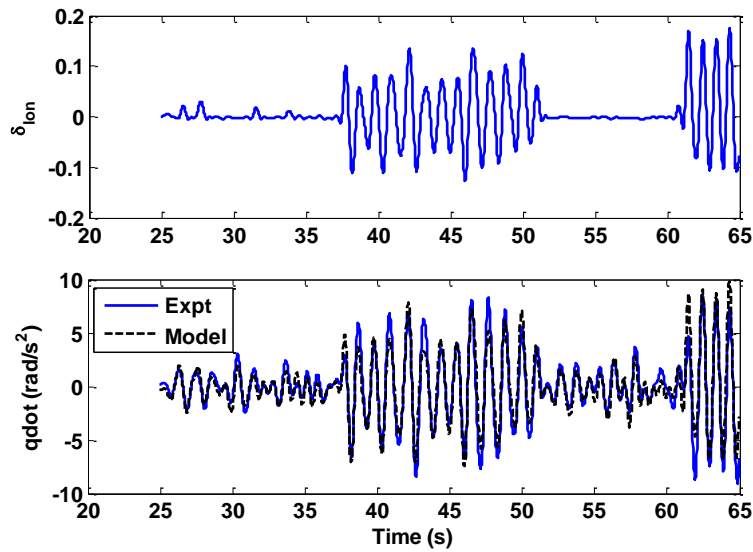
Figure 4.19: Time domain verification: Flybarless rotor (Longitudinal)
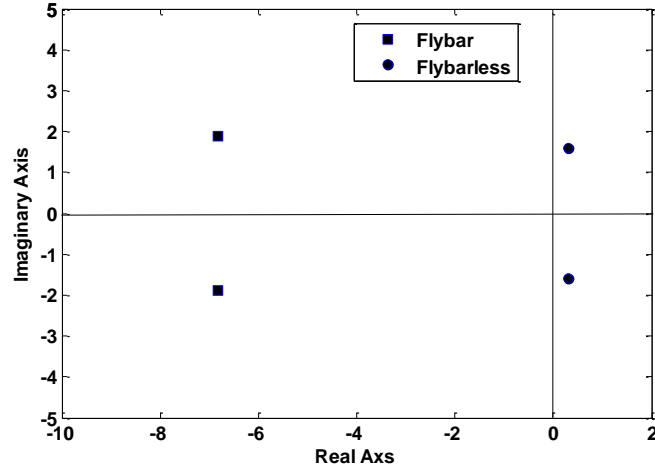
Figure 4.20: Location of poles for flybar and flybarless rotor

then $\Psi_c u$. An infinite-time controllability gramian W_c is determined to quantify this,

$$W_c = \Psi_c \Psi_c^T \qquad (4.31)$$

which can be computed from the dynamics model (A, B) using the continuous time Lyapunov equation (Ref. [165])

$$AW_c + W_c A^T + BB^T = 0 \qquad (4.32)$$

Note that the above computation is only possible when A matrix is stable as is the case for the flybar rotor. For cases when the A matrix is unstable as in the flybarless rotor, the reader is referred to Zhou. et al. (Ref. [167]) for detailed mathematical treatment. Here the A matrix is purely antistable (does not have stable eigenvalues). Using Zhou's method, a transformation matrix T

is computed which is the inverse of the eigenvector matrix of A. Following which,

$$\hat{A} = TAT^{-1}, \hat{B} = TB \tag{4.33}$$

The continuous time Lyapunov equation is then solved for,

$$-\hat{A}P - P\hat{A}^T + \hat{B}\hat{B}^T = 0 \tag{4.34}$$

The controllability gramian is then given by,

$$W_c = T^{-1}P(T^{-1})^T \tag{4.35}$$

Using the controllability gramians determined above, two control input ranking criteria can be computed (Ref. [166]):

1) D-norm: $\det(W_c^{1/2})$

2) Frobenius norm: $\sqrt{trace[(W_c^{1/2}).W_c^{1/2}]}$

These metrics are compared in Table 4.3 and Figs. 4.21 and 4.22.

	Flybar rotor	Flybar rotor (with same control derivatives as flybarless rotor	Flybarless rotor	Flybarless rotor (with same control derivatives as flybar rotor
D norm	42.2	186.7	3648	819
Frobenius norm	9.2	19.4	87	41

Table 4.3: Comparison in controllability metrics between flybar and flybarless rotor

It can be clearly seen that the flybarless rotor is much more controllable than the
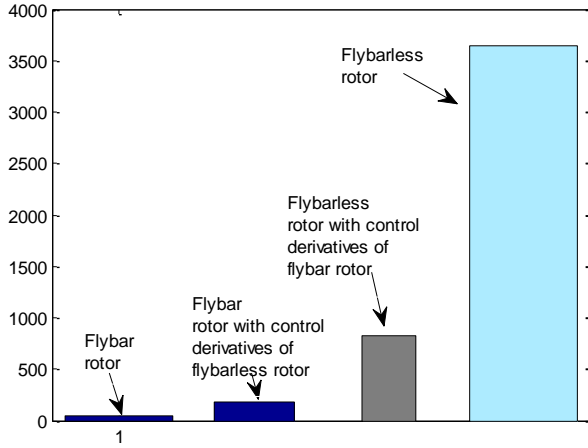
Figure 4.21: Comparison in $\det(W_c^{1/2})$ between flybar and flybarless rotor
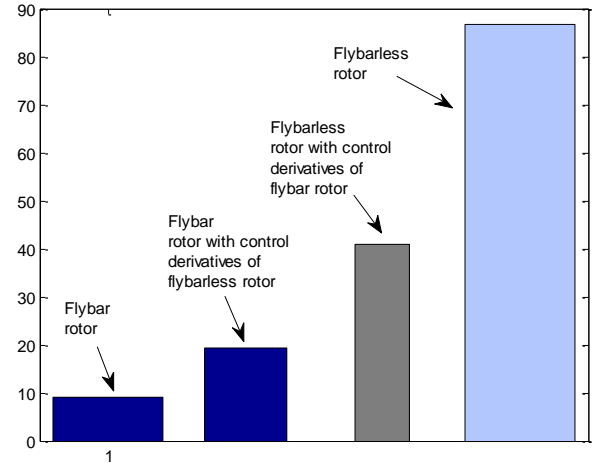
Figure 4.22: Comparison in Frobenius norm between flybar and flybarless rotor

flybar rotor. This implies that it can reach a wider span of states for a given control input energy. It can be seen that if only the control derivatives are doubled, the Frobenius norm doubles. In addition, the lack of damping in the flybarless rotor further amplifies the controllability. However, for practical applications, on-board damping will have to be provided and this effect on controllability will be removed.

4.6 Model based controller

An LQR controller based on the simplified 2 DOF linear atittude dynamics model of the vehicle was also designed. The state space attitude dunamics model of the vehicle can be written using the state vector x, state matrix A, control vector u and control matrix B, as:

$$\dot{x} = Ax + Bu \tag{4.36}$$

where,

$$x = \begin{bmatrix} p \\ q \\ \phi \\ \theta \\ \int \phi \\ \int \theta \end{bmatrix}, A = \begin{bmatrix} L_p & L_q & 0 & 0 & 0 & 0 \\ M_p & M_q & 0 & 0 & 0 & 0 \\ 1 & 0 & 0 & 0 & 0 & 0 \\ 0 & 1 & 0 & 0 & 0 & 0 \\ 0 & 0 & 1 & 0 & 0 & 0 \\ 0 & 0 & 0 & 1 & 0 & 0 \end{bmatrix} \tag{4.37}$$

$$B = \begin{bmatrix} L_{\delta_{lat}} & L_{\delta_{lon}} \\ M_{\delta_{lat}} & M_{\delta_{lon}} \\ 0 & 0 \\ 0 & 0 \\ 0 & 0 \\ 0 & 0 \end{bmatrix}, u = \begin{bmatrix} \delta_{lat} \\ \delta_{lon} \end{bmatrix} \tag{4.38}$$

The roll and pitch attitudes (ϕ,θ) as well as the integral of the roll and pitch attitudes ($\int \phi, \int \theta$) are incorporated in the state vector. This facilitates feedback of the integral, proportional and derivative of the vehicle Euler attitude angles. In the design of the control system, it is of interest in choosing the control vector u which minimizes a given performance index. For quadratic optimal control, the following performance index is chosen,

$$J = \int_0^\infty L(x, u) dt \tag{4.39}$$

where $L(x, u)$ is a quadratic function of x and u,

$$L = x^T Q x + u^T R u \tag{4.40}$$

where Q is a positive-definite (or positive semi-definite) real symmetric matrix, R is a positive-definite real symmetric matrix. The matrices Q and R determine the relative importance of the state error (x) and the expenditure of the energy of the control signals (u). A linear control law is used to minimize the performance index J.

$$u = -Kx \tag{4.41}$$

$$K = R^{-1}B^T P \tag{4.42}$$

where K is the LQR gain and P is the unique, positive-semidefinite solution to the algebraic Riccati equation:

$$A^T P + PA - PBR^{-1}B^T P + Q = 0 \tag{4.43}$$

The R matrix was set to unity and the elements in the Q matrix were decided based on the Zeigler-Nichols approach. The LQR gains were computed using the Control System Toolbox in LabVIEW. The LQR controller was implemented as shown in Fig. 4.23 and was found to successfully mitigate pitch and roll disturbances as can be seen from Fig. 4.24.

4.7 Summary

In this chapter, the development of a reduced order linear attitude dynamics model of the vehicle was described. In order to determine the empirical model, system identification was performed in the time domain using equation error and output error based on maximum likelihood techniques. Two rotor systems were considered for this - the flybar and flybarless rotor. The extracted model was
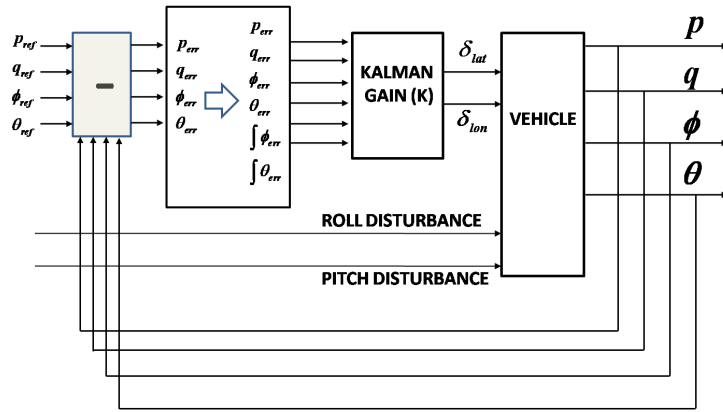
Figure 4.23: LQR feedback configuration
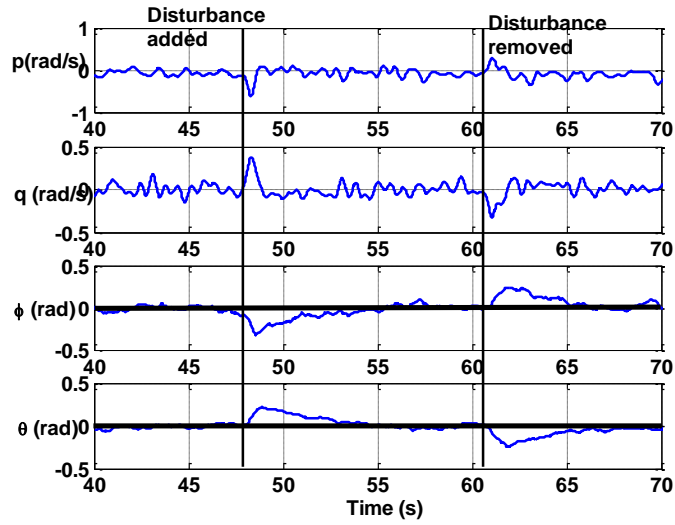
Figure 4.24: Attitude disturbance rejection on spherical gimbal set-up with LQR controller

found to satisfactorily represent the vehicle as a first order system with respect to attitude rates. Time domain verification indicated satisfactory comparison between model and truth. It was found that the flybarless rotor had up to 100% greater control power when compared to the flybar rotor. However, it was a marginally unstable system since the damping offered by the flybar was removed. As a result, flybarless rotor operation would require on-board electronic damping. Comparison in controllability metrics such as Frobenius norm derived from the controllability gramian indicates that the flybarless rotor is more controllable than the flybar rotor. The source of this increased controllability is the reduced damping and increased control moments.

Chapter 5

Performance and Control Moments of Shrouded Rotor in Edgewise Flow

5.1 Overview

The results described so far were for the shrouded rotor operating in quiescent flow conditions. In this chapter, the performance of the shrouded rotor when exposed to edgewise flow is described. The forces produced by a shrouded rotor operating in edgewise flow are measured and compared with those produced by an unshrouded rotor. Bench top experiments that include measurements of thrust, drag and pitching moment are made. An open jet wind tunnel was used as the source for edgewise flow. The shrouded and unshrouded rotor configurations were compared for their control moments and ability to overcome the destabilizing forces in these flows. A few strategies to minimize the adverse moments are discussed. Methods to improve the control moments of the rotor configurations through rotor planform design will be detailed. Finally, sufficient control margin to tolerate medium gusts of up to 2-3 m/s is ensured, that will aid in the gust disturbance rejection tests discussed in the next chapter.

5.2   Performance in Edgewise Flow

When a hovering shrouded rotor vehicle faces an edgewise flow, it experiences the following forces: (1) drag, in the direction of the flow and (2) pitching moment, that tends to pitch the vehicle away from the flow. This is schematically shown in Fig. 5.1. The side facing the flow is referred to as the windward side and the region of the shroud away from the flow is the leeward side. If the flow is along the negative X axis of the vehicle, the moment that pitches the vehicle away from the wind (i.e. about the positive Y axis) is positive. These forces can be many times in magnitude for a shrouded rotor when compared to an unshrouded rotor. They tend to destabilize the vehicle from hover and make it extremely difficult to achieve station keeping (hover in a constant position).
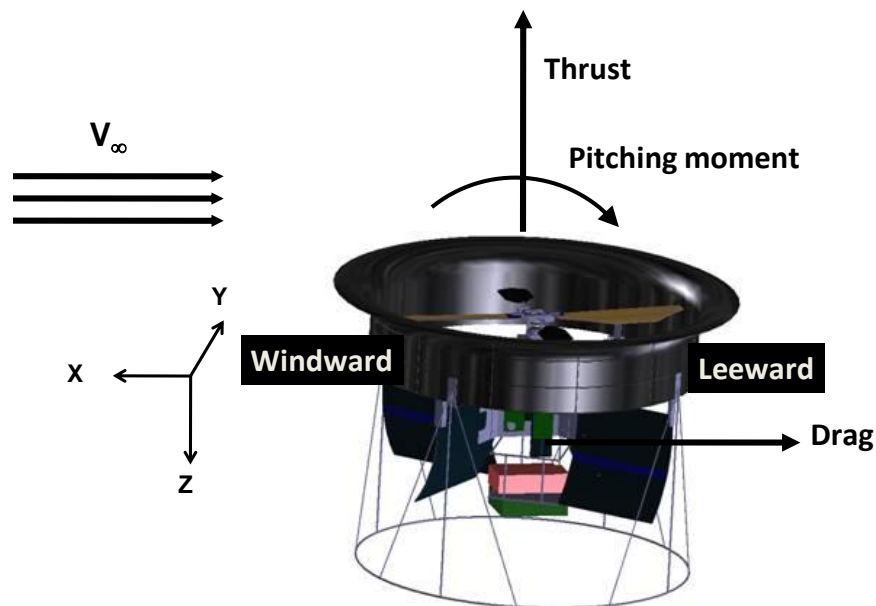
Figure 5.1: Forces acting on a hovering shrouded rotor in edgewise flow

5.2.1 Principle

The flow physics of a shrouded rotor in edgewise flow is complex. As the flow encounters the shroud inlet, due to the suction pressure generated by the rotor, it accelerates over the inlet through the diffuser. As it faces adverse pressure gradients during its transition through the diffuser, it causes flow separation near the inlet-diffuser junction, which can lead to energy losses. However, the pressure sustained over the inlet on the windward side is mostly suction. This suction pressure increases as the edgewise flow speed increases. Conversely on the leeward side, the suction pressure change may be negligible. As a result, there is an asymmetry in pressure distribution over the shroud. This asymmetry in pressure distribution results in a pitching moment about the vehicle C.G. The component of the suction pressure on the shroud inlet in the direction of the flow results in drag. This is schematically shown in Fig. 5.2

Hover   **Edgewise flow**
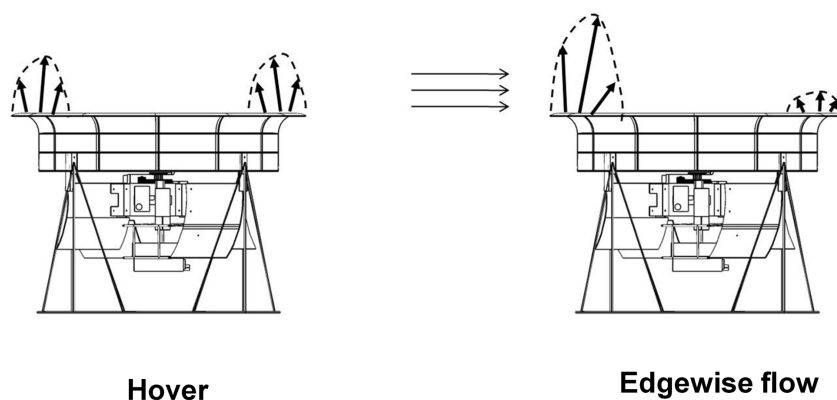
Figure 5.2: Asymmetric pressure distribution in a hovering shrouded rotor vehicle in edgewise flow

5.2.2 Shrouded rotor configurations

The baseline shroud discussed so far has a circular inlet profile. Now, a recent CFD study by Lakshminarayan and Baeder [124] showed that performance improvements can be made if an elliptic inlet is chosen for the design. Therefore, an elliptic inlet shroud was constructed using a two layer carbon fiber epoxy weave. The construction was similar to the process shown in Fig. 2.48. The schematics of the profiles along with the corresponding constructed shrouds are shown in Fig. 5.3. Here the ellipse has a major chord to minor chord ratio of 2:1. It must be noted that since the chord to diamter ratio of the shrouds were the same, the elliptic inlet shroud would have a greater mass owing to the excess area of the shroud inlet.
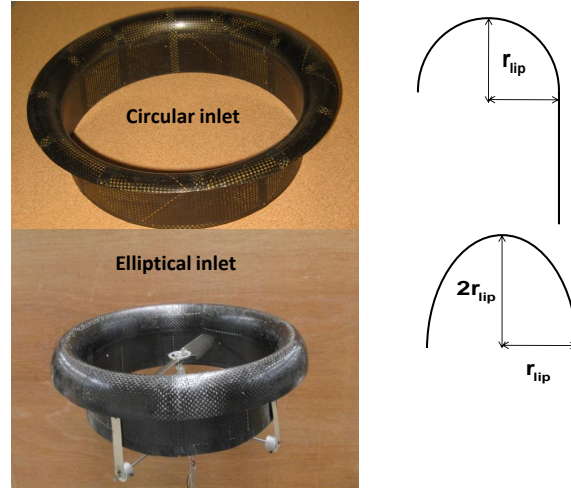
Figure 5.3: Circular and elliptical inlet shroud designs tested

The baseline rotor profile (a) from Fig. 2.55 was tested in the circular and elliptic inlet configuration using the micro rotor hover stand (Fig. 2.49) at different collectives. A tip clearance of about $0.02\,R$ was maintained. Figure 5.4 shows variation of thrust coefficient with blade root collective for the circular and elliptic inlet rotors respectively. It can be seen that at higher collectives,

the elliptic inlet shroud produces more thrust than the circular inlet shroud. Interestingly, the differences in power coefficient of both the configurations are small or within measurement error for the whole range of collectives. The best power-thrust curves for the circular inlet and elliptic inlet shrouded rotors are compared in Fig. 5.6. It was seen that a 10% improvement in power loading was achieved with the elliptic inlet shroud. It is of interest to measure how the forces produced in edgewise flow change for a more efficient shroud. To characterize these forces, the unshrouded rotor, circular inlet and elliptic inlet shrouded rotor were tested in edgewise flow conditions produced by an open jet wind tunnel.
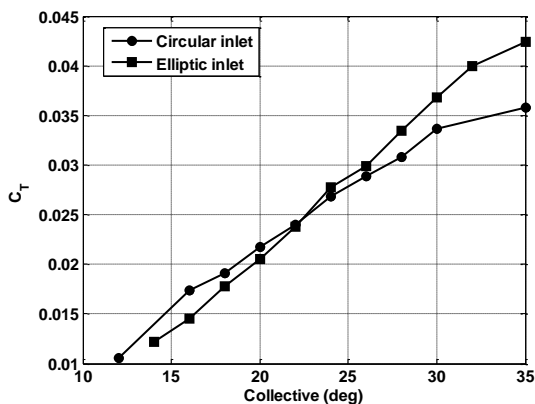
Figure 5.4: Variation of thrust coefficient with blade collective
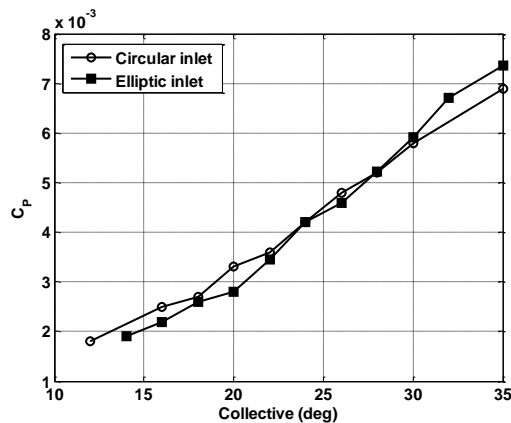
Figure 5.5: Variation of power coefficient with blade collective

5.2.3   Experiment set-up

It is of interest to measure the thrust, drag and pitching moment acting on the hovering shrouded vehicle when exposed to edgewise flow. For this, the vehicle was set-up in front of an open jet wind tunnel as shown in Fig. 5.7. The dimensions of the wind tunnel test section was 22" × 22" and a turbulence level
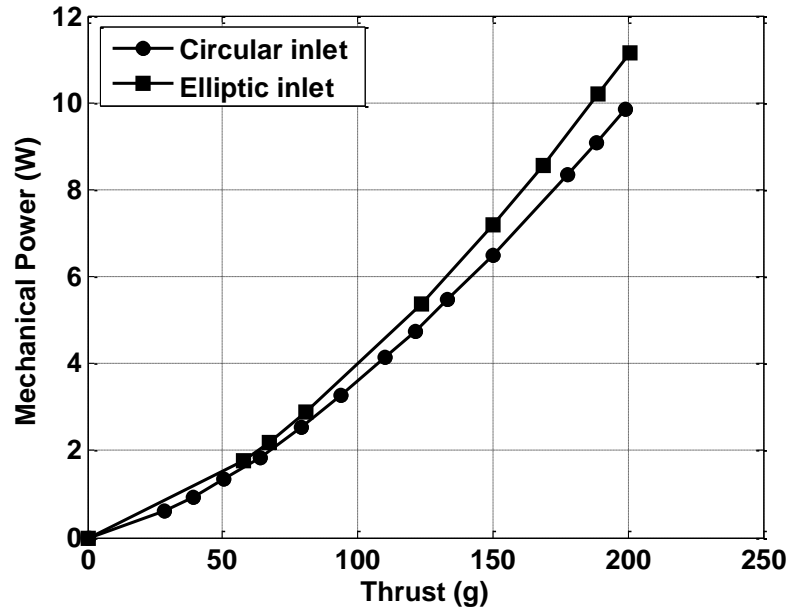
Figure 5.6: Performance comparison between circular inlet and elliptic inlet shroud

of 0.3%. A pressure transducer[1]with a full scale range of 50 Pa was used to measure the wind tunnel velocity. It had a resolution of about 0.025 Pa at an input voltage of 5 V. The pressure data was sampled at 1000 Hz with a 10-bit resolution using the NI-DAQ USB data acquisition system discussed in Chapter 2. Figure 5.8 shows filtered wind tunnel velocity data. As can be seen, a velocity measurement error of about 0.05 m/s was achieved. Additionally, the time to establish steady state velocity with the wind tunnel is satisfactorily low (about 2-3 s). In the vehicle set-up, the flow was along the negative X axis of the vehicle and the rotor was set to spin counterclockwise.

In order to measure vertical thrust, the micro rotor hover stand was mounted about 2" in front of the wind tunnel. An RPM sweep was conducted for each rotor configuration and wind tunnel speed. The rotor was fixed at a constant

---

[1]Setra Systems Model 267, www.setra.com
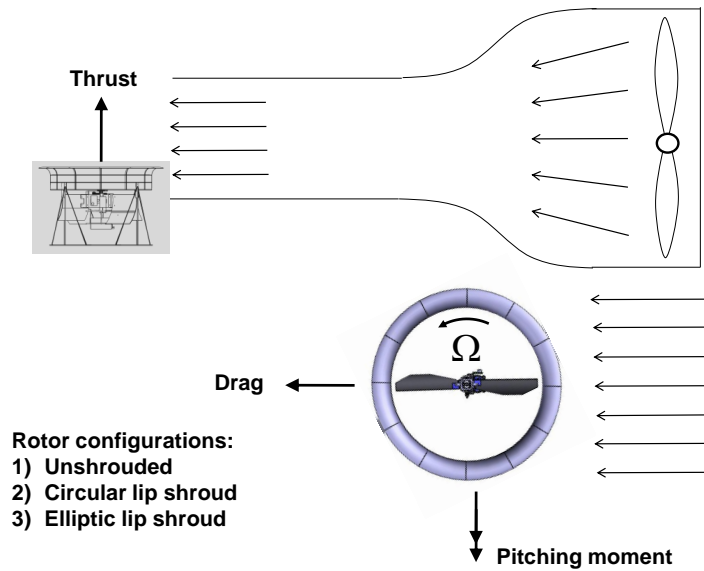
Figure 5.7: Rotor set-up in front of open jet wind tunnel
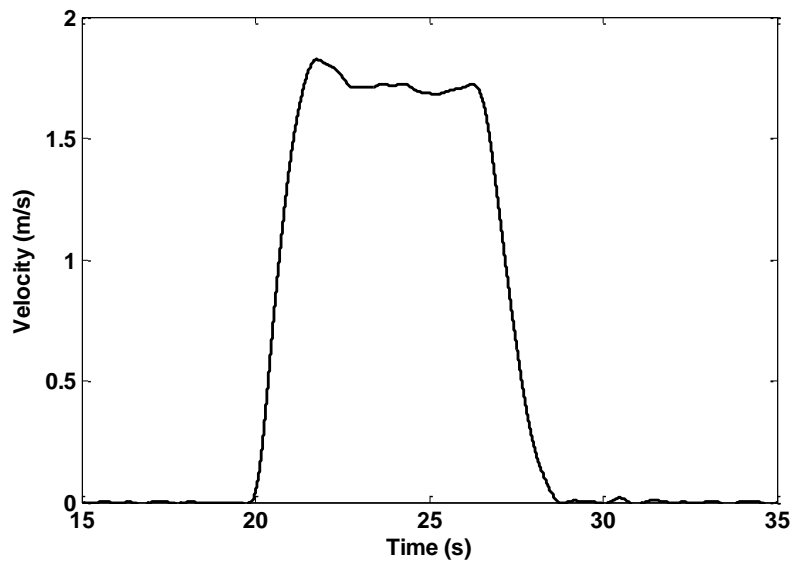
Figure 5.8: Sample velocity data from open jet wind tunnel

collective of 24 deg. The test procedure involved spinning the rotor up to a desired RPM followed by powering on the wind tunnel. This was done to prevent undesirable bending of the thrust stand before the rotor could reach the commanded RPM. Also, the rotor torque was not measured as a function of wind speed since the stand transferred bending moments to the torque load cell thereby affecting the torque readings. This could be circumvented by supporting the stand through radial bearings that would absorb the bending moments. However, since the thrust was of primary interest, this design modification was not made. For drag and pitching moment measurement, a separate stand was used that simultaneously measured both these forces. The rotor was mounted vertically at the end of a horizontal shaft with the other end of the shaft coupled with a torque load cell. The shaft was supported by two radial bearings that enabled complete transfer of loads to the torque load cell. It also ensured minimal friction due to bending moments. Therefore, the pitching moments produced by the vehicle were completely transferred to the load cell. The axis about which the pitching moment was measured was kept constant, about 100 mm below the rotor plane. The highest point of the circular lip shroud and elliptic lip shroud was about 120 mm and 140 mm above the moment axis respectively. For the drag, the rotor was mounted on a linear bearing mechanism that was connected to a thrust load cell, which enabled drag measurement in the direction of the flow without frictional losses. The pitching moment and drag measurement set-ups are shown in Figs. 5.9 and 5.10.

Figure 5.11 shows a representative measurement of the pitching moment. As explained in the previous chapter, vibration was due to rotor revolution which enabled application of a zero phase lag filter to remove the noise. A difference between the wind-off and rotor-on, and wind-on and rotor-on cases
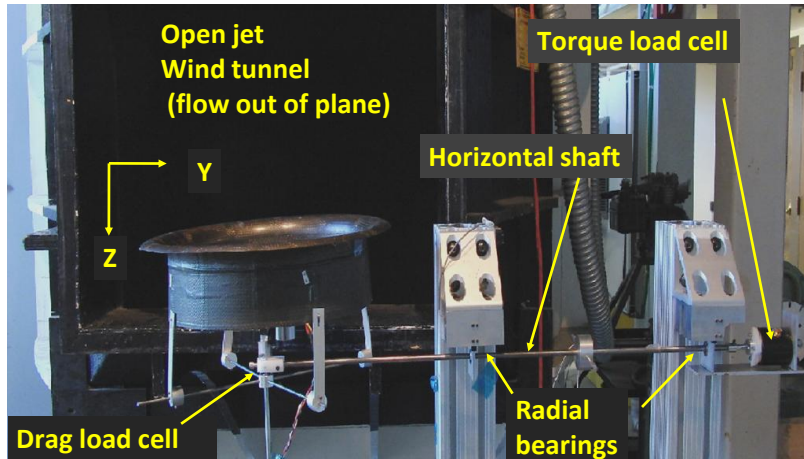
Figure 5.9: Pitching moment measurement set-up
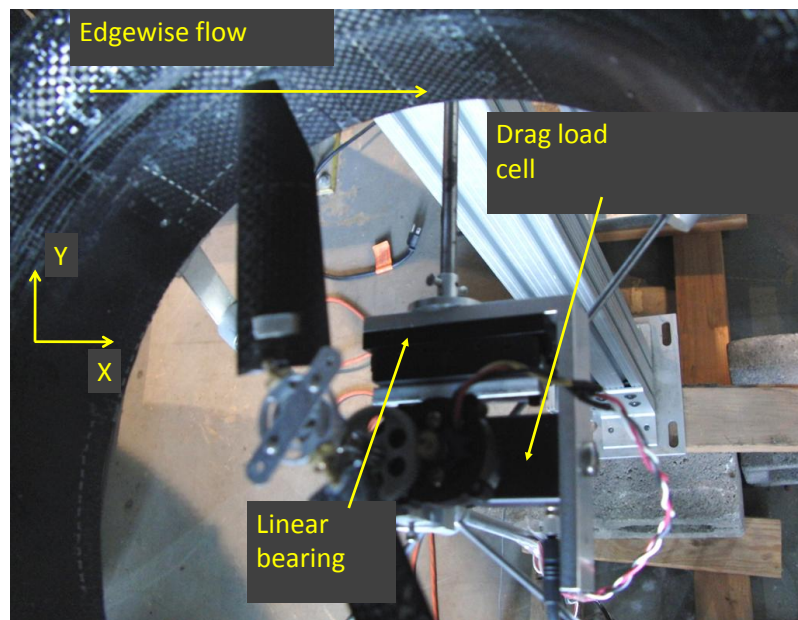
Figure 5.10: Drag measurement using linear bearing mechanism

gave an averaged pitching moment for that particular wind speed and rotor RPM. A similar procedure was adopted for the drag measurement. The average measurement errors for each were within 3-5 %. The magnitude of vibration recorded by the load sensors did not increase significantly when the wind was turned on. The recorded pitching moment and drag also included the effect of the bluff body in the flow. In order to remove this effect, tare measurements were conducted. Here, the drag and moment were measured with the set-up in the flow and the rotor unpowered. The tare values for the unshrouded rotor were about 1-3 grams and 10-15 gram-cm at 2 m/s for the drag and pitching moment respectively. This was considered to be within measurement error. The tare measurements for the two shrouded rotors were similar to each other and are shown in Figs. 5.12 and 5.13. These values were subtracted from the total measured values (Fig. 5.11). Therefore, the results presented will purely be the effect of a powered rotor in edgewise flow with bluff body drag and moment removed.
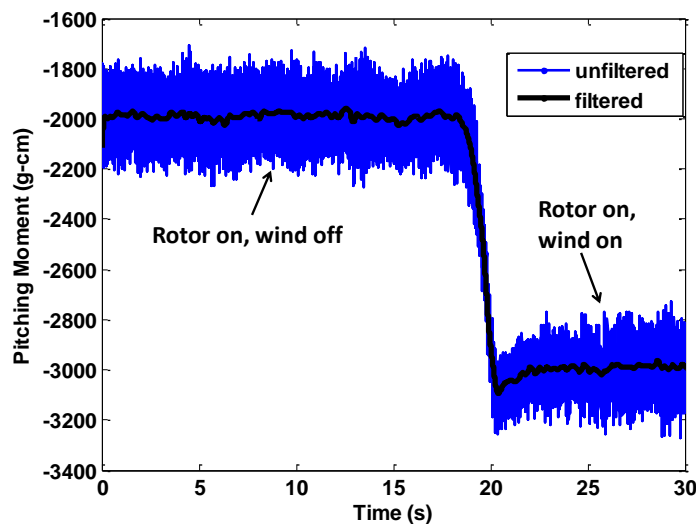
Figure 5.11: Filtered pitching moment data with wind switched on
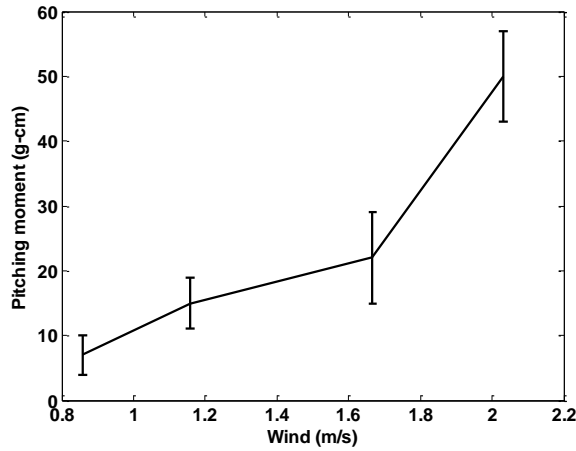
Figure 5.12: Tare measurements of pitching moment of unpowered shrouded rotor in flow
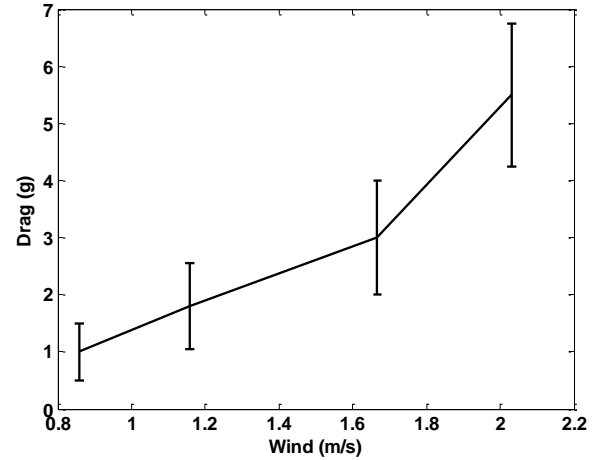
Figure 5.13: Tare measurements of drag of unpowered shrouded rotor in flow

5.2.4 Results and discussion

5.2.4.1 Thrust

When a hovering vehicle faces edgewise flow, it is of interest to see if the thrust that balances weight is sustained. Figures 5.14 and 5.15 show the thrust produced and power required by the unshrouded rotor as a function of RPM at different edgewise flow speeds. It can be clearly seen that there is negligible change in thrust produced and power required between quiescent and low edgewise flow speeds. Now, from Fig. 5.2, there is an asymmetric pressure distribution produced by a shrouded rotor in edgewise flow. Therefore the vertical thrust from the shrouded rotor may be different for both the conditions. However it can be seen from Figs. $5.16 - 5.19$ that neither the thrust nor power of the shrouded rotors change at these low edgewise flow speeds. The thrust and power measurement error at 3600 RPM was between 2-3%. This is interesting as it seems to suggest that the asymmetry in pressure distribution does not affect the net ver-

tical force produced. The other conclusion is that the operating RPM need not be changed in quiescent or low edgewise flow speed to produce trimmed thrust.
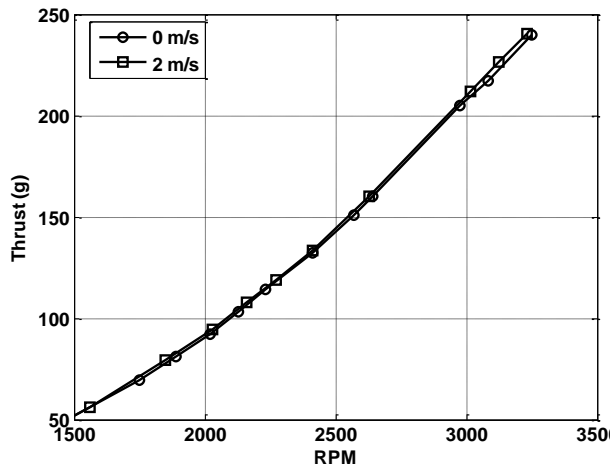
Figure 5.14: Thrust produced by un-shrouded rotor in edgewise flow
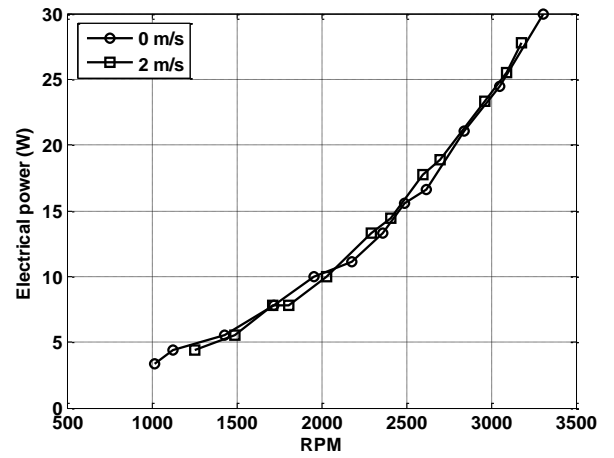
Figure 5.15: Electrical power input for unshrouded rotor in edgewise flow
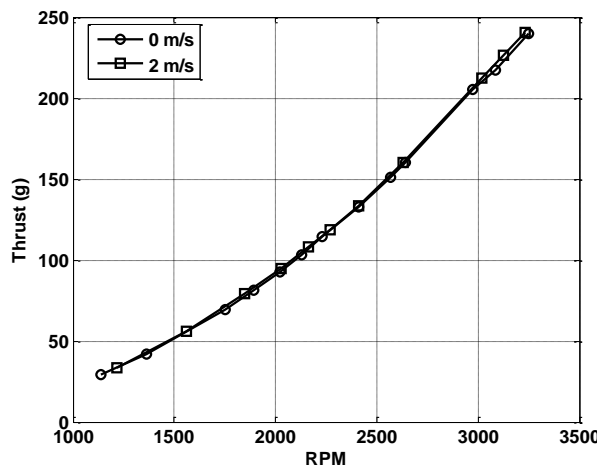
Figure 5.16: Thrust produced by circular inlet rotor in edgewise flow
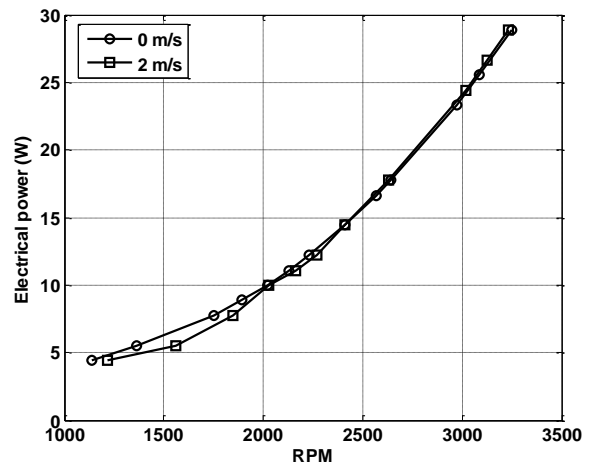
Figure 5.17: Electrical power input for circular inlet shrouded rotor in edgewise flow
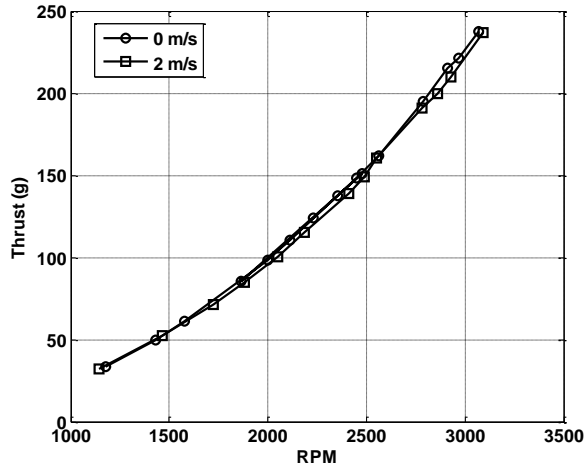
Figure 5.18: Thrust produced by elliptical inlet shrouded rotor in edgewise flow
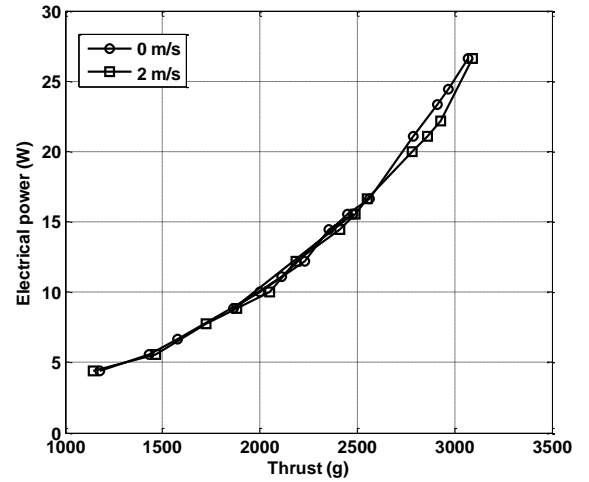
Figure 5.19: Electrical power input for elliptical inlet shrouded rotor in edgewise flow

5.2.4.2 Drag

As mentioned earlier, the drag produced by the rotors in edgewise flow was measured with the effect of bluff body drag removed. The measurement error was about 4-5%. The bluff body drag values for the shrouded rotors were about 10% of the total value recorded at 1800 RPM at different edgewise flow speeds. Figure 5.20 shows the variation of drag with rotor RPM at different edgewise flow speeds. It can be seen that the drag increased with RPM as well as flow speed. It was seen that the variation of drag with RPM was approximated by a quadratic trend. The resultant force (including vertical force and drag) produced by the rotor in edgewise flow increased as expected. Now, when the rotor was enclosed in the shroud, the effect of edgewise flow speed on the drag produced was more pronounced for the circular inlet shrouded rotor. The variation as a function of RPM was not seen to be significant for the circular inlet shrouded rotor and seemed to saturate at higher RPMs (Fig. 5.21). The effect of RPM on drag was

greater for the elliptic inlet shrouded rotor and produced up to 70% higher drag than the circular inlet shroud case at 2 m/s of edgewise flow speed (Fig. 5.22). A possible explanation for this is shown in Fig. 5.23. The component of the projected inlet area in the direction of the flow on the windward side is greater for the elliptic inlet shroud. As a result, the resolved forces due to the pressure distribution is higher for the elliptic inlet, thus producing higher drag. Figure 5.24 shows the drag produced by the three rotors as a function of edgewise flow speed at 3300 RPM. The variation of drag with speed was seen to be mostly linear. It was interesting to note that the slope of the drag-wind speed curve was about 100% greater for the shrouded rotors. The previous observation of drag variation with rotor RPM is better shown in Fig. 5.25. Here the drag is plotted as a function of rotor thrust for the three rotors in 2 m/s of edgewise flow. It can be seen that the magnitude of drag saturates as the rotor thrust increases. This is an interesting conclusion from an MAV operation point of view.
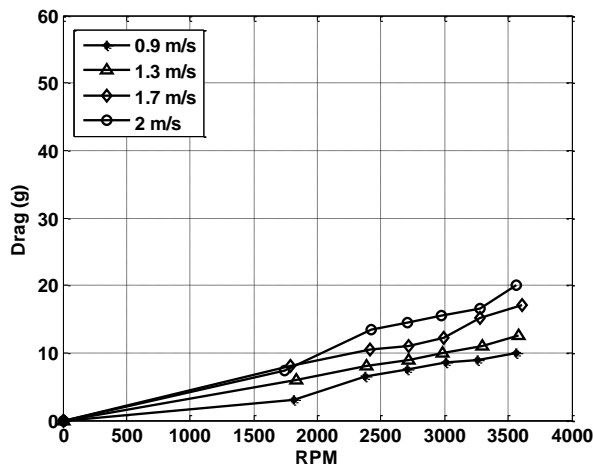
Figure 5.20: Drag versus RPM for un-shrouded rotor
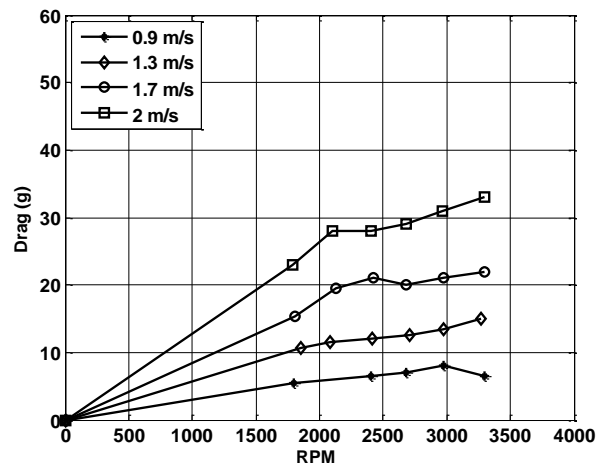
Figure 5.21: Drag versus RPM for circular inlet shrouded rotor
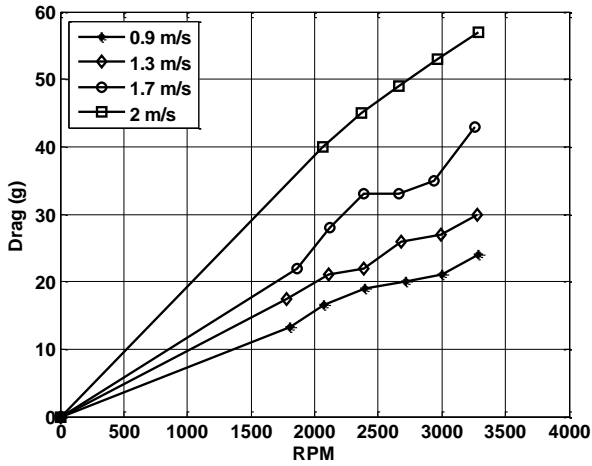
Figure 5.22: Drag versus RPM for elliptical inlet rotor
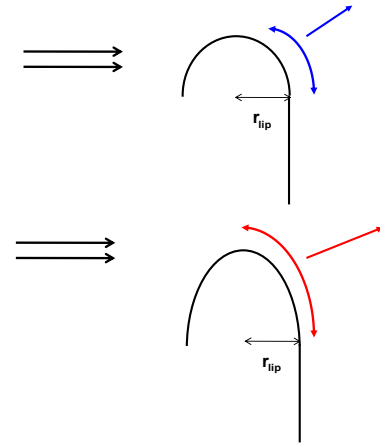
Figure 5.23: Projected area of shroud inlet in the direction of edgewise flow
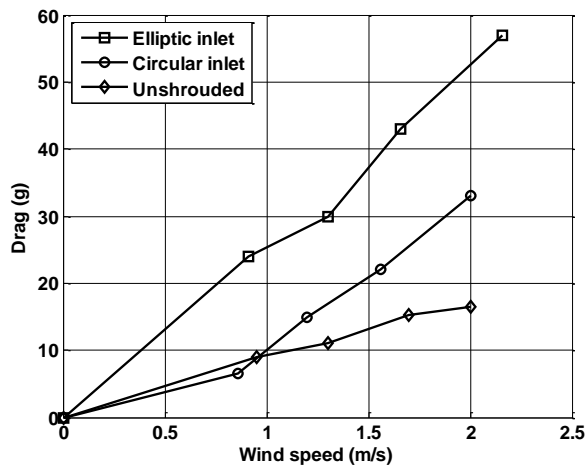
Figure 5.24: Variation of drag versus edgewise flow speed at 3300 RPM
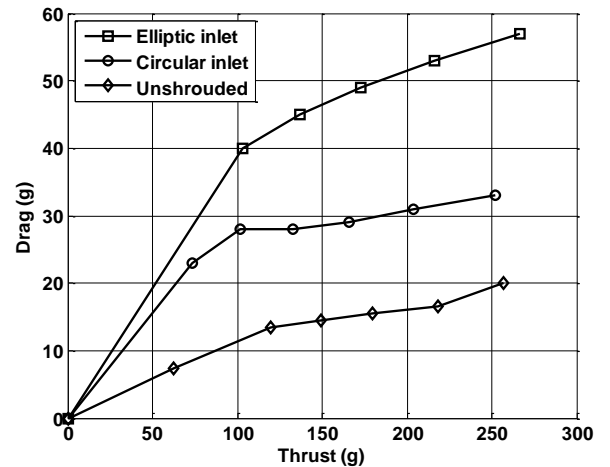
Figure 5.25: Variation of drag versus rotor thrust at 2 m/s of edgewise flow speed

5.2.4.3 Pitching moment

Figures 5.26− 5.28 show the pitching moments produced by the rotors in edge-wise flow with the effect of moment due to bluff body drag removed. The measurement error again was about 4-5%. The tare moment values for the shrodued rotors were about 8% of the total value recorded at 1800 RPM at different edgewise flow speeds. Each data point represents the difference in load cell measurements between the wind-on and off cases. It can be seen that all the configurations produced a positive pitching moment about the Y axis (nose-up) with edgewise flow speed. The magnitude of these pitching moments increased as the rotor RPM increased with the variation being approximately linear. As in the case for drag, the pitching moment from the unshrouded rotor was not as sensitive to edgewise flow speed as for the shrouded rotors. This effect can be clearly seen in Fig. 5.29 where the moment-speed slope is almost twice for the shrouded rotors. The circular and elliptical inlet shrouded rotors produced up to 3-4 times higher pitching moments than the unshrouded rotor, respectively. Analogous to the drag measurements, the pitching moments from the shrouded rotors also seemed to saturate as the rotor thrust was increased. This is shown in Fig. 5.30 at 2 m/s of edgewise speed. A possible explanation for this is that as the rotor thrust is increased, the horizontal flow is more effectively channeled through the shroud diffuser. This could explain the increased drag and pitching moment as the thrust is increased from low values of thrust. However, at higher values of thrust the momentum change of the edgewise flow through the diffuser does not differ significantly with rotor thrust. As a result, the drag and pitching moments may tend to saturate at high values of thrust. This has important implications for the control margin of a shrouded rotor MAV, i.e., the amount

of excess control power available to alleviate a given pitching moment. This will
be discussed in further detail later.
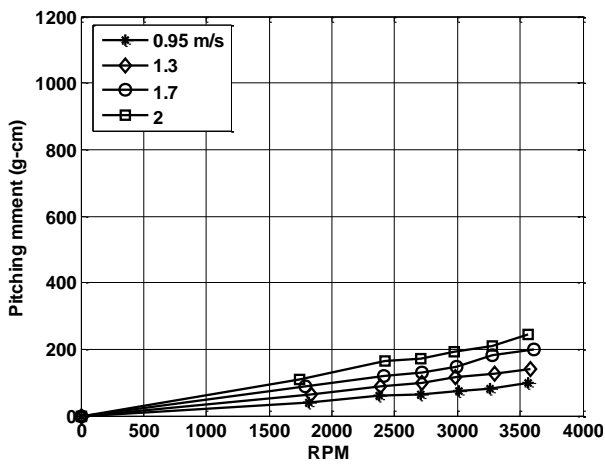
Figure 5.26: Nose-up pitching moment versus RPM for unshrouded rotor
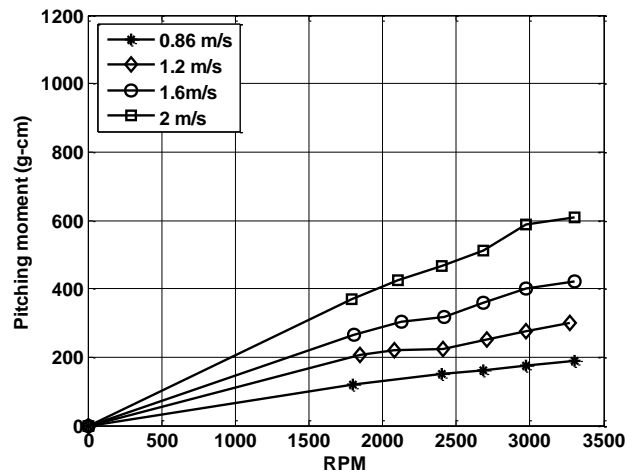
Figure 5.27: Nose-up pitching moment versus RPM for circular inlet shrouded rotor
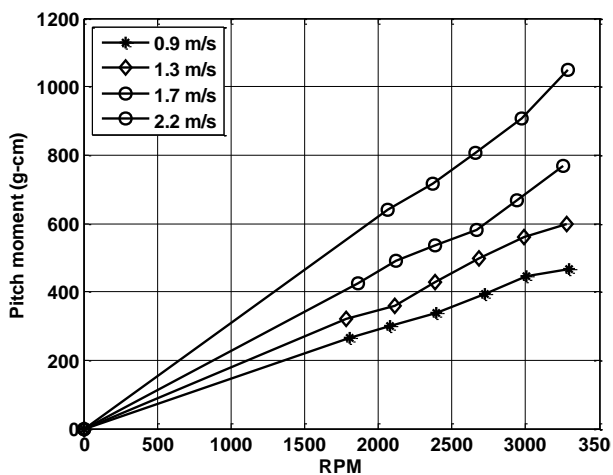
Figure 5.28: Nose-up pitching moment versus RPM for elliptical inlet rotor
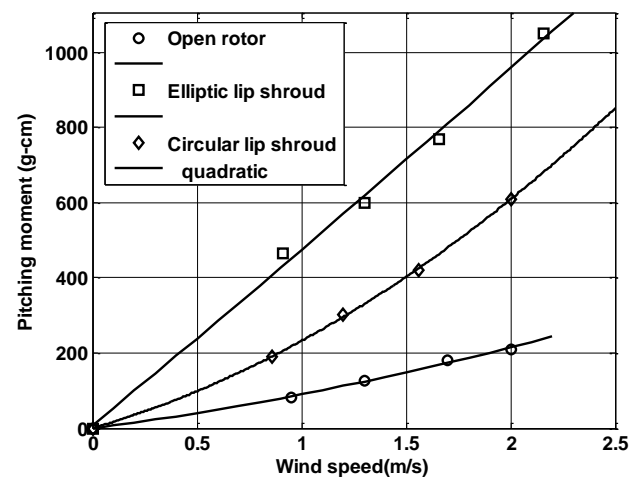
Figure 5.29: Variation of pitching moment versus edgewise flow speed at 3300 RPM
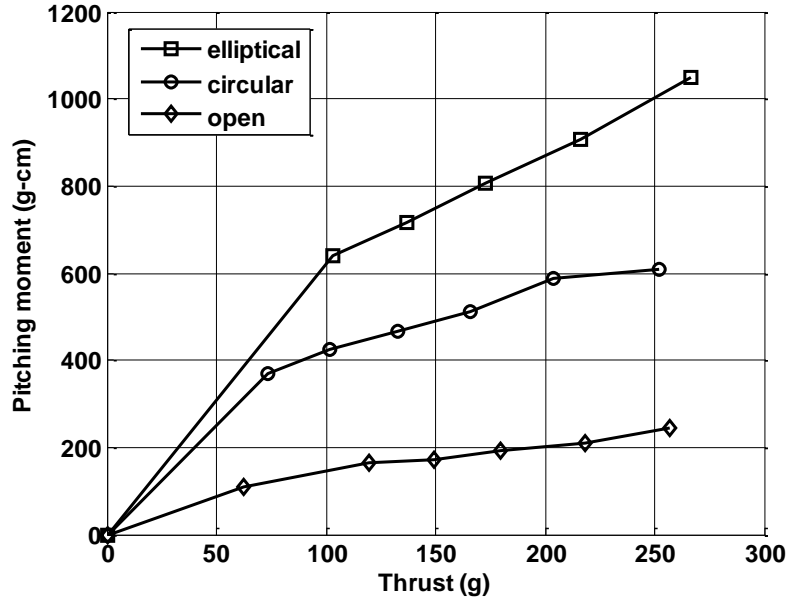
Figure 5.30: Variation of pitching moment versus rotor thrust at 2 m/s of edgewise flow speed

5.2.5   Shroud design modifications

From the results discussed in the last section, it can be seen that the shrouded rotors produce adverse pitching moments in edgewise flow many times in magnitude compared to the unshrouded rotor. It had been discussed that the main reason for this was the asymmetric pressure distribution on the windward and leeward sides of the shroud. One way of reducing this would be to remove any shroud surface on the windward and leeward side that sustain the asymmetric suction pressures. This is shown schematically in Fig. 5.31. This implies that we would like to selectively reduce the thrust generated by the shroud as it encounters edgewise flow and restore the original shroud geometry in quiescent flow. One way of reducing shroud thrust contribution is to cut open flaps or vents into the shroud surface, that are deployed as and when edgewise flow is encountered. The shroud flap design (Fig. 5.32) consisted of four flaps that were

cut out of a section of a shroud. Each flap was about 75 mm wide and used the curved section of the shroud. The flaps were spaced at 90 degree intervals and would actuate downwards to effectively remove a shroud section. The shroud vent design (Fig. 5.33) uses four rectangular vents cut ino the surface of the shroud. They were approximately 15 mm × 35 mm placed at the approximate suction peak location of the shroud surface and were spaced at 90 degree intervals. These vents would open during directional flight and gust situations to reduce suction pressure asymmetry on the windward and leeward side and thus minimize pitching moment.
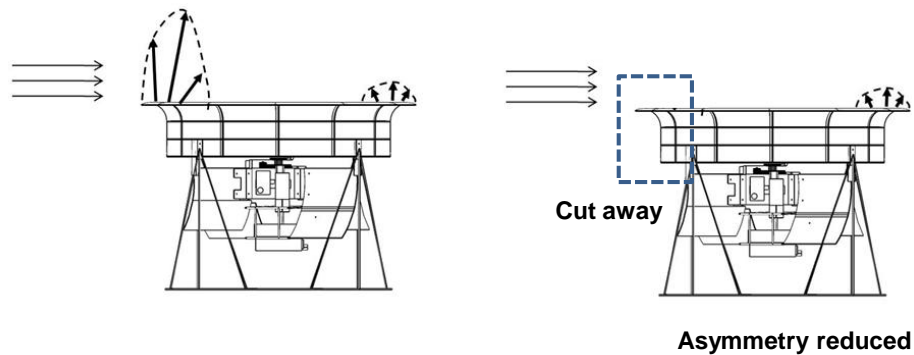
Figure 5.31: Reduction in asymmetric pressure distribution through a cut in shroud

A suitable method of analyzing the effectiveness of the flaps and vents was to measure how much the thrust produced by the shroud reduced upon their deployment in quiescent flow conditions. This was done using the shroud thrust stand shown earlier in Fig. 2.52. The ratio of the shroud thrust to total thrust was measured as a function of total thrust for each of the deployed configurations: (a) 1 flap, (b) 2 opposite flaps, (c) all flaps, (d) 1 vent, (e) 2 opposite vents and

Figure 5.32: Shroud flap design   Figure 5.33: Shroud vent design

(f) all vents. Figure 5.34 shows the effect of flap deployment on the shroud thrust ratio. It can be seen that as expected, the effectiveness of the flaps increased with the number of deployed flaps. The shroud thrust dropped by up to 30% with all the four flaps deployed. However, from Fig. 5.35, it can be seen that the vents did not reduce shroud thrust to the same extent (up to 20% with all vents deployed). This was because the area of the shroud inlet removed by the vents was lesser than the flaps. Figure 5.36 shows the pitching moment generated in hover condition for the one flap, two opposite flap and no flap deployed cases. It can be clearly seen that as expected, deployment of one flap created the maximum pitching moment since the asymmetry in pressure distribution is the greatest. Therefore, in order to reduce pressure distribution asymmetry in edgewise flow, deployment of one flap would be the most effective.

Expanding the cut section area of the shroud by either methods resulted in increased shroud vibrations due to a loss in structural stiffness of the shroud. Additionally, the flaps or vents would have to be deployed by actuators (Fig. 5.37) which would increase the empty weight fraction of the vehicle. This along

with the complex control strategy that would have to be employed made the flap or the vent design modification very unsuitable for implementation in the MAV shroud design.
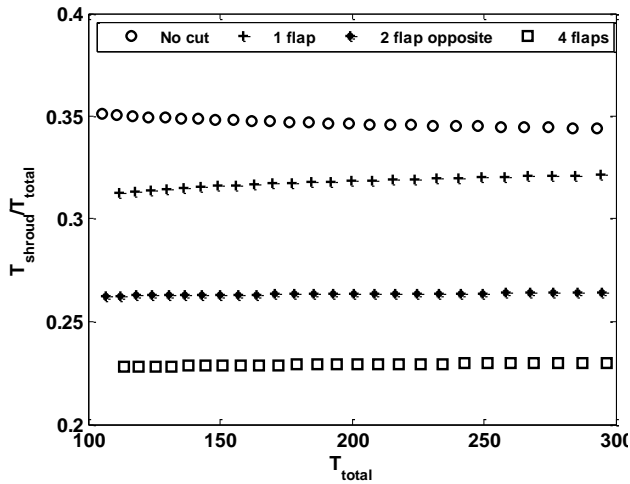
Figure 5.34: Shroud thrust ratio for different flap configurations. Reduced thrust ratio implies more effective alleviation of pitching moment
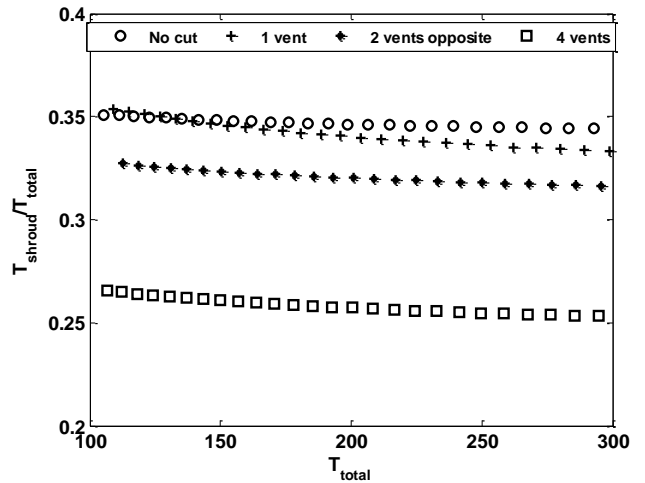
Figure 5.35: Shroud thrust ratio for different vent configurations
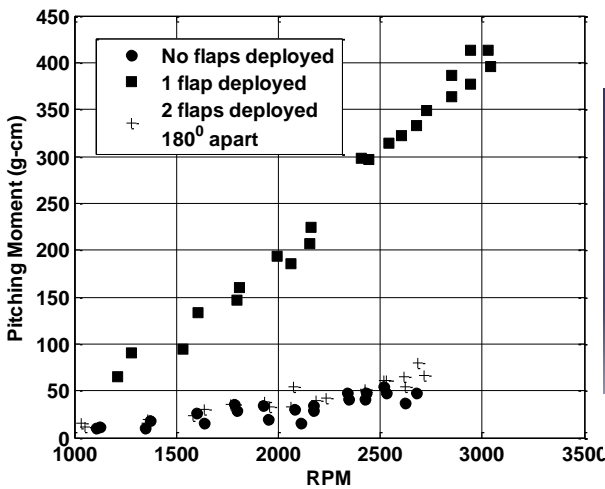
Figure 5.36: Pitching moment generated by different flap deployment configurations in quiescent hover conditions
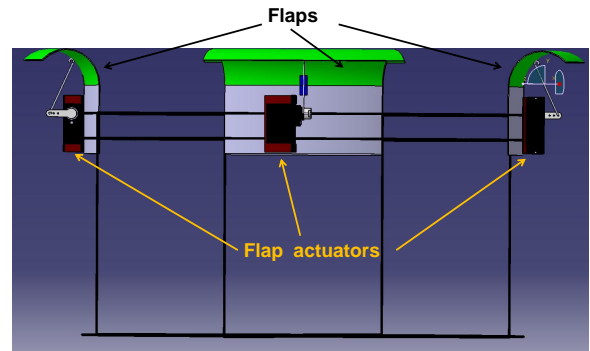
Figure 5.37: Actuators to deploy flaps or vents. Increase empty weight fraction of vehicle (not desirable)

5.3   Control Moment

The difficulties in implementing active flow control and shroud design modifications to aid in pitching moment alleviation in cross flow were discussed in the previous section. Therefore, to simplify control methodology, the control moments generated by cyclic input to the rotor itself are used to counter the adverse forces. In this section, the magnitude of control moments generated by the different rotor configurations (unshrouded, circular lip and elliptic lip shrouded rotor) are compared. Strategies to enhance control moment are identified. Finally, the control margin offered by the shrouded rotor which limits the gust tolerance limit is discussed.

5.3.1   Control moment comparison

5.3.1.1   Experiment set-up

The rotors were mounted on the stand shown in Fig. 4.4 for control moment measurements in hover and edgewise flow.

Hover: For each case, maximum positive and negative pitch control moments were measured by actuating maximum longitudinal cyclic of $\pm 10^0$. The sum of the positive and negative pitch control moment magnitudes were compared to remove any ambiguity in neutral swashplate setting. The baseline rotor from Fig. 2.55 was used. For each case, the rotor was set at a given collective and an RPM sweep was performed. At each RPM, positive and negative cyclic input was given and the total control moment was measured.

Edgewise flow: As was discussed previously, a nose-up pitching moment is generated when the rotors operate in edgewise flow. To alleviate this pitching moment, a nose-down control moment is required. It is possible that the magni-

tude of the nose down control moments may differ between quiescent operating conditions and in edgewise flow conditions. In order to determine this, the rotor set-up was mounted in front of an open jet wind tunnel that was used to generate edgewise flow of magnitude of up to 2 m/s. The control moments in the nose-up and nose-down direction were measured and compared to those generated in quiescent conditions.

5.3.1.2 Results and Discussion

Hover: The variation of control moment with RPM for different blade collectives and rotor configurations is shown in Figs. 5.38−5.40. The magnitude of control moment varied quadratically with RPM. Therefore, for maximum control moments, the rotor operating RPM should be increased. This creates a trade-off with rotor performance which will be discussed later. It can also be clearly seen that for each of the rotors, there is a range of collectives beyond which the maximum control moment at a given RPM drops. For the unshrouded rotor, the peak control moment was achieved at a collective of about $18^0 − 20^0$. At collectives greater than 26^0, the drop in control moment was at least 25%. For the shrouded rotors, the peak control moment was achieved at collectves between $18^0 − 22^0$. At higher collectives, a 12-14% reduction in control moment was observed. To explain this, consider a cyclic input given to a two bladed hingeless rotor, shown in Fig. 5.41. The lift on each blade can be written as,

$$L_{1,2} = L \pm \Delta L = \frac{1}{2}\rho \int_0^R (\Omega r)^2 cC_{l\alpha}(\theta_0 \pm \Delta\theta - \phi)dr \qquad (5.1)$$

where $C_{l\alpha}$ is the lift curve slope of a blade airfoil section. It is assumed that for the sake of simplicity that the angle of attack of all blade sections change

uniformly by $\pm\Delta\theta$, where $\Delta\theta$ is the magnitude of cyclic pitch variation allowed by the swashplate. For first order apporiximation, from Eq. (5.1), the hub moment (M) can be written as,

$$M \propto \Delta L$$
$$\propto \rho \int_0^R (\Omega r)^2 c C_{l\alpha} \Delta\theta dr \qquad (5.2)$$

Now, Eq. (5.2) assumes that the lift curve slope is constant. However, if the blade enters stall, the hub moments transferred will be reduced. This can happen when the blade is initially set at a high collective setting (θ_0) and receives an additional $\Delta\theta$ of cyclic input. Figure 5.42 shows the variation of thrust coefficient with blade collective for the three rotor configurations. This provides a good indication of the region where the blades enter stall. It can be seen that for the unshrouded rotor, the $C_T - \theta$ curve became non-linear at collectives beyond about 22^0, whereas for the shrouded rotors, linearity was achieved till collectives of about 30^0. As a result, the shrouded rotors were able to tolerate a wider range of blade collective settings without a noticeable deterioraion in control moments (Figs. $5.38-5.40$).

A very interesting observation is the comparison of the maximum control moments offered by the three rotor configurations. This is shown in Fig. 5.43. It can be seen that the circular lip and the elliptic lip shrouded rotors produced up to 80% and 100% higher control moments than the unshrouded rotor, respectively.

Inputs from CFD: Two interesting observations from a recent CFD study [124] may offer further insights into this phenomenon: (1) at the instant of blade passage, the suction force developed on the shroud inlet reaches a peak that is about

400% greater than the location that is 90^0 in azimuth ahead of the blade. This is shown in Fig. 5.44, and (2) the contribution to total thrust from the shroud increases (almost linearly) as the blade collective is increased. This is shown in Fig. 5.45. Now, Fig. 5.46 shows a schematic of a cyclic input given to a two bladed shrouded hingeless rotor. Taking points (1) and (2) into consideration, we can see that the region of the shroud where positive cyclic is given, the pressure distribution on the shroud surface is higher than the region where negative cyclic is provided. As a result, along with the rotor control moments, the shroud offers additional pitching moment from the difference in suction pressure distributions. Therefore we can see that cyclic input can be a very useful scheme incorporated in a shrouded rotor for control purposes.
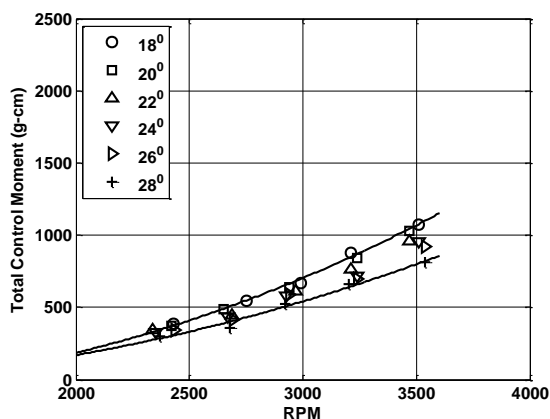
Figure 5.38: Variation of control moment versus RPM at different blade collectives for the unshrouded rotor
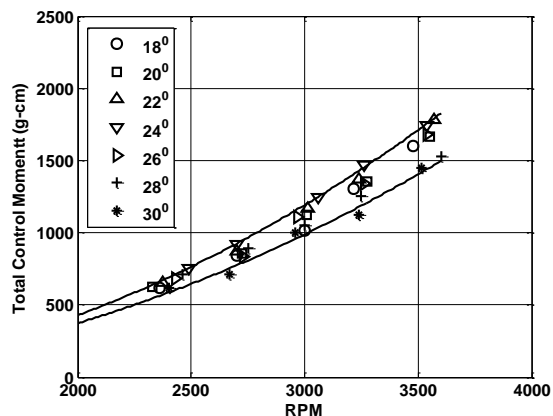
Figure 5.39: Variation of control moment versus RPM at different blade collectives for the circular lip shrouded rotor

Edgewise flow: From the hover results, an asymmetric pressure distribution on the shroud surface due to a cyclic input to the rotor augments the control moment of the shrouded rotor. In edgewise flow however, this asymmetry might be reduced and this may deteriorate the control moment of the rotor (Fig. 5.47).
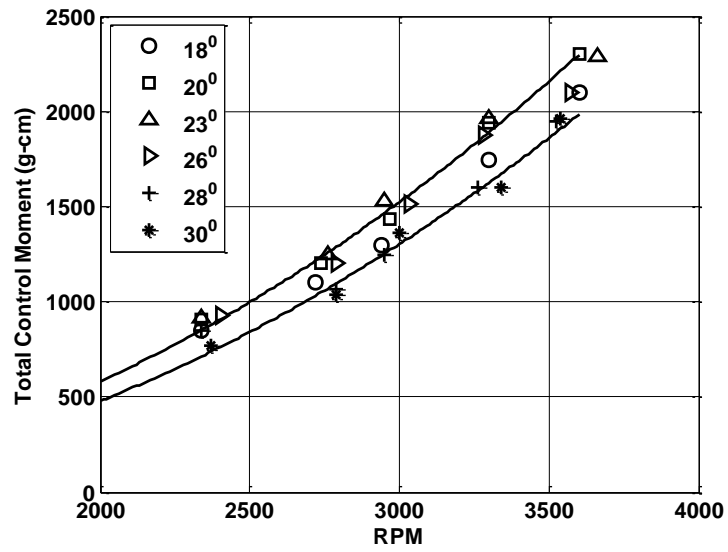
Figure 5.40: Variation of control moment versus RPM at different blade collectives for the elliptic lip shrouded rotor
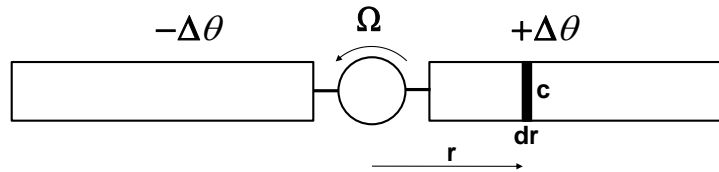
Figure 5.41: Cyclic input provided to a hingeless rotor
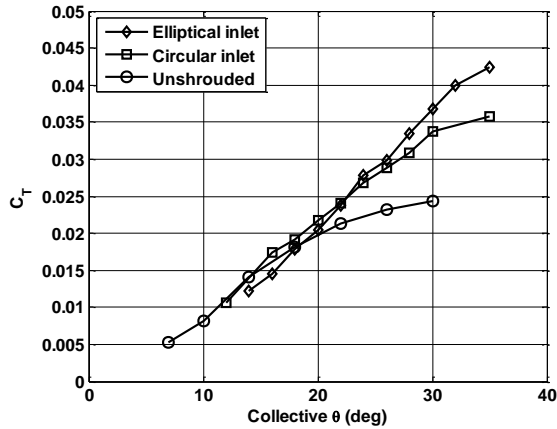
Figure 5.42: Variation of thrust coefficient with blade collective
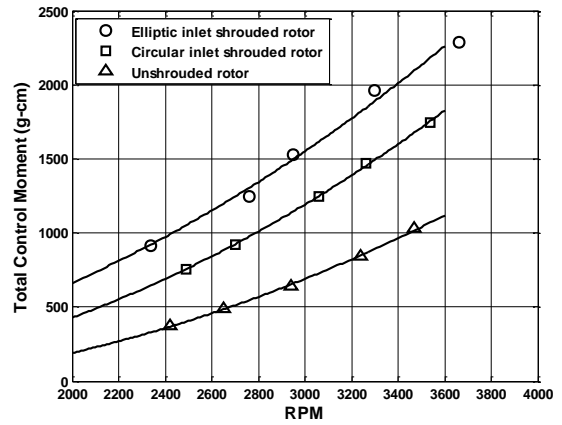
Figure 5.43: Maximum control moment comparison
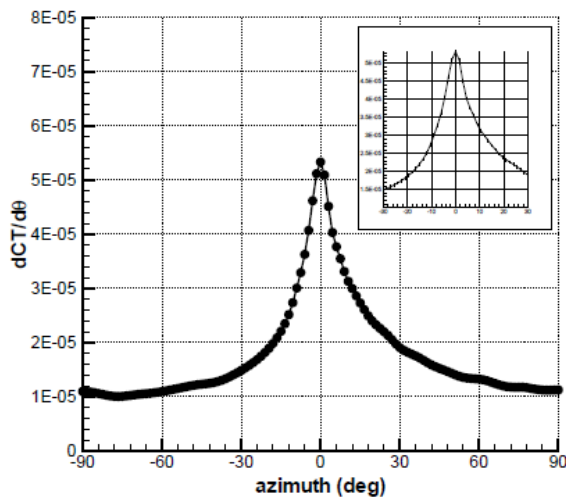
Figure 5.44: Thrust distribution on shroud surface as a function of blade azimuth (CFD [124])
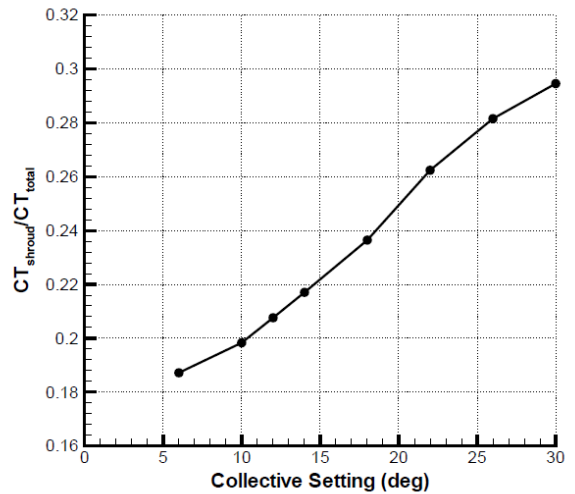
Figure 5.45: Effect of blade collective on shroud thrust ratio (CFD [124])
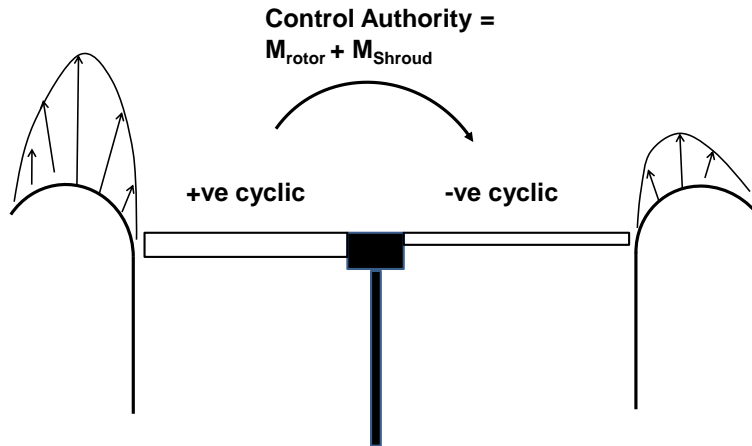
Figure 5.46: Control moment augmentation from shroud

Since alleviating the adverse pitching moment is of interest, the control moment (into the wind) generated for the rotor configurations in edgewise flow is compared with those generated in quiescent flow conditions. Figure 5.48 shows a representative variation of control moment with RPM at different flow speeds for the circular inlet shrouded rotor. It can be seen that there is a decrease in control moment as flow speed increases. Table 5.1 summarizes the change in control moment at an edgewise flow speed of about 2.2 m/s and a rotor RPM of about 3500 for the different rotor configurations. Here $M2$ is the pitching moment into the wind that counters the adverse pitching moment due to edgewise flow. The total control moment is given by $M1 + M2$. It can be seen that for the unshrouded rotor, there was no significant change in control moment with edgewise flow for the different collective settings. With the circular lip shrouded however, there was a drop in $M2$ of up to 20% at higher collectives. This can be minimized to about 8% at lower collectives (20^0 and below). For the elliptic lip shroud, there was a small decrease in control moment at low collective and

no change at high collective. Therefore, by selecting an optimum operating collective, the shrouded rotor can produce useful control moments in quiescent as well as in edgewise flow.
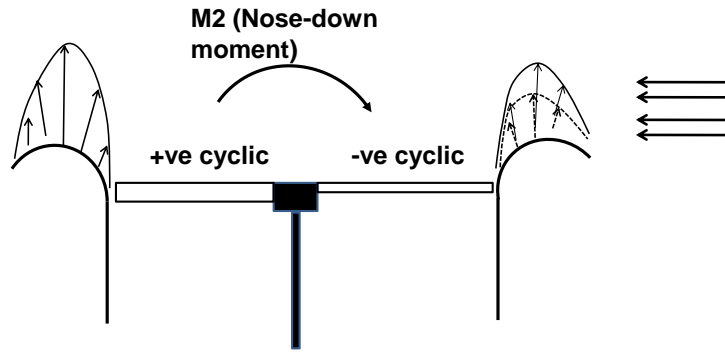
Figure 5.47: Control moments in edgewise flow
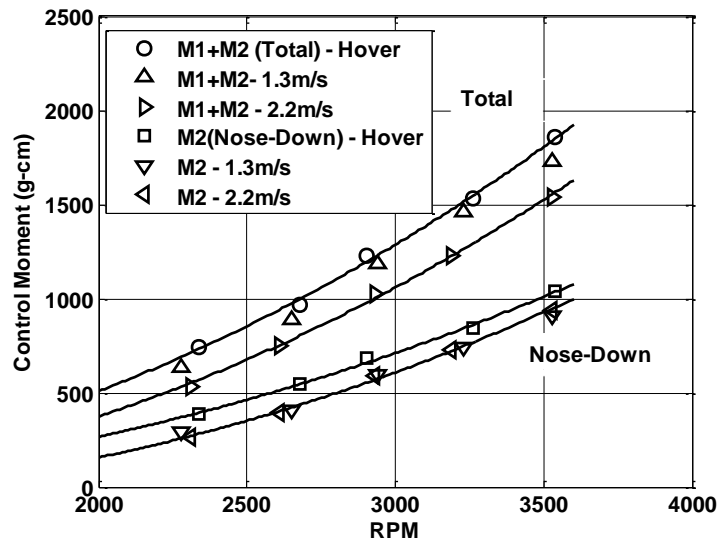
Figure 5.48: Effect of edgewise flow on control moments generated by the circular inlet shrouded rotor (M1 and M2 are the nose-up and nose-down moments respectively

Table 5.1: Change in control moment at 2.2 m/s wind speed and 3500 RPM compared to 0 m/s condition

Collective	Unshrouded		Circular lip		Elliptic lip	
	$\Delta(M1 + M2)$	$\Delta(M2)$	$\Delta(M1 + M2)$	$\Delta(M2)$	$\Delta(M1 + M2)$	$\Delta(M2)$
20 deg	-2%	0	-18%	-8%	-17%	-5%
22 deg	-4%	0	-13%	-8%	-11%	0
24 deg	-7%	+8%	-16%	-19%	-5%	+3%
26 deg	-	-	-19%	-19%	0	+3%
28 deg	-	-	-17%	-14%	0%	+15%

5.3.2 Increasing control moment

It is desired to improve the gust tolerance of the MAV. This can be achieved by, (1) reduce pitching moment on vehicle due to edgewise flow, and (2) increase control moments generated by the rotor. Since the pitching moment generated by the elliptic inlet shrouded rotor outweighs the benefit in hover performance, the circular inlet shrouded rotor is chosen for the studies described in the remaining sections. This section identifies two ways to increase the control moment of the shrouded rotor.

5.3.2.1 Cyclic pitch variation

It can be clearly seen from Eqs. (5.1) and (5.2) that the control moment can be improved by, (1) increasing the magnitude of cyclic input, and (2) increasing the differential lift on the two blades for a given cyclic input. To achieve the former, the swashplate and pitch link arms were increased. Figures 5.49 and 5.50 show the original swashplate design with $\pm 10^0$ cyclic input and the modified design with $\pm 15^0$ cyclic input. Figure 5.51 compares the control moments generated by the circular inlet shrouded rotor with maximum cyclic input using the two swashplate designs. The blade was set at a collective of 20^0. It can be clearly seen

that a 50% increase in cyclic pitch travel resulted in almost a 50% improvement in control moment. The cyclic travel however cannot be increased indefinitely due to stall limits as was discussed in the previous section.

Figure 5.49: Swashplate with cyclic travel of $\pm 10^0$

Figure 5.50: Swashplate with cyclic travel of $\pm 15^0$
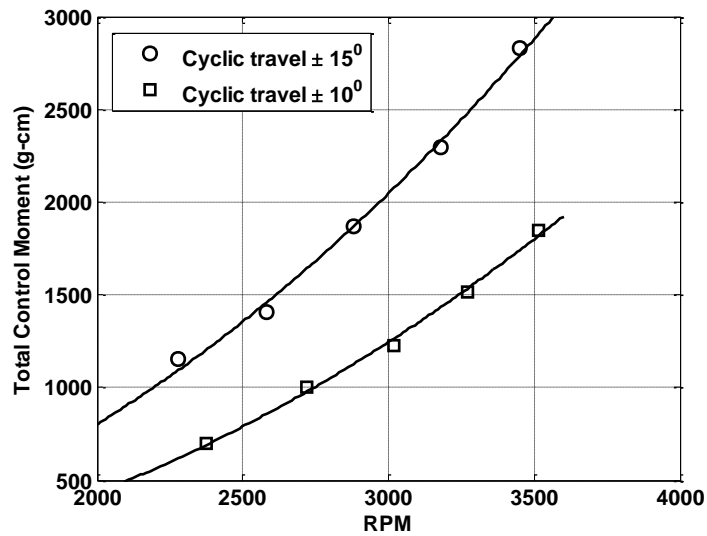
Figure 5.51: Effect of cyclic pitch travel on control moments

5.3.2.2 Blade planform

From Eq. (5.1), it can be seen that for a given cyclic pitch input, the differential lift can be increased by increasing the blade chord. For these tests, the circular arc airfoil section was kept fixed. Hence, by having a larger blade chord, the hub moment can be increased. Now, the thrust produced by the rotor increases with rotor RPM, blade collective and blade chord. In order to maintain the same operating thrust for a given vehicle, the larger chord (solidity) rotor must either operate at a lower RPM or at a lower collective setting. From the previous section, we have seen that the rotor must operate at high RPMs to generate more control moments. This implies that the collective setting of the high solidity rotor must be reduced. However, previous studies suggest that a low collective setting may not be very efficient in hover. Therefore, it was important to measure the trade-off between control moment and hover efficiency before arriving at an optimum blade planform. For this, a representative set of blade profiles were tested, shown in Fig. 5.52 (reproduced from Section 2.6 for clarity). These profiles are listed as follows: (1) the baseline tapered blade, (2) rectangular blade I with the same root chord as the baseline blade, (3) tapered blade with 140% of the baseline chord, (4) rectuangular blade II with the same root chord as blade profile 3, (5) inverse taper, and (6) rectangular hiller. Blade profiles 5 and 6 were designed with the same thrust weighted solidity values as blade 2. In order to evaulate the differential lift for a given cyclic input, the change in rotor thrust for a given change in blade collective was measured. Figure 5.53 shows the variation of thrust coefficient with blade collective in the shrouded rotor configuration. It can be seen that as the rotor solidity increased, the $C_T - \theta$ slope increased. The C_{T_θ} values for the rectangular blades I and II were about 50% and 100% higher

<div align="center">(a) Original planform</div>
<div align="center">$\sigma_e = 0.1096$</div>

<div align="center">(b) Rectangular</div>
<div align="center">$\sigma_e = 0.1322$</div>

<div align="center">(c) Taper 140% chord</div>
<div align="center">$\sigma_e = 0.1494$</div>

<div align="center">(d) Rectangular 140% chord</div>
<div align="center">$\sigma_e = 0.1784$</div>

<div align="center">(e) Inverse taper</div>
<div align="center">$\sigma_e = 0.1325$</div>

<div align="center">(f) Rectangular Hiller</div>
<div align="center">$\sigma_e = 0.132$</div>
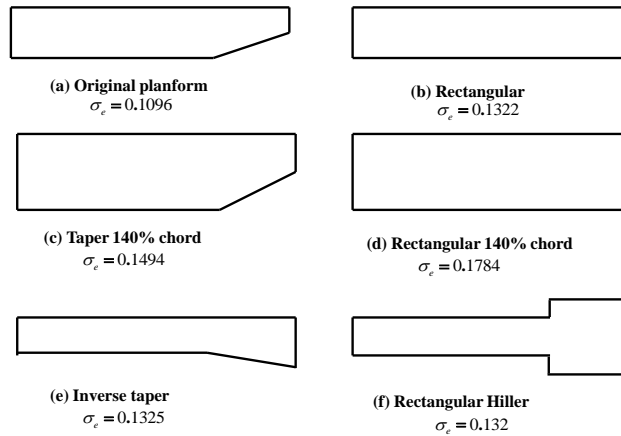
Figure 5.52: Different blade profiles tested to maximize control moment

than the original tapered planform blade respectively. This implies that a greater differential lift for a given cyclic input is produced by the rectangular blade when compared to the tapered blade that could result in higher control moments. This observation was supported by a comparison of the maximum control moments generated by these blades with a 10^0 cyclic pitch travel, shown in Fig. 5.54. It can be clearly seen that rectangular blade II produced the highest control moment and the control moment of rectangular blade I was superior to blade profiles 5 and 6. This suggests that higher solidity rectangular rotors are suitable for producing maximum control moments. However, for greatesst improvement in control moment, the higher solidity rotor has to operate at the same RPM as the lower solidity rotor. In other words, the collective setting of the higher solidity rotor should be lower. The trade-off is aerodynamic efficiency as can be seen from Fig. 2.62 discussed in Sec. 2.6. It was seen that the performance of the higher solidity blades were poor compared to the lower solidity blades at low collectives. The most interesting obervation was that the aerodynamic

performance of the lower chord rectangular blade was very similar to the original tapered blade. The rectangular blade I produced about 30% greater control moment than the original blade. The performance drop at low collectives (18^0) was the least among all the blade planforms. Therefore, it was chosen as the new blade design for incorporation in the shrouded rotor with a collective setting of 18^0.
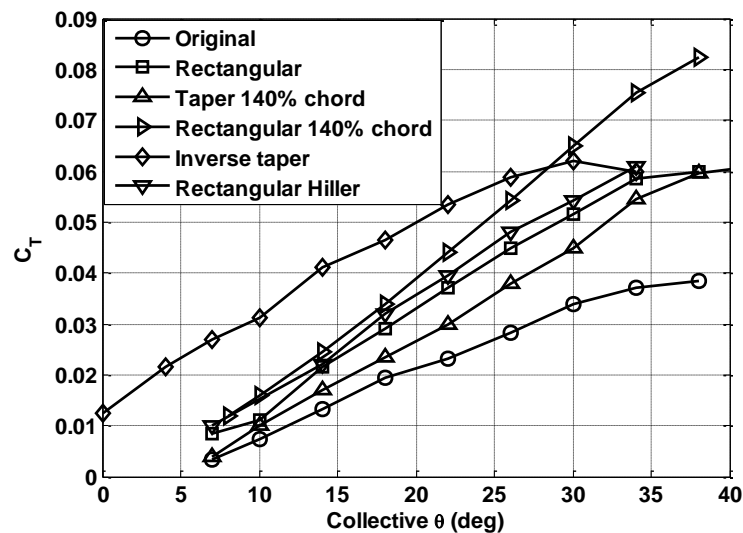
Figure 5.53: Variation of thrust coefficient with blade collective for different blade profiles in shrouded rotor

5.3.3 Control margin

From the above, the blade collective setting was shown to have an important effect on the magnitude of control moments produced and on hover performance. It is also of interest to find out whether the adverse pitching moment generated in edgewise flow is affected by the collective setting for a given operating thrust. In order to determine this, the rectangular blade circular inlet shrouded rotor was tested in the open jet wind tunnel. The pitching moment was measured as a
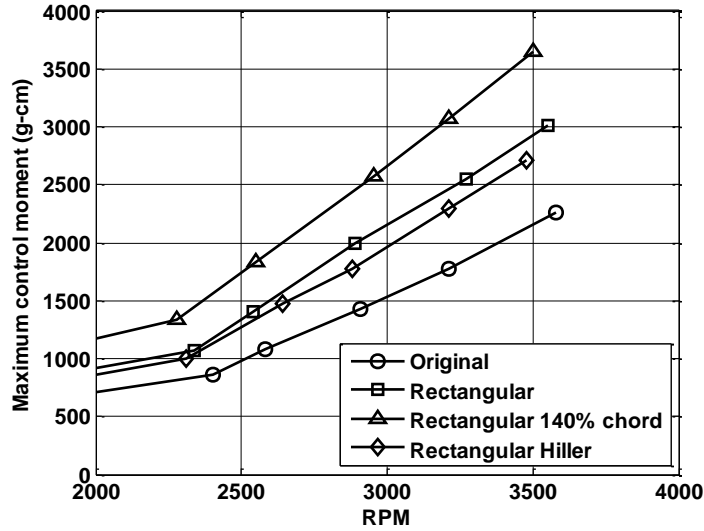
Figure 5.54: Maximum control moment comparison for the different blade planforms (10^0 cyclic input)

function of thrust for a range of collectives at 0.9 m/s and 2 m/s of edgewise flow. From Figs. 5.55 and 5.56, it can be seen that the pitching moment generated in edgewise flow did not differ significantly with the collective setting. Therefore, the driving factor behind the pitching moment at a given flow speed seems to be the operating thrust and not the operating thrust coefficient (or collective). With all the improvements in control moment discussed in the previous section, it is important to determine whether it is sufficient to overcome the adverse pitching moments. Figure 5.57 plots the nose down control moment of the rectangular blade shrouded rotor (with 15^0 cyclic travel) along with the adverse pitching moment at 2 m/s of edgewise flow as a function of operating thrust. It can be seen that the adverse pitching moment tends to saturate at higher operating thrusts, while the control moment increases almost linearly with thrust. Due to the excess control moment available to counter the adverse pitching moment, there was scope for improving the gust tolerance of the shrouded rotor vehicle

beyond 2 m/s.
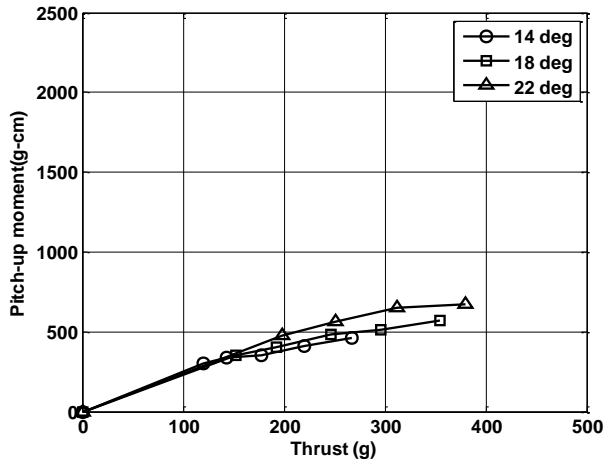
Figure 5.55: Effect of operating thrust on pitching moment at different blade collectives at 0.9 m/s of edgewise flow
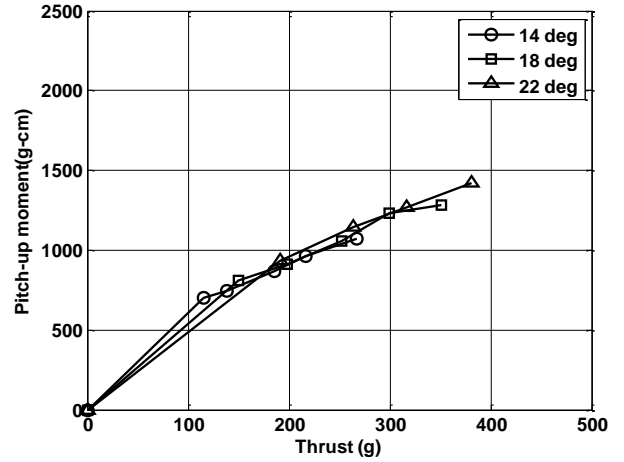
Figure 5.56: Effect of operating thrust on pitching moment at different blade collectives at 2.2 m/s of edgewise flow
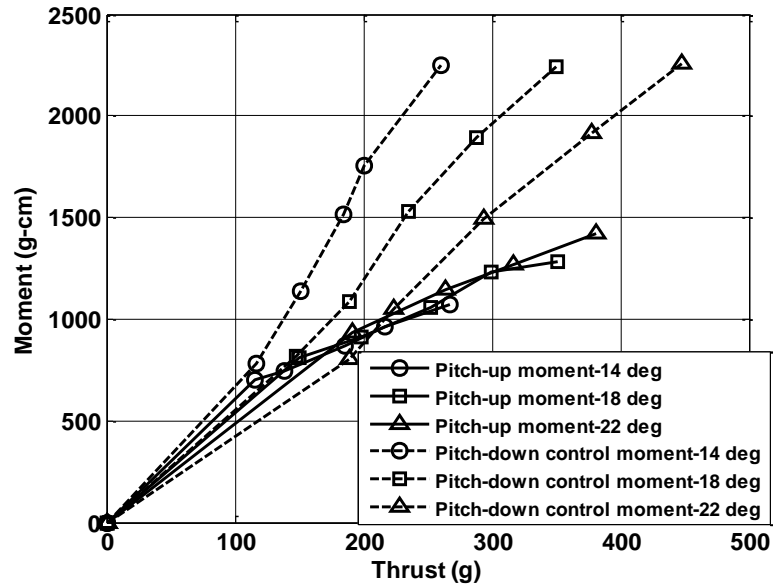
Figure 5.57: Pitch down control moment of the rectangular blade shrouded rotor (with 15^0 cyclic travel) and edgewise pitching moment as a function of thrust at 2 m/s of edgewise flow

5.4　Summary

This chapter discussed the performance of the shrouded rotor MAV when exposed to edgewise flow and control strategies to improve gust tolerance of the vehicle. Two shroud designs were tested - circular inlet shroud and an elliptic inlet shroud. Studies were conducted to compare the forces generated on the shrouded and unshrouded rotor MAV using an open jet wind tunnel for edgewise flow. Some of the key conclusions are:

(1)The elliptic inlet shrouded rotor with the highest hover efficiency (about 10% higher power loading than the circular inlet shroud) also had the greatest adverse pitching moment -up to 400% higher than the unshrouded rotor. Therefore, design metrics for MAV shroud must consider hover efficiency improvement as well as reduction in the adverse pitching moment.

(2) The elliptic inlet shrouded rotor, which has a higher projected surface area in the direction of the edgewise flow has greater drag (about 40% higher than the circular inlet shrouded rotor). The vertical thrust generated by the shrouded and unshrouded rotors remained unaffected by edgewise flow.

(3) The magnitude of the pitching moment depended on the operating thrust and not on the operating thrust coefficient of the rotor. It was found to saturate at higher values of thrust.

(4) The shrouded rotors produced up to 80-100% higher control moments than the unshrouded rotor. The shroud-augmented control moments were generated from the asymmetric pressure distribution due to cyclic input to the hingeless rotor. This is an important conclusion since it shows that cyclic pitch variation is a useful scheme for shrouded rotor MAV control.

(5) When exposed to edgewise flow of up to 2 m/s, there was no reduction in

control moment in the unshrouded rotor. There was an optimum rotor collective which resulted in the least reduction in control moment of the shrouded rotor. This was determined to be about 22^0 for the circular inlet shrouded rotor with an 8% drop in nose-down control moment.

(6) The onset of stall was delayed significantly in the shrouded rotor configuration by at least $5 - 10^0$. This implies that the shrouded rotor can tolerate a higher cyclic pitch range and initial collective setting without any degradation in control moments. An increase in cyclic pitch travel from 10^0 to 15^0 resulted in a 30% improvement in control moment of the vehicle.

(7) It is beneficial to operate the rotor at low C_T and high RPM for maximum control moment. Therefore blade profiles have to be chosen with the least reduction in power loading at lower collectives.

(8) By replacing a tapered planform blade with a rectangular blade of same rotor chord, the control moment was increased by about 30%, without significant penalty in hover performance at lower collectives.

(9) It was found that the control moment increased linearly with operating thrust while the pitching moment saturated at higher thrust levels. Therefore for a given shroud area, the control margin of the shrouded rotor increases at higher operating thrusts.

Chapter 6

Flight Tests in Edgewise Gusts: Bench Top and Free Flight

6.1 Overview

In the previous chapter, the forces acting on a shrouded rotor in edgewise flow were measured and compared to an unshrouded rotor. The key forces included the pitching moment acting on the vehicle that tended to pitch the nose of the vehicle away from the source of edgewise flow and drag that pushed the vehicle away from the source of flow. In this chapter, the ability of the vehicle provided with attitude feedback control to correct for this nose-up disturbance will be described through a series of experiments. First, the vehicle is tested on a spherical gimbal set-up, which constrains it in translation, with a table fan and wind tunnel as sources of edgewise gust. Salient comparisons in edgewise gust response and disturbance rejection with an unshrouded rotor vehicle will be made. Edgewise gust tolerance limits based on control margin determined in the previous chapter will be tested. Finally, the vehicle is flown in free flight hover and its ability to perform station keeping is tested in the presense of cross

flow generated from a pedestal fan (with flow straighteners). A retro-reflective marker pased position tracking system is used for position state information and feedback.

6.2   Bench-top tests

Bench top gust disturbance rejection tests were conducted on the spherical gimbal stand (Fig. 4.8). The study focused on the disturbance rejection characteristics of the vehicle when exposed to gusts from two sources: a standard table fan and an open jet wind tunnel. The table fan set-up serves to illustrate scenarios where the size of the gust source is comparable to the size of the vehicle. The wind tunnel set-up depicts situations where the vehicle is flown towards a large window with a steady wind blowing through it. The two cases differ in the amount of momentum drag generated and therefore require a different degree of control moment to overcome the respective disturbances. Figure 6.1 shows a schematic of these scenarios.

6.2.1   Table fan set-up

A Honeywell table fan was chosen for this purpose. It consisted of an 8" diameter fan with flow straighteners in its wake. As a result, the wake of the fan was mostly steady and irrotational. The fan had three levels of operation. Pitot tube measurements were made at different radial and axial locations for each level to determine the axial velocity magnitude. Figure 6.2 shows the velocity distribution at the exit of the fan structure. The vehicle was mounted on the spherical bearing set-up and placed at about 5"- 8" from the exit plane of the fan (Fig. 6.3. These tests were conducted with the flybar rotor set-up. A
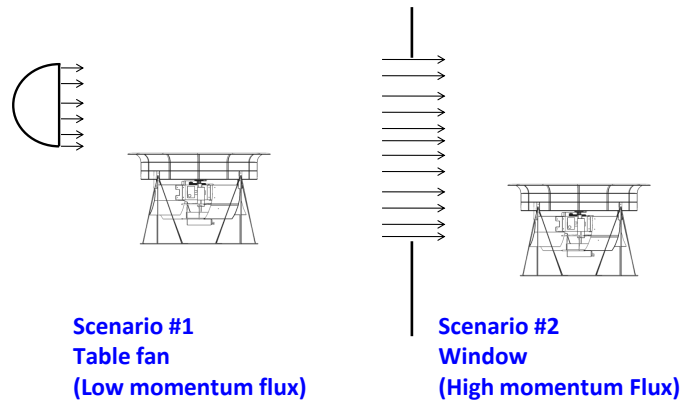
Figure 6.1: Sources of edgewise gust

proportional integral based attitude feedback control was implemented to reject disturbances and maintain hover attitude.   The pitching moment generated
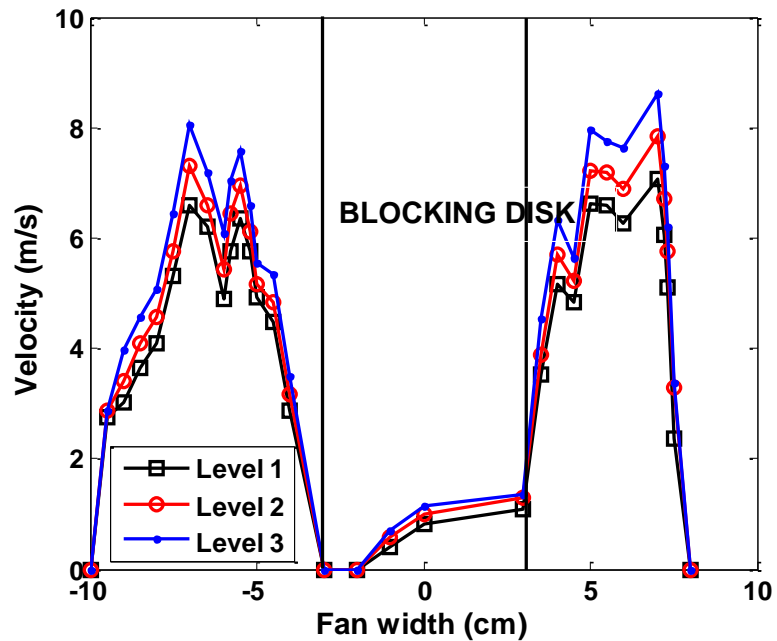
Figure 6.2: Axial velocity distribution at exit plane of Honeywell fan

by the vehicle placed in the fan wake is shown in Fig. 6.4. It can be seen
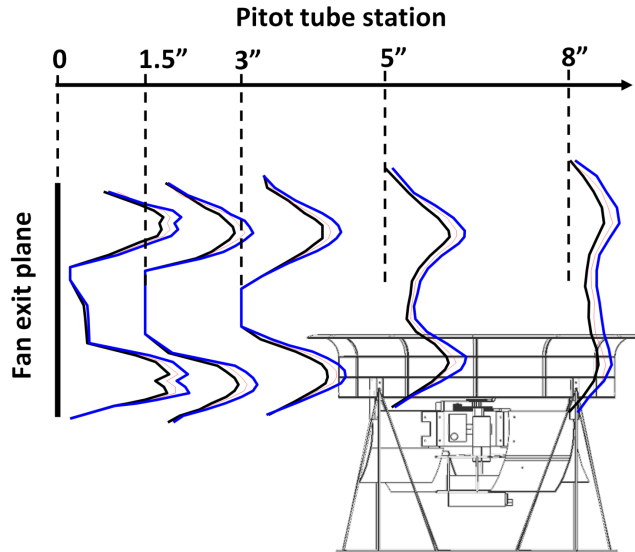
Figure 6.3: Axial velocity distribution at different station locations in the fan wake

that with the flybar rotor head, the control moment limits was reached at a free stream velocity of about 6 m/s (level 3). At this fan setting, the fan position was varied in height and angle to obtain a qualitative understanding of changes in controllability with fan orientation. It can be seen that as the angle between the free stream and the rotor reduced, the controllability increased (Fig. 6.5). This was expected since the momentum drag contribution to the pitching moment reduced. The worst case scenario was when the top half of the vehicle was exposed to the flow. Now, since the shroud inlet was not a closed profile, it may be possible that flow separation and recirculation underneath the outer portion of the inlet could affect controllability. To verify this, the outer portion of the shroud was closed using plastic material as shown in Fig. 6.6. Tests showed that this did not affect the magnitude of pitching moment for a given flow speed. In other words, there was little difference in controllability between

a closed and an open shroud inlet profile.   The vehicle was then mounted on
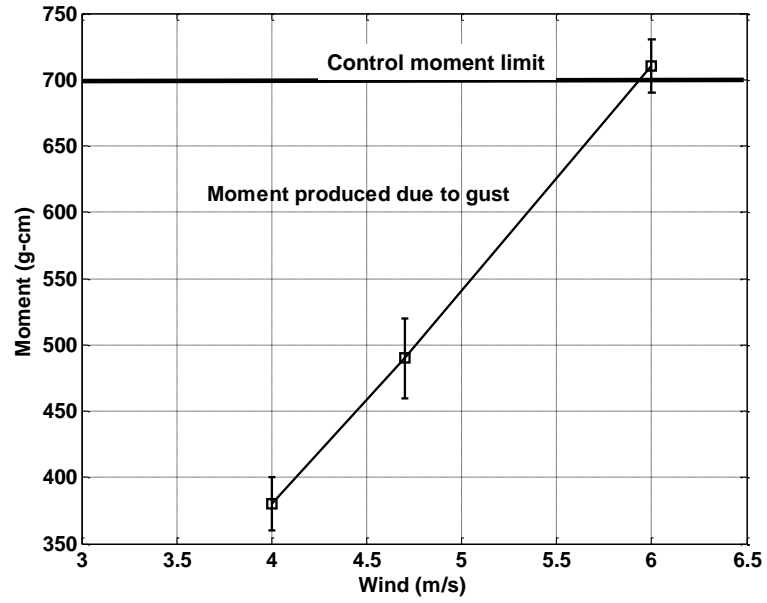
Figure 6.4: Nose up pitch moment at different fan setting (flybar rotor head)
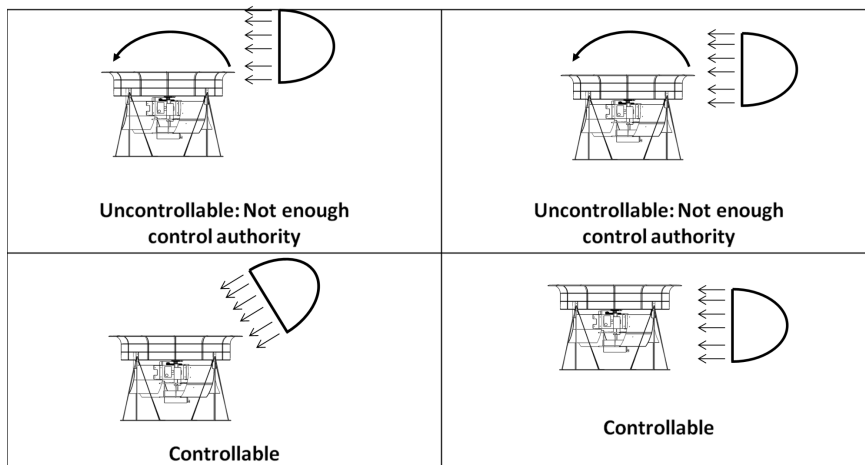
Figure 6.5: Effect of fan orientation on vehicle control
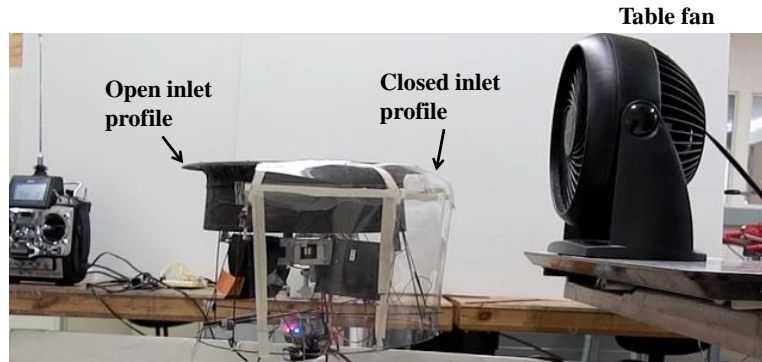
Figure 6.6: Closed shroud inlet profile

the spherical bearing set-up and placed in the wake of the fan with the flow perpendicular to the rotor thrust. Based on the above, the fan was operated at level 1 to ensure that the vehicle had sufficient control moment to overcome the edgewise gust disturbance. A pitot probe was placed close to the shroud inlet to synchronize the vehicle attitude response and the gust disturbance. Care was taken to minimize interference of the probe with the flow field and vehicle structure. The pitot probe was sampled by NI-USB hardware at 1000 Hz. The vehicle was initially commanded to hover attitude position at 3700 RPM. When the vehicle was subjected to the edgewise gust field, the subsequent attitude disturbance was sought to be mitigated by the attitude feedback controller. The control loop was closed at 200 Hz. The controller included a proportional and integral feedback of the error in euler attitude angles.

Step input: Figure 6.7 shows the response of the vehicle when subjected to a step input and removal of gust field. The gust field was along the negative X axis of the vehicle and the primary response was in the pitch axis. It can be seen that

in the step input phase, there was an initial sharp pitch back response which subsequently settled to hover attitude within a mean settling time of about 4-5 s[1]. Upon gust removal, the pre-existing control moment opposing the pitch back moment due to the edgewise gust resulted in a pitch forward response due to overcorrection. Ultimately it settled back to hover attitude within about 5 s. The proportional and integral gains were tuned to about 120% stick input range/radian and 10% stick input range/rad-s respectively.

Impulse: An impulse in the edgewise gust field could also be given by initially blocking the fan flow with a screen and impulsively removing and replacing the screen. The gust impulse response is shown in Fig. 6.8. It can be seen that for this case, the vehicle developed a larger attitude error than the step input case. This is because, for the step input case, there was a rise time of about 2 s before maximum gust speed was achieved. This gave the controller time to enable sufficient control moments to achieve hover attitude. This was not the case for the impulse case where the maximum gust speed was reached within a second. For the first gust impulse case, the vehicle began correcting itself before the maximum gust velocity was recorded. Additionally, it can be seen that although the peak velocity for the second impulse case was lower than the first, the magnitude of pitch back response was the same. This indicated that the rate of increase in gust velocity is as important a factor as the magnitude of the gust velocity in characterizing the vehicle response to gusts.

Attitude-hold control: The previous two tests showed the ability of the vehicle

---

[1]The settling time described here refers to the time required for the mean attitude level to reach within 95% of the hover level. Transient dynamics are not considered
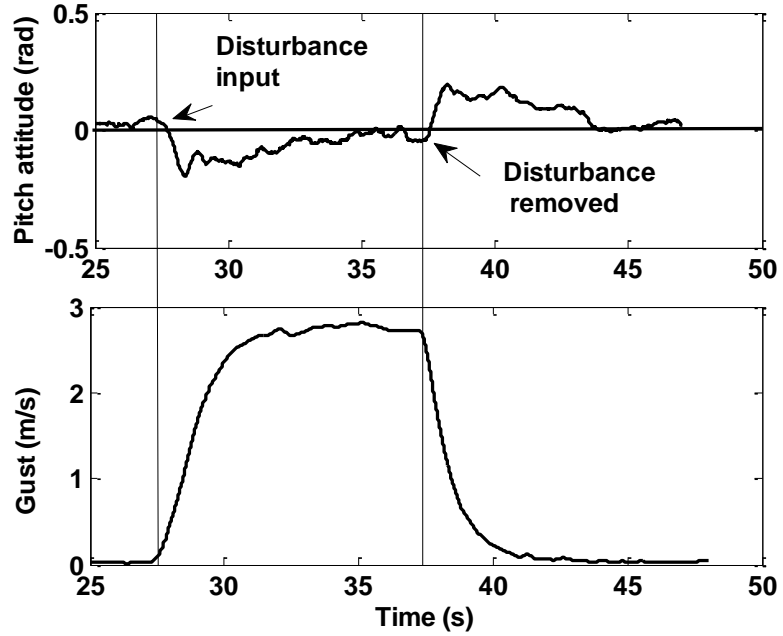
Figure 6.7: Edgewise gust disturbance response: step input. Gust 3 m/s
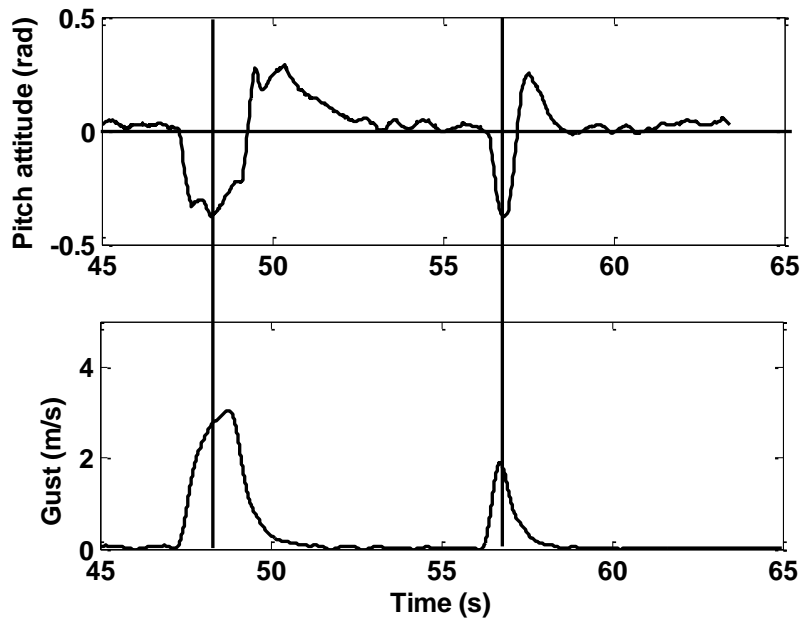
Figure 6.8: Edgewise gust disturbance response: Impulse. Peak gust 3 m/s

to maintain hover attitude in the presense of edgewise gusts. It was also of importance to test attitude-hold control of the vehicle in the presense of gusts. Of particular interest was the pitch forward attitude-hold of the vehicle into the flow (similar to a vehicle transitioning from hover to forward flight). For these tests, a gust step input was provided. Two cases were considered - (1) pitch forward command before edgewise flow input, and (2) pitch forward command after edgewise flow input. The effect of including P and PI feedback gains were studied for these cases. Figure 6.9 shows the response of the vehicle for the first case using a PI controller. Initially, the vehicle was commanded to a pitch forward position. Upon edgewise flow input, this position was disturbed which was subsequently restored. However, a comparison in attitude-hold performance of the vehicle before and after flow input showed that the PI controller performance deteriorated when the flow input was given. The presence of oscillations about the mean attitude position can be seen which suggested that the stability of the closed loop system was reduced in the presence of external disturbance and non-zero attitude reference. Figure 6.10 showed the vehicle performance with a proportional controller. It can be clearly seen that for this case, oscillations were significantly reduced. However, for disturbance rejection (original attitude regained after disturbance), proportional control was not very effective. This can be circumvented by tuning the gains and/or adjusting attitude reference in real time. By modifying the controller to 'PI' for hover and 'P' for non-zero attitude-hold, vehicle performance may be improved. This is shown in Fig. 6.11 where pitch forward command was given after flow input was turned on. Based on these tests, it can be seen that caution must be taken before including integral feedback in the controller. A combination of P and PI feedback may have to be incorporated.
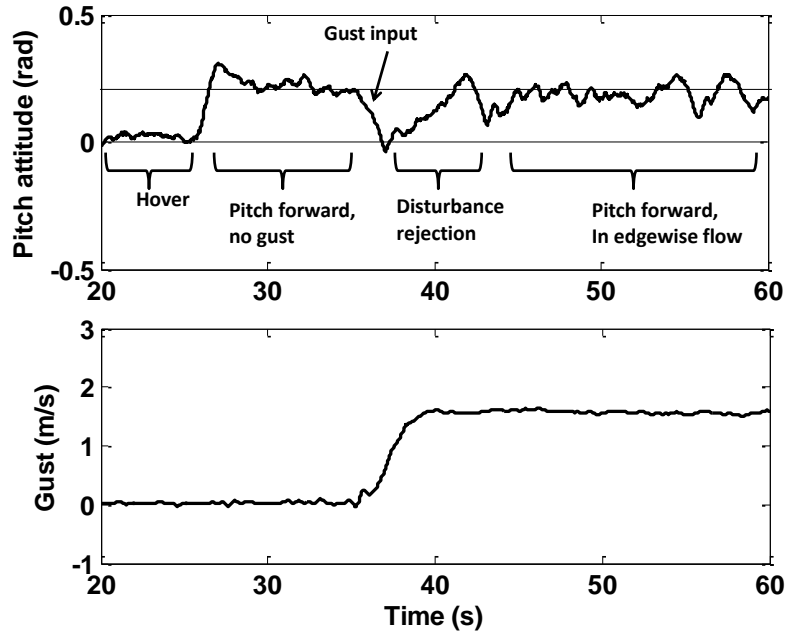
Figure 6.9: Pitch forward command before edgewise flow input: PI control
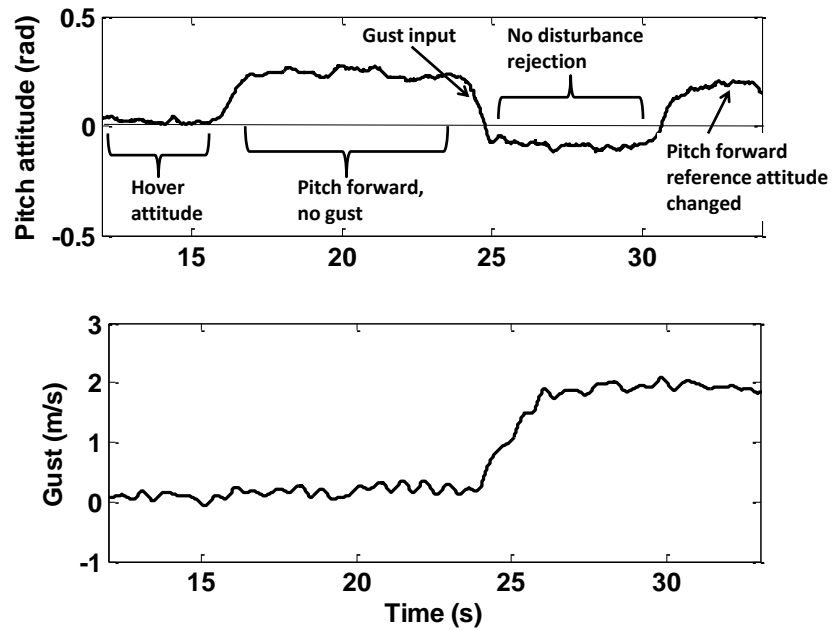
Figure 6.10: Pitch forward command before edgewise flow input: P control
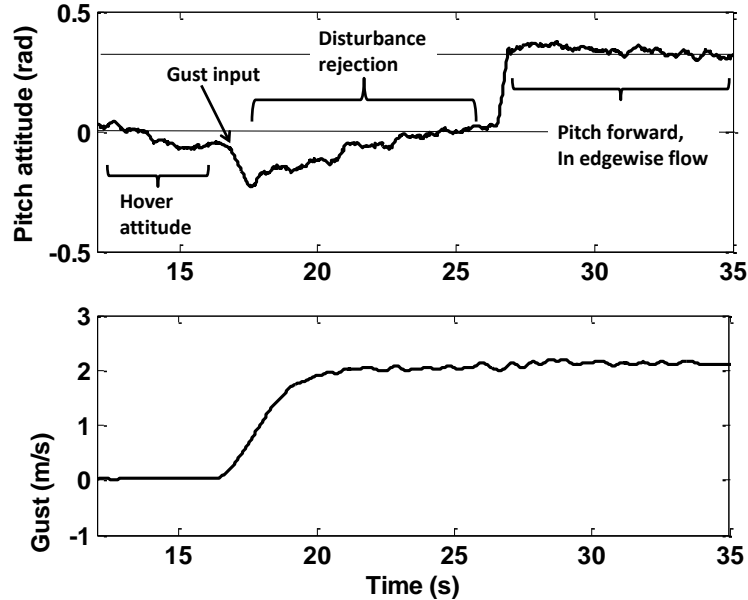
Figure 6.11: Pitch forward command after edgewise flow input: PI control for hover attitude and P control for non-hover attitude command

6.2.2 Wind tunnel set-up

The vehicle was also tested in the wind tunnel to observe the response when the vehicle was completely immersed in external flow. This scenario can be expected when the vehicle operating inside a building is flown in front of a large window with a steady draft of air flowing. For these tests, a flybarless rotor was incorporated due to increased demands on control moment.

For the experiments, there was a choice of using a closed jet or an open jet wind tunnel to generate the edgewise flow. The closed jet wind tunnel had a square cross section of about 20" width. Given the vehicle dimensions, this was a bad choice for testing the vehicle (Fig. 6.12) due to the downwash (inflow speed   15 m/s) and regions of recirculating flow that would not be convected by the relatively low speed edgewise flow (about 3 m/s). Figure 6.13 shows the pitch rate oscillations of the vehicle commanded in hover in the spherical gimbal

setup. It can be seen that hover stability was severely affected as the vehicle was transtioned into the test section of the wind tunnel. Since this would be detrimental to further testing, an open jet wind tunnel set-up was considered.

Figure 6.12: Closed jet wind tunnel set-up

Figures 6.14 and 6.15 show the open jet wind tunnel set-up for the shrouded and unshrouded rotor. The flybarless rotor with the original tapered planform, a cyclic travel of 10^0 and a collective setting of about 24^0 was used. The vehicle was placed on a height adjustable gimbal stand with the leading edge of the shroud about 2" from the exit plane of the wind tunnel. A pitot probe at the exit plane recorded the time history of the gust and was synchronized with the vehicle response data. Due to the size of the test section compared to vehicle dimensions, it was possible to assess the effect of the edgewise flow impinging on different regions of the shrouded and unshrouded rotor vehicles by adjusting the height of the gimbal stand. For this, three different positions were considered
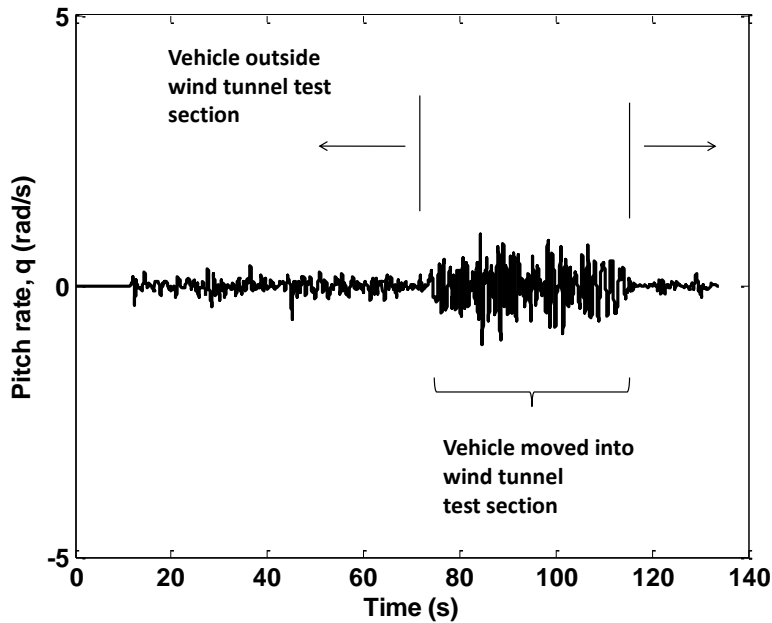
Figure 6.13: Deteriorated hover performance as vehicle is transitioned into closed jet wind tunnel test section

as shown in Fig. 6.16: (1) inlet in flow, (2) full body in flow, and (3) vanes in flow. A comparison in gust response characteristics between the shrouded and unshrouded rotors was made for these positions. The response of the shrouded and unshrouded rotor MAV was compared at operating power of the shrouded rotor.

The pitch up response when exposed to edgewise flow was seen for both the MAVs. The shrouded rotor had sufficient control moment to tolerate an edgewise gust of about 2 m/s. In contrast, the unshrouded rotor could tolerate edgewise gusts of up to 4.8 m/s. Figures 6.18−6.22 shows the response of the vehicles when subjected to an edgewise gust of about 1.9 m/s. The settling time of the PI controller did not differ significantly. However, the shrouded rotor showed a much larger pitch-up attitude error of up to 0.5 rad (Positions 1 and 2) when compared to the unshrouded rotor. This implies that in free flight,
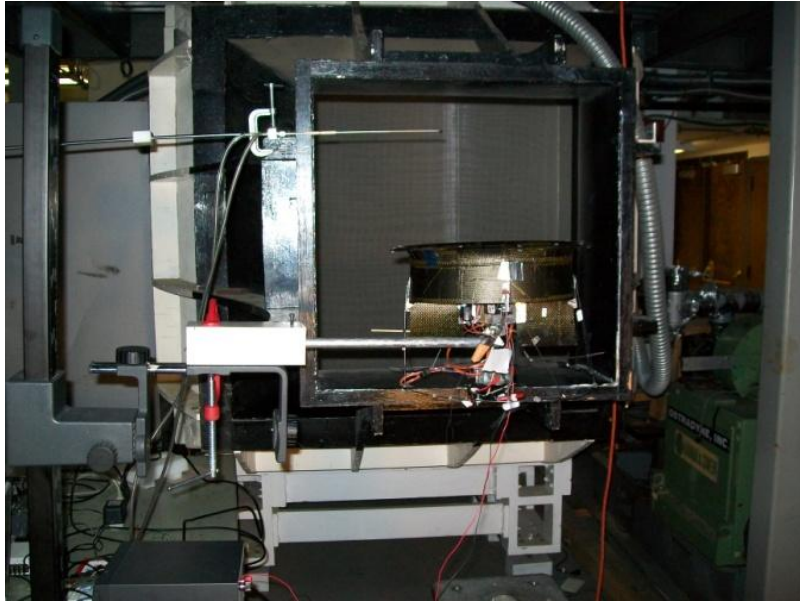
Figure 6.14: Open jet wind tunnel set-up: Shrouded rotor
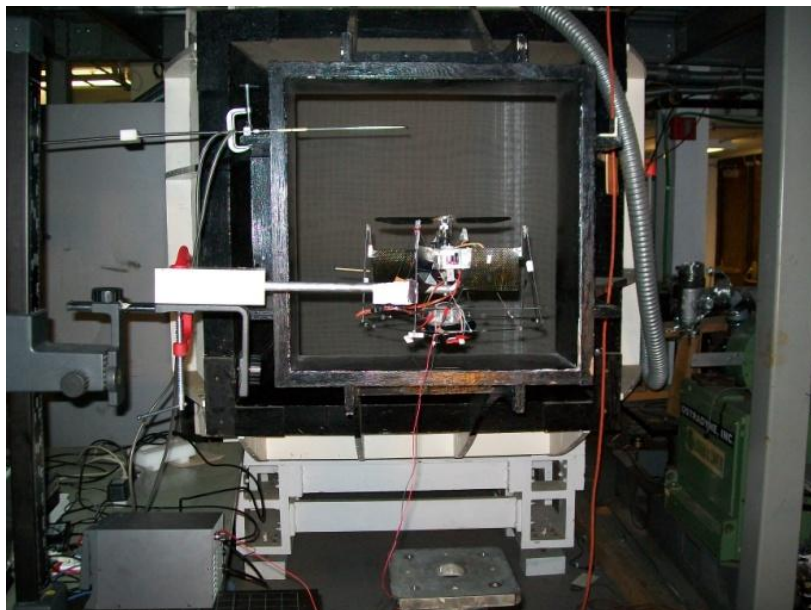
Figure 6.15: Open jet wind tunnel set-up: Unshrouded rotor
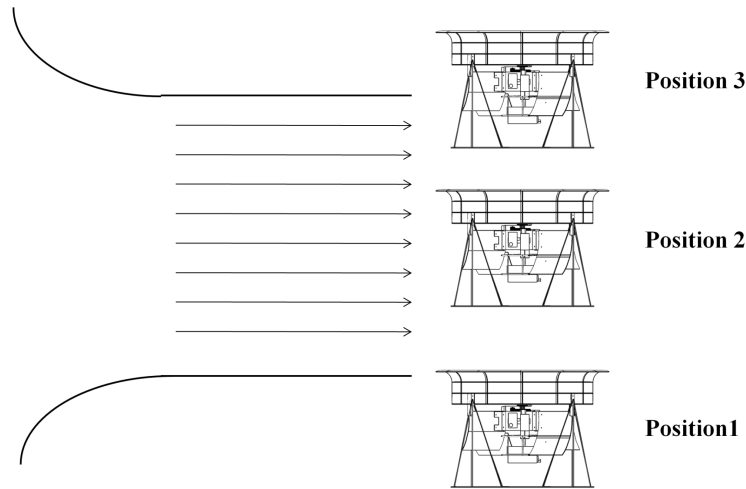
Figure 6.16: Different vehicle positions tested relative to flow

the thrust vector of the shrouded rotor vehicle would tilt (away from vertical) to a much larger angle. This would result in a faster drop in vehicle altitude when compared to the unshrouded rotor although, in reality, the vehicle is free to translate (away from the source of gust) which might make this attitude tilt less severe. In position 3, where the wakes of the rotors are affected by cross flow, the shrouded rotor experienced greater oscillations than the unshrouded rotor. However, in all cases, the controller was successfully able to reject the disturbances due to edgewise gust.

Figure 6.23 shows the response of the shrouded rotor when exposed to edge-wise flow of magnitudes greater than 2 m/s. It can be clearly seen that the control inputs were saturated and the vehicle was unable to return to hover attitude. By incorporating the optimized planform and swashplate design settings discussed in the previous chapter, the edgewise gust tolerance was increased to
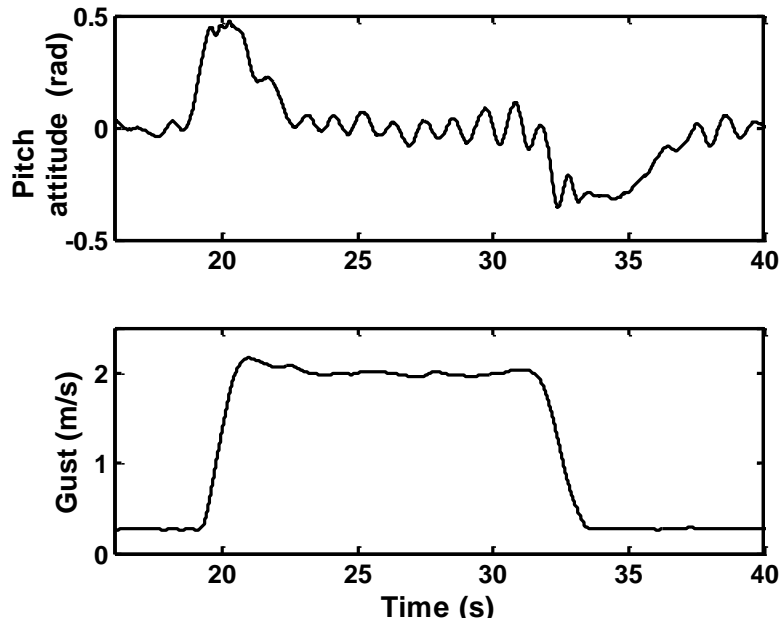
Figure 6.17: Position 1: Shrouded rotor, Gust   1.9 m/s
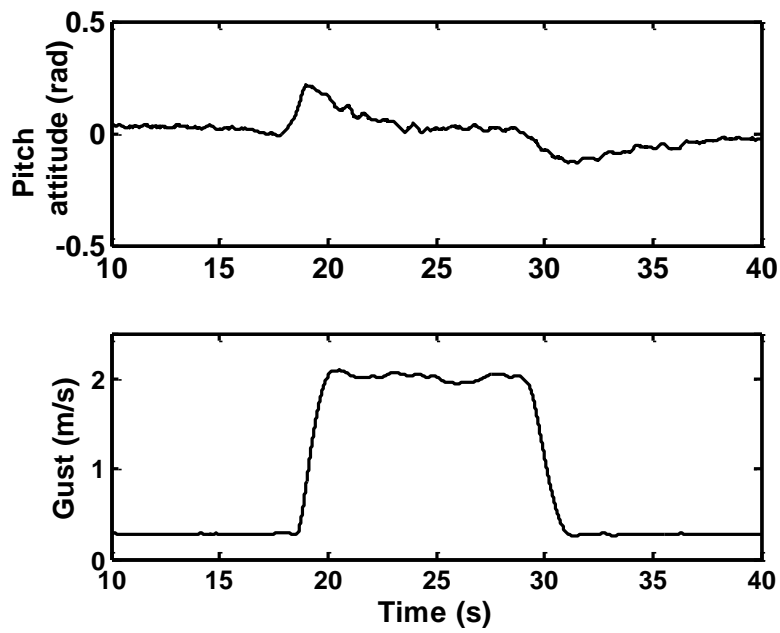
Figure 6.18: Position 1: Unshrouded rotor
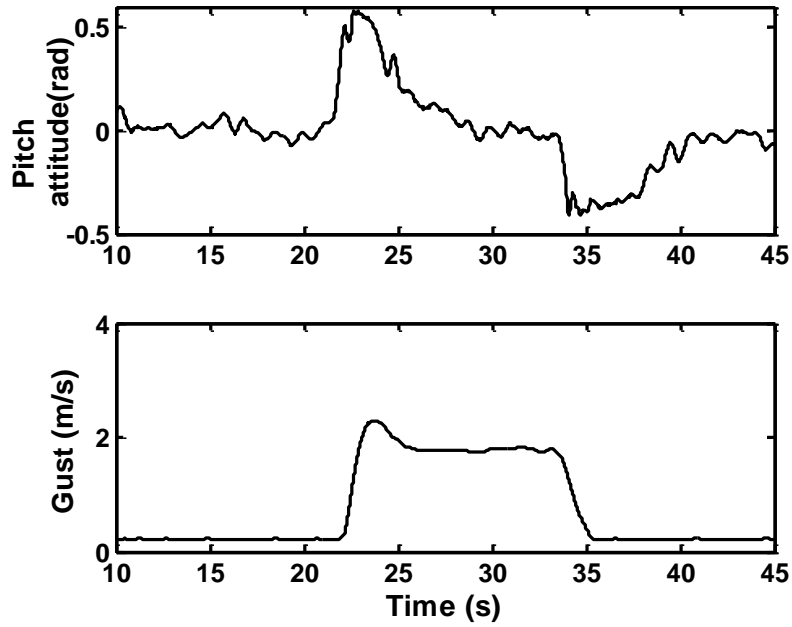
Figure 6.19: Position 2: Shrouded rotor
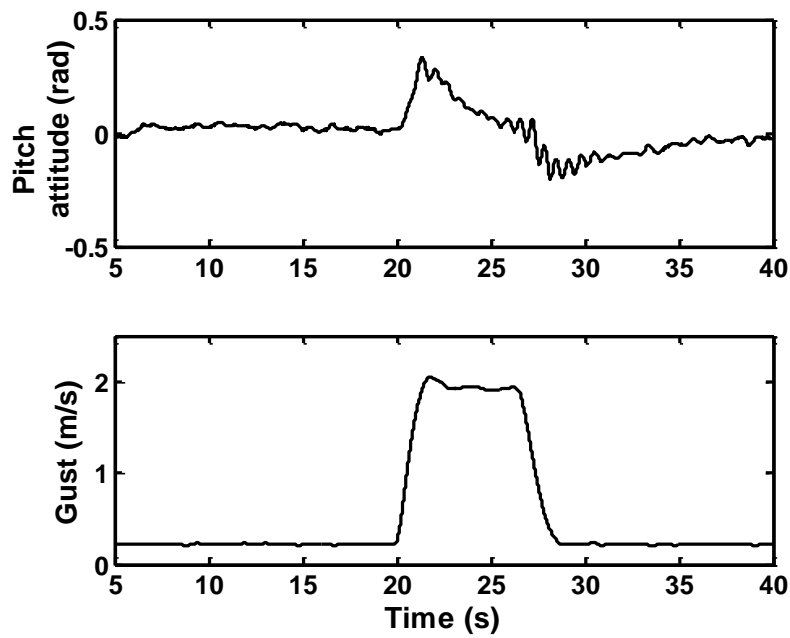
Figure 6.20: Position 2: Unshrouded rotor
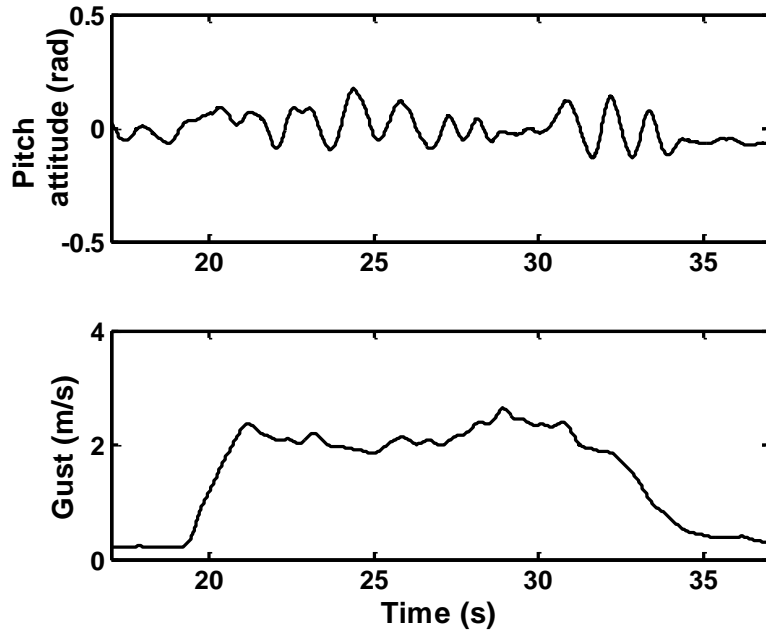
Figure 6.21: Position 3: Shrouded rotor
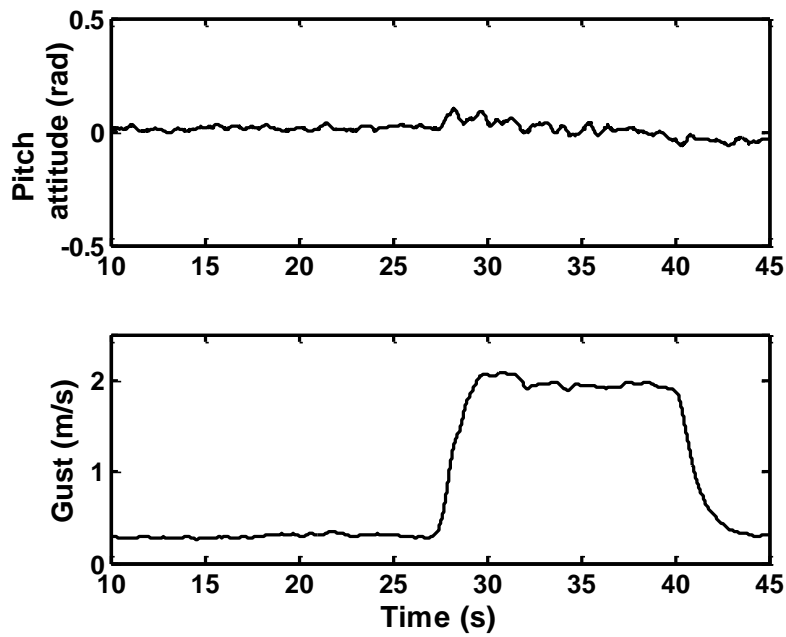
Figure 6.22: Position 3: Unshrouded rotor

more than 3 m/s as shown in Fig. 6.24. The reduced settling time and initial pitch-up attitude error can also be clearly seen.
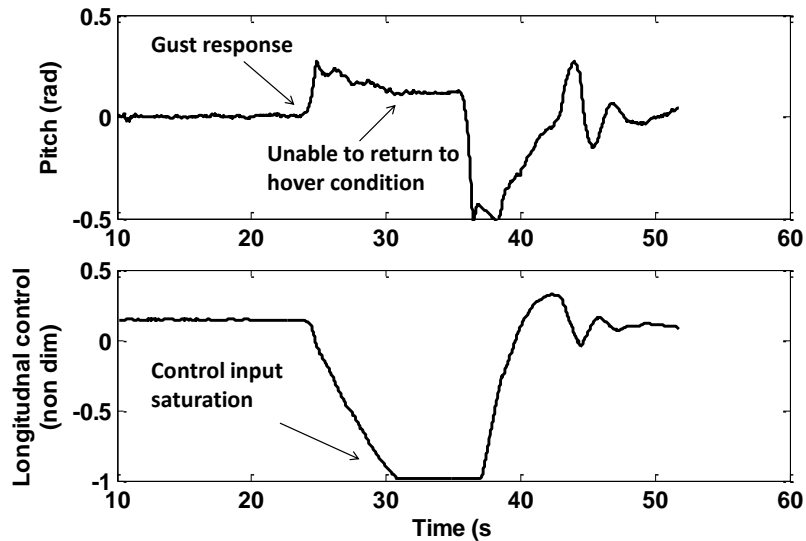
Figure 6.23: Control input saturation at gusts > 2 m/s

6.3   Free Flight Tests

The wind tunnel tests constrained the vehicle in position. Free flight tests were then conducted in order to observe the vehicle response to edgewise gusts in attitude and position. Additionally, the ability of the vehicle to maintain hover attitude and position in space (station keeping) was studied. For this, the vehicle was flown in a 30ft × 30ft × 40ft space [1]. The facility was equipped with VICON that tracked the vehicle motion and was used to provide position control of the vehicle. The shrouded rotor MAV was fitted with retro-reflective markers that

---

[1]Experiments conducted at Motile Robotics Inc., Joppa, Maryland
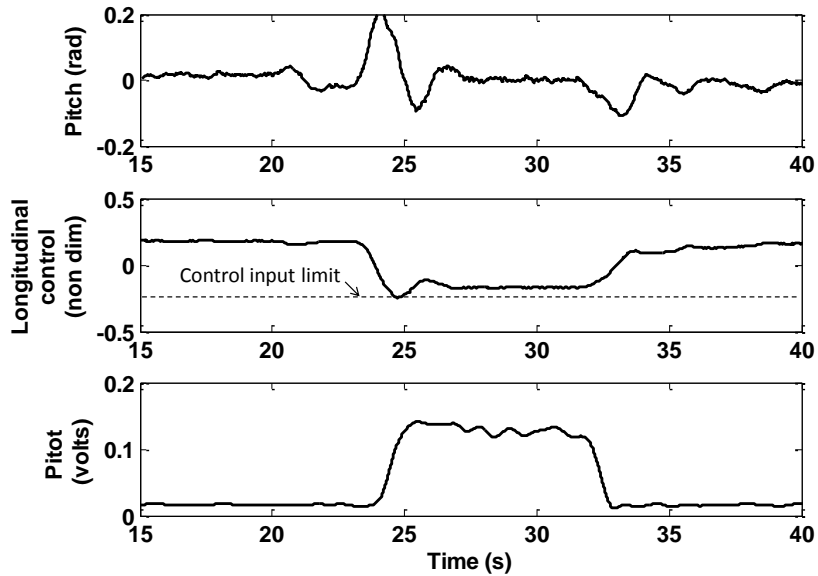
Figure 6.24: Improved gust tolerance ($3m/s$) due to increased control margin (Fig. 5.57)

were tracked by 16 infrared cameras at a loop rate of 100 Hz. A snapshot from the motion capture system is shown in Fig. 6.25. Changes in marker positions were converted to changes in rigid body attitude and position of the vehicle. Sensor fusion of an onboard IMU with the VICON data was done in LabVIEW. A schematic of the feedback controller used for attitude and position control is shown in Fig. 6.26. This was used to maintain the vehicle in hover at a single point on the X-Y plane. It can be seen that for control, a proportional feedback of the position error and a PID feedback of the Euler attitude error is given. For these tests, the altitude (Z) of the vehicle was manually controlled by adjusting the rotor RPM. In order to generate edgewise gust, three sources were used: (1) flapping board (Fig. 6.27), (2) 0.5 m table fan (Fig. 6.28), and (3) 0.7 m industrial fan (Fig. 6.29). The peak velocity of the gust from the flapping board was about 1.5 m/s. It was difficult to map the velocity profile
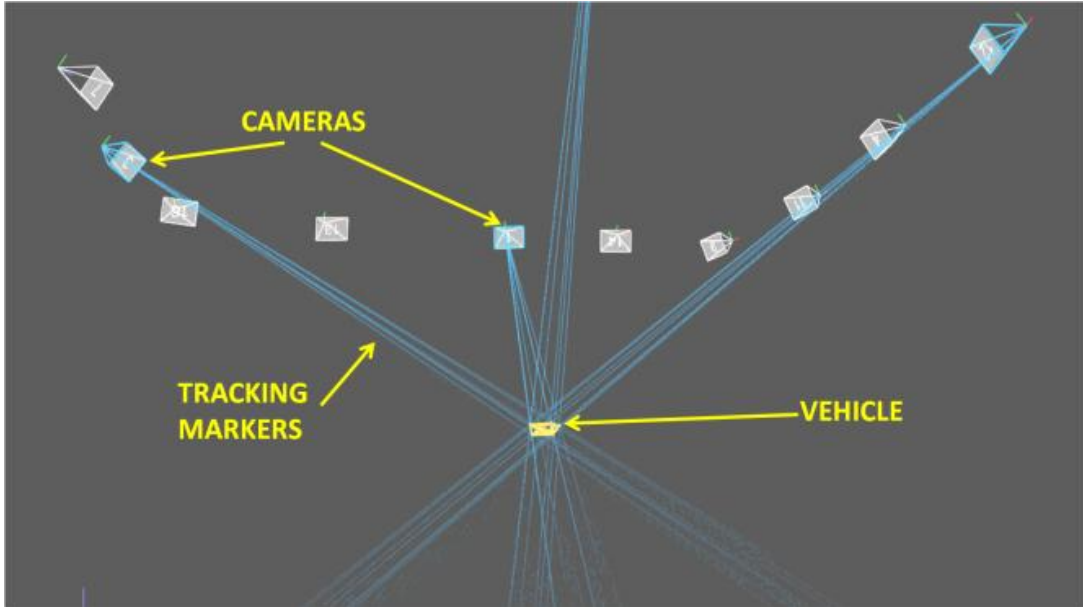
Figure 6.25: Position feedback for station keeping in edgewise gusts
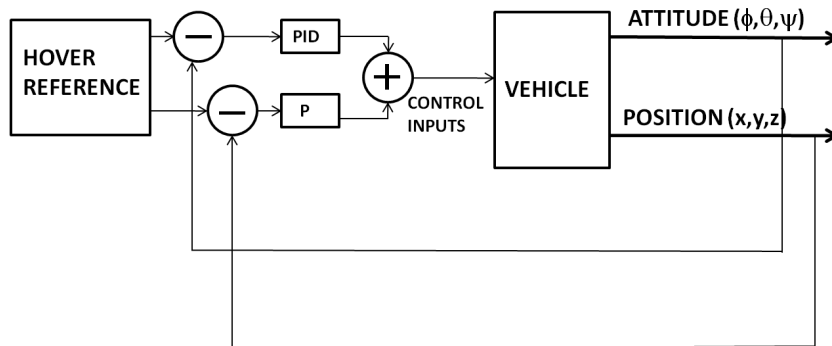
Figure 6.26: Feedback control implementation

of this gust spatially. Figures 6.30 and 6.31 show the velocity profiles of sources 2 and 3. Honeycomb flow straighteners were installed in front of both of these fans to ensure that the flow profile remain largely edgewise with minimum flow circulation. One metric for characterizing the vehicle motion as it operates in gust is the circular error probable (CEP). It is a circle that encircles 50% of the trajectory of the vehicle when exposed to gusts (Fig. 6.32). Therefore, the CEP is expected to be negligible in the absence of gusts.
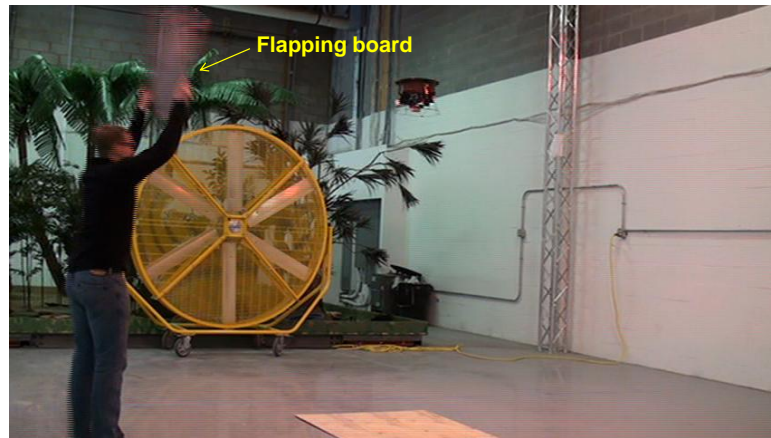
Figure 6.27: Flapping board as source of gust

The vehicle was first flown in hover to determine the performance of the feedback controller and for the purposes of determining suitable gains. Figure 6.33 shows the vehicle states commanded in the hover flight mode. It can be seen that the vehicle maintained a satisfactory hover attitude and the CEP of the vehicle was about 100 mm. Next, the controller was tested for its ability to reject disturbances in control inputs. Figure 6.34 shows the response of the vehicle to
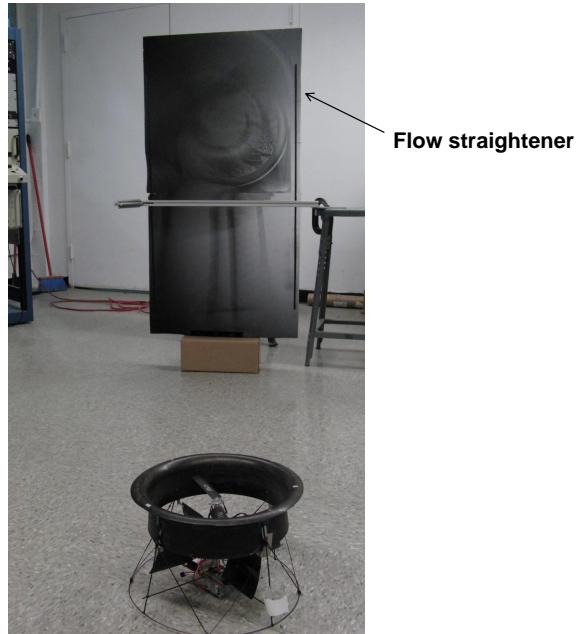
Figure 6.28: 0.5 m diameter fan gust setup

Figure 6.29: 0.75 m diameter fan gust setup
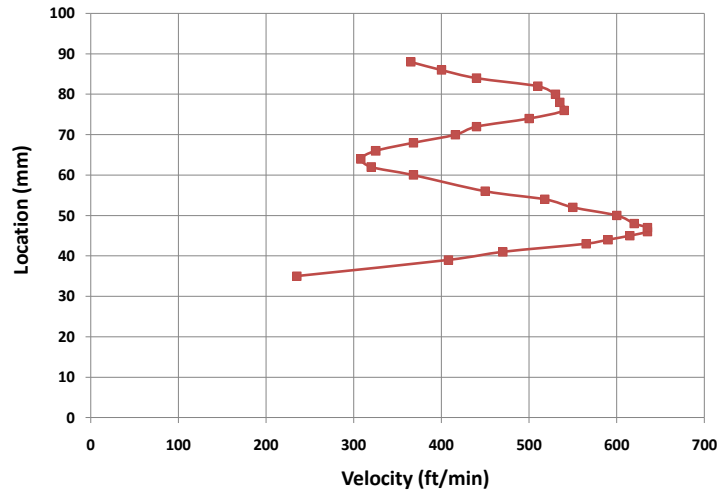
Figure 6.30: 0.5 m diameter fan velocity profile
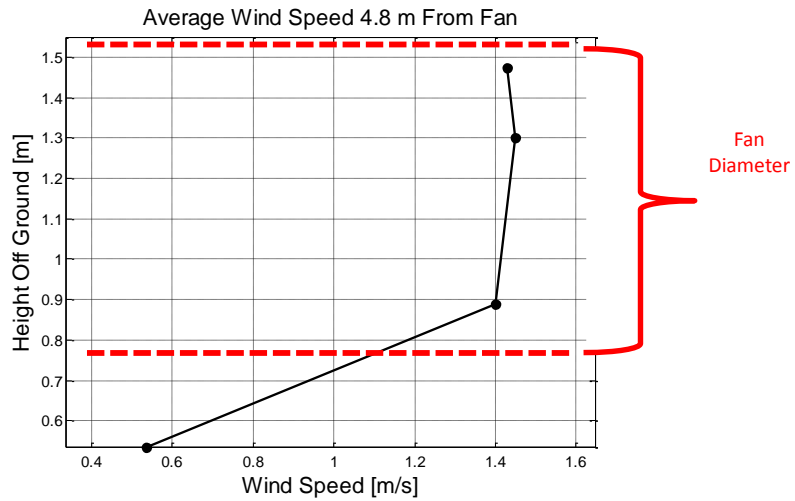
Figure 6.31: 0.75 m diameter fan velocity profile
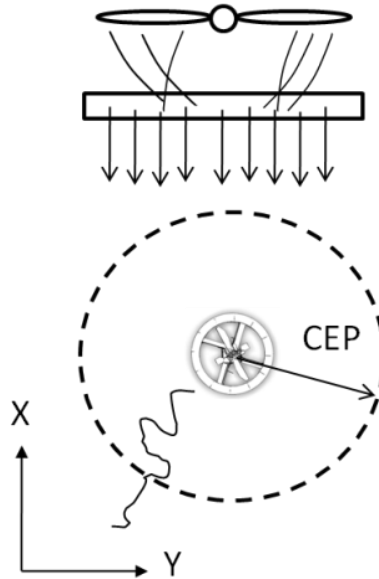
Figure 6.32: Circular error probable (CEP) metric to characterize vehicle trajectory

a control input disturbance. When the longitudinal control input disturbance was given, the vehicle quickly returned to hover and error in position was slowly damped out. This demonstrated the satisfactory performance of the controller in quiescent conditions and in the presence of non-serodynamic disturbances.

For flight tests in gusts, the vehicle was first flown in hover position, the edgewise gust input was then given and the vehicle was tracked as it attempted to maintain the hover position. Figure 6.35 shows the response of the vehicle to a gust from the flapping board. It can be seen that the vehicle responeded in both the primary (pitch) and secondary (roll) axis. Minimal motion in translation was observed. The attitude motion was damped within about 2 s which was what was observed in the wind tunnel tests. When the 0.5 m diameter fan was operated, the vehicle underwent an attitude error, deviated from position and returned back to position, with a CEP of about 0.75 m. (Fig. 6.36). This
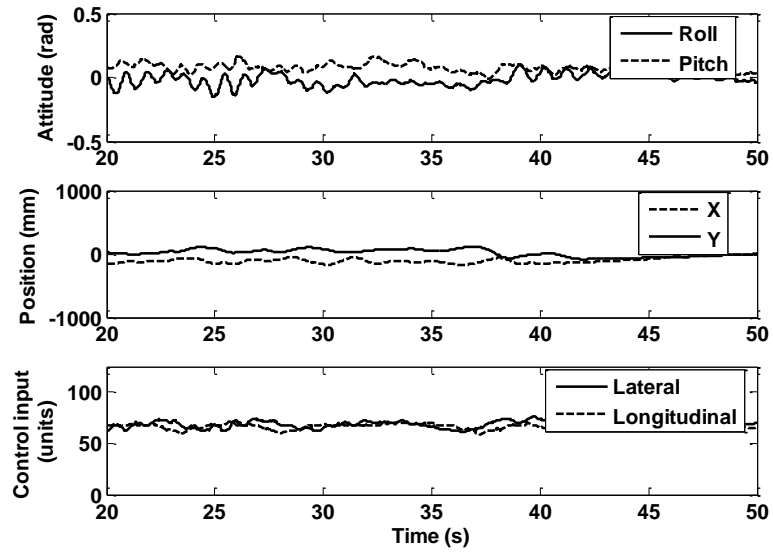
Figure 6.33: Hover position control of vehicle
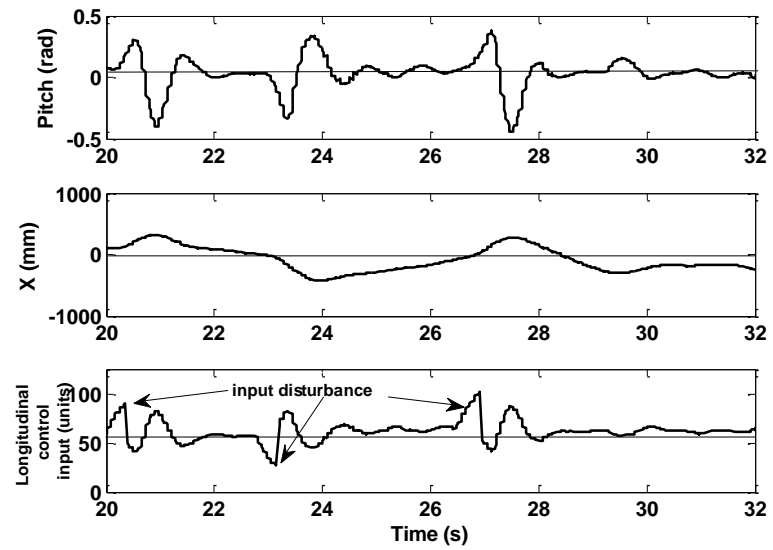
Figure 6.34: Response of vehicle to control input disturbances

represented a more persistent gust field than a flapping board. Minor oscillations were observed in the vehicle attitude as it was damped out. It must be mentioned that it was difficult to maintain a steady gust field and the orientation of the gust in an edgewise direction when compared to the wind tunnel tests. Finally, the vehicle was flown about 5 m in front of the 0.75 m diameter fan with the flow along the negative X axis. Figure 6.37 shows the vehicle response in a flow speed of 1.5 m/s. It can be seen that the vehicle response was highly coupled in pitch and roll as it attemped to maintain hover position. The CEP of the vehicle is shown in Fig. 6.38. It can be seen that the CEP of the vehicle at around 3 m/s of edgewise flow was about 15 times larger than in the no wind case. This re-iterates the enhanced sensitivity of the shrouded rotor MAV to external flow disturbances. Nevertheless, the vehicle was capable of satisfactory hover in the presense of low edgewise flow speeds. Many instances of gust inputs involved fairly turbulent, rotational flows which were difficult to characterize. It was also observed that on these occasions, the vehicle was unable to react to sudden changes in wind magnitude, leading to overcompensation and sudden crashes. Since the control inputs were not yet completely saturated, there is scope of improving the performance by increasing controller gains and bandwidth of the feedback system.

6.4 Summary

For the edgewise gust disturbance tests, the unshrouded and shrouded rotor vehicles were mounted on a spherical bearing setup to allow for pitch and roll motion while restricting it in translation. With an 8" diameter fan (with flow straighteners), the shrouded rotor vehicle could tolerate edgewise gusts of up to
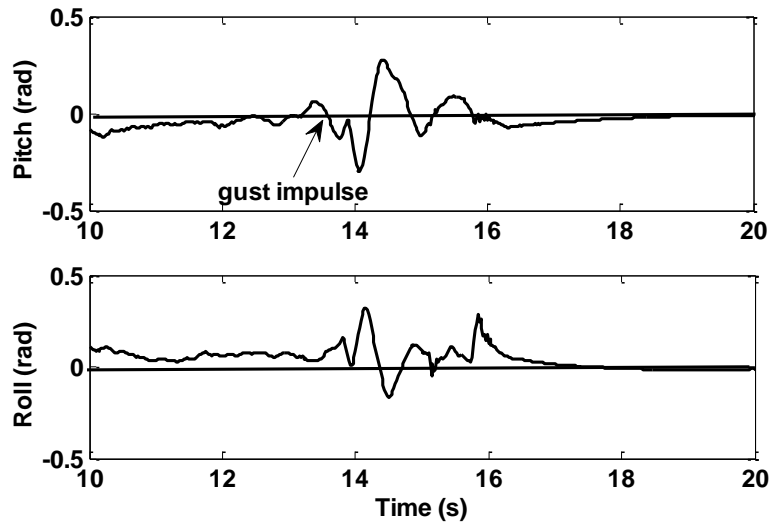
Figure 6.35: Response to gust from flapping board
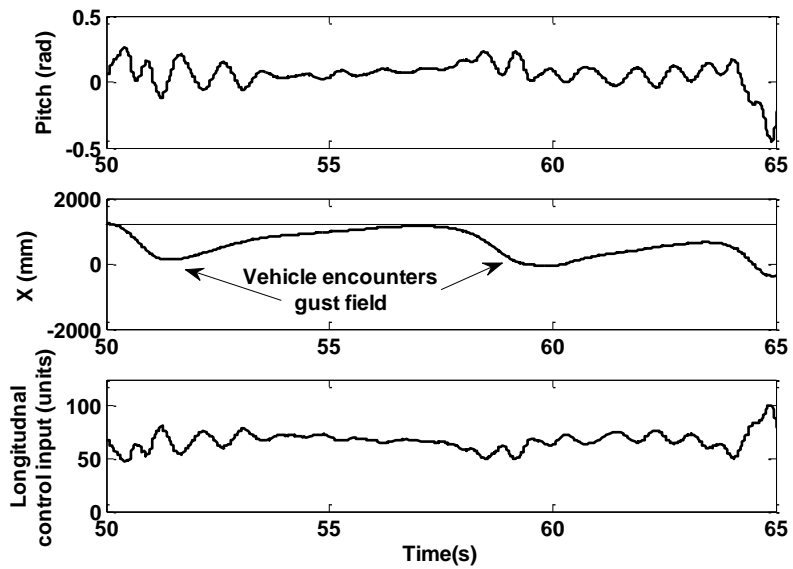
Figure 6.36: Response to gust from 0.5 m table-fan (1.4 m/s)
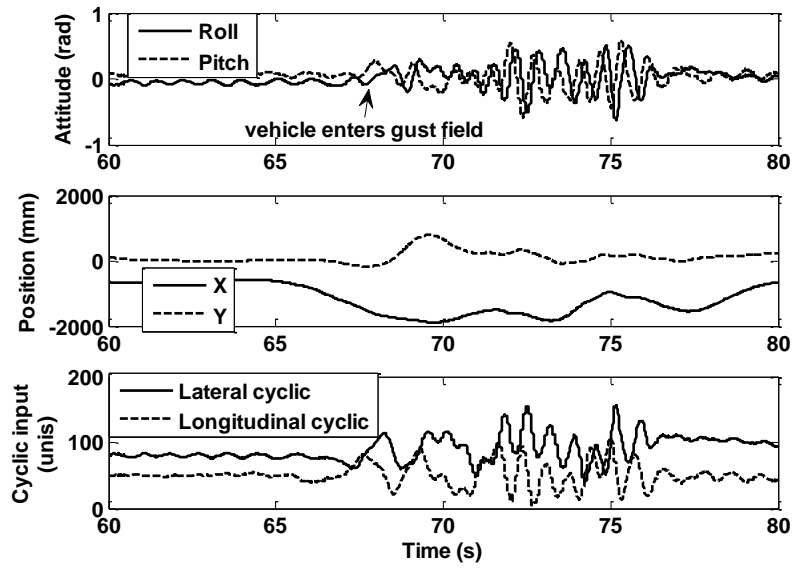
Figure 6.37: Response to gust from 0.75 m table-fan (1.5 m/s)
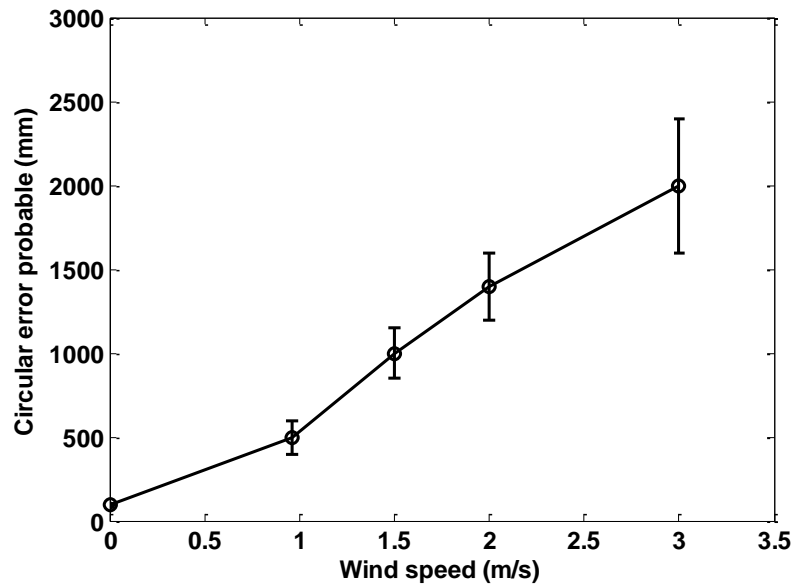
Figure 6.38: CEP of shrouded rotor with 0.75 m diameter fan as source of gust

263

6 m/s. The mean settling time after an input disturbance was less than 5 s.

The wind tunnel setup was viewed as a source of gust when the vehicle is operating near a large window. When the edgewise flow was introduced, the shrouded rotor developed a higher nose-up attitude error than the unshrouded rotor. This means that the shrouded rotor would have a larger tilt of the thrust vector in its initial response to an edgewise gust. The mean settling time after the introduction of the disturbance was about 5 s for both the vehicles. The shrouded rotor could tolerate up to 3 m/s gusts while the tolerance was greater than 5 m/s for the unshrouded rotor.

Free flight tests on the vehicle, using VICON for feedback control, indicated the capability of the vehicle to recover from gust impulse inputs from a pedestal fan. When exposed to edgewise flow, the vehicle could tolerate up to 3 m/s of wind speed. The circular error probable of the vehicle trajectory was up to 15 times at 3 m/s as compared to the no wind case. This re-iterates the enhanced sensitivity of the shrouded rotor to edgewise flow.

Chapter 7

Conclusions and Recommendations for Future Work

In the past decade, with the progress of microsystem technology in electronics and manufacturing, Micro Air Vehicles (MAVs) are fast emerging as viable aerial platforms that can be used in a wide area of applications in the military and civilian domain. These include perimeter surveillance, targeting, biochemical sensing, traffic monitoring and many other operations that are dangerous, impractical or inconvenient for human involvement. They can be used to enhance situational awareness, minimize risk exposure, aid manned-unmanned teaming and integrate communication with Unmanned Ground Vehicles (UGVs). For many of these applications, platforms are required that have hover and slow-loiter capability, ability to perform quick and complex maneuvers, avoid obstacles as well as tolerate aerodynamic disturbances such as wind gusts and flow recirculation that may occur when flying close to ground or in the vicinity of walls.

Rotary wing platforms have the potential to meet many of these requirements primarily due to their ability to be aerodynamically efficient in hover (when

compared to fixed and flapping wing platforms). To provide high aerodynamic control forces, fixed wing platforms must be travelling at high speeds. Flapping wing MAVs would require high flapping frequencies which can be detrimental to the life span of the vehicle due to high wear and tear from the unsteady inertial forces. Rotary wing MAVs, on the other hand, can generate high dynamic pressures by allowing for sufficiently high rotational speeds (steady inertial forces). This translates to increased maneuverability at hover or near-hover conditions. Due to many of these factors, there has been a lot of research into the development of single and multi-rotor platforms.

However, there are significant technical challenges involved in the development of small scale rotary wing systems. Some of these include: (1) poor aerodynamic efficiency at the highly viscous, separation prone, low Reynolds number flow regimes, (2) increased sensitivity to external disturbances (inertia scales down by the fifth power of scale whereas the weight scales by only the cube of scale), (3) limited high-bandwidth on-board electronics for feedback implementation, (4) lack of robust, stiff and lightweight structures, (5) poor energy density and efficiency of micropropulsion technologies, among many more. It can be seen that this is truly a multidisciplinary venture that involves advancements in many areas in order to develop efficient, novel and fully functional platforms.

In the scope of this research, the aerodynamic performance, and flight stability and control (with and without input disturbances) were studied as applicable to one such novel MAV rotary wing configuration - the shrouded rotor. This configuration offers three key operational benefits: (1) increased system thrust for a given power input, (2) enhanced structural rigidity, rotor protection and operational safety and (3) shroud can be retrofitted into an optimized rotary wing platform, thus complementing efforts to optimize a conventional rotary wing

system as well as minimizing design costs to reconfigure platforms. However, there are two significant challenges in the development of these platforms at micro scales: (1) development of a stiff and lightweight shroud so that the excess system thrust offsets the excess weight due to the shroud, and (2) increased sensitivity to flow disturbances when compared to conventional rotary wing systems, especially edgewise gusts.

In this dissertation, these key aspects were addressed and studied in order to assess the capability of the shrouded rotor as a platform of choice for MAV applications. First, a low disk loading shrouded rotor vehicle was designed and constructed with key shroud design variables derived from previous studies on micro shrouded rotors. The different components such as the rotor, stabilizer bar, yaw control vanes and the shroud were designed and systematically studied for system efficiency and overall aerodynamic improvements. Risk reduction prototypes were built to sequentially arrive at the final configuration. The passive stability of the shrouded and unshrouded rotor systems were then studied in hover in quiescent conditions. Specific constraints related to rotor tip path plane variation inside the shroud were derived. An attitude proportional-integral-derivative (PID) controller based on wireless telemetry was implemented to augment stability in hover. The PID gains were tuned based on the Ziegler-Nichols tuning approach. In order to enhance maneuverability and reduce profile losses, the stabilizer bar was removed. Implications on attitude dynamics were then studied using a time domain system identification approach. A linear reduced order attitude dynamics model was derived to enable implementation of a model based controller using the linear quadratic regulator. Next, the ability of the unshrouded and shrouded rotor systems to reject external aerodynamic disturbances (edgewise gusts from table fan and wind tunnel) while maintaining

hover attitude were studied. The aeromechanical forces generated on these systems in edgewise flow were systematically measured. A few design modifications to the rotor system were identified and studied to improve the control moment of the shrouded rotor system with the aim of improving edgewise gust tolerance. Finally, with the aid of a motion capture system using retroreflective markers and infrared cameras, a PID feedback controller was implemented with translational and attitude feedback. The purpose was to study the response of the shrouded rotor vehicle to an edgewise gust and track its motion as it attempted to hover at a particular station. The present research was concluded at this stage to open up further research and development required in the area of MAV flight performance in degraded flow conditions.

7.1 Conclusions

The following are some specific conclusions from the present work.

7.1.1 Vehicle design and hover performance

The vehicle consists of a two bladed single rotor enclosed in a shroud with anti-torque vanes placed in the rotor downwash to counter rotor torque. The final vehicle weighed about 280 g with a rotor diameter of about 244 mm.

1. Airfoil: In both the shrouded and unshrouded rotor configurations, the use of a sharpened leading edge (LE) with a circular camber airfoil yielded better hover performance over an unsharpened leading edge airfoil. This was clearly illustrated in hover flight tests, where rotors with sharpened and unsharpened LE would produce the same thrust, while the rotor torque

produced by the unsharpened LE resulted in severe loss of yaw trim. This shows that the profile power losses with the unsharpened LE is greater.

2. Rotor planform: Parametric studies were conducted on different rotor planforms in the shrouded and unshrouded rotor configurations (the effect of rotor twist alone was not measured to be a significant factor). In the unshrouded rotor configuration, a 2:1 taper ratio at 80% radial location gave the highest Figure of Merit of about 0.64 (blade loading of between 0.15-0.2). It is noted that the blade loadings for efficient performance of MAV blades are higher than for full scale rotors. It is difficult to reconcile the rotor performance with the airfoil characteristics. A complete explanation of this phenomenon requires a detailed experimental study of low Re airfoils. At operating thrust, tapered blades (10g/W) had a 15% improvement in power loading over rectangular blades(8.5 g/W). However, for a shrouded rotor configuration, the rectangular planform was as efficient as the tapered blade (power loading of about 14-15 g/W at operating thrust). An explanation for this could be that in the shrouded rotor configuration, the tip vortex is diffused and extra thrust is extracted from the tip of the rectangular blade.

3. Shrouded rotor performance comparison: At an operating thrust of 300 grams, the power loading of the shrouded rotor was approximately 30% higher than the unshrouded rotor (the rotor disk area was kept constant and a tip clearance of 0.015R was maintained). For example, at an input mechanical power of 15 watts, the shrouded rotor thrust was about 70 grams higher than the unshrouded rotor. After taking the weight of the shroud into consideration (40-45 grams), this translates to a payload

benefit of about 20-30 grams.

4. A measurement of the individual thrust contributions showed that the shroud produced up to 30-35% of the total system thrust in hover. This result agreed well with CFD calculations.

5. The blades stalled at about 30 deg for the unshrouded rotor, while the stall angle was close to 40 deg for the shrouded rotor. This delay in stall is due to the fact that the inflow velocity in the shrouded configuration is higher, resulting in a lower effective angle of attack.

6. Analysis of the above empirical data showed that the optimum shroud diameter to lift an unshrouded rotor (or payload) of 250 g is about 14 cm. This results in less than a 5% reduction in hover power compared to the present set-up. Therefore, the shroud size chosen in this research is close to optimum for a 250 g design payload.

7. Operation of the Hiller stabilizer bar reduced the effective rotor FM from 0.64 to about 0.61. This is primarily due to the profile losses associated with the Hiller paddles. These losses can be minimized by choosing an optimum pitch setting of the paddles. It was found to be about 12 deg. The optimized Hiller bar configuration that minimized profile losses had a radius of 60 mm and a paddle area of 8.5 cm^2.

8. For countering rotor torque, a compact configuration was to incorporate circular camber vanes in the downwash of the rotor. The vanes could either be placed in an X or an H fashion. It was seen that either of these configurations were effective in countering rotor torque irrespective of rotor

thrust. The penalty in power to maintain a constant thrust was about 10% of the main rotor power, due to the downforce acting on these vanes.

9. The anti-torque effectiveness of these vanes reduced drastically in ground effect (IGE) due to the modified structure of the rotor wake. Perfect bi-directional yaw control was not achieved in IGE condition with the same vane trim settings as for the out of ground effect condition.

7.1.2 Attitude dynamics and flight tests in hover (no flow disturbances)

The differences in passive stability in attitude between a shrouded and unshrouded rotor MAV were compared. Implementation of a classical feedback control system and flight testing is described. Open loop time domain system identification was conducted to extract the attitude dynamics of a flybar and flybarless shrouded rotor. Specific controllability metrics were extracted from these models to enable quantitative comparison.

1. While a teetering rotor along with a stabilizer bar offers rotor damping in the unshrouded rotor configuration, it induces limit cycle oscillations in the shrouded rotor setup. This is due to the movement of the rotor tip path plane, that results in asymmetric pressure distribution on the shroud. This leads to a shift in center of lift and ultimately causes oscillations.

2. To prevent this, it is necessary to incorporate a rigid/hingeless rotor in the shrouded rotor vehicle to minimize tip path plane movement.

3. The Hiller bar has to be appropriately phased with respect to the hingeless rotor pitching axis to prevent active and passive cross coupling in pitch and

roll attitude motion. The hingeless rotor in the present vehicle has a non dimensional rotating natural frequency of about 1.4. This requires the Hiller bar to be phased about 40-45 degrees with respect to the main rotor pitching axis at operating RPM. The phasing angle was experimentally shown to monotonically increase with rotor RPM.

4. A proportional-integral-derivative feedback controller was successfully able to stabilize the shrouded rotor vehicle in hover. The gains were tuned based on the Ziegler-Nichols approach. A knowledge of the trim values was seen to be a significant factor for achieving stable flight. Integral feedback reduced stability margin of the vehicle and was only used in conditions where trim values were not known.

5. The shrouded rotor vehicle was seen to be especially prone to oscillations in pitch and roll close to the ground, probably due to asymmetric pressure distribution on a tilted shroud surface in IGE conditions. In order to minimize this ground effect induced instability, fast start-ups of the vehicle were commanded.

6. A reduced order linear attitude dynamics model was identified using the time domain system identification approach. This model compared satisfactorily with flight test data at desired input frequencies below 2 Hz. The yaw DOF was decoupled from vehicle pitch and roll.

7. In order to improve maneuverability and efficiency of the vehicle, it was necessary to remove the stabilizer bar (flybar). A comparison in attitude dynamics of the flybar and flybarless rotor showed that in the flybar setup, the vehicle had stable poles while the flybarless rotor was marginally un-

stable.

8. Comparison in controllability metrics such as Frobenius norm derived from the controllability gramian indicates that the flybarless rotor is more controllable than the flybar rotor. The source of this increased controllability is the reduced damping and increased control moments.

7.1.3 Force measurement and flight testing in hover with edgewise flow imposed

Two shroud designs were tested - circular inlet shroud and an elliptic inlet shroud. Studies were conducted to measure and compare the forces generated on the shrouded and unshrouded rotor MAV using an open jet wind tunnel for edgewise flow. For flight tests, bench top (table fan and wind tunnel) and free flight tests (using motion capture facility) were conducted to assess flight performance and disturbance rejection characteristics of the shrouded rotor with closed loop feedback control in adverse flow conditions.

1. The elliptic inlet shrouded rotor with the highest hover efficiency (about 10% higher power loading than the circular inlet shroud) also had the greatest adverse pitching moment,up to 4 times higher than the unshrouded rotor. Therefore, design metrics for MAV shroud must consider hover efficiency improvement as well as reduction in the adverse pitching moment.

2. The elliptic inlet shrouded rotor, which has a higher projected surface area in the direction of the edgewise flow has greater drag (about 40% higher than the circular inlet shrouded rotor). The vertical thrust generated by the shrouded and unshrouded rotors remained unaffected by edgewise flow.

3. The magnitude of the pitching moment depended on the operating thrust and not on the operating thrust coefficient of the rotor. It was found to saturate at higher values of thrust.

4. The shrouded rotors produced up to 80-100% higher control moments than the unshrouded rotor. The shroud-augmented control moments were generated from the asymmetric pressure distribution due to cyclic input to the hingeless rotor. This is an important conclusion since it shows that cyclic pitch variation is a useful scheme for shrouded rotor MAV control.

5. When exposed to edgewise flow of up to 2 m/s, there was no reduction in control moment in the unshrouded rotor. There was an optimum rotor collective which resulted in the least reduction in control moment of the shrouded rotor. This was determined to be about 22^0 for the circular inlet shrouded rotor with an 8% drop in nose-down control moment.

6. The onset of stall was delayed significantly in the shrouded rotor configuration by at least $5-10^0$. This implies that the shrouded rotor can tolerate a higher cyclic pitch range and initial collective setting without any degradation in control moments. An increase in cyclic pitch travel from 10^0 to 15^0 resulted in a 30% improvement in control moment of the vehicle.

7. It is beneficial to operate the rotor at low C_T and high RPM for maximum control moment. Therefore blade profiles have to be chosen with the least reduction in power loading at lower collectives.

8. By replacing a tapered planform blade with a rectangular blade of same rotor chord, the control moment was increased by about 30%, without significant penalty in hover performance at lower collectives.

9. It was found that the control moment increased linearly with operating thrust while the pitching moment saturated at higher thrust levels. Therefore for a given shroud area, the control margin of the shrouded rotor increases at higher operating thrusts.

10. For the gust disturbance tests, the unshrouded and shrouded rotor vehicles were mounted on a spherical bearing setup to allow for pitch and roll motion while restricting it in translation. With an 8" diameter fan (with flow straighteners), the shrouded rotor vehicle could tolerate edgewise gusts of up to 6 m/s. The mean settling time after an input disturbance was less than 5 s.

11. The wind tunnel setup was viewed as a source of edgewise gust when the vehicle is operating near a large window. When the edgewise flow was introduced, the shrouded rotor developed a higher nose-up attitude error than the unshrouded rotor. This means that the shrouded rotor would have a larger tilt of the thrust vector in its initial response to an edgewise gust. The mean settling time after the introduction of the disturbance was about 5 s for both the vehicles. The shrouded rotor could tolerate up to 3 m/s gusts while the tolerance was greater than 5 m/s for the unshrouded rotor.

12. Free flight tests on the vehicle, using VICON for feedback control, indicated the capability of the vehicle to recover from gust impulse inputs from a pedestal fan. When exposed to edgewise flow, the vehicle could tolerate up to 3 m/s of wind speed. The circular error probable of the vehicle trajectory was up to 15 times at 3m/s as compared to the no wind case. This re-iterates the enhanced sensitivity of the shrouded rotor to edgewise

flow.

7.2   Future Work

The present vehicle incorporates a two bladed hingeless rotor due to the relative simplicity in integrating cyclic control. CFD studies suggest that a major portion of the suction pressure on the shroud surface is due to the pressure peak at the instant a rotor blade passes a given location. Therefore, by increasing the number of rotor blades, the number of suction pressure peaks can be increased that can potentially improve hover performance. In addition to hover performance, the effect of rotor control moment for a given operating thrust can be measured as a function of number of blades. The generation of the adverse pitching moments also will be affected. A systematic measurement of all these effects will be an interesting and useful study.

A relatively simplified attitude dynamics model was identified in this research with the yaw DOF decoupled. An obvious improvement for this would be to improve the model fidelity by including higher order effects. It would be useful to extend it to a 6 DOF model by incorporating translational DOF and measure the effect of the longitudinal and lateral moment derivatives on the vehicle dynamics. By appropriately filtering these effects into the feedback controller, the vehicle response to a generalized gust disturbance can be improved. This will also help in vehicle transition to forward flight, which is another flight regime not explored in this research.

Control moment of the vanes were measured to be lower than a typical conventional tail rotor. Mechanisms to improve this (either by imposing a higher rotor downwash or vane area) need to be investigated. This will be required as

the vehicle enters into more demanding flight operations.

Onboard computation of Euler angles and rates would enable increased closed loop control bandwidth. This would potentially improve disturbance rejection characteristics of the vehicle.

Flight performance in uniform, steady edgewise flow was investigated in this work. This can be extended to more complicated, time varying rotational flow fields that typically exist in outdoor conditions.

A low disk loading for the rotor is beneficial for good hover performance, but is deterimental to flight stability in disturbed flow. This trade-off can be measured and verified using different shrouded rotor sizes and operating thrust levels.

Finally, the utility of the shrouded rotor should be assessed at smaller scales (3" and below) with a focus on the trade-off between thrust improvement and material weight penalty. Due to the ubiquity of quad rotor systems today, it would seem worthwhile to extend the performance benefits of a shrouded rotor to a micro quad rotor configuration.

Bibliography

[1] McMichael, J.M, and Francis, USAF (Ret.), C. M. S., "Micro Air Vehicles: Toward a New Dimension in Flight, " *U.S Department of Defense Weaponse Systems Technology Information Analysis Center (WSTIAC) Newsletter*, Vol. 1, No. 1-3, Jan-Jul 2000.

[2] D.W. Beekman, J.N. Mait and T. L. Dogliaski, "Micro Autonomous Systems and Technology at the Army Research Laboratory, " in Proceedings of the National Aerospace and Electronics Conference 2008.

[3] Grasmeyer, J., and Keenon, M.,"Development of the Black Widow Micro Air Vehicle," AIAA Paper 2001-0127, Jan. 2001.

[4] Morris, S. J., "Design and Flight Test Results for Micro-Sized Fixed- Wing and VTOL Aircraft," 1st International Conference on Emerging Technologies for Micro Air Vehicles, 1997, pp. 117-131.

[5] Ifju, P. G., Jenkins, D. A., Ettinger, S., Lian, Y., Shyy, W. and Waszak, M. R., "Flexible-Wing-Based Micro Air Vehicles," 40th AIAA Aerospace Sciences Meeting and Exhibit, Reno, Nevada, January 2003.

[6] Peterson, B., Erath, B., Henry, K., Lyon, M., Walker, B., Powell, N., Fowkes, K. and Bowman, W. J., "Development of a Micro Air Vehicle for Maximum Endurance and Minimum Size," 41st AIAA Aerospace Sciences Meeting and Exhibit, Reno, Nevada, January 2003.

[7] Stewart, K.C., Blackburn, K., Wagener, J., Czabaranek, J., and Abate, G., "Development and Initial Flight Tests of a Single-Jointed Articulated-wing Micro Air Vehicle," AIAA Atmospheric Flight Mechanics Conference and Exhibit, Honolulu, Hawaii, August, 2008.

[8] Kroo, I., and Kunz, P., "Meso-Scale Flight and Miniature Rotorcraft Development," Fixed and Flapping Wing Aerodynamics for Micro Air Vehicle Applications, edited by T. J. Mueller, Progress in Astronautics and Aeronautics, AIAA, Reston, VA, 2001, pp. 503-517.

[9] Young, L. A., Aiken, E.W., Johnson, J. L., Demblewski, R., Andrews, J., and Klem, J., "New Concepts and Perspectives on Micro-Rotorcraft and Small Autonomous Rotary Wing Vehicles," Proceedings of the 20th AIAA Applied Aerodynamics Conference, AIAA, Reston, VA; also AIAA Paper 2002-2816, June 2002.

[10] Bohorquez, F., Samuel, P., Sirohi, J., Pines, D., Rudd, L., and Perel, R., "Design, Analysis and Hover Performance of a Rotary Wing Micro Air Vehicle," Journal of the American Helicopter Society, Vol. 48, No. 2, Apr 2003, pp. 8090.

[11] Sirohi, J., Tishchenko, M., and Chopra, I., "Design and Testing of a Micro-Aerial Vehicle with a Single Rotor and Turning Vanes," American Helicopter Society 61st Annual Forum Proceedings, Grapevine, TX, Jun 13, 2005.

[12] Pines, D., and Bohorquez, F., "Challenges Facing Future Micro-Air-Vehicle Development," Journal of Aircraft, Vol. 43, (2), March/April 2006, pp. 290 305.

[13] Deal. N.C. and Huang, P.A., "Remote Control Hovering Ornithopter," 46th AIAA Aerospace Sciences Meeting and Exhibit, Reno, Nevada, Jan., 2008.

[14] Grauer, J., and Hubbard, J., "Inertial Measurements from Flight Data of a Flapping-Wing Ornithopter," *Journal of Guidance, Control and Dynamics*, Vol. 32, No. 1, pp. 326-331.

[15] Kinkade, S., "Hobby Technik," www.appingight.com, 2008.

[16] Ellington, C. P., "The Aerodynamics of Hovering Insect Flight," Philosophical Transanctions of the Royal Society of London Series B, Vol. 305, No. 1122, Feb 1984, pp 1-181.

[17] Dickinson, M. H. and Gotz, K. G., "Unsteady Aerodynamic Performance of Model Wings at Low Reynolds Numbers," *Journal of Experimental Biology*, Vol. 174, 1993, pp. 45-64.

[18] Singh, B., and Chopra, I., Insect-Based Hover-Capable Flapping Wings for Micro Air Vehicles: Experiments and Analysis, *AIAA Journal*, Vol. 46, No. 9, 2008, pp. 21152135.

[19] Shyy, W., Berg, M., and Ljungqvist, D., Flapping and Flexible Wings for Biological and Micro Air Vehicles, Progress in Aerospace Sciences, Vol. 35, No. 5, 1999, pp. 455506.

[20] Pornsin-Sirirak, T. N., Lee, S. W., Nassef, H., Grasmeye, J., Tai, Y. C., Ho, C.M., and Keennon, M., "MEMS Wing Technology for a Battery-Powered Ornithopter," Proceedings of the 13th IEEE Annual International Conference on MEMS 2000, pp. 779-804.

[21] Kornbluh, R., "Project Mentor: Biologically Inspired Platform," Keynote Presentation at the 8th AIAA/CEAS Aeroacoustics Conference, 17-19 June 2002, Breckenridge, Colorado.

[22] Zdunich, P., Bilyk, D., MacMaster, M., Loewen, D., DeLaurier, J., Kornbluh, R., Low, T., Stanford, S., and Holeman, D., "Development and Testing of the Mentor Flapping-wing Micro Air Vehicle," *Journal of Aircraft*, Vol. 44, No. 5, September- October 2007, pp. 1708-1711.

[23] R. J. Wood, "Design, fabrication, and analysis, of a 3DOF, 3 cm flapping wing MAV," in Proc. IEEE/RSJ Int. Conf. Intell. Robots Syst., San Diego, CA, Oct. 2007, pp. 15761581.

[24] Nano Hummingbird: http://www.avav.com/uas/adc/nano/

[25] Baxter, D.R.J., East, R.A., "A Survey of Some Fundamental Issues in Micro- Air-Vehicle Design," Proceedings 14th UAVs - Unmanned Air Vehicle Systems International Conference, United Kingdom; 12-14 Apr. 1999. pp. 34.1-34.13. 1999.

[26] Anderson, G., "Fundamental Physics of Micro Air Vehicles: Challenges and Opportunities," Nano Air Vehicle Program, September, 2005.

[27] Leishman, J. G., *Principles of Helicopter Aerodynamics*, 1st ed., Cambridge Aerospace Series. Cambridge University Press, New York, NY, 2000.

[28] McMasters, J. H., and Henderson, M. L., Low Speed Single Element Airfoil Synthesis, *Technical Soaring*, Vol. 6, No. 2, 1980, pp. 121.

[29] Laitone, E.V., "Aerodynamic Lift at Reynolds Numbers Below 70,000," AIAA Journal, Vol. 34, No. 9, pp 1941-1942.

[30] Laitone, E.V., "Wind Tunnel Tests of Wings at Reynolds Numbers Below 70000," Experiments in Fluids Vol. 23, 1997, pp 405-409.

[31] Pelletier, A. and Mueller, T.J., "Low Reynolds Number Aerodynamics of Low- Aspect-Ratio, Thin/Flat/Cambered-Plate Wings," Journal of Aircraft, Vol. 37, No. 5, pp. 825-832, September-October 2000.

[32] Schmitz, F. W., "Aerodynamics of Model Aircraft wing Measurements I," R.T.P. Translation No 2460. Issued by Ministry of Aircraft Production. 1983.

[33] Bohorquez, F., *Rotor Hover Performance And System Design Of An Efficient Coaxial Rotary Wing Micro Air Vehicle* PhD thesis, University of Maryland, College Park, Department of Aerospace Engineering, 2007.

[34] Hein, B. R., and Chopra, I., "Hover Performance of a Micro Air Vehicle: Rotors at Low Reynolds Number," Journal of the American Helicopter Society, Vol. 52, No. 3, Jul 2007, pp. 254262.

[35] Bohorquez, F., and Pines, D., "Hover Performance of Rotor Blades at Low Reynolds Numbers for Rotary Wing Micro Air Vehicles: An Experimental Study," American Helicopter Society 59th Annual Forum Proceedings, Phoenix, AZ, May 68, 2003.

[36] Ramasamy, M., Leishman, J. G., and Lee, T. E., "Flow Field of a Rotating Wing MAV," *Journal of Aircraft*, Vol. 44, (4), July 2007, pp. 12361244.

[37] Ramasamy, M., Johnson, B., and Leishman, J. G., "Understanding the Aerodynamic Efficiency of a Hovering Micro-Rotor," *Journal of the American Helicopter Society*, Vol. 53, (4), October 2008, pp. 412428.

[38] Schroeder, E., and Baeder, J. D., "Using Computational Fluid Dynamics for Micro-Air Vehicle Airfoil Validation and Prediction," AIAA 2005-4841, 23rd AIAA Applied Aerodynamics Conference, Toronto, Canada, June 69, 2005.

[39] Lakshminarayan, V. K. and Baeder, J. D., "Computation Investigation of Micro Hovering Rotor Aerodynamics," *Journal of the American Helicopter Society*, Vol. 55, No. 2, April 2010, pp. 220001-25.

[40] Mettler, B., *Identification Modeling and Characteristics of Small Scale Rotorcraft*, Kluwer Academic Publishers, 2003.

[41] Weilenmann, M.W., Christen, U., and Geering, H.P., "Robust Helicopter Position Control at Hover, " Proceedings of the 1994 American Control Conference, Baltimore, MD, June, 1994, pp. 2491-2495.

[42] Gavrilets, V., Mettler, B., and Feron, E., "Nonlinear Model for a Small-Size Acrobatic Helicopter," AIAA 2001-4333, Proceedings of the AIAA Guidance, Navigation and Control Conferece, Montreal, Canada, Aug, 2001.

[43] Gavrilets, V., Mettler, B., and Feron, E., "Control Logic for Automated Aerobatic Flight of a Miniature Helicopter," Proceedings of the AIAA Guidance, Navigation and Control Conferece, Monterey, CA, Aug, 2002.

[44] Prasad, J.V.R., Calise, A.J., Corban, J.E., and Pei, Y., "Adaptive Nonlinear Controller Synthesis and Flight Test Evaluation on an Unmanned Helicopter," IEEE International Conference on Control Applications, 1999.

[45] Mettler, B., Tischler. M., and Kanade, T., "System Identification of Small-Size Unmanned Helicopter Dynamics," American Helicopter Society 55th Annual Forum Proceedings, Montreal, Quebec, Canada, May 25-27, 1999, Vol. 2, pp.1706-1717.

[46] Cheng, R.M., Tischler, M., and Schulei, G., "R-MAX Helicopter State-Space Model Identification in Hover and Forward-Flight," Journal of the American Helicopter Society, Vol. 51, (2), April 2006, pp. 202-210.

[47] Tischler, M., Fletcher,J. and Morris,P., "Applications of Flight Control System Methods to an Advanced Combat Rotorcraft," NASA Technical Memorandum 101054, 1989.

[48] Conroy, J.K., Humbert, S.J., and Pines, D.J., "System Identification of a Rotary-Wing Micro Air Vehicle," *Journal of the American Helicopter Society*, Vol. 56, (2), Apr 2011, pp. 1-4.

[49] LaCivita, M., Papageorgious, G., Messner, W.C., and Kanade, T., "Design and Flight Testing of a High-Bandwidth H_∞ Loop Shaping Controller for a Robotic Helicopter, " AIAA-2002-4836, AIAA Guidance, Navigation and Control Conference, Monterey, CA, Aug., 2002.

[50] Pereira, J. L., *Hover and Wind-Tunnel Testing of Shrouded Rotors for Improved Micro Air Vehicle Design* Ph.D Thesis, Department of Aerospace Engineering, University of Maryland College Park, September 2008.

[51] Hamel, G., "Aeroplane," US Patent No. 1,463,694, Jul 31, 1923 Application filed Apr 4, 1922; Serial No. 549,576.

[52] Thurston, S., and Amsler, R. C., "Review of Marine Propellers and Ducted Propeller Propulsive Devices," Journal of Aircraft, Vol. 3, No. 3, MayJun 1966, pp. 255261.

[53] Kort, L., "Combined Device of a Ships Propeller Enclosed by a Nozzle," US Patent No. 2,030,375, Feb 11, 1936 Application filed Sep 7, 1933; In Germany Jul 25, 1933; Serial No. 688,505.

[54] Stipa, L., "Stipa Monoplane with Venturi Fuselage," NACA TM 753, Washington, DC, Sep 1934 Translated from Rivista Aeronautica, Vol. IX, No. 7, pp. 1337, Jul 1933.

[55] Stipa, L., "Experiments with Intubed Propellers," NACA TM 655, Jan 30, 1932 Translated from LAerotecnica (Rome), pp. 923-953, Aug 1931.

[56] Robertson, A.C., and Stuart, J., "Vertical Take-off Flying Platform," United States Patent US 2,953,321, Sep. 20, 1960.

[57] Web source: http://www.piasecki.com/geeps$_p$a59k.php

[58] Web source: http://www.aviastar.org/helicopters$_e$ng/doak$_v$z − 4.php

[59] Web Source: http://aerospaceweb.org/aircraft/research/x22/

[60] Web source: http://www.flightglobal.com/pdfarchive/view/1964/1964%20-%202594.html

[61] Web source: http://www.aiaa.org/tc/vstol/unbuilt/vanguard/

[62] Lazareff, M., "Aerodynamics of Shrouded Propellers," The Aerodynamics of V/STOL Aircraft, AGARD-VKI Lecture Series, AGARDograph 126, Rhode- Saint-Genese, Belgium, May 1317, 1968, P. E. Colin and J. Williams, Eds., no. D, AGARD and Von Karman Institute, pp. 237289.

[63] Gerdes, R.M., "Lift-Fan Aircraft - Lessons Learned from XV-5 flight experience," AIAA-1993-4838, AIAA International Powered Lift Conference, Santa Clara, CA, Dec 1-3, 1993.

[64] Web source: http://www.ae.msstate.edu/rfrl/pages/marvel.html

[65] Web source: http://www.piasecki.com/compound$_1$6h1a.php

[66] Mouille, R., "The Fenestron, Shrouded Tail Rotor of the SA.341 Gazelle," Journal of the American Helicopter Society, Vol. 15, No. 4, Oct 1970, pp. 31 37.

[67] Mouille, R., and dAmbra, F., "The Fenestron A Shrouded Tail Rotor Concept for Helicopters," American Helicopter Society 42nd Annual Forum Proceedings, Washington, D.C., Jun 25, 1986, pp. 597606.

[68] Vuillet, A., "Operational Advantages and Power Efficiency of the Fenestron as Compared to a Conventional Tail Rotor," Vertiflite, Vol. 35, No. 5, Jul/Aug 1989, pp. 2429.

[69] Niwa, Y., "The Development of the New Observation Helicopter (XOH-1)," AHS International 54th Annual Forum Proceedings, Washington, D.C., May 2022, 1998, pp. 12851297.

[70] "Airborne Remotely Operated Device (1982-1988)," World-Wide Web document, http://www.spawar.navy.mil/robots/air/arod/arod.html, Dec 10, 1999.

[71] Thornberg, C. A., and Cycon, J. P., "Sikorsky Aircrafts Unmanned Aerial Vehicle, Cypher: System Description and Program Accomplishments," American Helicopter Society 51st Annual Forum Proceedings, FortWorth, TX, May 911, 1995, pp. 804811.

[72] Walsh, D., and Cycon, J. P., "The Sikorsky Cypher(R) UAV: A Multi-Purpose Platform with Demonstrated Mission Flexibility," AHS International 54th Annual Forum Proceedings, Washington, D.C., May 2022, 1998, pp. 1410 1418.

[73] Mraz, S.J., *Machine Design*, Penton Media Publication, New York, NY, Dec 9, 2009, pp. 48.

[74] Lipera L., Colbourne J. D., Tischler M. B., Hossein Mansur M., Rotkowitz M.C., and Patangui P., "The Micro Craft ISTAR Micro-Air Vehicle: Control System Design and Testing," American Helicopter Society 57th Annual Forum Proceedings, Washington, DC, May 9-11, 2001.

[75] Johnson,E., and Turbe,M., "Modeling, Control and Flight Testing of a Small Ducted Fan Aircraft," AIAA-2005-6281, AIAA Guidance, Navigation, and Control Conference and Exhibit, San Francisco, CA, Aug. 15-18, 2005.

[76] Hrishikeshavan, V., Sirohi, J., Tishchenko, M., and Chopra, I., "Design, Development and Testing of a Shrouded Rotor Micro Air Vehicle with Anti Torque Vanes," Journal of the American Helicopter Society, Vol. 56, (1), Jan. 2011, pp. 1-11.

[77] Sacks, A. H., and Burnell, J. A., "Ducted Propellers A Critical Review of the State of the Art," In Progress in Aeronautical Sciences, A. Ferri, D. Kuchemann, and L. H. G. Sterne, Eds., Vol. 3. Pergammon Press, The Macmillan Company, New York, NY, 1962, Ch. Part 2, pp. 85135.

[78] Krüger, W., "On Wind Tunnel Tests and Computations Concerning the Problem of Shrouded Propellers," NACA TM 1202, Feb 1949 Translation of ZWB Forschungsbericht Nr. 1949, Aerodynamischen Versuchsanstalt (AVA), Gottingen, Germany, Jan 21, 1944.

[79] Soloviev, U.I., Churmack, D.A. *Marine Propulsion Devices*. Pub. by Military Publishing House, Ministry of the Armed Forces, Moscow, USSR, 1948. Translated by Rose Jermain, University of Alabama, March, 1951.

[80] van Manen, J.D., "Recent research on propellers in Nozzles", Journal of Ship Research, pp. 13-46, July, 1957.

[81] Küchemann, D., and Weber, J., "The Flow over Annular Aerofoils. Report No. VII - The Shrouded Propeller," Translated and issued by TPA3, Technical Information Bureau for Chief Scientist, Ministry of Supply, Great Britaine. (NASA N-109).

[82] Regenscheit, B., " Standschubmessungen an zwei ummantel-tenLuftschrauben," AVA Report No. 42/W/32, Sep. 7, 1942.

[83] Platt, Jr., R. J., "Static Tests of a Shrouded and an Unshrouded Propeller," NACA RM L7H25, Langley Memorial Aeronautical Laboratory, Langley Field, VA, Feb 9 1948.

[84] Hubbard, H. H., "Sound Measurements for Five Shrouded Propellers at Static Conditions," NACA TN 2024, Langley Memorial Aeronautical Laboratory, Langley Field, VA, Apr 1950.

[85] Mort, K. W., "Summary of Large-Scale Tests of Ducted Fans," Conference on V/STOL and STOL Aircraft, Ames Research Center, Moffett Field, CA, Apr 1966, no. 8 in NASA-SP-116, NASA, pp. 97113.

[86] Mort, K. W., and Gamse, B., "A Wind-Tunnel Investigation of a 7-Foot-Diameter Ducted Propeller," NASA TN D-4142, Ames Research Center, Moffett Field, CA, Aug 1967.

[87] Parlett, L. P., "Aerodynamic Characteristics of a Small-Scale Shrouded Propeller at Angles of Attack from 0^0 to 90^0," NACA TN 3547, Langley Memorial Aeronautical Laboratory, Langley Field, VA, Nov 1955.

[88] Taylor, R. T., "Experimental Investigation of the Effects of Some Shroud Design Variables on the Static Thrust Characteristics of a Small-Scale Shrouded Propeller Submerged in a Wing," NACA TN 4126, Langley Memorial Aeronautical Laboratory, Langley Field, VA, Jan 1958.

[89] Black, D. M., Wainauski, H. S., and Rohrbach, C., "Shrouded Propellers A Comprehensive Performance Study," AIAA 5th Annual Meeting and Technology Display, Philadelphia, PA, Oct 2124, 1968, no. AIAA-68-994, AIAA.

[90] Lee, T., *Design and Performance of a Ducted Coaxial Rotor in Hover and Forward Flight* MS Thesis, Department of Aerospace Engineering, University of Maryland College Park, 2010.

[91] Cycon, J. P., Rosen, K. M., and Whyte, A. C., "Unmanned Flight Vehicle Including Counter Rotating Rotors Positioned Within a Toroidal Shroud and Operable to Provide All Required Vehicle Flight Controls," US Patent No. 5,152,478, Oct 6, 1992 Filed May 18, 1990.

[92] Gupta, N., and Plump, J., "Design of a VTOL Micro Air Vehicle that Incorporates Counter-Rotating, Reversible Thrust Propellers," AUVSI Unmanned Systems Conference, Baltimore, MD, Jul 31 Aug 2, 2001.

[93] Dyer, K. G., *Aerodynamic Study of a Small, Ducted VTOL Aerial Vehicle* PhD thesis, Massachusetts Institute of Technology, Department of Aeronautics and Astronautics, Cambridge, MA, Jun 2002.

[94] Martin, P., and Tung, C., "Performance and Flowfield Measurements on a 10- inch Ducted Rotor VTOL UAV," American Helicopter Society 60th Annual Forum Proceedings, Baltimore, MD, Jun 710, 2004.

[95] Martin, P. B., and Boxwell, D. A., "Design, Analysis and Experiments on a 10-inch Ducted Rotor VTOL UAV," AHS International Specialists Meeting on Unmanned Rotorcraft: Design, Control and Testing, Chandler, AZ, Jan 1820, 2005.

[96] Graf, W., Fleming, J., and Gelhausen, P., "Ducted Fan Aerodynamics in Forward Flight," AHS International Specialists Meeting on Unmanned Rotorcraft: Design, Control and Testing, Chandler, AZ, Jan 1820, 2005.

[97] Yaggy, P. F., and Goodson, K. W., "Aerodynamics of a Tilting Ducted Fan Configuration," NASA TN D-785, Ames Research Center, Moffett Field, CA and Langley Research Center, Langley, VA, Mar 1961.

[98] Yaggy, P. F., and Mort, K. W., "A Wind-Tunnel Investigation of a 4-Foot-Diameter Ducted Fan Mounted on the Tip of a Semispan Wing," NASA TN D-776, Ames Research Center, March 1961.

[99] Grunwald, K. J., and Goodson, K. W., "Aerodynamic Loads on an Isolated Shrouded-Propeller Configuration for Angles of Attack from -10^0 to 110^0," NASA TN D-995, Langley Research Center, Jan 1, 1962.

[100] Grunwald, K. J., and Goodson, K. W., "Division of Aerodynamic Loads on a Semispan Tilting Ducted-Propeller Model in Hovering and Transition Flight," NASA TN D-1257, Langley Research Center, May 1, 1962.

[101] Fletcher, H. S., "Experimental Investigation of Lift, Drag and Pitching Moment of Five Annular Airfoils," NACA TN 4117, Langley Memorial Aeronautical Laboratory, Langley Field, VA, Oct 1957.

[102] Moser, H. H., "Some Effects of the Shroud on the Forward Flight Performance of the Lifting Fan," Journal of the American Helicopter Society, Vol. 4, No. 2, Apr 1959, pp. 3944.

[103] Spreemann, K. P., "Wind-Tunnel Investigation of Longitudinal Aerodynamic Characteristics of a Powered Four-Duct-Propeller VTOL Model in Transition," NASA TN D-3192, Langley Research Center, Langley Station, Hampton, VA, Apr 1966.

[104] Giulianetti, D. J., Biggers, J. C., and Maki, R. P., "Longitudinal Aerodynamic Characteristics in Ground Effect of a Large-Scale, V/STOL Model with Four Tilting Ducted Fans Arranged in a Dual Tandem Configuration," NASA NASA TN-D-4218, Ames Research Center, Moffett Field, CA, Oct 1967.

[105] Weir, R. J., "Aerodynamic Design Considerations for a Free-Flying Ducted Propeller," AIAA Atmospheric Flight Mechanics Conference, Minneapolis, MN, Aug 1988, no. AIAA-88-4377, pp. 420431.

[106] Fleming, J., Jones, T., Lusardi, J., Gelhausen, P., and Enns, D., "Improved Control of Ducted Fan UAVs in Crosswind Turbulence," AHS 4th Decennial Specialists Conference on Aeromechanics, San Francisco, CA, Jan 2123, 2004.

[107] Pereira, J., and Chopra, I., "Performance and Surface Pressure Measurements on a MAV-Scale Shrouded Rotor in Translational Flight," American Helicopter Society 63rd Annual Forum, Virginia beach, Virginia, May 2007.

[108] Kuchemann, D., and Weber, J., "Concerning the Flow About Ring-Shaped Cowlings, Parts I-XIII," NACA TM 1325-1360, 1951-1953.

[109] Kriebel, A. R., "Theoretical Stabiity Derivatives for a Ducted Propeller," Journal of Aircraft, Vol. 1, No. 4, JulAug 1964, pp. 203210.

[110] Mendenhall, M. R., and Spangler, S. B., "Theoretical Study of Ducted Fan Performance," NASA CR 1494, Jan 1, 1970.

[111] Mendenhall, M. R., and Spangler, S. B., "A Computer Program for the Prediction of Ducted Fan Performance," NASA CR 1495, Feb 1, 1970.

[112] Fairchild, J. E., Batra, N. N., and Stewart, R. L., "Influence of Design Parameters on Fan-in-Fin Static Performance," American Helicopter Society 29th Annual National Forum, May 1973.

[113] Goodman, T. R., "The Tip Correction for Wind-Tunnel Tests of Propellers," Journal of the Aeronautical Sciences, Vol. 23, No. 12, Dec 1956, pp. 10941098.

[114] Clark, D. R., "Aerodynamic Design Rationale for the Fan-in-Fin on the S-67 Helicopter," American Helicopter Society 31st Annual National Forum, Washington, D.C., May 1315, 1975, no. Preprint No. 904.

[115] Wright, G. P., Driscoll, J. T., and Nickerson, Jr., J. D., "Handling Qualities of the H-76 FANTAIL TM Demonstrator," American Helicopter Society 47th Annual Forum Proceedings, 1991, pp. 123135.

[116] Guerrero, I., Londenberg, K., Gelhausen, P., and Myklebust, A., "A Powered Lift Aerodynamic Analysis for the Design of Ducted Fan UAVs," 2nd AIAA Unmanned Unlimited Systems, Technologies and Operations Aerospace, San Diego, CA, Sep 1518, 2003, no. AIAA-2003-6567.

[117] Rajagopalan, R. G., and Zhaoxing, Z., "Performance and Flow Field of a Ducted Propeller," AIAA/ASME/SAE/ASEE 25th Joint Propulsion Conference, Monterey, CA, Jul 1012, 1989, no. AIAA-89-2673.

[118] Vuillet, A., and Morelli, F., "New Aerodynamic Design of the Fenestron for Improved Performance," Twelfth European Rotorcraft Forum, Garmisch-Partenkirchen, Federal Republic of Germany, Sep 2225, 1986, no. Paper No.8.

[119] Rajagopalan, R. G., and Zhaoxing, Z., "Performance and Flow Field of a Ducted Propeller," AIAA/ASME/SAE/ASEE 25th Joint Propulsion Conference, Monterey, CA, Jul 1012, 1989, no. AIAA-89-2673.

[120] Rajagopalan, R. G., and Keys, C. N., "Detailed Aerodynamic Design of the RAH-66 FANTAILTM Using CFD," American Helicopter Society 49th Annual Forum Proceedings, St. Louis, MO, May 1921, 1993, pp. 11931206.

[121] Ruzicka, G. C., Strawn, R. C., and Meadowcroft, E. T., "Discrete Blade CFD Analysis of Ducted Tail Fan Flow," 42nd AIAA Aerospace Sciences Meeting and Exhibit, Reno, NV, Jan 58, 2004, no. AIAA-2004-48.

[122] Lee, H. D., Kwon, O. J., and Joo, J., "Aerodynamic Performance Analysis of a Helicopter Shrouded Tail Rotor Using an Unstructured Mesh Flow Solver," 5th Asian Computational Fluid Dynamics, Busan, Korea, Oct 2730, 2003, no. Paper No. 8.

[123] Ahn, J., and Lee, K., "Performance Prediction and Design of a Ducted Fan System," 40th AIAA/ASME/SAE/ASEE Joint Propulsion Conference and Exhibit, Fort Lauderdale, FL, Jul 1114, 2004, no. AIAA-2004-4196.

[124] Lakshminarayan, V. and Baeder, J., "Computational Investigation of a Micro-Scale Shrouded Rotor Aerodynamics in Hover," American Helicopter Society Specialists Meeting on Aeromechanics, San Francisco, CA, Jan 20-22, 2010.

[125] Abrego, A. I., and Bulaga, R. W., "Performance Study of a Ducted Fan System," American Helicopter Society Aerodynamics, Acoustics, and Test and Evaluation Technical Specialists Meeting, San Francisco, CA, Jan 2325, 2002.

[126] Piasecki, F. N., 1965, "Flying platform," U.S. Patent No: 3184183.

[127] Boyd, E. S., Mallory, M., and Skinner, L. R., 1970, "Vertical takeoff and landing aircraft," U.S. Patent No: 3519224.

[128] Moller, P. S., 1989, "Robotic or remotely controlled flying platform," U.S. Patent No: 4795111.

[129] Yoeli, R., 2007, "Ducted fan vehicles particularly useful as vtol air- craft," U.S. Patent No: 7275712.

[130] Cycon, J. P., Scott, M. W., and DeWitt, C. W., 2001, "Method of reducing a nose-up pitching moment on a ducted unmanned aerial ve- hicle," U.S. Patent No: 6170778.

[131] Kondor. S., M. Heiges, ."Active Flow Control For Control of Ducted Rotor Systems," AIAA Paper 2001-117, Proceedings, 39th AIAA Aerospace Sciences Meeting & Exhibit, January 8-11, 2001, Reno, Nevada, 2001.

[132] Fung, P. H., M. Amitay, "Control of a Miniducted-Fan Unmanned Aerial Vehicle Using Active Flow Control," Journal of Aircraft, Vol. 39, No. 4, 2002, pp. 561-571.

[133] Ohanian, O.J., *Ducted Fan Aerodynamics and Modeling, with Applications of Steady and Synthetic Jet Flow Control* PhD thesis, University of Virginia, Blacksburg, Department of Mechanical Engineering, 2011.

[134] Camci. C., and Akturk, A., "Double Duct Fan," A technology description document, Department of Aerospace Engineering, Pennsylvania State University, Sep. 2010.

[135] Binetti. P., Trouchet. D., Pollini. L., Innocenti. Mario., Hamel. T., and Bras. F.L., "The Flight Control System of the Hovereye VTOL UAV," Symposium for Platform Innovations and System Integration for Unmanned Air, Land and Sea Vehicles, May, 2007, Neuilly-sur-Seine, France.

[136] W.B. Dunbar, M.B. Milam, R. Franz, and R. M. Murray, " Model predictive control of a thrust-vectored flight control experiment," In 15th IFAC World Congress, 2002.

[137] Franz, R., M. Milam, and J. Hauser, "Applied Receding Horizon Control of the Caltech Ducted Fan, " Proceedings of the American Control Conference, Anchorage, AK, May 8-10, 2002.

[138] Pflimlin, J. M., P. Soures, and T. Hamel, "Hovering Flight Stabilization in Wind Gusts for Ducted Fan UAV," 43rd IEEE Conference on Decision and Control, Atlantis, Paradise Island, Bahamas, December 14-17, 2004.

[139] Hess, R. A., and Ussery, T. M., "Frequency-domain sliding mode design technique applied to the control of a ducted fan micro-air vehicle," *Journal of the American Helicopter Society*, 49(1), 457467.

[140] Hess, R. A., and Bakhtiari-Nejad, M.," Sliding mode control of a nonlinear ducted-fan UAV model," In Proceedings of the AIAA guidance, navigation, and control conference and exhibit. Keystone, CO.,August 2124, 2006

[141] Spaulding, C. M., M. H. Nasur, M. B. Tischler, R. A. Hess, and J. A. Franklin, "Nonlinear Inversion Control for a Ducted Fan UAV," AIAA Paper 2005-6231, AIAA Atmospheric Flight Mechanics Conference and Exhibit, San Francisco, California, 15- 18 August 2005.

[142] Johnson, E.N., and Turbe, M., , "Modeling, Control, and Flight Testing of a Small- Ducted Fan Aircraft," *Journal of Guidance, Control, and Dynamics*, Vol. 29, No. 4, 2006, pp. 769-779.

[143] Li, D., "Flight Control Design for Ducted Fan VTOL UAV," Paper AIAA-2006-6714, AIAA Guidance, Navigation, and Control Conference and Exhibit, 21-24 August, Keystone, CO, 2006.

[144] Avanzini, G., U. Ciniglio, and G. de Matteis, "Full-Envelope Robust Control of a Shrouded-Fan Unmanned Vehicle," *Journal of Guidance, Control, and Dynamics*, Vol. 29, No. 2, March-April 2006.

[145] Peddle, I., and Jones,T.J.T., "Practical near hover flight control of a ducted fan," . *Control Engineering Practice*, Vol. 17,2009, pp. 4858.

[146] Pflimlin, J. M., Binetti, P., Soures, P., Hamel, T., Trouchet, D., "Modeling and attitude control analysis of a ducted-fan micro aerial vehicle," *Control Engineering Practice*, Vol. 18, 2010, pp 209-218.

[147] Tennekes, H., *The Simple Science of Flight*, MIT Press, Cambridge, MA, 1996.

[148] Nelson R. C., *Flight Stability and Automatic Control*, 1998, 2nd ed, McGraw-Hill, New York.

[149] Spedding, G.R., and Lissaman, P.B.S., "Technical aspects of microscale flight systems," *Proceedings of the International Symposium on Optimal Migration*, 2001.

[150] Holmes J. D., *Wind Loading of Structures*, 2001, Spon Press, London (ISBN 0-419-24610-X).

[151] Hoover A., "The size of Bluejays: Tiny planes to show their stuff in competition,", 1999 http://www.napa.ufl.edu/99news/MAV99.htm

[152] Jenkins, D.A., Ifju, P.G., Abdulrahim, M. and Olipra, S., " Assessment of controllability of Micro Air Vehicles," Proceedings of the 16th International Conference on UAVs, 2-4 April, 2001, Bristol, UK.

[153] Watkins, S., "Development of a Micro Air Vehicle," Proceedings of the 17th Bristol International Conference on Unmanned Air Vehicle Systems, April 8-10, 2002, Bristol University, UK.

[154] Milbank, J., Loxton, B.J., Watkins, S., and Melbourne, W.H., "Replication of Atmospheric Conditions for the Purpose of Testing MAVs," USAF Project No: AoARD 05-4075, Dec. 23, 2005.

[155] Watkins, S., Milbank, J., Loxton, B. J., and Melbourne, W. H., "Atmospheric winds and their implications for microair vehicles," *AIAA Journal* , Vol. 44(11), 2006, pp. 25912600.

[156] Loxton, B.J., Abdulrahim, M., and Watkins, S., "An Investigation of Fixed and Rotary Wing MAV Flight in Replicated Atmospheric Turbulence, " 46th AIAA Aerospace Sciences Meeting and Exhibit, Reno, Nevada, Jan., 2008.

[157] Patel, C. K. and Kroo, I., "Control Law Design for Improving UAV Performance using Wind Turbulence," AIAA Aerospace Sciences Meeting and Exhibit, AIAA Paper 2006-0231, Reno, Nevada, January 2006.

[158] Bieniawski, S. R., Halaas, D., and Vian, J.," Micro-Aerial Vehicle Flight in Turbulent Environments: Use of an Indoor Flight Facility, for Rapid Design and Evaluation," AIAA GNC Conference, Honolulu HI, August 18-21, 2008.

[159] Waslander, S., and Wang,C., " Wind disturbance estimation and rejec- tion for quadrotor position control," In AIAA Infotech@Aerospace Conference and AIAA Unmanned..Unlimited Conference, Seattle, Washington, Apr. 6-9, 2009.

[160] Patrick, B., *Optic flow based station-keeping and wind rejection for small flying vehicles*, MS Thesis, Department of Aerospace Engineering, University of Maryland College Park, 2010.

[161] Zarovy. S., Costello, M., Mehta,A., Gremillion, G., Miller, D., Ranganathan, B., Humbert, J.S., and Samuel, P., "Experimental Study of Gust Effects on Micro Air Vehicles," AIAA Atmospheric Flight Mechanics Conference, Toronto, Ontario, Aug. 2-5, 2010.

[162] Null, W., and Shkarayev,S., "Effect of Camber on the Aerodynamics of Adaptive-Wing Micro Air Vehicles," *Journal of Aircraft*, Vol. 42, (6), 2005, pp. 1543-1547.

[163] Woolfson. M et al., "Dependece of inertial measurements of distance on accelerometer noise," *Measurement Science Technology* Vol. 13, pp. 1163-1172, 2002.

[164] Morelli, E., "System Identification Programs for Aircraft (SIDPAC)," AIAA Atmospheric Flight Mechanics Conference, Monterey, CA, August, 2002.

[165] Skogestad, S. and Postlethwaite, I., "Multivariable Feedback Control," *Wiley Publishers*, 2005.

[166] Humbert, J.S., and Faruque, I., "Analysis of Insect-Inspired Wingstroke Kinematic Perturbatinos for Longitudinal Control," *Journal of Guidance, Control and Dynamics*, Vol. 34, (2), 2011, pp. 618-622.

[167] Zhou, K., Salomon, G., and Wu, E., "Balanced Realization and Model Reduction for Unstable Systems," *International Journal of Robust and Nonlinear Control*, Vol. 9, 1999, pp. 183-199.